

Advances in Civil Engineering

# Deformation Control and Long-term Safety Assessment of Soft Rock Tunnels

Lead Guest Editor: Guowen Xu

Guest Editors: Chunchi Ma and Ziquan Chen





---

**Deformation Control and Long-term Safety  
Assessment of Soft Rock Tunnels**

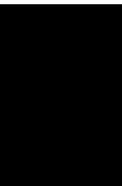
Advances in Civil Engineering

---

## **Deformation Control and Long-term Safety Assessment of Soft Rock Tunnels**

Lead Guest Editor: Guowen Xu

Guest Editors: Chunchi Ma and Ziquan Chen



---

Copyright © 2022 Hindawi Limited. All rights reserved.

This is a special issue published in "Advances in Civil Engineering." All articles are open access articles distributed under the Creative Commons Attribution License, which permits unrestricted use, distribution, and reproduction in any medium, provided the original work is properly cited.




# Chief Editor

Cumaraswamy Vipulanandan, USA














## Associate Editors

Chiara Bedon , Italy  
Constantin Chalioris , Greece  
Ghassan Chehab , Lebanon  
Ottavia Corbi, Italy  
Mohamed ElGawady , USA  
Husnain Haider , Saudi Arabia  
Jian Ji , China  
Jiang Jin , China  
Shazim A. Memon , Kazakhstan  
Hossein Moayedi , Vietnam  
Sanjay Nimbalkar, Australia  
Giuseppe Oliveto , Italy  
Alessandro Palmeri , United Kingdom  
Arnaud Perrot , France  
Hugo Rodrigues , Portugal  
Victor Yepes , Spain  
Xianbo Zhao , Australia

## Academic Editors

José A.F.O. Correia, Portugal  
Glenda Abate, Italy  
Khalid Abdel-Rahman , Germany  
Ali Mardani Aghabaglou, Turkey  
José Aguiar , Portugal  
Afaq Ahmad , Pakistan  
Muhammad Riaz Ahmad , Hong Kong  
Hashim M.N. Al-Madani , Bahrain  
Luigi Aldieri , Italy  
Angelo Aloisio , Italy  
Maria Cruz Alonso, Spain  
Filipe Amarante dos Santos , Portugal  
Serji N. Amirkhanean, USA  
Eleftherios K. Anastasiou , Greece  
Panagiotis Ch. Anastasopoulos , USA  
Mohamed Moafak Arbili , Iraq  
Farhad Aslani , Australia  
Siva Avudaiappan , Chile  
Ozgur BASKAN , Turkey  
Adewumi Babafemi, Nigeria  
Morteza Bagherpour, Turkey  
Qingsheng Bai , Germany  
Nicola Baldo , Italy  
Daniele Baraldi , Italy

Eva Barreira , Portugal  
Emilio Bastidas-Arteaga , France  
Rita Bento, Portugal  
Rafael Bergillos , Spain  
Han-bing Bian , China  
Xia Bian , China  
Huseyin Bilgin , Albania  
Giovanni Biondi , Italy  
Hugo C. Biscaia , Portugal  
Rahul Biswas , India  
Edén Bojórquez , Mexico  
Giosuè Boscato , Italy  
Melina Bosco , Italy  
Jorge Branco , Portugal  
Bruno Briseghella , China  
Brian M. Broderick, Ireland  
Emanuele Brunesi , Italy  
Quoc-Bao Bui , Vietnam  
Tan-Trung Bui , France  
Nicola Buratti, Italy  
Gaochuang Cai, France  
Gladis Camarini , Brazil  
Alberto Campisano , Italy  
Qi Cao, China  
Qixin Cao, China  
Iacopo Carnacina , Italy  
Alessio Cascardi, Italy  
Paolo Castaldo , Italy  
Nicola Cavalagli , Italy  
Liborio Cavaleri , Italy  
Anush Chandrappa , United Kingdom  
Wen-Shao Chang , United Kingdom  
Muhammad Tariq Amin Chaudhary, Kuwait  
Po-Han Chen , Taiwan  
Qian Chen , China  
Wei Tong Chen , Taiwan  
Qixiu Cheng, Hong Kong  
Zhanbo Cheng, United Kingdom  
Nicholas Chileshe, Australia  
Prinya Chindaprasirt , Thailand  
Corrado Chisari , United Kingdom  
Se Jin Choi , Republic of Korea  
Heap-Yih Chong , Australia  
S.H. Chu , USA  
Ting-Xiang Chu , China




Zhaofei Chu , China  
Wonseok Chung , Republic of Korea  
Donato Ciampa , Italy  
Gian Paolo Cimellaro, Italy  
Francesco Colangelo, Italy  
Romulus Costache , Romania  
Liviu-Adrian Cotfas , Romania  
Antonio Maria D'Altri, Italy  
Bruno Dal Lago , Italy  
Amos Darko , Hong Kong  
Arka Jyoti Das , India  
Dario De Domenico , Italy  
Gianmarco De Felice , Italy  
Stefano De Miranda , Italy  
Maria T. De Risi , Italy  
Tayfun Dede, Turkey  
Sadik O. Degertekin , Turkey  
Camelia Delcea , Romania  
Cristoforo Demartino, China  
Giuseppe Di Filippo , Italy  
Luigi Di Sarno, Italy  
Fabio Di Trapani , Italy  
Aboelkasim Diab , Egypt  
Thi My Dung Do, Vietnam  
Giulio Dondi , Italy  
Jiangfeng Dong , China  
Chao Dou , China  
Mario D'Aniello , Italy  
Jingtao Du , China  
Ahmed Elghazouli, United Kingdom  
Francesco Fabbrocino , Italy  
Flora Faleschini , Italy  
Dingqiang Fan, Hong Kong  
Xueping Fan, China  
Qian Fang , China  
Salar Farahmand-Tabar , Iran  
Ilenia Farina, Italy  
Roberto Fedele, Italy  
Guang-Liang Feng , China  
Luigi Fenu , Italy  
Tiago Ferreira , Portugal  
Marco Filippo Ferrotto, Italy  
Antonio Formisano , Italy  
Guoyang Fu, Australia  
Stefano Galassi , Italy

Junfeng Gao , China  
Meng Gao , China  
Giovanni Garcea , Italy  
Enrique García-Macías, Spain  
Emilio García-Taengua , United Kingdom  
DongDong Ge , USA  
Khaled Ghaedi, Malaysia  
Khaled Ghaedi , Malaysia  
Gian Felice Giaccu, Italy  
Agathoklis Giaralis , United Kingdom  
Ravindran Gobinath, India  
Rodrigo Gonçalves, Portugal  
Peilin Gong , China  
Belén González-Fonteboa , Spain  
Salvatore Grasso , Italy  
Fan Gu, USA  
Erhan Güneyisi , Turkey  
Esra Mete Güneyisi, Turkey  
Pingye Guo , China  
Ankit Gupta , India  
Federico Gusella , Italy  
Kemal Hacıefendioğlu, Turkey  
Jianyong Han , China  
Song Han , China  
Asad Hanif , Macau  
Hadi Hasanzadehshooiili , Canada  
Mostafa Fahmi Hassanein, Egypt  
Amir Ahmad Hedayat , Iran  
Khandaker Hossain , Canada  
Zahid Hossain , USA  
Chao Hou, China  
Biao Hu, China  
Jiang Hu , China  
Xiaodong Hu, China  
Lei Huang , China  
Cun Hui , China  
Bon-Gang Hwang, Singapore  
Jijo James , India  
Abbas Fadhil Jasim , Iraq  
Ahad Javanmardi , China  
Krishnan Prabhakan Jaya, India  
Dong-Sheng Jeng , Australia  
Han-Yong Jeon, Republic of Korea  
Pengjiao Jia, China  
Shaohua Jiang , China

MOUSTAFA KASSEM , Malaysia  
Mosbeh Kaloop , Egypt  
Shankar Karuppannan , Ethiopia  
John Kechagias , Greece  
Mohammad Khajehzadeh , Iran  
Afzal Husain Khan , Saudi Arabia  
Mehran Khan , Hong Kong  
Manoj Khandelwal, Australia  
Jin Kook Kim , Republic of Korea  
Woosuk Kim , Republic of Korea  
Vaclav Koci , Czech Republic  
Loke Kok Foong, Vietnam  
Hailing Kong , China  
Leonidas Alexandros Kouris , Greece  
Kyriakos Kourousis , Ireland  
Moacir Kripka , Brazil  
Anupam Kumar, The Netherlands  
Emma La Malfa Ribolla, Czech Republic  
Ali Lakirouhani , Iran  
Angus C. C. Lam, China  
Thanh Quang Khai Lam , Vietnam  
Luciano Lamberti, Italy  
Andreas Lampropoulos , United Kingdom  
Raffaele Landolfo, Italy  
Massimo Latour , Italy  
Bang Yeon Lee , Republic of Korea  
Eul-Bum Lee , Republic of Korea  
Zhen Lei , Canada  
Leonardo Leonetti , Italy  
Chun-Qing Li , Australia  
Dongsheng Li , China  
Gen Li, China  
Jiale Li , China  
Minghui Li, China  
Qingchao Li , China  
Shuang Yang Li , China  
Sunwei Li , Hong Kong  
Yajun Li , China  
Shun Liang , China  
Francesco Liguori , Italy  
Jae-Han Lim , Republic of Korea  
Jia-Rui Lin , China  
Kun Lin , China  
Shibin Lin, China

Tzu-Kang Lin , Taiwan  
Yu-Cheng Lin , Taiwan  
Hexu Liu, USA  
Jian Lin Liu , China  
Xiaoli Liu , China  
Xuemei Liu , Australia  
Zaobao Liu , China  
Zhuang-Zhuang Liu, China  
Diego Lopez-Garcia , Chile  
Cristiano Loss , Canada  
Lyan-Ywan Lu , Taiwan  
Jin Luo , USA  
Yanbin Luo , China  
Jianjun Ma , China  
Junwei Ma , China  
Tian-Shou Ma, China  
Zhongguo John Ma , USA  
Maria Macchiaroli, Italy  
Domenico Magisano, Italy  
Reza Mahinroosta, Australia  
Yann Malecot , France  
Prabhat Kumar Mandal , India  
John Mander, USA  
Iman Mansouri, Iran  
André Dias Martins, Portugal  
Domagoj Matesan , Croatia  
Jose Matos, Portugal  
Vasant Matsagar , India  
Claudio Mazzotti , Italy  
Ahmed Mebarki , France  
Gang Mei , China  
Kasim Mermerdas, Turkey  
Giovanni Minafò , Italy  
Masoomah Mirrashid , Iran  
Abbas Mohajerani , Australia  
Fadzli Mohamed Nazri , Malaysia  
Fabrizio Mollaioli , Italy  
Rosario Montuori , Italy  
H. Naderpour , Iran  
Hassan Nasir , Pakistan  
Hossein Nassiraei , Iran  
Satheeskumar Navaratnam , Australia  
Ignacio J. Navarro , Spain  
Ashish Kumar Nayak , India  
Behzad Nematollahi , Australia

Chayut Ngamkhanong , Thailand  
Trung Ngo, Australia  
Tengfei Nian, China  
Mehdi Nikoo , Canada  
Youjun Ning , China  
Olugbenga Timo Oladinrin , United Kingdom  
Oladimeji Benedict Olalusi, South Africa  
Timothy O. Olawumi , Hong Kong  
Alejandro Orfila , Spain  
Maurizio Orlando , Italy  
Siti Aminah Osman, Malaysia  
Walid Oueslati , Tunisia  
SUVASH PAUL , Bangladesh  
John-Paris Pantouvakis , Greece  
Fabrizio Paolacci , Italy  
Giuseppina Pappalardo , Italy  
Fulvio Parisi , Italy  
Dimitrios G. Pavlou , Norway  
Daniele Pellegrini , Italy  
Gatheeshgar Perampalam , United Kingdom  
Daniele Perrone , Italy  
Giuseppe Piccardo , Italy  
Vagelis Plevris , Qatar  
Andrea Pranno , Italy  
Adolfo Preciado , Mexico  
Chongchong Qi , China  
Yu Qian, USA  
Ying Qin , China  
Giuseppe Quaranta , Italy  
Krishanu ROY , New Zealand  
Vlastimir Radonjanin, Serbia  
Carlo Rainieri , Italy  
Rahul V. Ralegaonkar, India  
Raizal Saifulnaz Muhammad Rashid, Malaysia  
Alessandro Rasulo , Italy  
Chonghong Ren , China  
Qing-Xin Ren, China  
Dimitris Rizos , USA  
Geoffrey W. Rodgers , New Zealand  
Pier Paolo Rossi, Italy  
Nicola Ruggieri , Italy  
JUNLONG SHANG, Singapore

Nikhil Saboo, India  
Anna Saetta, Italy  
Juan Sagaseta , United Kingdom  
Timo Saksala, Finland  
Mostafa Salari, Canada  
Ginevra Salerno , Italy  
Evangelos J. Sapountzakis , Greece  
Vassilis Sarhosis , United Kingdom  
Navaratnarajah Sathiparan , Sri Lanka  
Fabrizio Scozzese , Italy  
Halil Sezen , USA  
Payam Shafigh , Malaysia  
M. Shahria Alam, Canada  
Yi Shan, China  
Hussein Sharaf, Iraq  
Mostafa Sharifzadeh, Australia  
Sanjay Kumar Shukla, Australia  
Amir Si Larbi , France  
Okan Sirin , Qatar  
Piotr Smarzewski , Poland  
Francesca Sollecito , Italy  
Rui Song , China  
Tian-Yi Song, Australia  
Flavio Stochino , Italy  
Mayank Sukhija , USA  
Piti Sukontasukkul , Thailand  
Jianping Sun, Singapore  
Xiao Sun , China  
T. Tafsirojjan , Australia  
Fujiao Tang , China  
Patrick W.C. Tang , Australia  
Zhi Cheng Tang , China  
Weerachart Tangchirapat , Thailand  
Xiixin Tao, China  
Piergiorgio Tataranni , Italy  
Elisabete Teixeira , Portugal  
Jorge Iván Tobón , Colombia  
Jing-Zhong Tong, China  
Francesco Trentadue , Italy  
Antonello Troncone, Italy  
Majbah Uddin , USA  
Tariq Umar , United Kingdom  
Muahmmad Usman, United Kingdom  
Muhammad Usman , Pakistan  
Mucteba Uysal , Turkey




Ilaria Venanzi , Italy  
Castorina S. Vieira , Portugal  
Valeria Vignali , Italy  
Claudia Vitone , Italy  
Liwei WEN , China  
Chunfeng Wan , China  
Hua-Ping Wan, China  
Roman Wan-Wendner , Austria  
Chaohui Wang , China  
Hao Wang , USA  
Shiming Wang , China  
Wayne Yu Wang , United Kingdom  
Wen-Da Wang, China  
Xing Wang , China  
Xiuling Wang , China  
Zhenjun Wang , China  
Xin-Jiang Wei , China  
Tao Wen , China  
Weiping Wen , China  
Lei Weng , China  
Chao Wu , United Kingdom  
Jiangyu Wu, China  
Wangjie Wu , China  
Wenbing Wu , China  
Zhixing Xiao, China  
Gang Xu, China  
Jian Xu , China  
Panpan , China  
Rongchao Xu , China  
HE YONGLIANG, China  
Michael Yam, Hong Kong  
Hailu Yang , China  
Xu-Xu Yang , China  
Hui Yao , China  
Xinyu Ye , China  
Zhoujing Ye, China  
Gürol Yildirim , Turkey  
Dawei Yin , China  
Doo-Yeol Yoo , Republic of Korea  
Zhanping You , USA  
Afshar A. Yousefi , Iran  
Xinbao Yu , USA  
Dongdong Yuan , China  
Geun Y. Yun , Republic of Korea





Hyun-Do Yun , Republic of Korea  
Cemal YİĞİT , Turkey  
Paolo Zampieri, Italy  
Giulio Zani , Italy  
Mariano Angelo Zanini , Italy  
Zhixiong Zeng , Hong Kong  
Mustafa Zeybek, Turkey  
Henglong Zhang , China  
Jiupeng Zhang, China  
Tingting Zhang , China  
Zengping Zhang, China  
Zetian Zhang , China  
Zhigang Zhang , China  
Zhipeng Zhao , Japan  
Jun Zhao , China  
Annan Zhou , Australia  
Jia-wen Zhou , China  
Hai-Tao Zhu , China  
Peng Zhu , China  
QuanJie Zhu , China  
Wenjun Zhu , China  
Marco Zucca, Italy  
Haoran Zuo, Australia  
Junqing Zuo , China  
Robert Černý , Czech Republic  
Süleyman İpek , Turkey

# Contents







## **Automatic Extraction of Rock Discontinuities from the Point Cloud Using Dynamic DBSCAN Algorithm**

Ming Tang, Song Yang, Guohua Huang, Xiongyao Xie, Jiafu Guo, and Junli Zhai   
Research Article (8 pages), Article ID 7754179, Volume 2022 (2022)



## **Numerical Simulation of Large Compression Deformation Disaster and Supporting Behavior of Deep Buried Soft Rock Tunnel with High In Situ Stress Based on CDEM**

Hao Tang , Xiang Ji , Hongyi Zhang , and Tianbin Li   
Research Article (13 pages), Article ID 5985165, Volume 2022 (2022)

## **Experimental Study on the Effect of Freezing and Thawing on the Shear Strength of the Frozen Soil in Qinghai-Tibet Railway Embankment**

B. Wang , J. H. Gao , Y. Q. Wang , X. J. Quan , Y. W. Gong , and S. W. Zhou   
Research Article (12 pages), Article ID 9239460, Volume 2022 (2022)

## **Mechanical Behavior, Energy Release, and Crack Distribution Characteristics of Water-Saturated Phyllite under Triaxial Cyclic Loading**

Yang Zhou , Shengrui Su , and Peng Li  
Research Article (16 pages), Article ID 3681439, Volume 2021 (2021)


## **Experimental Research on Key Factors Influencing the Expansion Performance of New Type Sealing Materials**

Yaobin Li , Xin Guo , Sheng Xue , Chun-Shan Zheng , Maoliang Shen , and Yang Xu   
Research Article (10 pages), Article ID 6849650, Volume 2021 (2021)




## **Researches on the Influence of Blasting of Newly Built Tunnel on the Existing Tunnel Structure with Small Cross Angle**

Xian Du, Qinghua Xiao , Congming Li, Qiang Xiong, and Jianyou Yu  
Research Article (10 pages), Article ID 1865694, Volume 2021 (2021)


## **Water Inrush Risk Assessment Based on AHP and Advance Forecast Approach: A Case Study in the Micangshan Tunnel**

Tao Song , Jun Zeng , Jiayi Ma , Chunchi Ma , Tianbin Li , and Tao Xia   
Research Article (15 pages), Article ID 9750447, Volume 2021 (2021)

## **Deformation and Mechanical Properties of a Constant-Friction-Force Energy-Absorbing Bolt**

Tao Song , Tianbin Li , Lubo Meng, Chunchi Ma , Chaofei Li, and Feng Peng  
Research Article (9 pages), Article ID 4120873, Volume 2021 (2021)

## **Viscoelastoplastic Displacement Solution for Deep Buried Circular Tunnel Based on a Fractional Derivative Creep Model**



Yi-Hang Gao, Zhou Zhou, Hang Zhang, Shuang Jin , Wen Yang, and Qing-Hua Meng  
Research Article (7 pages), Article ID 3664578, Volume 2021 (2021)

**Numerical Study of Wave- and Current-Induced Oscillatory Seabed Response near a Fully Buried Subsea Pipeline**

Lunliang Duan, Meiling Fan, Duoyin Wang, Caixia Meng, and Lei Xing 



Research Article (15 pages), Article ID 9976278, Volume 2021 (2021)

**An Analysis of Relationship between the Microfracture Features and Mineral Morphology of Granite**

Meiben Gao , Tianbin Li , Junxun Zhu, Hongyu Yin, and Yongyi Yang

Research Article (6 pages), Article ID 4765731, Volume 2021 (2021)

**Stability of a Rock Tunnel Passing through Talus-Like Formations: A Case Study in Southwestern China**

Shaoqiang Zhang, Wenqiang Li, Jiashan Tan, Bokuan Li, Xiaochang Li , Shuaifeng Wang , and Zixin Zhang

Research Article (17 pages), Article ID 5453764, Volume 2021 (2021)

**Investigation on Physicomechanical Properties and Constitutive Model of Tuff in Mila Mountain Tunnel under Dry and Saturated Conditions**

Zhihao He, Xiangjun Pei , Shenghua Cui , Wentai Sun, Luguang Luo, and Chengruiwei He

Research Article (12 pages), Article ID 7725185, Volume 2021 (2021)

## Research Article

# Automatic Extraction of Rock Discontinuities from the Point Cloud Using Dynamic DBSCAN Algorithm

Ming Tang,<sup>1</sup> Song Yang,<sup>1</sup> Guohua Huang,<sup>1</sup> Xiongyao Xie,<sup>2,3</sup> Jiafu Guo,<sup>1</sup> and Junli Zhai <sup>2,3</sup>

<sup>1</sup>Powerchina Roadbridge Group CO., LTD, Beijing 100000, China

<sup>2</sup>Key Laboratory of Geotechnical & Underground Engineering of Ministry of Education, Tongji University, Shanghai 200092, China

<sup>3</sup>Zhejiang Scientific Research Institute of Transport, Hangzhou, 311305, China

Correspondence should be addressed to Junli Zhai; 707043292@qq.com

Received 8 July 2021; Accepted 10 March 2022; Published 18 April 2022

Academic Editor: Chunchi Ma

Copyright © 2022 Ming Tang et al. This is an open access article distributed under the Creative Commons Attribution License, which permits unrestricted use, distribution, and reproduction in any medium, provided the original work is properly cited.

Detection and mapping of rock discontinuities are important during excavation. The terrestrial laser scanning (TSL) technology is widely used to acquire accurate quantitative. However, there is rarely study about the influence of discontinuities parameters on the detection. Through the 3D printing technology, we have built discontinuity models with different roughness and connectors with different angles. Therefore, we can control the variables in the scanning. Several open-source packages were applied to derive the information from the point cloud acquired by TSL. The result shows that the recognition effect decreases with the angle between discontinuities. Moreover, the presence of roughness of discontinuity makes it prone to lead to lousy classification in the detection process. The proposed method has successfully extracted discontinuity dip, dip direction, and roughness automatically from the point cloud. The application on the two datasets showed great adaptability and accuracy. Consequently, the method could meet realistic engineering needs.

## 1. Introduction

Detection and mapping of rock discontinuities are important during excavation. The intersections between discontinuities, known as faults, joints, and bedding planes, divide a body of rock into fragments that detach from the larger body of rock when revealed by tunnel construction. Therefore, acquiring accurate quantitative discontinuity data, which are not affected by biases and censoring, is critical. The field mapping and handheld direct measuring with a scan-line method or a scan-window method require direct access to the excavation face. Consequently, collecting geological information on rock discontinuities is difficult, time-consuming, and often dangerous, especially in unstable areas.

Recently, the applications in geosciences of remote sensing investigations for the investigation of rock mass have rapidly improved. The most common techniques used to generate highly detailed 3D point clouds are terrestrial laser

scanning and digital photogrammetry [1–5]. Several approaches have been used to construct the 3D point clouds of rock surface to obtain Digital Outcrop Model (DOM) about the excavation face. The DOM formed by these dense point clouds allows engineers to perform the information extraction on a computer. Many researchers have been working on automatically extracting discontinuity parameters (e.g., orientation, spacing, trace persistence, and roughness) from the DOM. Assali et al. [6] developed a semiautomatic process that classifies rock discontinuities into subsets according to their orientation. Chen et al. [7] presented a new method for extracting discontinuity orientation automatically from rock mass surface 3D point cloud. Chen et al. [8] discussed the accuracy of the 3D laser scanning technique and demonstrated the potential of 3D laser scanning techniques to replace traditional window mapping. Idrees and Pradhan [9] investigated the influence of rock geostructure on cave channel development. They assessed the cave's stability by determining areas susceptible

to different failure types using surface discontinuity data extracted from laser scanning point cloud. Li et al. [10] presented an automatic characterization method for rock mass discontinuities that uses 3D point clouds. The orientation, trace, spacing, roughness, and aperture are extracted automatically by this method. Monsalve et al. [11] generated the DFNs by characterizing discontinuities in an underground limestone mine by laser scan.

Unfortunately, there are some intractable technical bottlenecks. First, these studies mainly cluster the point cloud through statistical analyses of the geometric features of triangular mesh units in a TIN generated from the point clouds. However, this method only considers the small-scale local features of point cloud data. Consequently, the automatic clustering process is prone to make mistakes by uneven rock mass surfaces. Second, these approaches are mainly based on the k-means algorithm. It means that the clustering is sensitive to the selection of initial centers and the number of clusters. Third, the resample process was widely used in these methods to get uniform point clouds. Consequently, the information on the discontinuities could be varied and dismissed.

This paper proposed a novel method to extract rock discontinuities from unstructured raw point clouds automatically. Our key innovation is to achieve the goal of point cloud classification without resampling and the TIN process. The remainder of this paper is organized as follows. In Section 2, we summarize proposed methods for LiDAR point cloud classification. In Section 3, we experiment to verify the performance of our method. In Section 4, the case study was carried out. Finally, the paper is discussed and concluded in Sections 5 and 6.

## 2. Methodology

In this section, we introduce the proposed algorithm for extracting rock discontinuities from point clouds. Section 2.1 describes the random forest algorithm as a classifier for point clouds. In Section 2.2, the dynamic DBSCAN algorithm is presented.

**2.1. Random Forest Algorithm.** RF [12] is always found to be the highest performing classifier for point clouds. RF is natively a multi-class algorithm, meaning that a single run of the model could predict all class labels. The output class probability scores represent the proportion of trees that voted for each class, and the sum of all probabilities is equal to 1 by definition. The RF classifier we trained was used to classify the point clouds into discontinuities and edges. Consequently, the input features we used in this study are the geometry features at multiple scales. The main idea behind these features is to characterize the local dimensionality properties of the scene at each point with different scales. The discontinuity looks like a 3D at a few millimeter-scale because of the roughness, and the edge also looks like a 3D object. Consequently, it is challenging to distinguish them. At a larger scale (i.e., 10 cm), the edge still looks like a 3D. By contrast, the discontinuity now looks more 2D than

3D. When combining geometry information from different scales, we can thus build signatures that identify the discontinuity and edge. Consequently, the eigenvalues of the covariance matrix of the neighborhood point  $X$ ,  $Y$ , and  $Z$  coordinates, searched with different scales, are calculated and sorted from largest to smallest. The eigenvalues  $\lambda_1^{r_j}, \lambda_2^{r_j}, \lambda_3^{r_j}$  ( $\lambda_1^{r_j} > \lambda_2^{r_j} > \lambda_3^{r_j}$ ) are then normalized as equation (1).

$$p_i^j = \frac{\lambda_i^{r_j}}{\lambda_1^{r_j} + \lambda_2^{r_j} + \lambda_3^{r_j}} \quad (i = 1, 2, 3). \quad (1)$$

The  $j$  indicates the scale of the scene. These proportions characterize the degree to which the point neighborhood can be considered 1-D, 2-D, or 3-D. These three proportions are calculated for each of the nine scene scales for 27 geometry features.

**2.2. Dynamic DBSCAN Algorithm.** DBSCAN [13] can find several clusters with irregular shapes based on the estimated density distribution as one of the developed density-based clustering algorithms. It does not need to know the number of clusters in advance. The methodology of the traditional DBSCAN algorithm is illustrated as shown in the left part of Figure 1. Starting from a random unvisited point  $A$ , DBSCAN retrieves all points in the neighborhood with a user-defined radius  $\epsilon$ . The density threshold  $MinPts$  is the minimum number of points required to form a dense region. If at least  $MinPts$  points are within the  $\epsilon$ -neighborhood, point  $A$  would be regarded as a core point. And all its neighborhoods would be arranged into the density-reachable set. Then an unvisited point in this set will be visited randomly, and the above procedure will be repeated. If the number of  $\epsilon$ -neighborhood is less than  $MinPts$ , like point  $B$ , the point will be regarded as a border point. The loop will be carried on until there is no point unvisited in the density-reachable set. The other points, like point  $C$ , which is density-unreachable, should be allocated into another cluster or noise.

However, in the TSL points cloud, the density of points is anisotropic and inhomogeneous so that the hyper-parameters  $MinPts$  and  $\epsilon$  can hardly be determined reasonably. The dynamic DBSCAN algorithm is proposed in this paper to address this shortage, as shown in the right part of Figure 2. The number of  $\epsilon$ -neighbor points of every point is treated as a constant  $MinPts$ . Moreover, the radius  $\epsilon$  is a variable according to the density rather than a constant in the traditional DBSCAN algorithm.

After the border points are distinguished, the search operation shown in Figure 2 will be carried out following these steps: first, the original point  $P_i$  will be selected from the points cloud set  $R$  by chance. If the  $P_i$  is not a border point, its  $\epsilon$ -neighbor points will be retrieved from  $R$  into set  $Q$ . Otherwise, the operation should be suspended and the first step repeated. Then the points in set  $Q$  will be visited and operated the same way as  $P_i$  until there is no unvisited point in  $Q$ . The points in set  $Q$  come from the same discontinuity. Finally, the points in set  $Q$  will be removed from the  $R$ , and

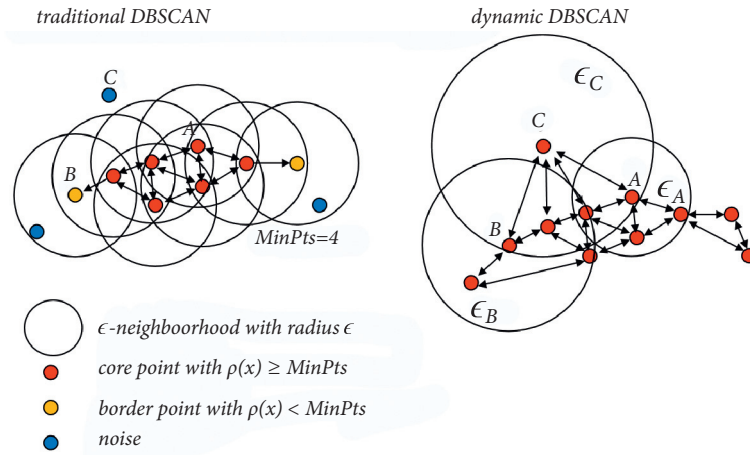


FIGURE 1: The dynamic DBSCAN algorithm.

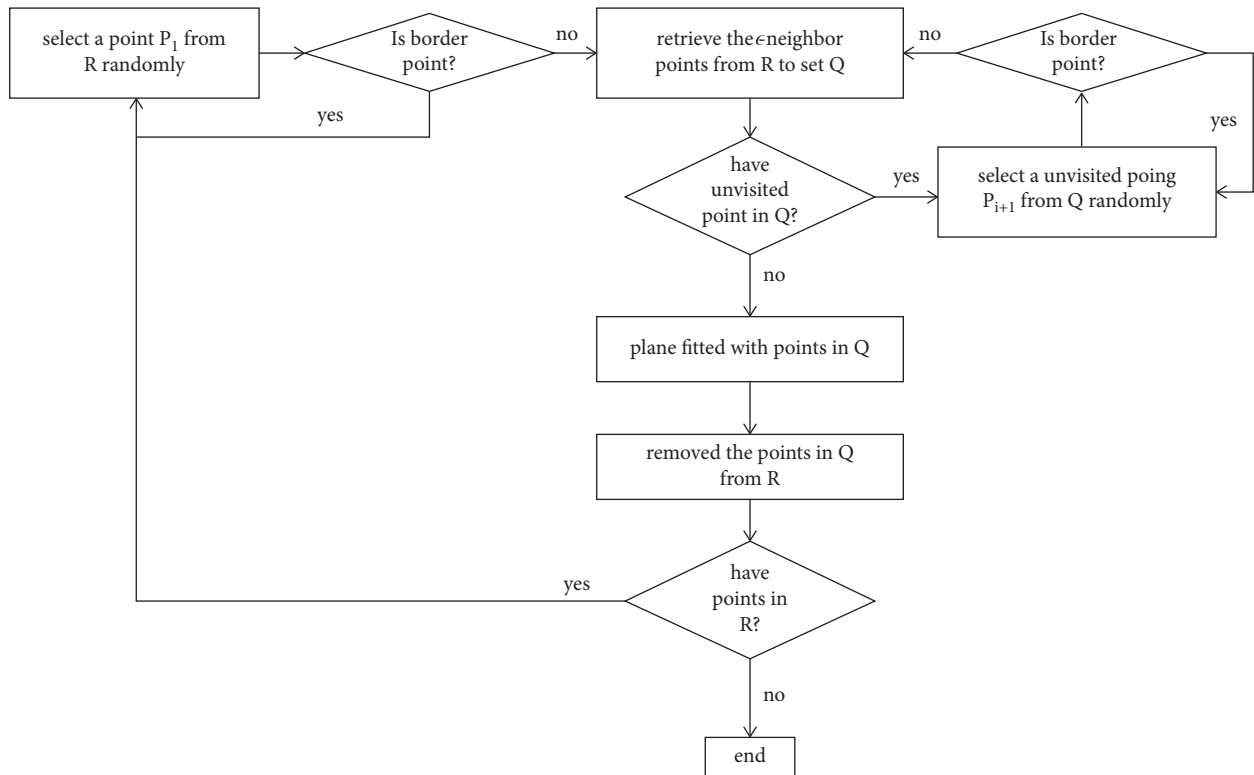


FIGURE 2: The workflow of discontinuities clustering.

the first step will be executed repeatedly until the  $R$  is empty. As shown in Figure 3, the points retrieved with the dynamic DBSCAN method from point clouds in an application are recognized as rough surfaces. Its oration will be calculated by the best plane fitted algorithm with these points instead of by the facet generated from a triangular mesh. So, the pseudosurface caused by the small-scale roughness can be avoided rationally.

### 3. Experiment

This section scans discontinuities with different roughness and angles by a laser scanner to learn how the accuracy is affected. First, the model and data preparations are

described. Then, the influence of various levels of roughness and angles is shown.

**3.1. Model Design and Data Collection.** As shown in Figure 4, to investigate the influence of roughness and included angle, we design a series of plates with different roughness surfaces and connectors with different included angles. The models were scanned with a Leica C10 terrestrial laser scanner (Figure 3(b)). The scanner was positioned at 1 m to the models and operated at the highest possible angular resolution. The resulting point cloud contained about 1.2 million points on the model surface with a point-spacing of 1 mm on

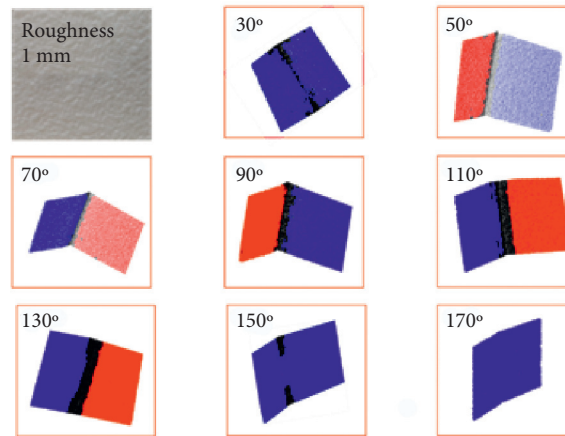


FIGURE 3: The segmentation results of discontinuities.

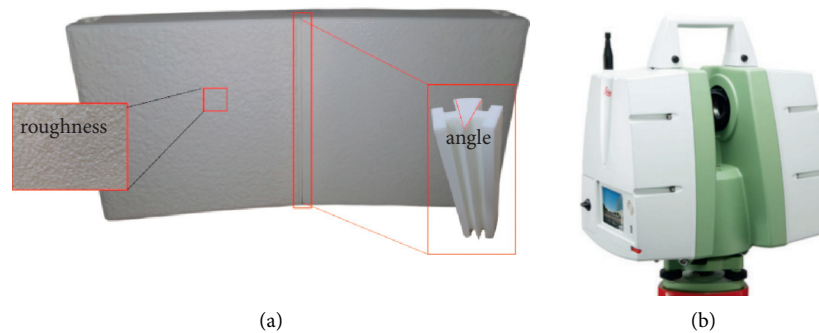


FIGURE 4: The experiment design.

average. According to the technical. Since the model is placed on the desk, a random rotation was carried out to get a random model.

## 4. Result and Analysis

**4.1. Classification Result.** Figure 5 is the classification result of the test point cloud, and it can be seen that the overall classification accuracy can be stabilized at about 97.3%. Table 1 is the recall of the decomposition line under the conditions of different surface roughness and different included angles. When the roughness of the discontinuity is less than 5 mm, and the included angle is less than  $130^\circ$ , the classifier can achieve a 100% recognition effect on the boundary. With the increase of angle and roughness of the structural plane, the classification accuracy gradually decreases. With the increase of the angle, the three-dimensional feature of the point cloud at the junction line gradually decreases, and it shows a 2D feature at each scale, so it is classified into the discontinuity category. When the roughness is large, the point cloud of discontinuity presents three-dimensional features in the multiscale field. The classifier divides the point cloud of discontinuity into the boundary category.

**4.2. Segmentation Result.** Figure 6 shows the segmentation effect of discontinuities by the DBSCAN algorithm under the conditions of 0.5 mm and 1 mm roughness of discontinuities. The black point cloud data are the identified

decomposition line points. When the included angle of the structural plane is  $170^\circ$ , the two discontinuities are considered as a single surface. Consequently, the segmentation of the discontinuities cannot be realized.

Figure 3 shows the segmentation effect of discontinuities under the condition of 5 mm roughness. It can be seen that when the included angle of the structural plane reaches  $150^\circ$ , the segmentation cannot be realized. Furthermore, when the included angle is equal to  $30^\circ$ , the segmentation still fails, although the boundary between the discontinuities is identified. This is because when the included angle of the discontinuities is slight, and the roughness of the discontinuities is large, the distance between the two discontinuities near the boundary is relatively close. Therefore, the DBSCAN algorithm is prone to cross between different discontinuities point clouds when searching the neighbors, leading to the error.

## 5. Case Study

The application in two cases is introduced in this section. Case A consists of regular polygons scanned in laboratory conditions; case B is points from a portion of a rock slope, available at <http://www.3D-landslide.com/projects/discontinuity/>.

**5.1. Case A.** As shown in Figure 7, two representative geometric shapes, cube, and dodecahedron, were selected for analysis. The cube is represented using 60,488 points, and the

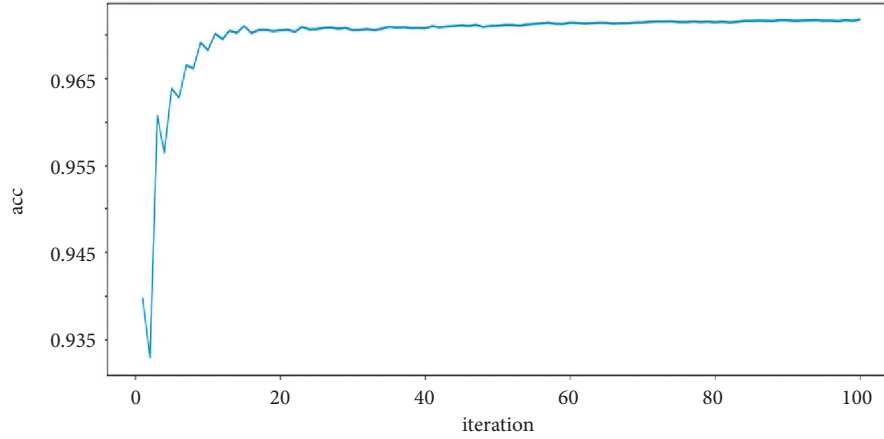


FIGURE 5: The RF learning curve.

TABLE I: The recall in classification.

Roughness (mm)	Angle							
	30°	50°	70°	90°	110°	130°	150°	170°
0.5	1	1	1	1	1	0.98	0.84	0.66
1	1	1	1	1	1	0.99	0.72	0.61
5	1	0.97	0.97	0.99	0.95	0.96	0.55	0.51

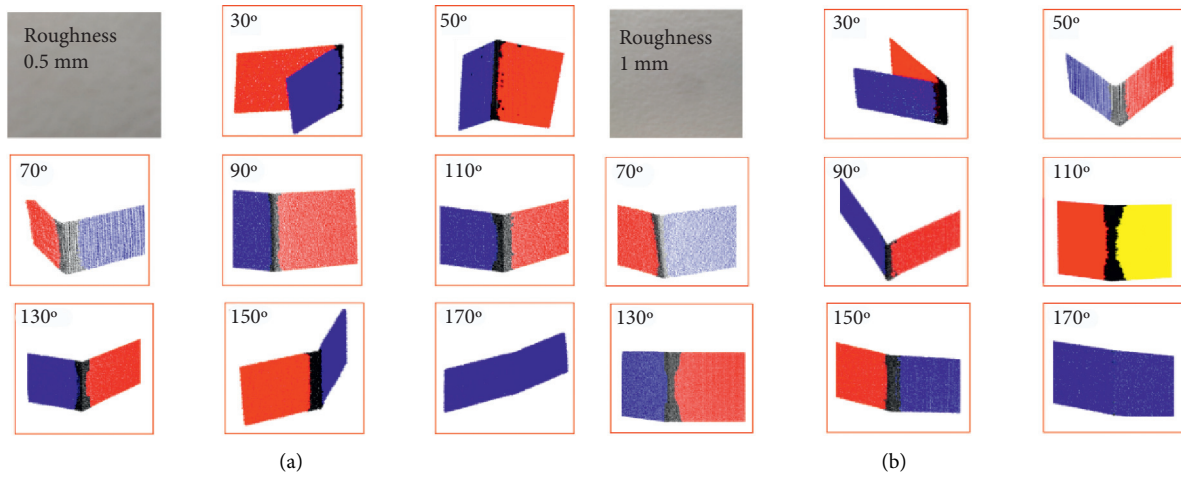


FIGURE 6: The segmentation results of discontinuities.

dodecahedron is represented using 80,828 points. Data were obtained using a 3D digitizer (Konica Minolta, Vivid 9i) through progressive rotation of the objects around a fixed platform axis and subsequent scanning.

Figure 8 shows the result of the automatic grouping of the cube and dodecahedron point clouds. The cube can be grouped into five different discontinuities, and the dodecahedron can be grouped into six different discontinuities. Different colors represent each discontinuity. The Silhouette validity index (SVI) is calculated to evaluate the validity of the clustering as follows.

$$S(x_i) = \frac{b(x_i) - a(x_i)}{\max\{a(x_i), b(x_i)\}} \quad (2)$$

The  $x_i$  is a sample in one of the clusters.  $a(x_i)$  is defined as the average distance of  $x_i$  to all other samples in its cluster, and  $b(x_i)$  is defined as the minimum of the average distance between  $x_i$  and samples in other clusters. A  $S(x_i)$  value close to 1 indicates that  $x_i$  is assigned to an appropriate cluster. If  $S(x_i)$  is close to -1,  $x_i$  is misclassified and lies somewhere between the clusters. The average SVI is all data points in the whole dataset. The SVI is shown in Figure 8 and compared with reference [6].

The Silhouette values corresponding to different methods are shown in Figure 8. The hollow mark presented the results from reference [6]. As the number of clusters must define manually, the maximum SVI corresponds to three and six for the cube and the dodecahedron. However,



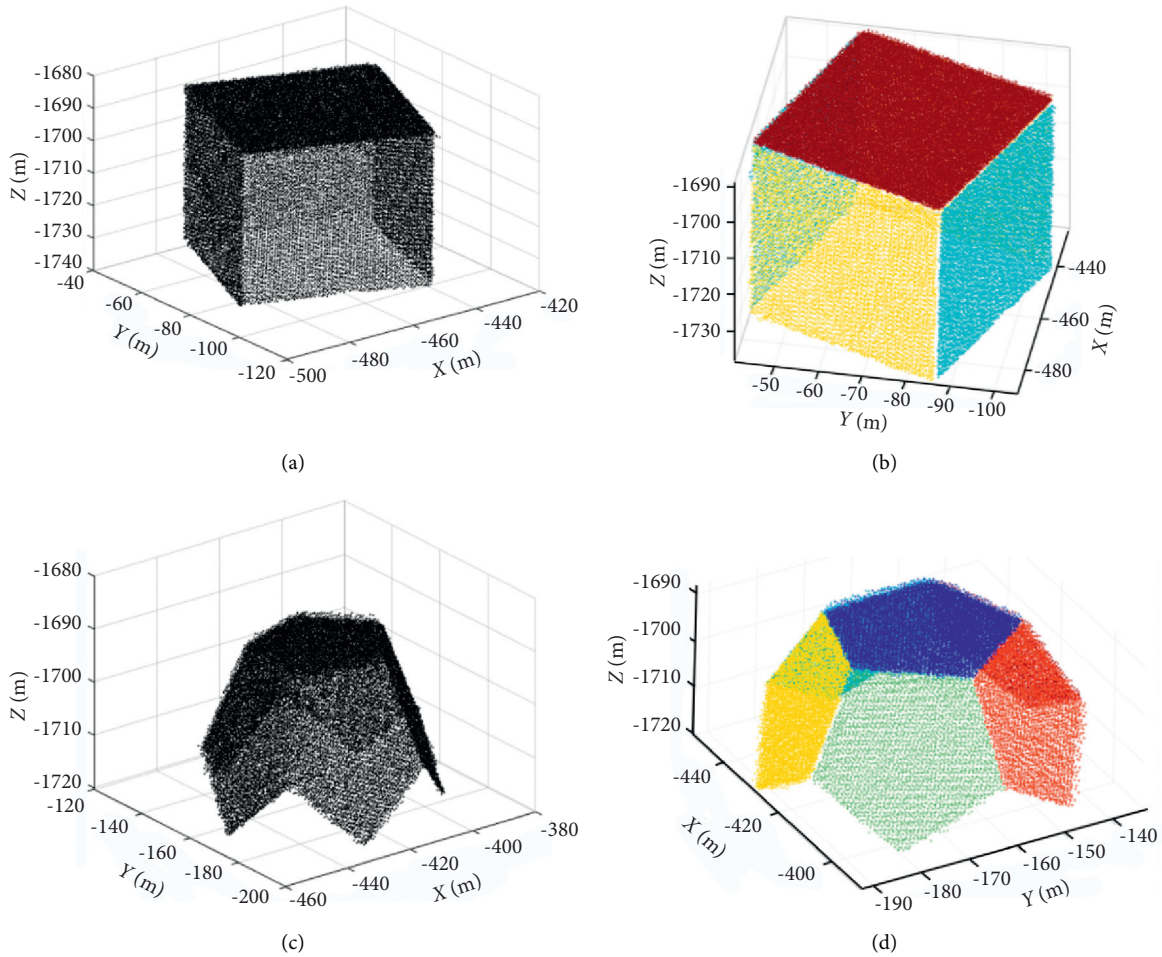


FIGURE 7: Automatic clustering analysis results.

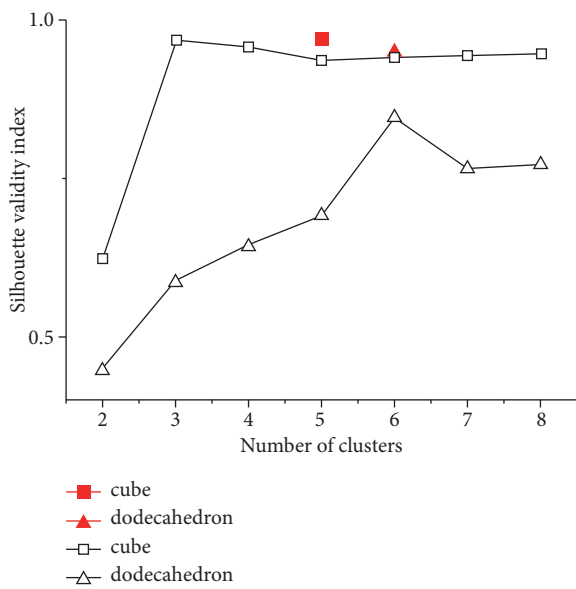


FIGURE 8: SVI compared with reference [6] in different numbers of clusters. The solid marks depict the results of the dynamic DBSCAN algorithm, and the hollow marks present the result from the reference [6].

the preknowledge in the number of clusters could be ignored in the dynamic DBSCAN algorithm. Furthermore, in our method, the SVI, presented by the red solid mark, is better than that in reference [6].

5.2. Case B. As shown in Figure 9, case B was a portion of a rock slope, which covers an area of approximately 6 m<sup>2</sup> with an average point spacing of 0.0055 m. After classifying points to discontinuities, the RANSAC plane fitting algorithm considers the volatility and produces an objective estimate of the discontinuity orientations. Details of the RANSAC method have been introduced in reference [8]. Figure 9(b) shows the result of the automatic grouping of the discontinuities.

$$\text{dip} = \frac{180 \times \arctan \sqrt{A^2 + B^2} / |C|}{\pi}, \quad (3)$$

$$\text{dip - direction} = 180 \times \arctan |B/A| / \pi.$$

The dip and dip direction statistics are represented in Figure 10. The discontinuities could be divided into five groups according to the density distribution characteristics

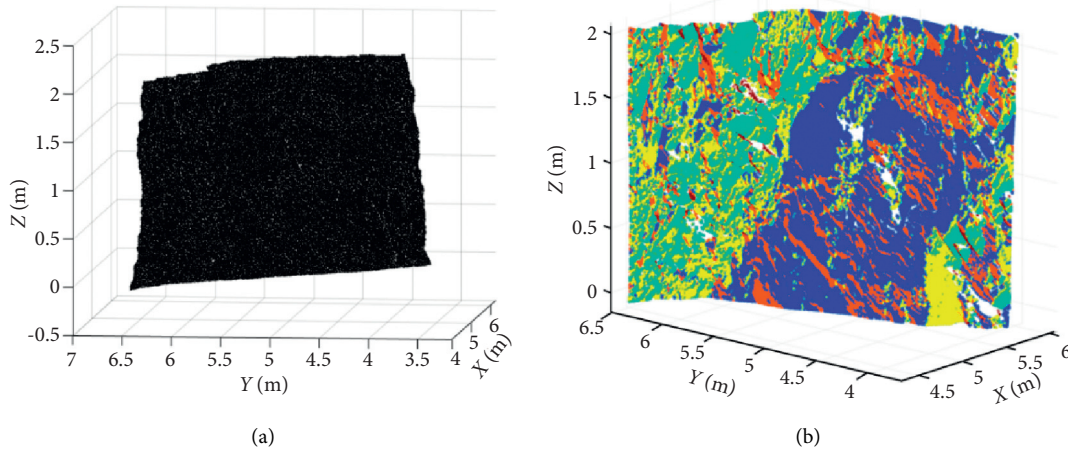


FIGURE 9: Automatic clustering results. Consequently, the discontinuity plane parameters could be obtained. Furthermore, assuming the plane equation is  $Ax + By + C(z) + D = 0$ , the discontinuity dip and dip direction could be recovered with equation (3).

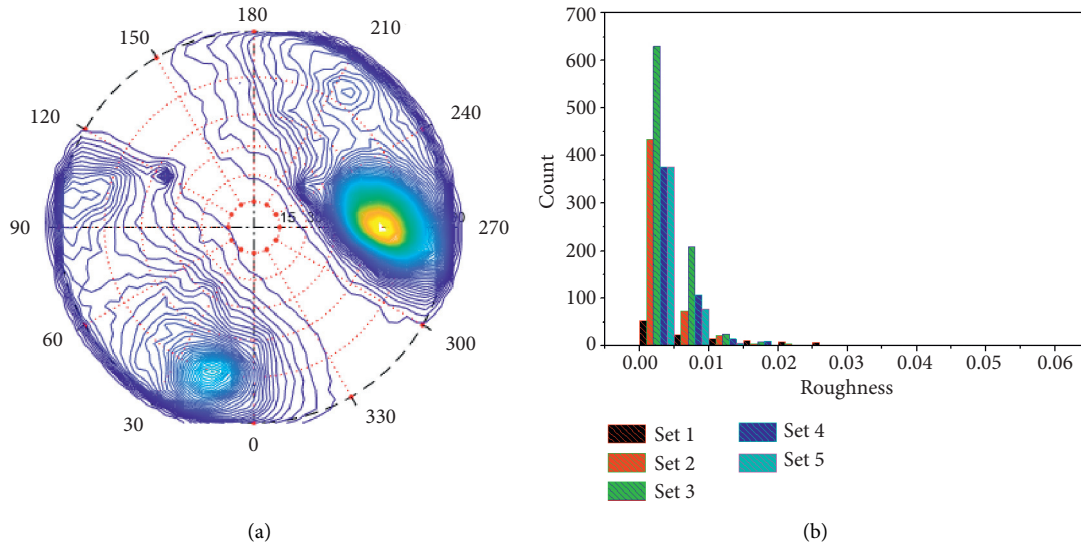


FIGURE 10: The extracted discontinuities information.

of dip and dip direction: set1:  $217^\circ \angle 20^\circ$ , set2:  $277^\circ \angle 40^\circ$ , set3:  $277^\circ \angle 40^\circ$ , set4:  $100^\circ \angle 15^\circ$ , and set5:  $120^\circ \angle 50^\circ$ . As there is no triangulation and resampling for the point cloud in the calculation process, we can extract the roughness of discontinuities. In this paper, the roughness of discontinuities is defined as the average distance between the point cloud of the same discontinuity and the fitting plane. As shown in Figure 10(b), it can be seen that the roughness is less than 1 cm for most discontinuities, and only a few have a roughness of more than 2 cm.

## 6. Discussion

In the TSL point cloud, the density of points is anisotropic and inhomogeneous so that the hyperparameters  $MinPts$  and  $\epsilon$  in the DBSCAN algorithm can hardly be determined reasonably. Consequently, we proposed a dynamic DBSCAN algorithm, which only needs one

hyperparameter. During this study, the effectiveness and accuracy of the dynamic DBSCAN algorithm are compromised by several factors. The influence of these factors was studied by model test. When the roughness of the structural plane is less than 5 mm, and the included angle is  $170^\circ$  or less, the discontinuities could be segmented. However, when the structural plane's roughness reaches 5 mm, the angle between the discontinuities needs to be less than  $150^\circ$  to realize the segmentation. Meanwhile, due to the increase of roughness, when the angle between the two discontinuities is  $30^\circ$  or less, the point clouds of the two discontinuities are too close to the dividing line, so the segmentation tends to fail.

The computation efficiency and accuracy of the dynamic DBSCAN algorithm are acceptable for practical usage but still need improvement. For case B, when gravel piles are between two discontinuities, it is easy to cause wrong structural plane segmentation. The point cloud classification takes a lot of

computing time because it needs multiple cycles to extract the features of point clouds at different scales.

## 7. Conclusions

This paper proposed a novel algorithm for automatic discontinuity information extraction from a point cloud. The proposed method consists of three steps: (1) through the Random Forest (RF) algorithm, the point cloud is classified automatically, and the point cloud is divided into plane points and boundary points. (2) The dynamic DBSCAN algorithm segments the point cloud data between different discontinuities. (3) The plane fitting of the same structural plane is carried out by the RANSAC algorithm. The dip, dip direction, and roughness of the structural discontinuity are calculated. The process could be carried out without manual intervention and shows good robustness to the roughness and unevenness of rock mass surface. Through the physical model, the application showed great adaptability and accuracy. Consequently, the method could meet realistic engineering needs.

Future research could be focused on the following aspects to improve the method: (1) Through matrix calculation, a large number of cyclic calculations in the algorithm is avoided, and the multiscale spatial features of the point cloud are extracted quickly; (2) automatic interference removal of debris pile to improve the signal to noise ratio of point cloud data. [14–17].

## Data Availability

The datasets are available at <http://www.3D-landslide.com/projects/discontinuity/>.

## Conflicts of Interest

The authors declare that there are no conflicts of interest.

## Acknowledgments

This research was funded by the Key projects of Zhejiang Provincial Department of Communications (2021014) and National Natural Science Foundation of China (52038008 and 42107216). The authors gratefully acknowledge their financial support.

## References

- [1] R. Roncella, G. Forlani, and F. Remondino, "Photogrammetry for geological applications: automatic retrieval of discontinuity orientation in rock slope," in *Electronic Imaging 2005*, pp. 17–27, International Society for Optics and Photonics, 2005.
- [2] M. Sturzenegger and D. Stead, "Close-range terrestrial digital photogrammetry and terrestrial laser scanning for discontinuity characterization on rock cuts," *Engineering Geology*, vol. 106, no. 3–4, pp. 163–182, 2009.
- [3] D. Tannant, "Review of photogrammetry-based techniques for characterization and hazard assessment of rock faces," *International journal of geohazards and environment*, vol. 1, no. 2, pp. 76–87, 2015.
- [4] X. Li, J. Chen, and H. Zhu, "A new method for automated discontinuity trace mapping on rock mass 3D surface model," *Computers & Geosciences*, vol. 89, pp. 118–131, 2016.
- [5] G. Gigli and N. Casagli, "Semi-automatic extraction of rock mass structural data from high resolution LIDAR point clouds," *International Journal of Rock Mechanics and Mining Sciences*, vol. 48, no. 2, pp. 187–198, 2011.
- [6] P. Assali, P. Grussenmeyer, T. Villemin, N. Pollet, and F. Viguier, "Surveying and modeling of rock discontinuities by terrestrial laser scanning and photogrammetry: semi-automatic approaches for linear outcrop inspection," *Journal of Structural Geology*, vol. 66, pp. 102–114, 2014.
- [7] J. Chen, H. Zhu, and X. Li, "Automatic extraction of discontinuity orientation from rock mass surface 3D point cloud," *Computers & Geosciences*, vol. 95, pp. 18–31, 2016.
- [8] S. Chen, M. L. Walske, and I. J. Davies, "Rapid mapping and analysing rock mass discontinuities with 3D terrestrial laser scanning in the underground excavation," *International Journal of Rock Mechanics and Mining Sciences*, vol. 110, pp. 28–35, 2018.
- [9] M. O. Idrees and B. Pradhan, "Geostructural stability assessment of cave using rock surface discontinuity extracted from terrestrial laser scanning point cloud," *Journal of Rock Mechanics and Geotechnical Engineering*, vol. 10, no. 3, pp. 534–544, 2018.
- [10] X. Li, Z. Chen, J. Chen, and H. Zhu, "Automatic characterization of rock mass discontinuities using 3D point clouds," *Engineering Geology*, vol. 259, Article ID 105131, 2019.
- [11] J. J. Monsalve, J. Baggett, R. Bishop, and N. Ripepi, "Application of laser scanning for rock mass characterization and discrete fracture network generation in an underground limestone mine," *International Journal of Mining Science and Technology*, vol. 29, no. 1, pp. 131–137, 2019.
- [12] L. Torre-Toaj, A. Bastarrika, A. Boyano, J. M Lopez Guede, and M Grana, "Above-ground biomass estimation from LIDAR data using random forest algorithms," *Journal of Computational Science*, vol. 58, Article ID 101517, 2022.
- [13] H. Chen, M. Liang, and W. Liu, "An approach to boundary detection for 3D point clouds based on DBSCAN clustering," *Pattern Recognition*, vol. 124, Article ID 108431, 2022.
- [14] N. Barton, R. Lien, and J. Lunde, "Engineering classification of rock masses for the design of tunnel support," *Rock Mechanics Felsmechanik Mcanique des Roches*, vol. 6, no. 4, pp. 189–236, 1974.
- [15] Isrm, "Suggested methods for the quantitative description of discontinuities in rock masses," *International Journal of Rock Mechanics and Mining Science & Geomechanics Abstracts*, vol. 15, pp. 319–368, 1978.
- [16] J. A. Franklin, N. H. Maerz, and C. P. Bennett, "Rock mass characterization using photoanalysis," *International Journal of Mining and Geological Engineering*, vol. 6, no. 2, pp. 97–112, 1988.
- [17] S. D. Priest, *Discontinuity Analysis for Rock Engineering*, Chapman & Hall, London, UK, 1993.

## Research Article

# Numerical Simulation of Large Compression Deformation Disaster and Supporting Behavior of Deep Buried Soft Rock Tunnel with High In Situ Stress Based on CDEM

Hao Tang <sup>1,2,3</sup>, Xiang Ji <sup>1,2</sup>, Hongyi Zhang <sup>4</sup>, and Tianbin Li <sup>1,2</sup>

<sup>1</sup>College of Environment and Civil Engineering, Chengdu University of Technology, Chengdu, Sichuan 610059, China

<sup>2</sup>State Key Laboratory of Geohazard Prevention and Geoenvironment Protection, Chengdu University of Technology, Chengdu, Sichuan 610059, China

<sup>3</sup>Sichuan Expressway Construction and Development Group Co. Ltd, Chengdu, Sichuan 610041, China

<sup>4</sup>Sichuan Mianjiu Expressway Co. Ltd, Chengdu, Sichuan, China

Correspondence should be addressed to Tianbin Li; [lbt@cdut.edu.cn](mailto:lbt@cdut.edu.cn)

Received 18 October 2021; Revised 9 January 2022; Accepted 11 January 2022; Published 3 March 2022

Academic Editor: Qian Chen

Copyright © 2022 Hao Tang et al. This is an open access article distributed under the Creative Commons Attribution License, which permits unrestricted use, distribution, and reproduction in any medium, provided the original work is properly cited.

Large compressive deformation of tunnels is a phenomenon involving plastic deformation and failure of surrounding rocks and often refers to the weak surrounding rock self-bearing capacity loss or partial loss. This research discusses the formation and evolution of large compressive deformation and effectiveness of the combined support of high in situ stress tunnel. From the new perspective of large deformation disaster caused by the structural failure of high in situ stress surrounding rock to clarify it, this paper illustrates the mechanism of progressive cracking and large deformation of high in situ stress soft rock tunnel from the aspects of the formation of self-bearing system, deformation evolution of the surrounding rock, mechanical properties of the surrounding rock, and failure characteristics. Accordingly, the continuous and discontinuous numerical simulation methods are used. The following conclusions are drawn by comparing the simulation results of surrounding rock under combined support with no support. (1) The supporting structure constitutes the self-supporting system with the surrounding rock and plays the roles of codeformation and load-bearing. (2) The support structure has evident reinforcing effect on the rock mass in the relaxation zone, thereby leading to the phenomenon of weakened rock mass failure. Moreover, the shear area develops to the compaction zone. (3) The supporting structure improves the bearing capacity of rock mass in the relaxation zone. It also increases the surrounding rock stress and reduces the range of the compaction zone. Simulation results verify that the combined support measures have a good suppression effect on the large compressive deformation, thereby providing a reference for similar projects and research on the large compressive deformation of soft rock.

## 1. Introduction

The continuous development of national highway construction and highway grade has resulted in the daily increase in the construction scale and number of highway tunnels. However, considering the constraints of geological conditions, planning requirements, and environmental protection, some tunnels have to be built in areas where the surrounding rock is weak and structurally developing. Thus, these tunnels' surrounding rock lacks sufficient strength and self-stabilizing capacity, and peripheral convergence and

vault subsidence displacement are relatively large. Thereafter, selecting reserved deformation in accordance with specifications often leads to intrusion limits and replacement of arch frame. This outcome will cause secondary disturbance to the surrounding rock, thereby affecting the stability of the surrounding rock, and also delay the construction period, resulting in hidden safety hazards.

At present, there are no clear and unified criteria for the large deformation of surrounding rock. Some scholars have indicated that large deformation happens when the surrounding rock deformation exceeds the specified amount

[1, 2]. Others have defined large deformation by whether the deformation of the surrounding rock exceeds the reserved deformation [3]. Scholars' deepening research have indicated that large deformation could not be defined solely by the extent of deformation. Hence, large deformation is a type of plastic failure, and progressive and evident time effect was proposed [4–7]. Furthermore, a new definition of large deformation of surrounding rock was proposed according to the geological conditions and mechanical mechanism [8].

Research directions of large tunnel deformation mainly include tunnel surrounding rock convergent deformation mechanism [9–12], prediction of surrounding rock convergent deformation [13], and risk evaluation of large deformation [14]. In numerical simulation, the finite element method is used for the numerical simulation of large deformation supporting measures [15], research on response of tunnelling form to tunnel deformation [16], treatment of large deformation of soft broken surrounding rock [17], and research on the influence of large deformation on tunnel excavation [18]. Scholars have used the finite difference numerical simulation method as basis in conducting rock mass deformation analysis [19], studied the damage evolution of tunnels' secondary lining under the combined action of initial support corrosion and surrounding rock creep [20], and analysed the convergence deformation mechanism of tunnel excavation in composite stratum [21]. On the basis of combined finite-discrete element method (FDEM), which is a numerical simulation method, the failure and swelling deformation of soft surrounding rock was simulated [22]. Han et al. [23] studied the critical roles of the location and the dip angle of the fault in determining the rockburst development around the tunnel. Scholars have used the continuous discontinuous element method (CDEM), which is a simulation method, to conduct comparative studies on different support measures [24] and simulate the progressive failure process of tunnel lining under different water pressure conditions [25]. Yang et al. [26] simulated the evolution of stress and fracture in tunnel excavation. Feng et al. [27, 28] discussed the macroscopic mechanical properties of brittle soil-rock mixture materials and realized the accurate calculation of rock mass explosive force and description of rock mass damage and fracture process through CDEM. Meanwhile, CDEM has been used in seismic stability analysis of bedding slope, damage and fracture process of rocks under explosion load, and progressive failure process of rock and soil medium under impact load [29, 30]. However, CDEM has been rarely used in large deformation of tunnel surrounding rock. Previous studies on large deformation have been conducted mostly from the continuous perspective, such as deformation amount and stress field characteristics, without considering the influence of structural failure on large deformation and the interpretation of discontinuous process. Therefore, CDEM should be introduced to substantially simulate the progressive failure process of large deformation disasters.

In terms of supporting measures, conventional measures for surrounding rock with a certain load-bearing capacity include shotcrete support, bolt support, steel arch support, and advanced small pipe support. However, joint support

measures have been commonly used in projects. For considerably developed rock masses, such as extreme fracture, fault fracture and squeezed rock zones, and extremely weak layer, conventional support measures occasionally fail. Thus, a special support measure must be adopted. For example, constant resistance large deformation bolt [31] absorbs the deformation energy of rock mass through the three stages of elastic deformation, structural deformation, and ultimate deformation. Hence, energy in the surrounding rock is completely released to a stable state. Small-diameter rock anchor cable [32] restricts large deformation through friction between the grouting body in the external anchorage section and bore wall and the suspension anchoring effect of the point anchor. Steel fiber shotcrete [33] is made of ordinary concrete mixed with steel fiber to achieve the functions of crack resistance, reinforcement, and toughness. Wu et al. [34] proposed a new reinforcement support system that combines filler wall, shotcrete, grouting cable, prestressed anchorage, and U-shaped steel support. However, only a few studies on the effectiveness of various supporting measures have explained the effectiveness of supporting measures from the perspective of the impact of structural damage of surrounding rocks on large deformation disasters and supporting structures.

Therefore, this study uses the preceding problems as bases in taking the construction of the Jiuming High-speed Baima Tunnel as research background and utilizes CDEM to simulate the large deformation disaster of high in situ tunnel and combined support measures. The forming and evolution mechanism of large deformation of high-stress tunnel and the effectiveness of combined support are discussed from the new perspective of large deformation disaster caused by the structural failure of high-stress surrounding rock.

## 2. Overview of Surrounding Rock Self-Supporting System and Large Squeezing Deformation

The occurrence of squeezing large deformation disaster is characterized by the significant deformation and failure of surrounding rocks. Figure 1 shows such examples as deformation and distortion of steel arch, cracking of shotcrete, spalling, initial support invasion limit, vault settlement, side wall extrusion, and floor heave. To explore the internal mechanism based on these typical large-deformation external failure phenomena, actual engineering should be used as a background, combined with numerical simulation, and the formation and evolution mechanism of large-deformation based on the theoretical results obtained from previous studies must be analysed and clarified.

Therefore, the current study uses Baima Tunnel as engineering background to study the formation, development, and failure process of large squeezing deformation and the state of the surrounding rock self-supporting system when the large squeezing deformation of soft rock occurs. On the basis of self-supporting system of surrounding rock, combined with the results of numerical simulation, the mechanism of large squeezing deformation is clarified from the

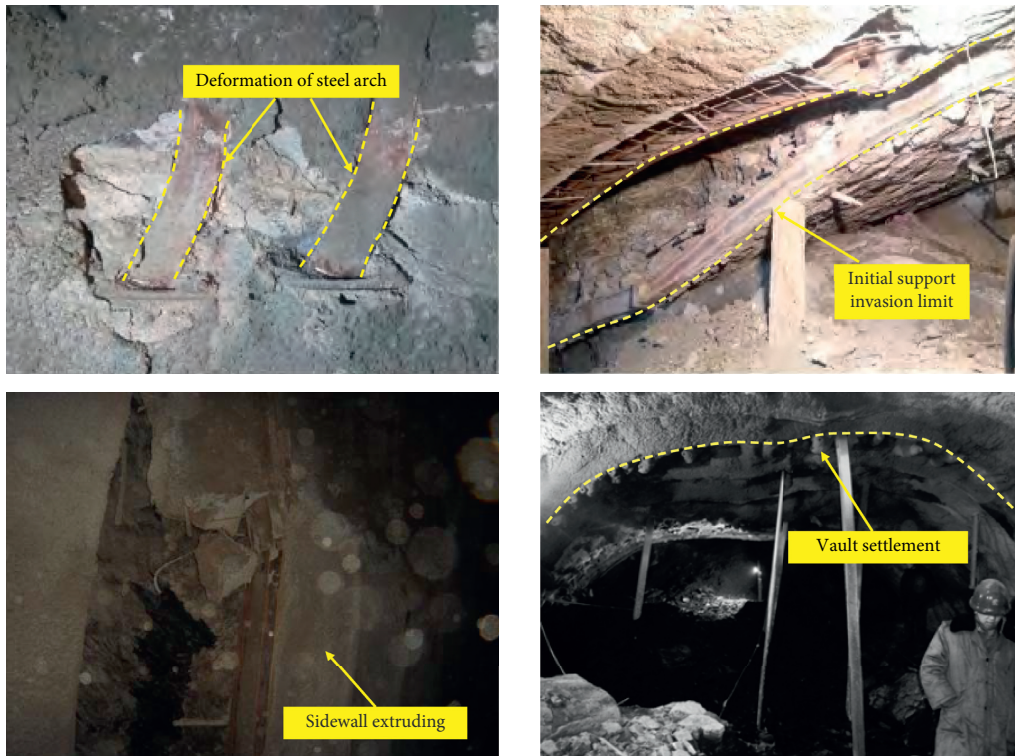


FIGURE 1: Typical failure characteristics of large deformation.

formation of surrounding rock self-supporting system, evolution of surrounding rock deformation, evolution of the mechanical behavior of rock mass, and failure characteristics.

The self-supporting system of surrounding rock [35] refers to the deformation of surrounding rock owing to stress adjustment during tunnel excavation. When the deformation of the surrounding rock converges and reaches a stable state, a self-supporting system structure is formed inside the surrounding rock to bear the pressure of the surrounding rock. The surrounding rock deformation of a tunnel is divided into the relaxation, compaction, and original stress zones from the inside to the outside of the tunnel wall (see Figure 2(a)). Relaxation zone refers to the tensile deformation of a certain range of rock mass around the cavern. Compaction zone refers to the area where the rock mass is in a state of compressive deformation in a certain deep part around the tunnel. The original rock stress zone is the area where the rock mass is in the original rock stress state. When the internal stress of the rock mass is dominated by horizontal tectonic stress, the original compaction zone will evolve into a stress-bearing arch at the top and bottom and a zone where stresses on the left and right sides expand and release to the deep from a horizontal perspective (see Figure 2(b)).

Therefore, the formation mechanism of the large deformation of the surrounding rock self-supporting system can be summarized as when the rock mass around the tunnel wall undergoes tensile deformation and fails to form a relaxation zone. During stress adjustment and redistribution, the rock mass at the deep part of the surrounding rock

undergoes tangential compression to form compaction and original rock stress zone. However, under the influence of such factors as high tectonic stress, structural cracking, and strength characteristics of soft rock, the self-supporting capacity of the rock mass in the relaxation zone is lost, further development of deformation and failure cannot be converged, and the self-supporting system of the surrounding rock fails, thereby ultimately leading to large deformation disasters.

### 3. Numerical Simulation of Large Compression Deformation Mechanism of Soft Rock in Tunnel

CDEM is based on the Lagrange equation to realize the coupling of finite and discrete elements and simulate the internal and boundary fractures of the block to realize the progressive failure process of the material by block representing the continuous properties and interface representing the discontinuous properties (see Figure 3). The GDEM software used in this study is based on CDEM to simulate the entire dynamic process of block from continuous deformation to fracture movement. GDEM has certain advantages compared with the commonly used finite element and discrete element software. GDEM can describe the nonlinear mechanical behavior of rock mass deformation and failure under high in situ stress, solve nonlinear and dynamic unstable problems using explicit calculation method, and simulate large deformation failure process through the block boundary and internal fracture. GDEM is capable of GPU

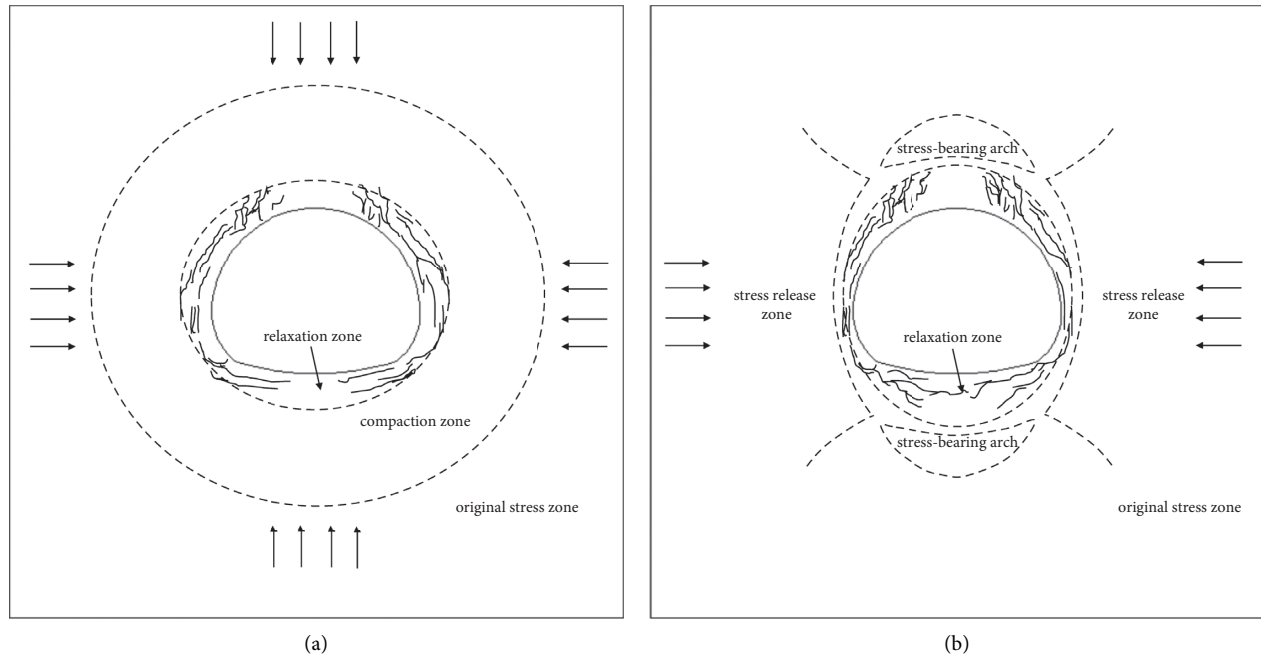


FIGURE 2: Schematic of the surrounding rock self-supporting system. (a) Horizontal and vertical tectonic stress. (b) Horizontal tectonic stress.

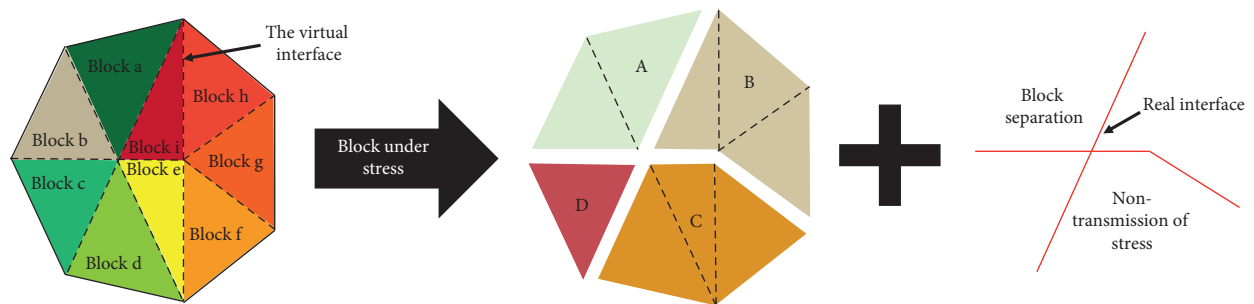


FIGURE 3: Block and interface diagram of CDEM [28].

and CPU parallel acceleration and can be equipped with various core modules of numerical computation, which can be integrated and managed.

**3.1. Large Deformation Numerical Simulation Scheme Based on CDEM.** This study designed two simulation schemes to significantly clarify the mechanism of large extrusion deformation and support effect: (1) large section excavation A without support measures and (2) large section excavation B with combined support measures. The significance of the two simulation schemes is to compare the formation process of the surrounding rock self-supporting system without support measures and the timely adoption of combined support measures. Scheme A aims to clarify the formation and evolution mechanism of large compression deformation. Scheme B is designed to compare support effect from the perspectives of deformation, rock mass mechanical behavior changing process, and failure characteristics. Deformation of rock mass was analysed from vault settlement,

floor uplift, and surrounding convergent displacement, while the original contour line of the tunnel was used to clearly compare deformation changes. Therefore, displacement monitoring points of the tunnel contour line are arranged, as shown in Figure 4. The mechanical behavior of the surrounding rock is reflected in the stress cloud map, and the formation of the self-bearing system of surrounding rock is observed. Lastly, the failure properties and characteristics of the surrounding rock are analysed using the failure type diagram.

This study uses GDEM-BlockDyna in numerical simulation to simulate large compression deformation. The model is based on the K39+714–726 section of the left inclined shaft of Baima Tunnel, and the size of the calculation model is 50 m × 50 m. The specific model size and monitoring point layout are shown in Figure 4. The specific model size of plan B is shown in Figure 5. The linear elastic constitutive model is selected as the constitutive model of the solid unit, and the Mohr-Coulomb strain softening model is adopted for the contact surface. In the elastic-plastic

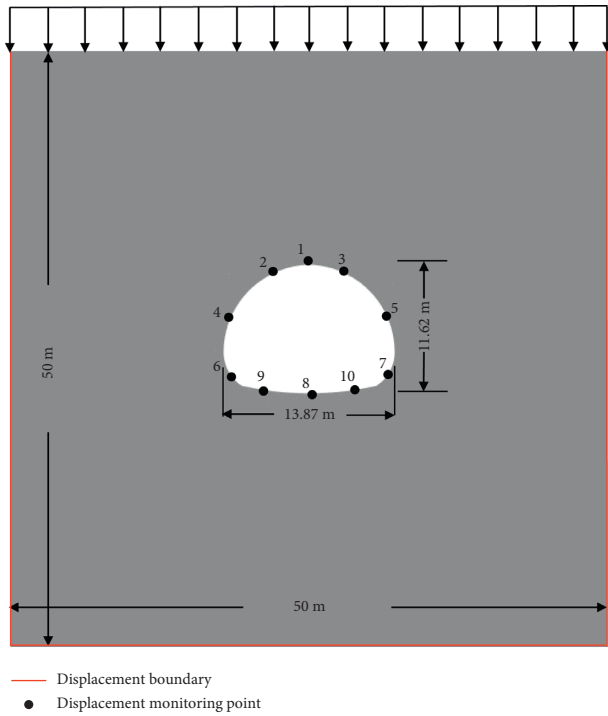


FIGURE 4: Model size diagram of the model without support.

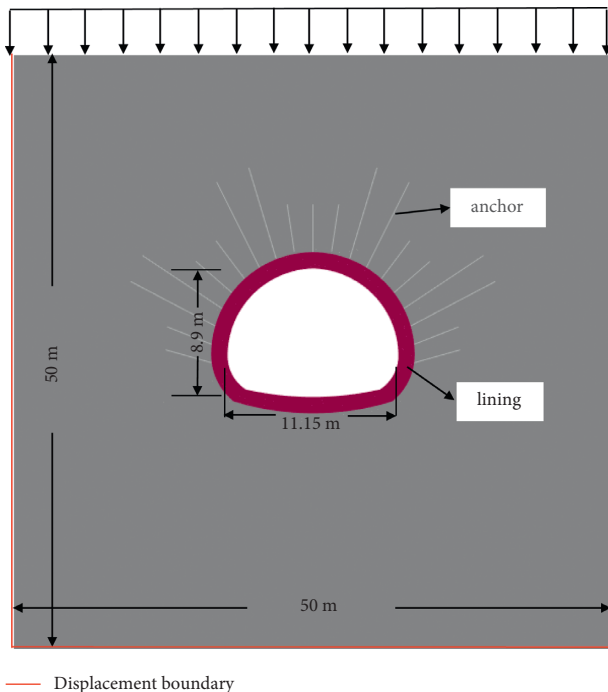


FIGURE 5: Model size diagram of the combined support measures.

calculation, displacement constraints are imposed on the left, right, and lower boundaries of the model, and the stress constraints are imposed on the upper part of the model. Vertical force of the overlying rock mass on the upper part of the model is applied in the form of uniformly distributed load. Thereafter, three-dimensional normal stress and shear stress are applied to each block to simulate structural stress.

Displacement and velocity generated in the elastic-plastic calculation are cleared, and stress boundary conditions of the model are changed to viscous boundary conditions. The reason is that viscous boundary will absorb stress, thereby avoiding false reflection of the stress wave, and dynamic calculation is performed.

Baima Tunnel is located at the junction of Pingwu County and Jiuzhaigou County in Sichuan Province. This tunnel is a dominant engineering of the highway from Jiuzhaigou (Sichuan-Gansu boundary) to Mianyang. The geological structure of the tunnel is complex. That is, the lithology is mainly slate and phyllite, and the uniaxial saturated compressive strength of the rock is mostly below 30 MPa. Hence, Baima Tunnel is a typical soft rock tunnel. Faults in this area are relatively developed, with 6 faults intersecting the tunnel body, and the surrounding rocks of grades IV and V account for approximately 90% of the tunnel length. The tunnel is in a section dominated by slate, and the surrounding rock is dominated by grade V. Based on the actual surrounding rock exposure of the K39 + 714–726 section of the left line of the inclined shaft of the tunnel, rock mechanics, anchor, and lining parameters of large deformation simulation are shown in Table 1. Ground stress parameters are presented in Table 2.

### 3.2. Analysis of the Simulation Results of Large Compression Deformation without Support

3.2.1. Deformation Evolution of the Surrounding Rock. Figure 6 shows the displacement cloud map, in which the white-dotted line is the original contour line of the tunnel. By comparing the original contour line, the deformation of the surrounding rock is evidently reflected. This study analyses the deformation characteristics from vault settlement, floor uplift, and surrounding convergent displacement.

The maximum cumulative displacement data of monitoring points are shown in Figure 7. As soon as the excavation is completed, the surrounding rock immediately deforms because excavation leads to the redistribution of surrounding rock stress, and the strength of soft rock itself is weak. In the absence of support conditions, the rebound caused by stress release process and dilatation caused by stress adjustment open the originally closed structural plane of the rock mass. Therefore, from 0 to 30,000 steps, the maximum displacement of the vault settlement increases to 175 mm, surrounding convergent displacement increases to 222 mm, and floor uplift reaches 344 mm. From 40,000 to 310,000 steps, the overall displacement of the surrounding rock enters a stable stage, maximum settlement displacement of the vault is 189 mm, surrounding convergence displacement is 233 mm, and displacement of floor uplift is 357 mm. At this time, the surrounding rock is in a state of temporary stability, but further attrition crushing of surrounding rock further reduces the strength of the rock mass. Consequently, from 320,000 to 340,000 steps, the maximum cumulative settlement displacement of the vault increases by 17 mm, maximum surrounding convergent displacement increases by 25 mm, and maximum floor uplift displacement



TABLE 1: Parameters of large deformation simulation.

	Density of material ( $\text{kg/m}^3$ )	Modulus of elasticity (GPa)	Poisson's ratio	Cohesive forces (MPa)	Tensile strength (MPa)	Angle of internal friction ( $^\circ$ )
Rock	2346	2.6	0.35	25	25	27
Lining	2300	3.0	0.3	27	27	30
Anchor	7800	10	0.25	500	500	75

TABLE 2: In situ stress parameters for large deformation simulation.

Stress component (MPa)					
$\delta_x$	$\delta_y$	$\delta_z$	$\tau_{xy}$	$\tau_{yz}$	$\tau_{xz}$
40.94	25.15	41.08	3.38	3.5	1.7

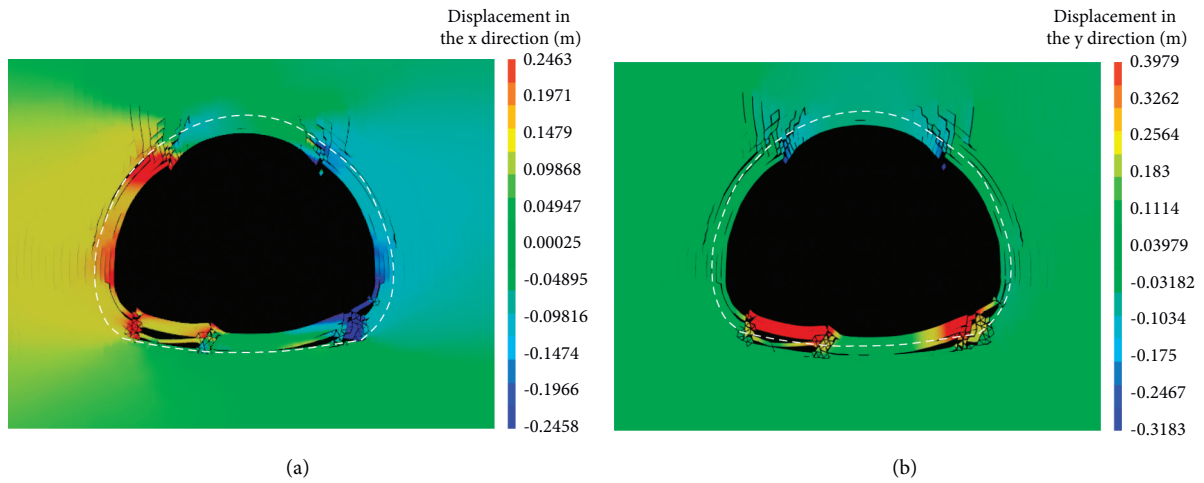


FIGURE 6: Displacement cloud maps. (a) X-direction displacement. (b) Y-direction displacement.

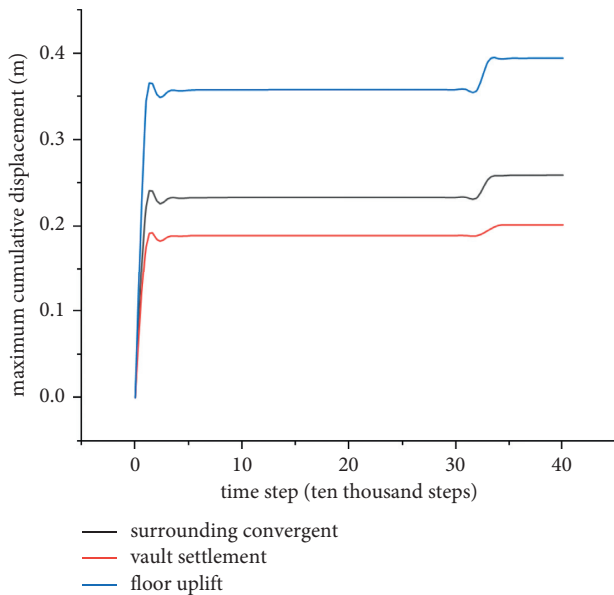


FIGURE 7: Maximum cumulative displacement of the tunnel contour.

increases by 37 mm. Lastly, large compression deformation occurs.

The deformation characteristics of soft rock with high stress are summarized as follows: (1) The occurrence of large compression deformation with soft rock is instantaneous. (2) Crushing of soft rock will change the stable stress state of rock mass and reduce the strength of rock mass, leading to the occurrence of large deformation disaster when deformation is temporarily stabilized.

### 3.2.2. Mechanical Behavior Evolution Surrounding Rock.

Given that the simulated objects are mainly subjected to horizontal tectonic stress, the horizontal stress cloud maps of 20,000 and 420,000 steps and large principal stress cloud maps are selected. In the stress cloud diagram, tension is positive and pressure is negative. The entire surrounding rock is under pressure. According to the self-bearing system of the surrounding rock, the formation of compaction zone is the result of the change of large principal stress to tangential direction along the tunnel and numerical increase. In Figure 8, the surrounding rock mass in a certain range is

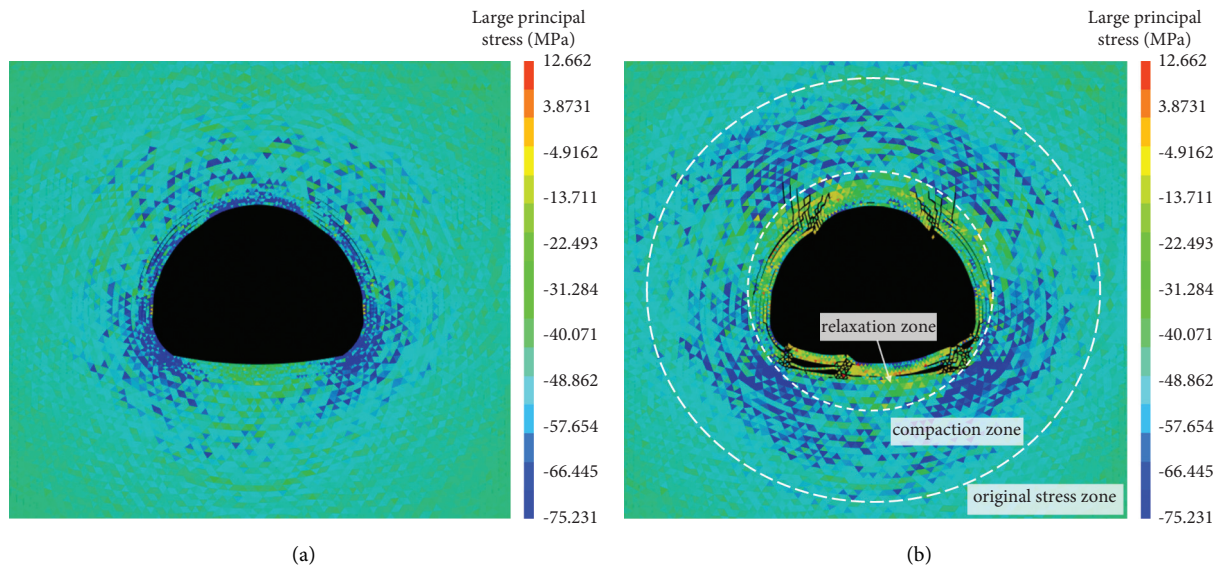


FIGURE 8: Cloud diagram of the large principal stress. (a) 20,000 steps. (b) 420,000 steps.

subjected to tangential compression, and the large principal stress forms a region distributed along the tangential direction of the tunnel. Meanwhile, the stress and range of this area gradually increase to form a compaction zone. The surrounding rock breaks owing to extrusion, cracks expand, and relaxation zones are formed. Stress of the compaction zone is larger than the original rock stress, and the original rock stress is greater than the relaxation zone. The reason is that the rock mass of the compaction zone is under confining pressure and its ultimate strength increases with an increase in confining pressure. Owing to the excavation, the rock mass in the relaxation zone changes from a three-way stress state to a two-way stress state, resulting in tensile failure. However, owing to friction, viscosity, and mutual mosaic among rocks, the rock mass in the relaxation zone continues to have integrity, which can provide resistance constraints to the rock mass in the compaction zone.

Relaxation, compaction, and original rock stress zones are formed in the horizontal stress cloud map (Figure 9), and the compaction zone is transformed into stress bearing arch and stress release zone in the horizontal stress cloud map. When the surrounding rock is mainly subjected to horizontal tectonic stress, rock mass in the compaction zone of the vault and arch bottom will have substantially high bearing capacity because of tangential compression and confining pressure. Thus, stress distribution similar to the arch, called stress-bearing arch, is formed. With the gradual formation of relaxation zone on the left and right sides of the tunnel, stress is constantly adjusted and gradually expanded and released to the deep rock mass, forming the stress release zone.

The mechanical behavior of large compression deformation of soft rock with high stress can be summarized as follows: (1) Stress of compaction zone is larger than the original rock stress, and the original rock stress is greater than the relaxation zone. (2) Rock mass in the relaxation zone has integrity and can provide certain resistance

constraints to the rock mass in the compaction zone. (3) When the surrounding rock is mainly subjected to horizontal tectonic stress, the compaction zone will form stress-bearing arch and stress release zone.

**3.2.3. Failure Characteristics.** Figure 10 shows the failure types of large compression deformation (0, undamaged; 1, current tensile failure; 2, current shear failure; 4, past tensile failure; and 8, past shear failure). After excavation, the shallow surface of the surrounding rock is gradually cracked, such as a few cracks along the contour line of the tunnel appearing at the left and right arch shoulders (Figure 10(a)). Then, shear failure blocks are mainly concentrated in the shallow surface of surrounding rock (Figures 10(b) and 10(c)). Furthermore, cracks extended towards the vault to form vertical cracks, and cracks in the bottom floor developed through, leading to the formation of the relaxation zone (Figure 10(d)). As the surrounding rock is strongly crushed by structural compression, the spalling and block dropping phenomenon occurs in the arch shoulder, and the floor is uplifted owing to the connection of cracks in the arch bottom, and self-bearing capacity of the relaxation zone is gradually lost and large deformation occurs. The relaxation zone is mainly tensile failure, while the compression zone is shear failure. By comparing Figures 10(c) and 10(d), the shear failure zone of the surrounding rock clearly extends from the relaxation zone to the deep part of the compaction zone. Moreover, shear failure gradually occurs in the compaction zone in the gradual formation of the relaxation zone, as well as gradual loss of the self-bearing capacity of the relaxation zone and gradual formation of the shear failure of the rock mass in the compaction zone. The reason is that, after excavation, the rock mass around the tunnel moves towards the tunnel clearance surface, resulting in tensile deformation and tensile failure. The self-bearing capacity of the rock mass in the relaxation zone gradually is lost, and

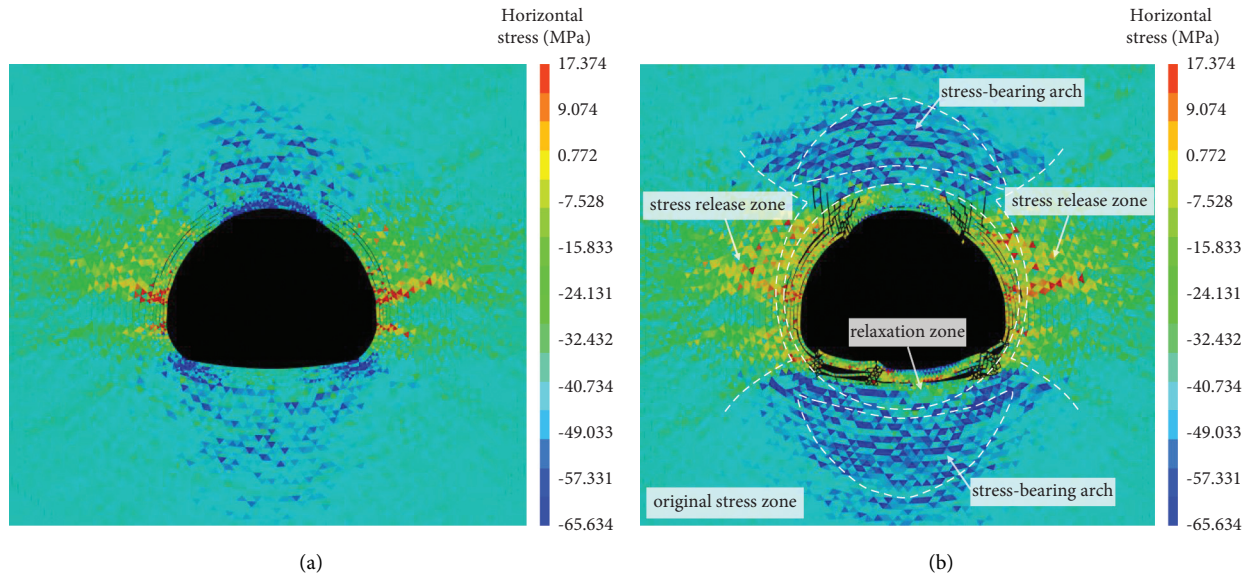


FIGURE 9: Horizontal stress cloud diagram. (a) 20,000 steps. (b) 420,000 steps.

stress is redistributed. Consequently, the rock mass in the compaction zone is further subjected to tangential compression and shear failure occurs.

### 3.3. Study on the Effectiveness of the Simulation of Combined Support Based on CDEM

#### 3.3.1. Deformation Evolution of the Surrounding Rock.

The maximum cumulative displacement data of the monitoring point are shown in Figure 11. Compared with the no support condition, the maximum cumulative displacement of vault settlement is reduced by 22.3%, maximum convergence displacement is reduced by 18.5%, and maximum displacement of floor uplift is reduced by 47.7%. These results indicate that support structure strengthens the rock mass in the relaxation zone, and the self-supporting system formed by the support structure and surrounding rock relatively inhibits the surrounding rock deformation. Compared with the condition without support, the stable period increases because the existence of support structure delays the occurrence of large deformation. At 390,000–400,000 steps, the maximum cumulative settlement displacement of vault, periphery convergence, and floor uplift increase suddenly. Compared with the sudden increase in surrounding rock deformation under the no support condition, the presence of support structure significantly reduces the strength reduction of soft rock caused by extrusion and crushing and makes the final convergence of deformation.

The simulation results indicate that the combined support structure has evident restraining effect on the surrounding rock deformation. The supporting structure and surrounding rock constituting the self-supporting system of surrounding rock play a role in strengthening rock mass in the relaxation zone and collaborative deformation. It not only prolongs the development period of large

deformation, but also alleviates the crushing degree of surrounding rock due to extrusion, thus leading to the inhibitory effect on large deformation.

#### 3.3.2. Mechanical Behavior Evolution Surrounding Rock.

In the final horizontal stress cloud map that compares the no support (Figure 12(a)) with combined support (Figure 12(b)), the surrounding rock and supporting measures are generally compressed, and the supporting measures have an evident reinforcing effect on rock mass around the tunnel. The failure phenomenon of rock mass in the relaxation zone is alleviated and bearing capacity is improved, leading to the narrowing of the stress-bearing arch and stress release zone. At this time, the supporting structure and surrounding rock form a self-bearing system together and collaborate deformation. From the crack development state, under the condition of combined support, the crack only develops along the tunnel contour at the left and right shoulder but does not extend further to the arch bottom and waist, and the crack penetration at the arch bottom is effectively suppressed. The large principal stress cloud map indicates that, compared with the no support condition (Figure 13(a)), the increase in stress in the compacting zone and the relaxation zone and the trend of the compaction zone extending to the deep surrounding rock are obviously inhibited, which is in contrast to the expansion of the compaction zone to the depth of surrounding rock without support condition, indicating that the supporting structure participates in the load bearing of surrounding rock and shares part of the stress in the compacted zone.

In summary, the reinforcement effect of support structure on rock mass in the relaxation zone increases the bearing capacity and the stress of rock mass in the relaxation zone and decreases range in the compaction zone. The trend of the compaction zone extending to the deep surrounding rock is obviously inhibited. Moreover, the supporting

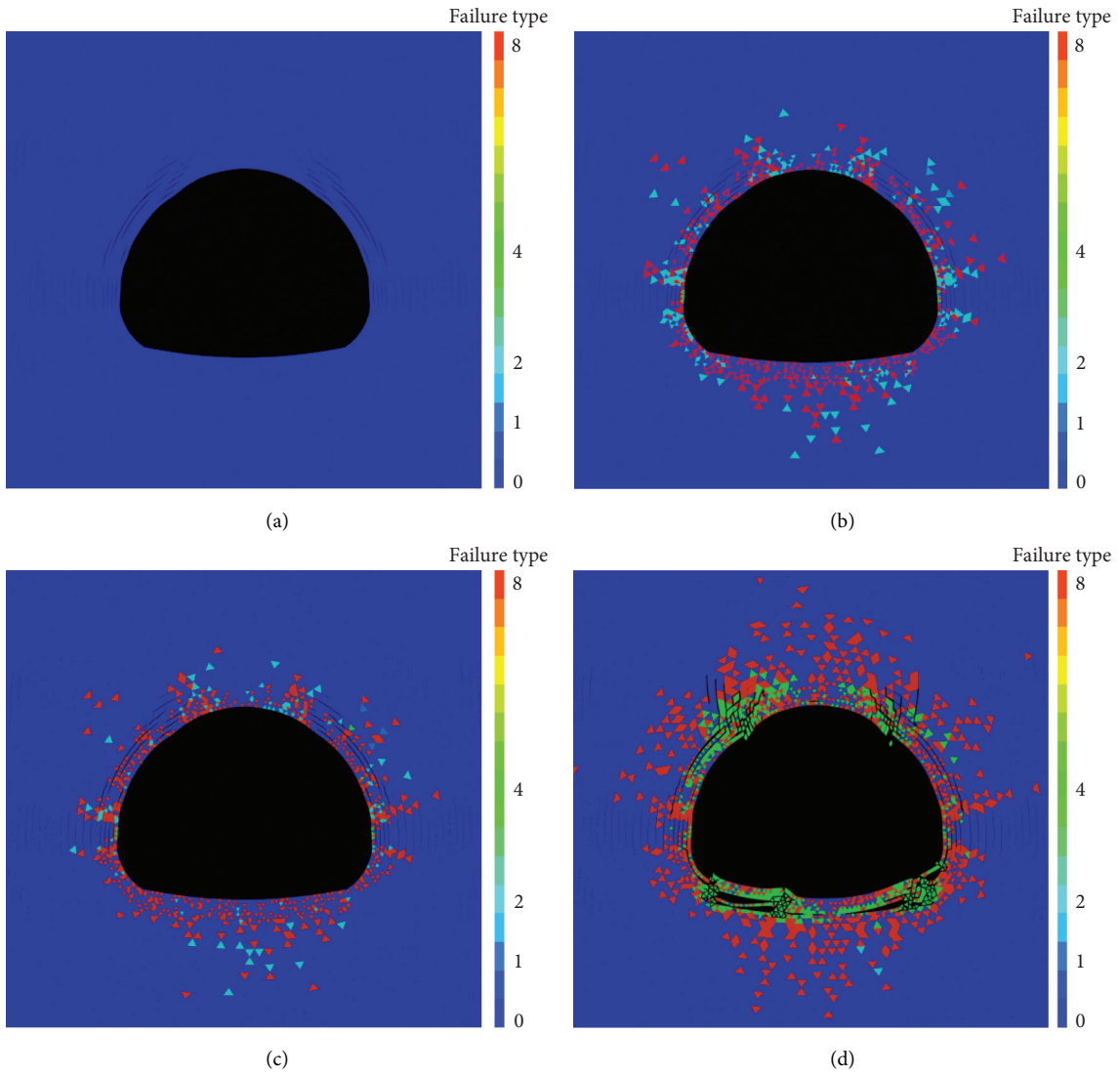


FIGURE 10: Diagram of the failure types. (a) 200,000 steps. (b) 300,000 steps. (c) 350,000 steps. (d) 420,000 steps.

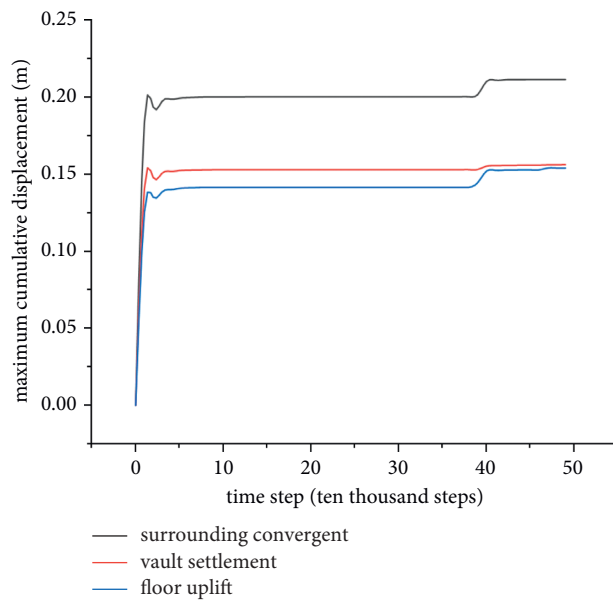


FIGURE 11: Maximum cumulative displacement of the tunnel contour.

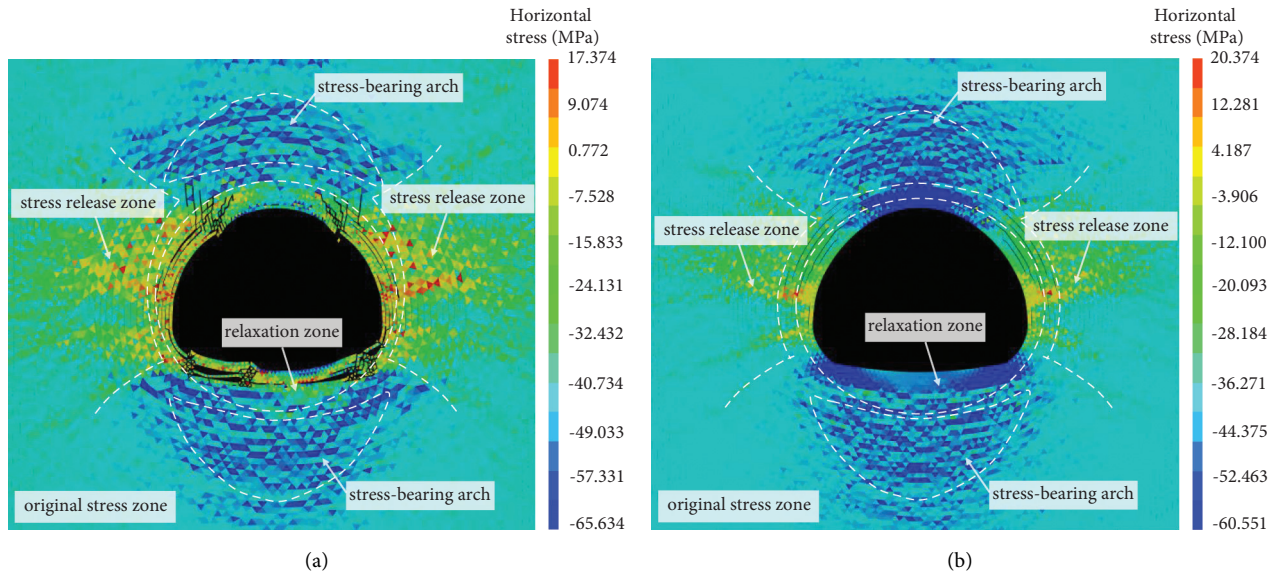


FIGURE 12: Comparison of horizontal stress cloud images. (a) No support. (b) Combined support.

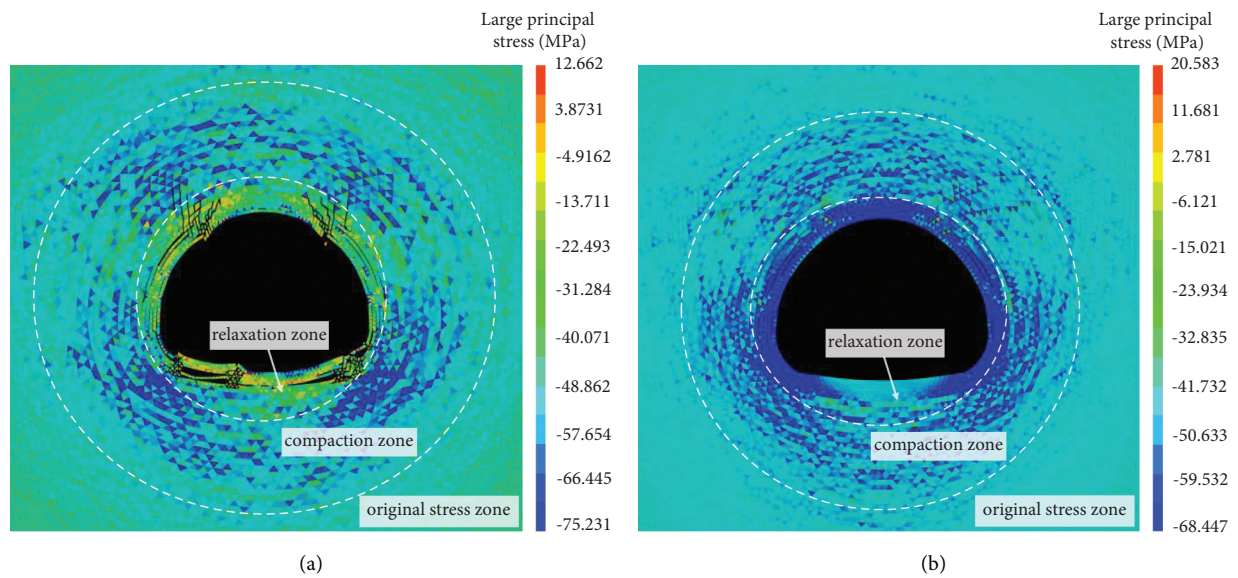


FIGURE 13: Comparison of large principal stress cloud images. (a) No support. (b) Combined support.

structure and surrounding rock form a self-bearing system to bear the load.

**3.3.3. Failure Characteristics.** Figure 14 shows the comparison of the final failure types of no support and combined support measures (0, undamaged; 1, current tensile failure; 2, current shear failure; 4, past tensile failure; and 8, past shear failure). Some cracks along the tangential direction of the tunnel appear in the support structure and shallow surrounding rock. Some cracks along the tangential direction of the tunnel appear in the support structure and shallow surrounding rock. Furthermore, the main failure characteristics are shear failure and the phenomenon of tension failure in the relaxation zone has disappeared.

Compared with the condition without support, the failure area of rock mass in the relaxation zone under the combined support measures is significantly reduced, and the number of cracks is also significantly suppressed, especially the failure phenomenon of the bottom of arch and the vault. The degree of rock mass fracture due to tectonic stress is obviously suppressed and the integrity of surrounding rock is effectively improved. Meanwhile, the shear failure area also expands deep in surrounding rock because the support structure strengthens the rock mass in the relaxation zone, resulting in the failure phenomenon developing to the compaction zone and deep surrounding rock. This result proves that the support structure and surrounding rock jointly form a self-supporting system to suppress the failure phenomenon.

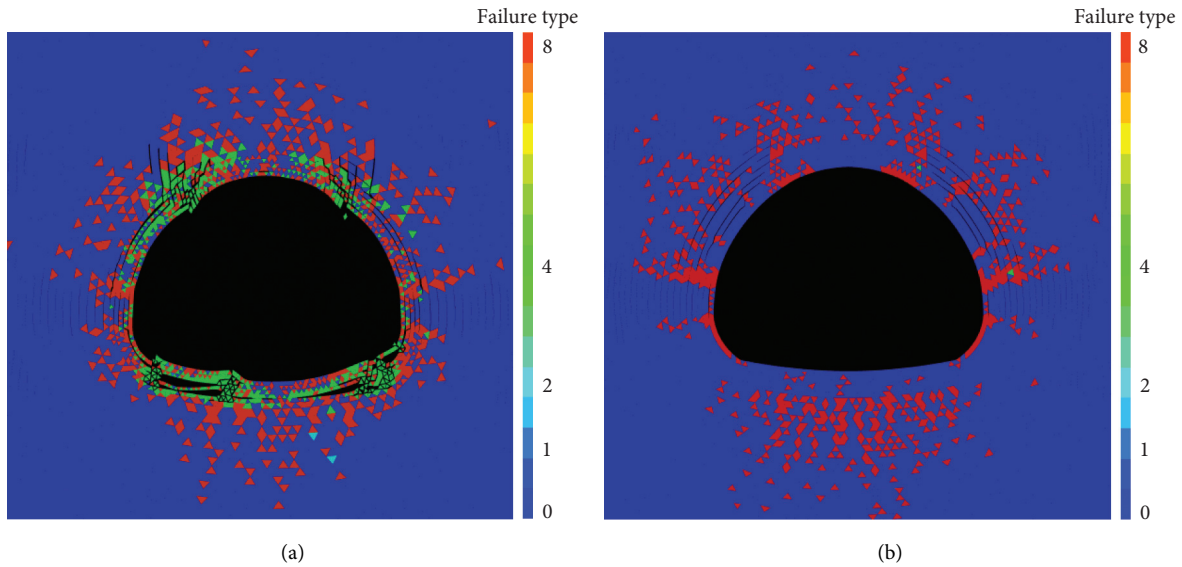


FIGURE 14: Diagram of failure types. (a) No support. (b) Combined support.

#### 4. Conclusions

This study takes Baima Tunnel as background and compares the numerical simulation results of the two cases of unsupported and combined support measures. The following conclusions are drawn:

- (1) The occurrence of large compressive deformation of soft rock with high in situ stress is instantaneous, and the further crushing of soft rock will change the stress stability state and reduce the strength of rock mass, leading to the occurrence of large deformation disasters.
- (2) The stress of compaction zone is larger than the original rock stress, and the original rock stress is greater than the relaxation zone. Rock mass in the relaxation zone has integrity and can provide certain resistance constraints to the rock mass in the compaction zone. When the surrounding rock is mainly subjected to horizontal tectonic stress, the compaction zone will form stress-bearing arch and stress release zone.
- (3) Tension and shear failures mainly occur in the relaxation and compaction zones, respectively. In the process of gradually losing the self-bearing capacity of the relaxation zone, the shear failure area of surrounding rock evidently extends from the relaxation zone to the deep compaction zone.
- (4) The supporting structure and surrounding rock constitute the surrounding rock self-bearing system, which prolongs the development period of large deformation and alleviates the crushing degree of surrounding rock due to extrusion, thus leading to the inhibitory effect on large deformation.
- (5) The supporting structure and surrounding rock constitute the surrounding rock self-bearing system, which strengthens the rock mass in the relaxation zone. Thus, the failure phenomenon of the rock mass

in the relaxation zone is suppressed, bearing capacity is improved, stress in the compaction zone increases, and range of the compaction zone is reduced. The supporting structure plays a role in collaborative deformation and sharing the load together.

- (6) With the support structure, the rock mass in the relaxation zone and the compaction zone is mainly shear failure. The degree of rock mass fracture due to tectonic stress is obviously suppressed and the integrity of surrounding rock is effectively improved. The shear failure area extends from relaxation zone to compaction zone and deep surrounding rock.

There are still some problems to be further discussed in this paper:

- (1) In this paper, the quasi-static process of sudden unloading is adopted in the simulated excavation. However, in the actual excavation process of tunnel chamber, the mechanism of large compression deformation is under dynamic disturbance. Therefore, the mechanism of large compression deformation can be further studied from the perspective of static and dynamic load combined action.
- (2) The simulation effect of large compression deformation depends on mesh division, which is untrue to some extent. So, a more appropriate numerical calculation model needs to be established from the optimization of model modelling and reduce reliance on mesh.
- (3) The simulation process in this paper does not consider geological structure and other complex conditions, which requires further study.

#### Data Availability

The data used to support the findings of this study are available from the corresponding author upon request.

## Conflicts of Interest

The authors declare that they have no conflicts of interest.

## Acknowledgments

This paper was supported by the National Natural Science Foundation of China (nos. 41807255, 41772329, and U19A20111), the State Key Laboratory of Geohazard Prevention and Geoenvironment Protection Independent Research Project (SKLGP2020Z010), Sichuan Science and Technology Project (no. 2021YJ0041), and Transportation Science and Technology Project (2020-MS5-146).

## References

- [1] Z. M. Xu and R. Q. Huang, *Deep Buried Extra-long Tunnel and its Construction Geological Hazards*, p. 220, Southwest Jiaotong University Press, Shanghai, China, 2000.
- [2] G. Z. Bian, "The criterion and treatment measures of large deformation of tunnel surrounding rock are discussed," *Science and Technology Bulletin*, no. 2, pp. 15–17, 1998.
- [3] Y. Yu, "Serious deformation of surrounding rock in squeezing ground," *Modern tunnelling technology*, no. 1, pp. 46–51, 1998.
- [4] Y. Jiang, Y. L. Li, and T. B. Li, "Study of the classified system of types and mechanism of great distortion in tunnel and underground engineering," *Geological hazards and environmental protection*, vol. 15, no. 4, pp. 46–51, 2004.
- [5] C. H. Wang, P. Sha, and Y. F. Hu, "Study of Squeezing Deformation Problems during Tunneling," *Rock and Soil Mechanics*, vol. 32, no. A2, pp. 143–147, 2011.
- [6] C. D. Martin, P. K. Kaiser, and D. R. McCreath, "Hoek-Brown parameters for predicting the depth of brittle failure around tunnels," *Canadian Geotechnical Journal*, vol. 36, no. 1, pp. 136–151, 1999.
- [7] B. Singh and R. K. Geol, *Rock Mass Classification: A Practical Approach in Civil Engineering*. Elsevier Science, Amsterdam, Netherlands, 1999.
- [8] T. B. Li, Y. L. Li, and L. S. Wang, *Study on Mechanism, Prediction and Prevention of Large Deformation of Tunnel under High In-Situ Stress*, Chengdu University of Technology, vol. 22, no. A1, pp. 2405–2408, Chengdu, China, 2008.
- [9] K. Wang, S. Xu, Y. Zhong, Z. Han, and E. Ma, "Deformation failure characteristics of weathered sandstone strata tunnel: a case study," *Engineering Failure Analysis*, vol. 127, Article ID 105565, 2021.
- [10] C. Xu and C. Xia, "A new large strain approach for predicting tunnel deformation in strain-softening rock mass based on the generalized Zhang-Zhu strength criterion," *International Journal of Rock Mechanics and Mining Sciences*, vol. 143, Article ID 104786, 2021.
- [11] A. Vrakas and G. Anagnostou, "A finite strain solution for the elastoplastic ground response curve in tunnelling: rocks with non-linear failure envelopes," *International Journal for Numerical and Analytical Methods in Geomechanics*, vol. 41, no. 7, pp. 1077–1090, 2017.
- [12] K. H. Park, "Large strain similarity solution for a spherical or circular opening excavated in elastic-perfectly plastic media," *International Journal for Numerical and Analytical Methods in Geomechanics*, vol. 39, no. 7, pp. 724–737, 2015.
- [13] C. Li, S. Hou, Y. Liu, P. Qin, F. Jin, and Q. Yang, "Analysis on the crown convergence deformation of surrounding rock for double-shield TBM tunnel based on advance borehole monitoring and inversion analysis," *Tunnelling and Underground Space Technology*, vol. 103, Article ID 103513, 2020.
- [14] C. H. Bai, Y. G. Xue, D. H. Qiu, M. X. Su, X. M. Ma, and H. T. Liu, "Analysis of factors affecting the deformation of soft rock tunnels by data envelopment analysis and a risk assessment models," vol. 116, Article ID 10411, 2021.
- [15] X. F., *Numerical Simulation of Asymmetric Large-Deformation Energy-Releasing Bolt Support for Layered Soft Rock Tunnel*, Chengdu University of Technology, vol. 4, no. 2, pp. 1–125, Chengdu, China, 2020.
- [16] Y. Hu, H. Y. Lei, G. Zheng et al., "Assessing the deformation response of double-track overlapped tunnels using numerical simulation and field monitoring," *Journal of Rock Mechanics and Geotechnical Engineering*, 2021, vol. 21, In Press.
- [17] C. Pan, Z. Q. Feng, T. Liu, and W. Li, "A numerical simulation of the treatment for weak and broken rock tunnel of large deformation," *Journal of Guangxi University*, vol. 37, no. 1, pp. 141–146, 2012.
- [18] D. Kim, "Large deformation finite element analyses in TBM tunnel excavation: CEL and auto-remeshing approach," *Tunnelling and Underground Space Technology*, vol. 116, no. 1, Article ID 104081, 2012.
- [19] J. Luo, D. Zhang, Q. Fang, D. Liu, and T. Xu, "Mechanical responses of surrounding rock mass and tunnel linings in large-span triple-arch tunnel," *Tunnelling and Underground Space Technology*, vol. 113, Article ID 103971, 2021.
- [20] G. Xu and M. Gutierrez, "Study on the damage evolution in secondary tunnel lining under the combined actions of corrosion degradation of preliminary support and creep deformation of surrounding rock," *Transportation Geotechnics*, vol. 27, Article ID 100501, 2021.
- [21] S.-Q. Yang, Y. Tao, P. Xu, and M. Chen, "Large-scale model experiment and numerical simulation on convergence deformation of tunnel excavating in composite strata," *Tunnelling and Underground Space Technology*, vol. 94, Article ID 103133, 2019.
- [22] Q. S. Liu, P. H. Deng, C. Bi, W. W. Li, and J. Liu, "FDEM numerical simulation of the fracture and extraction process of soft surrounding rock mass and its rockbolt-shotcrete-grouting reinforcement methods in the deep tunnel," *Rock and Soil Mechanics*, vol. 40, no. 1, pp. 4065–4083, 2019.
- [23] H. Y. Han, D. Fukuda, H. Y. Liu et al., "Combined finite-discrete element modellings of rockbursts in tunnelling under high in-situ stresses," *Computers and Geotechnics*, vol. 137, Article ID 104261, 2021.
- [24] T. F. Ma, "Research on failure mechanism and supporting Technology for surrounding rock in soft rock roadways based on CDEM method," *Shanxi Coking Coal Science & Technology*, vol. 41, no. 11, pp. 43–47, 2019.
- [25] L. T. Peng, P. Lu, T. Yang, and C. D. Cheng, "Research on anti-water pressure capability of railway tunnel lining by continuous-discontinuous element method," *Journal of Chongqing University*, vol. 42, no. 11, pp. 98–107, 2019.
- [26] Y. Ju, Y. Wang, C. Su, D. Zhang, and Z. Ren, "Numerical analysis of the dynamic evolution of mining-induced stresses and fractures in multilayered rock strata using continuum-based discrete element methods," *International Journal of Rock Mechanics and Mining Sciences*, vol. 113, pp. 191–210, 2019.
- [27] C. Feng, Z. G. Li, and S. H. Li, "Study on uniaxial compression characteristics of brittle rock and soil aggregate," *Chinese Journal of Computational Mechanics*, vol. 35, no. 3, pp. 356–363, 2018.

- [28] C. Feng, S. H. Li, B. X. Zheng, X. R. Cui, and J. J. Jia, "Numerical simulation on complete process of three-dimensional bench blasting in an open-pit mine based on CDEM," *Explosion and Shock Waves*, vol. 39, no. 2, pp. 110–120, 2019.
- [29] C. Feng, S. H. Li, and J. Wang, "Stability analysis method for bedding rock slopes under seismic load," *Chinese Journal of Geotechnical Engineering*, vol. 34, pp. 717–724, 2012.
- [30] C. Feng, S. H. Li, D. Zhou, and Q. B. Zhang, "Numerical analysis of damage and crack process of rock under explosive loading," *Chinese Journal of Geotechnical Engineering*, vol. 36, no. 7, pp. 1262–1270, 2014.
- [31] C. Feng, S. H. Li, W. H. Hao, and W. Ge, "Numerical simulation for penetrating and blasting process of EPW based on CDEM," *Journal of Vibration and Shock*, vol. 36, no. 16, pp. 11–18, 2017.
- [32] M. C. He and Z. B. Guo, "Mechanical property and engineering application of anchor bolt with constant resistance and large deformation," *Chinese Journal of Rock Mechanics and Engineering*, vol. 33, no. 7, pp. 1297–1308, 2014.
- [33] Z. T. Wang, "Application of small diameter anchor cable in high in-situ stress and large deformation tunnel construction," *Tunnel construction*, vol. 25, no. 3, pp. 42–45, 2005.
- [34] Z. D. Wu, H. W. Zhou, and J. F. Liu, "The application of steel fiber concrete in support of soft rock roadway at depth in the No.8 hebi coal mine," *Metal Mine*, vol. 6, no. 420, pp. 32–35, 2011.
- [35] S. H. Zhong, *Promoting Effect of Shotcrete Anchor Support on Self-Supporting System in Surrounding Rock of Tunnel*, 1982.



## Research Article

# Experimental Study on the Effect of Freezing and Thawing on the Shear Strength of the Frozen Soil in Qinghai-Tibet Railway Embankment

B. Wang <sup>1</sup>, J. H. Gao <sup>1</sup>, Y. Q. Wang <sup>2</sup>, X. J. Quan <sup>1</sup>, Y. W. Gong <sup>1</sup> and S. W. Zhou <sup>1</sup>

<sup>1</sup>Key Laboratory of Transportation Tunnel Engineering, Ministry of Education, Southwest Jiaotong University, Chengdu 610031, China

<sup>2</sup>Key Laboratory of Highway Bridges and Tunnels of Shaanxi Province, Chang'an University, Xi'an 710054, China

Correspondence should be addressed to Y. Q. Wang; [ys08@gl.chd.edu.cn](mailto:ys08@gl.chd.edu.cn) and X. J. Quan; [quanxiaojuan@swjtu.edu.cn](mailto:quanxiaojuan@swjtu.edu.cn)

Received 21 October 2021; Accepted 2 December 2021; Published 5 January 2022

Academic Editor: Chunchi Ma

Copyright © 2022 B. Wang et al. This is an open access article distributed under the Creative Commons Attribution License, which permits unrestricted use, distribution, and reproduction in any medium, provided the original work is properly cited.

The direct shear tests of different dry density and moisture content samples at different temperatures of the frozen soil in the Qinghai-Tibet Railway embankment between Tanggula South and Anduo section were carried out to analyze the influence rules of each experimental factor on the mechanical properties of frozen soil during the freeze-thaw process. The results show the following. (1) When the frozen soil temperature is below 0°C and continues to drop during the freezing and thawing process, each sample shows the law of a significant increase in cohesion and a slight decrease in the internal friction angle. In the meantime, the cohesion obtained during the thawing process of the sample at the same temperature point is higher than that obtained during the freezing process. In contrast, the internal friction angles exhibit an opposite law, where the internal friction angle during the melting process is lower than the internal friction angle during the freezing process. After freezing-thawing action, it deserves to be mentioned that the cohesion increases slightly while the internal friction angles present a slight decrease trend compared to the initial state. (2) With the decrease in temperature and the gradual increase in cohesion, the temperature curve can be divided into a fast-growing section from 0 to -2°C, a slow-growing section from -2 to -8°C, and a second fast-growing section from -8 to -10°C owing to the combined effect of the pressure-thawing action and ice-water phase change. In addition, the rate of decrease in the internal friction angle also shows a similar pattern. (3) The cohesion and the internal friction angle of samples both tend to increase first and then decrease with the rise of the initial moisture content, and the critical initial moisture content is near the optimal moisture content of 15%. (4) Both the cohesion and the internal friction angle of the samples increase with dry density growth. The growth rate of cohesion will gradually increase as the temperature decreases. Moreover, the growth rate of cohesion of low dry density samples is more susceptible to temperature, while the internal friction angle growth rate is not affected by temperature.

## 1. Introduction

Permafrost is generally defined as a negative temperature or ice-bearing zero-temperature rock and soil that has been in a frozen state for more than two years [1]. The combined effects of human activities and global warming have resulted in significant degradation of permafrost areas and a continuous increase in average ground temperature worldwide [2]. From 1964 to the present, permafrost has degraded at least 25 km northward in southern Yukon, Canada, and at the southern

boundary of the Alaska North Highway corridor [3]. Since the 1980s, permafrost degradation has accelerated its way in Scandinavia, northern Sweden, with nine permafrost layers decreasing in thickness and three permafrost areas disappearing completely [4, 5]. It is notable that, in recent years, the growth rate of the permafrost active layer in the border areas of Russia and Mongolia is 3–5 cm per year, and in some regions, it exceeds 5 cm per year with a continuously expanding range. Similarly, the Qinghai-Tibet Plateau, the “world’s third pole” in China, has also seen a 30% decrease in

permafrost areas [6]. In the process of permafrost degradation to seasonally frozen soil, undesirable phenomena such as thawing mudflow and thermal thawing subsidence emerge to infinity, posing a significant threat to the stability and safety of structures like railways, highways, and pipelines [7–12], where the yearly freeze-thaw cycle is critical for the deterioration of permafrost foundation engineering properties. The Qinghai-Tibet Railway currently has built about 960 km of lines, located 4000 m above sea level, with over 500 km of lines passing through permafrost regions [13]. Inevitably, the risk of potential safety hazards associated with the abovementioned frozen soil degradation increases year by year [14, 15]. Therefore, it is particularly important to ascertain the deterioration law of mechanical properties of railway subgrade frozen soil under freeze-thaw action.

Concerning the influence of freezing and thawing on the mechanical properties of frozen soil, the current research focuses mainly on the characteristics of strength, module, and stress-deformation curve, among others. In the study of the effect of freezing and thawing on the strength of soil, many scholars have carried out research on the shear strength change pattern under multiple freezing and thawing cycles for different soil samples. In summary, a large number of research results indicate that the shear strength of different types or even the same type of soil samples may have large differences in the changes in shear strength under the effects of freezing and thawing [16–24]. Generally, the shear strength is influenced by the particle skeleton, mineral composition, and structural arrangement of frozen soil; in addition, the temperature, moisture content, external pressure, and load duration of frozen soil will also affect its shear strength [25]. At the same time, the main direction of current research is to focus on the influence of freezing and thawing cycles on the strength of frozen soil, while there are few studies on the evolution of frozen soil strength during the freezing and thawing process. However, the mechanical degradation of engineering frozen soil is a long-term and continuous process. In order to have a clearer understanding of the evolution of the mechanical properties of the Qinghai-Tibet Railway subgrade permafrost under the effects of freezing and thawing, direct shear tests were carried out on frozen plateau powder clay collected from the embankment of the subgrade of the Tanggula South and Anduo section of Qinghai-Tibet Railway at different initial moisture contents and dry densities under various temperatures during the freeze-thaw process. The results can further supplement the research field of the impact of freezing-thawing on the mechanical properties of permafrost on the Qinghai-Tibet railway subgrade and provide a theoretical reference basis for the study of the perennial deformation of the roadbed of Qinghai-Tibet Railway and the safe operation and maintenance of Qinghai-Tibet Railway in the future.

## 2. Sample Preparation and Experimental Method

**2.1. Sample Preparation.** The test in-situ soil samples were taken from the subgrade of the Qinghai-Tibet Railway between Tanggula South and Anduo section, inspected and

processed on site after sampling, sealed and labeled for packaging, and then transported back to the laboratory for the following testing.

As shown in Table 1, the basic physical property parameters of the soil samples were obtained through the indoor soil test. Subsequently drying the undisturbed soil samples naturally, milling them to fine particles with a wooden whisk, and then passing them through a 2 mm sieve allowed insight into the graph of the soil grain gradation curve shown in Figure 1, with the unevenness coefficient  $C_u=5.73$  and the curvature coefficient  $C_c=1.25$ , which proved it to be unevenly graded soil.

The direct shear tests were conducted using remodeled soil, and the samples were prepared in accordance with the Chinese Standard for Geotechnical Test Methods (GBT 50123-2019): a certain quality of sieved soil was blended and mixed thoroughly according to the experimentally set moisture content to ensure uniform distribution of coarse and fine soil particles. Then the well-mixed samples were sealed in plastic bags and left to stand for 24 hours to make the moisture fully and uniformly penetrate the soil particles. After completing the standing, the required mass of the cylindrical sample with  $D=61.8$  mm and  $h=20$  mm was weighed according to the test expectations, and the soil sample was compacted in three layers by using compaction equipment (Figure 2), and the surface of the soil sample was entirely scraped with a knife immediately following each compaction to enhance the connection between the layers for the sake of obtaining various dry density samples. After that, the prepared samples were wrapped tightly with preservative film to prevent moisture loss and subsequently put into the low-temperature freezer for freezing, as shown in Figure 3.

**2.2. Experimental Method.** The experimental method involved three concerning factors: moisture content, dry density, and temperature. The moisture content of the sample was, respectively, set to 12%, 15%, 18%, and 20%. In the meantime, the dry density was set to  $1.6$  g/cm<sup>3</sup>,  $1.7$  g/cm<sup>3</sup>, and  $1.8$  g/cm<sup>3</sup>. On this basis, 12 groups of samples with different moisture content and dry density (each group contained at least eight samples to meet the requirements of the parallel experiment) were prepared and are shown in Table 2. Simultaneously, the shear temperature points during freeze-thaw were sequentially set to  $2.0^\circ\text{C}$ ,  $0^\circ\text{C}$ ,  $-2.0^\circ\text{C}$ ,  $-5.0^\circ\text{C}$ ,  $-8.0^\circ\text{C}$ ,  $-10.0^\circ\text{C}$ ,  $-8.0^\circ\text{C}$ ,  $-5.0^\circ\text{C}$ ,  $-2.0^\circ\text{C}$ ,  $0^\circ\text{C}$ , and  $2.0^\circ\text{C}$ , which indicated that the direct shear test was carried out at the same temperature point on the freezing and thawing path.

To ensure the accuracy of the soil sample temperature during shearing and to prevent heat migration due to excessive temperature discrepancy during the tests from affecting the experimental results, the samples and the direct shear test boxes were stored separately in a low-temperature freezer with constant computerized temperature control in the range of  $-30\sim 10^\circ\text{C}$ . The direct shear tests were carried out in the programmable high- and low-temperature ambient temperature test chamber that can be configured at a

TABLE 1: Basic physical properties parameters of soil samples.

Dry density ( $\text{g}/\text{cm}^3$ )	Optimal moisture content (%)	Liquid limit (%)	Plastic limit (%)	Plasticity index (%)
1.6	15	27.6	12.6	15

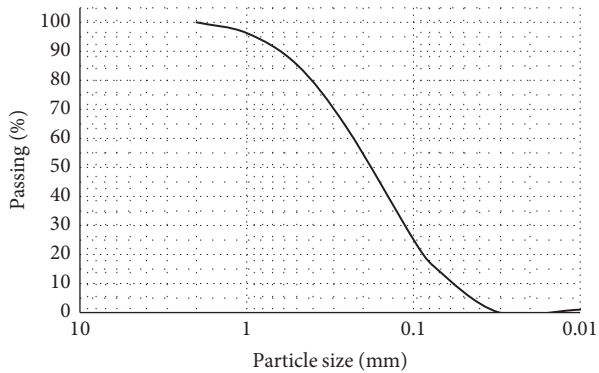


FIGURE 1: Particle gradation curve of soil samples.



FIGURE 2: Compacted soil samples.

constant temperature in the range of  $-50\sim 20^\circ\text{C}$  (Figures 4 and 5) at the Key Laboratory of High-Speed Railway Engineering, Ministry of Education, Southwest Jiaotong University.

Before the tests, all the samples and the direct shear test boxes were placed in the constant temperature freezer separately with the temperature adjusted to  $2^\circ\text{C}$  for 24 hours to ensure the uniform initial temperature distribution of the soil samples and reduce the influence of heat migration between the test boxes and samples. And then, the samples were quickly moved to the thermostatic test chamber with the same temperature set in advance to start the first direct shear test. Afterward, the temperature of the thermostatic freezer was adjusted to each shear temperature point in sequence for 8 hours to ensure that the samples reached the specified temperature; then the next

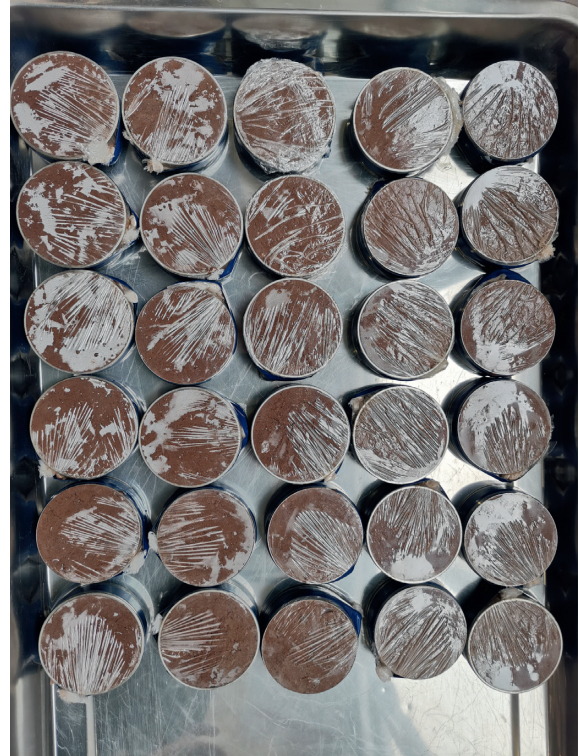


FIGURE 3: Physical image of the samples.

direct shear test was carried out and repeated until freeze-thaw was complete.

Since the long loading time of vertical pressure in the direct shear test would cause a certain amount of heat transfer to the samples, the direct fast shear tests were conducted in this test. And because the samples were taken from the shallow layer of the railway subgrade, the vertical pressure setting for the tests was small. Consequently, the test rate was set to  $0.8\text{ mm}/\text{min}$ , and the vertical pressure was set to 50, 100, 150, and 200 kPa, respectively, in order.

### 3. Analysis

#### 3.1. Variation of Shear Strength and Temperature of Frozen Soil during Freezing-Thawing Process

**3.1.1. Variation of Cohesion with Temperature.** Since the variation pattern of cohesion with temperature is similar for each sample group, four groups of FT1, FT2, FT3, and FT4 with the same dry density of  $1.6\text{ g}/\text{cm}^3$  as the in-situ soil were selected to plot the results of cohesion with temperature change as shown in Figures 6(a)–6(d). In Figure 6, the blue line represents the freezing process with the direction from left to right, while the red line represents the thawing process with the opposite direction.

TABLE 2: Samples of direct shear tests.

No.	Dry density (g/cm <sup>3</sup> )	Moisture content (%)	No.	Dry density (g/cm <sup>3</sup> )	Moisture content (%)	No.	Dry density (g/cm <sup>3</sup> )	Moisture content (%)
FT1	1.6	12	FT5	1.7	12	FT9	1.8	12
FT2		15	FT6		15	FT10		15
FT3		18	FT7		18	FT11		18
FT4		20	FT8		20	FT12		20



FIGURE 4: Programmable high- and low-temperature environment temperature test chamber.



FIGURE 5: Direct shear tester in the chamber.

It can be seen from Figure 6 that the cohesion of each moisture content sample remains unchanged above 0°C regardless of being in freezing or thawing stage, indicating that the water in the samples exists in the form of liquid at this time, which basically does not affect cohesion. While the temperature is below 0°C and is decreasing continuously, the cohesion commences increasing, which indicates that the rising of ice content is due to the gradual crystallization of water, resulting in the gradual increase of ice cementation. Taking the FT2 group for example, with the same moisture content as the undisturbed soil, the freezing process temperature varying from 0°C to -10°C, the cohesive force raises from 16.83 kPa to 57.38 kPa, with an increase of about 255%, showing that the temperature of frozen soil has a significant

effect on its cohesion. While the thawing process temperature varies from -10°C to 0°C, the cohesive force decreases to 19.23 kPa, increasing by 14.3% compared to the state before freezing. Moreover, the curve of each thawing process is located above that of the freezing process, indicating that the freeze-thawing action increases the cohesion of the sample. And the cohesion obtained from the thawing process of the sample is higher than that of the freezing process at the same shear temperature, which is different from the conclusion that the cohesion of the sample is reduced by the freeze-thawing effect mentioned in some literature [22–27]. The main reason for the difference is that the cohesion of the soil is related to the connection way of the soil. The freeze-thaw action would destroy the original

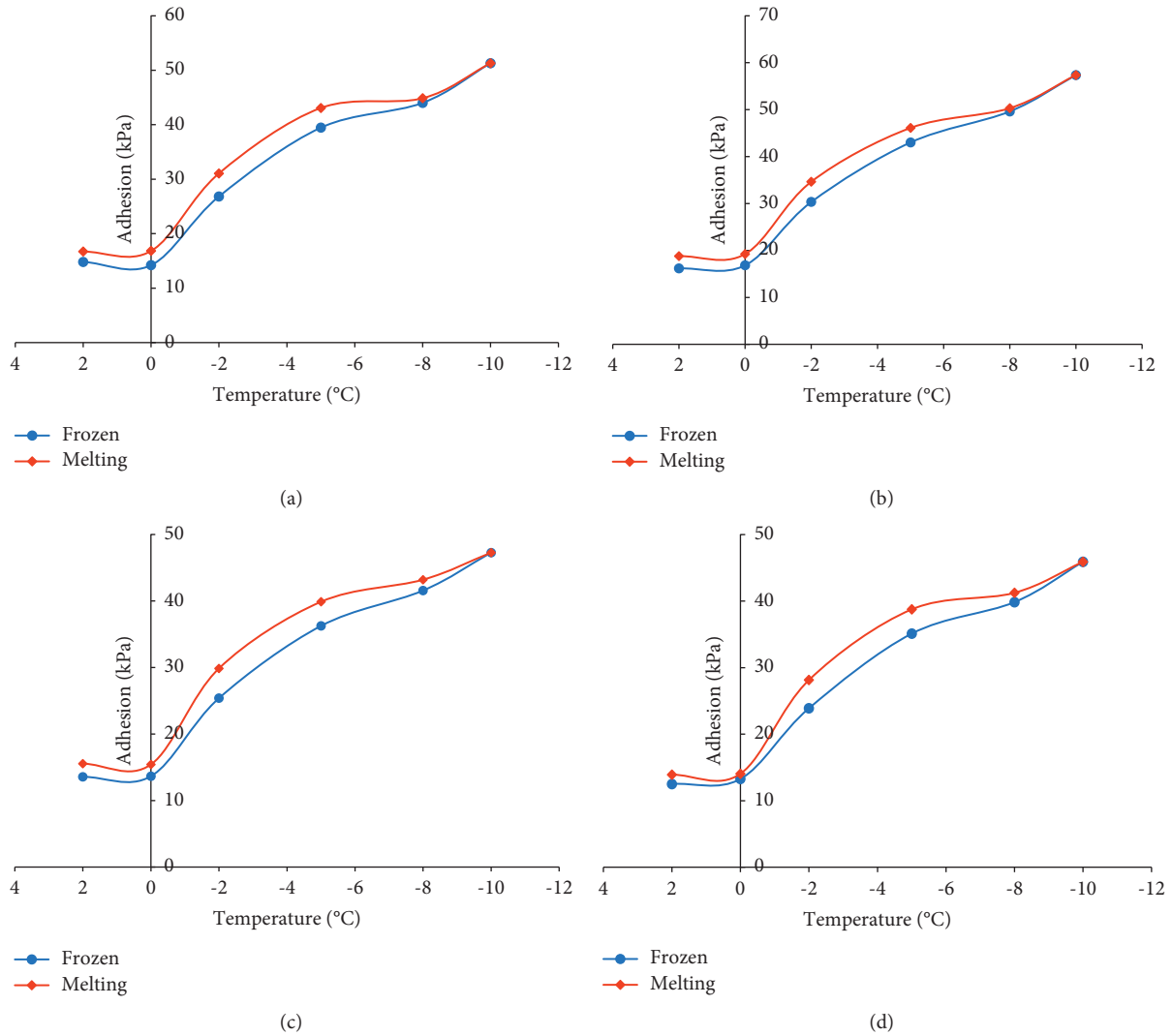


FIGURE 6: Variation curve of cohesion  $c$ -temperature of  $1.6 \text{ g/m}^3$  dry density sample groups. (a) FT1. (b) FT2. (c) FT3. (d) FT4.

connection between soil particles and rearrange them by frost-heave and thawing settlement, which may change the cohesion of the sample. However, when the soil particles of the sample are rearranged and the connection way produced is inferior to the original sample, the cohesion is naturally reduced. However, when the connection is superior to the original sample, it performs an opposite property. Obviously, the case of the sample in this paper belongs to the latter.

The experimental results of other sample groups were similar. Based on the value of the cohesive strength at  $0^\circ\text{C}$  during the freezing process, the cohesion of the remaining sample groups increased by 241~295% when frozen at  $-10^\circ\text{C}$  compared with that before freezing, and the cohesive force of the heating and melting to  $0^\circ\text{C}$  was also increased by 0.5%~21.1% compared with that before freezing.

It is also worth noting that the  $0\sim-10^\circ\text{C}$  section of each curve can be roughly divided into three parts according to the change of the slope, where it is firstly steeper in the range of  $0\sim-2^\circ\text{C}$ , while it gradually tends to slow down in the range

of  $-2\sim-8^\circ\text{C}$ ; finally, it presents a second steepening in the range of  $-8\sim-10^\circ\text{C}$ . During freezing and thawing at test temperatures below  $0^\circ\text{C}$ , two phenomena affect the curve change pattern: the ice-water phase change and the pressure-thawing effect. When the sample temperature changes in the range of  $0\sim-2^\circ\text{C}$ , it is close to the freezing point of water in the soil; hence the ice-water phase changes drastically. Although the pressure-thawing effect exists, it is dominated by ice-water phase transformation. With the decrease in temperature, a large amount of free water in the soil will be rapidly transformed into ice crystals, rapidly exerting strength and producing a cementing effect on the soil particles, resulting in a dramatic increase in the cohesion between soil particles. When the temperature is in the range of  $-2$  to  $-8^\circ\text{C}$ , most of the water has frozen into ice, and as the temperature continues to drop, only a small amount of water remains to continue the phase change. In the meantime, the pressure-thawing effect also inhibits the rate of transformation of the remaining water into ice, which leads to a slowing down of the curve slope. However, the

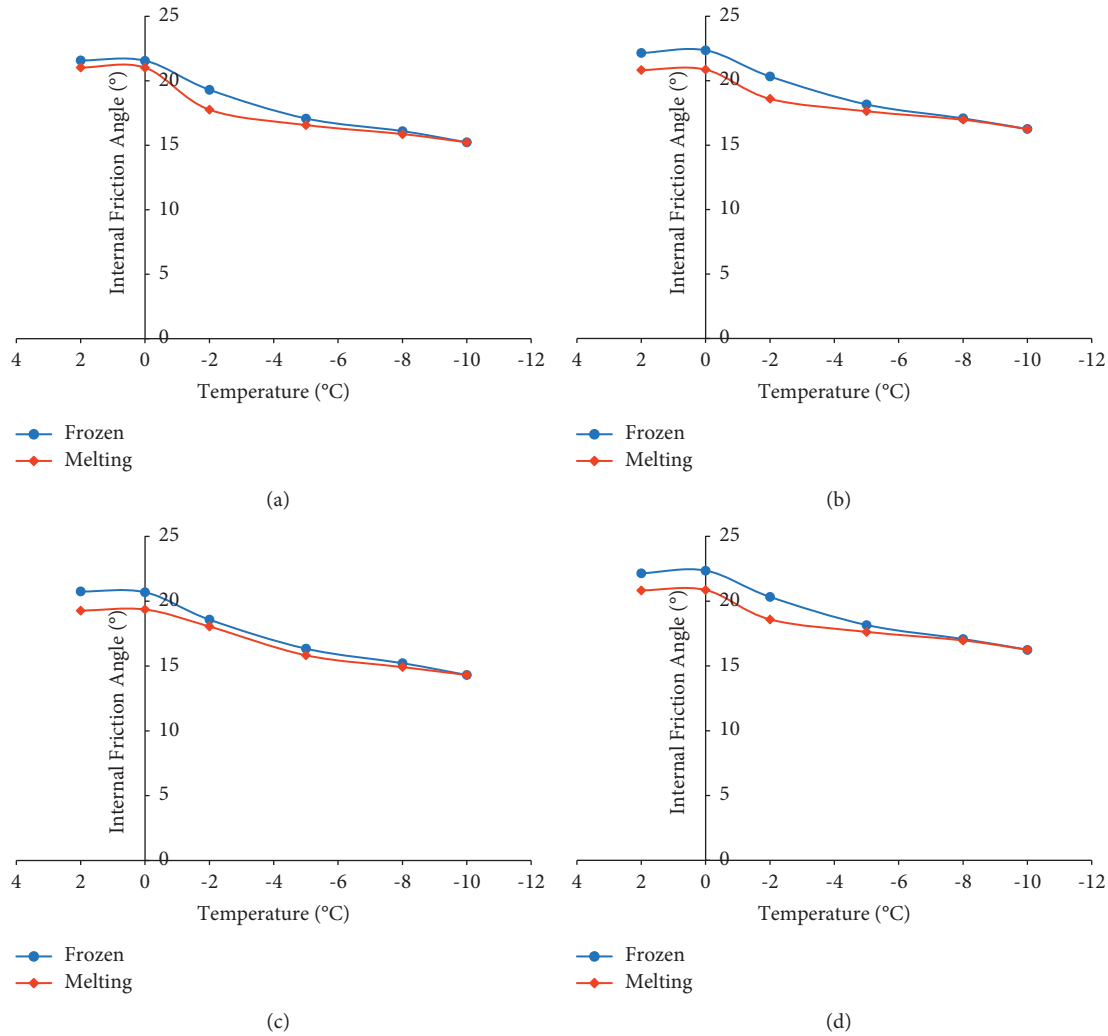


FIGURE 7: Internal friction angle  $\phi$ -temperature curve of  $1.6 \text{ g/m}^3$  dry density sample groups. (a) FT1. (b) FT2. (c) FT3. (d) FT4.

pressure-thawing effect of frozen soil will gradually disappear with the decrease of temperature [21]. Therefore, when the temperature is in the range of  $-8 \sim -10^\circ\text{C}$ , the remaining water phase change speed increases due to the weakening of the pressure-thaw effect, resulting in a second remarkable increase in cohesion.

**3.1.2. Variation of the Internal Friction Angle with Temperatures.** For the same reason as above, four groups of FT1, FT2, FT3, and FT4 samples with the same dry density as the undisturbed soil of  $1.6 \text{ g/cm}^3$  with different moisture contents were selected to draw the curve of internal friction angle  $\phi$  with various temperatures, and only the quantitative analysis of FT2 sample group was carried out, as shown in Figure 7.

It can be seen from Figure 7 that the internal friction angle is not affected by the temperature at  $2 \sim 0^\circ\text{C}$ . As the temperature is lower than  $0^\circ\text{C}$  and continues to decrease, the internal friction angle will decrease accordingly during the freezing and thawing process. This is because, in the process of ice-water phase transformation, the conversion of water

to ice will cause volume expansion, crowding, and expanding the soil pores, which results in a lower degree of soil particle occlusion. And the strength of ice crystals is much lower than that of soil particles, which will further lead to a decrease in the internal friction angle of the samples. Meanwhile, the reduction rate within the  $0 \sim -2^\circ\text{C}$  section is significantly faster than that of the  $-2 \sim -8^\circ\text{C}$  section, and the reduction rate within the  $-8 \sim -10^\circ\text{C}$  is also slightly faster than that of the  $-2 \sim -8^\circ\text{C}$  section, and the reason is similar to the cohesion influenced by the ice-water phase change and pressure-thawing action. While, in terms of values, taking FT2 for example, the freezing process temperature decreases from  $0^\circ\text{C}$  to  $-10^\circ\text{C}$ , the internal friction angle drops from  $22.36^\circ$  to  $16.25^\circ$ , decreasing by about 26.6%. With thawing process temperature varying from  $-10^\circ\text{C}$  to  $0^\circ\text{C}$ , the internal friction angle rises from  $16.25^\circ$  to  $20.86^\circ$ , reducing by about 6.7% compared with the state before freezing. And, the internal friction angle obtained during the thawing process at the same shear temperature point is lower than that of the freezing process, which is related to the expansion and deformation of the pores during the freezing process, leading to the decrease of the occlusion between soil particles.

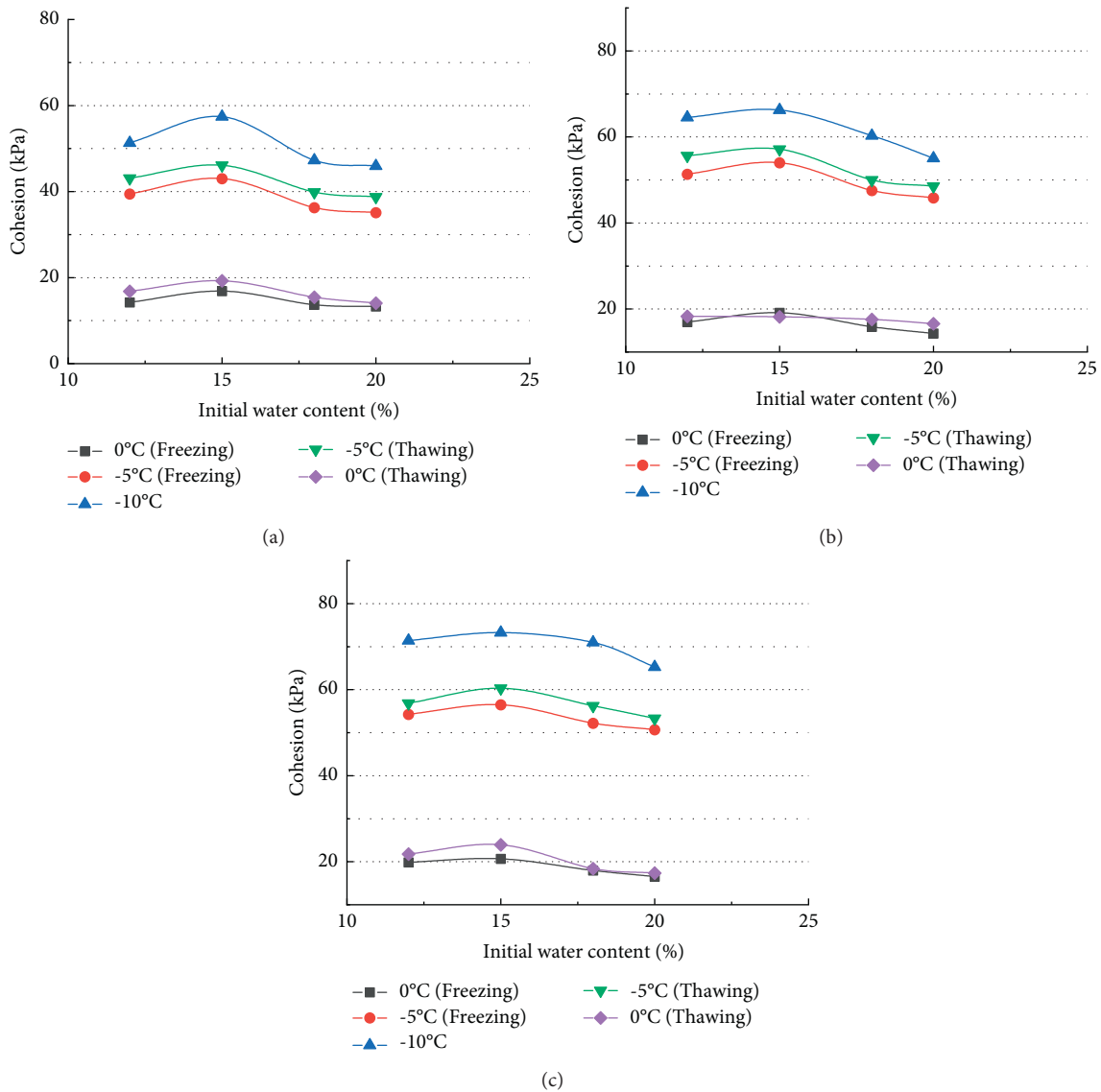


FIGURE 8: Relationship curve between cohesion  $c$  of the sample group and initial moisture content under freeze-thaw action. (a) Dry density 1.6 g/cm<sup>3</sup>. (b) Dry density 1.7 g/cm<sup>3</sup>. (c) Dry density 1.8 g/cm<sup>3</sup>.

The experimental results of other sample groups are similar. Based on the value of internal friction angle before freezing at 0°C, the internal friction angle of other sample groups decreased by 23.5%~34.5% when frozen at -10°C, and the internal friction angle of other sample groups decreased by 2.1%~8.4% when thawed to 0°C. In general, temperature has a smaller effect on the angle of internal friction compared to cohesion.

**3.2. Effect of Initial Moisture Content on the Shear Strength of Frozen Soil during Freezing and Thawing Process.** In order to explore the influence of the initial moisture content of the sample on the shear strength of the frozen soil during the freezing and thawing process, the typical temperatures (0°C, -5°C, -10°C) were selected in each group of the same dry density. The relationship was plotted between cohesion and internal friction angle  $\varphi$  with initial moisture

content during the freeze-thaw process, as shown in Figures 8 and 9.

Figures 8 and 9 reveal that there are some similar rules for the curves of cohesion and internal friction angle. Whether it is during the freezing or thawing process, the cohesion and internal friction angle both increase first and then decrease with the rising of initial moisture content, and the maximum values of both parameters are obtained at the initial moisture content of 15%, which is also the optimum moisture content. It indicates that a certain critical moisture content exists at or near the optimal point at each test temperature, which gives the sample the maximum cohesion or internal friction angle. And the optimal moisture content in this work is defined as the moisture content corresponding to the maximum compaction state of the soil under a certain number of ramming times; that is, the soil particles are easily compressed and connected closely under this moisture content, and the sample is accessible to obtain

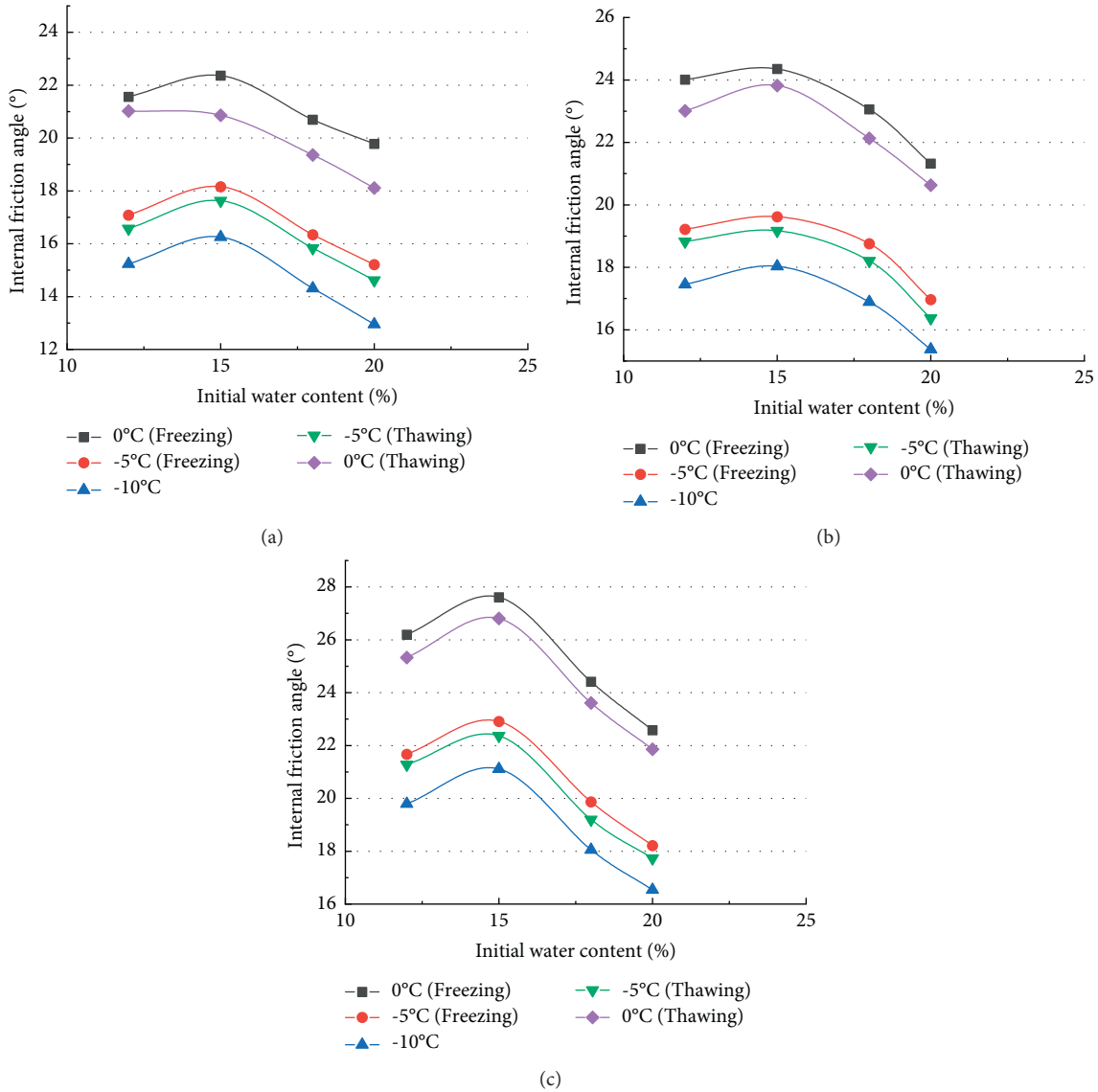


FIGURE 9: Relationship curve between internal friction angle  $\phi$  of the sample group and initial moisture content under freeze-thaw action. (a) Dry density  $1.6\text{ g/cm}^3$ . (b) Dry density  $1.7\text{ g/cm}^3$ . (c) Dry density  $1.8\text{ g/cm}^3$ .

the maximum shear strength parameters at this time. However, as the temperature decreased, the water crystallization inside the soil sample frosted and heaved, and the water content may change. The reason for this rule is analyzed as follows: when the moisture content is lower than the critical moisture content, the phase change occurs with the decrease of temperature, and the internal pores of the soil are gradually filled with ice crystals, which reinforces the soil strength. However, as the moisture content continues to increase, the ice crystals gradually fill up and further frost-heave the large pores, which increases the gap between soil particles and weakens the intermolecular force and occlusion of soil particles, thereby weakening the soil strength.

3.3. Effect of Dry Density on the Shear Strength of Frozen Soil during Freezing and Thawing Process. In order to explore the influence of sample dry density on the shear strength of

frozen soil during the freeze-thaw process, the typical temperatures ( $0^\circ\text{C}$ ,  $-5^\circ\text{C}$ ,  $-10^\circ\text{C}$ ) were selected in each sample group with the same initial moisture content. The relationship curves of cohesion  $c$  and internal friction angle  $\phi$  with dry density during the process were drawn correspondingly as shown in Figures 10 and 11.

It can be seen from Figures 10 and 11 that the sample's cohesive force and internal friction angle increase with the dry density growth at each stage of freezing and thawing, but the growth curves of the cohesive force and internal friction angle are different.

For the cohesion, the curve characteristics of each water content curve group are similar. Taking Figure 10(a) as an example, when the temperature is  $0^\circ\text{C}$ , the cohesion increases linearly and the growth rate is relatively slow. As the temperature drops to  $-5^\circ\text{C}$ , the linear characteristics of the curve disappear, showing that the front-end growth rate is greater than the back-end, and the front-end growth rate is



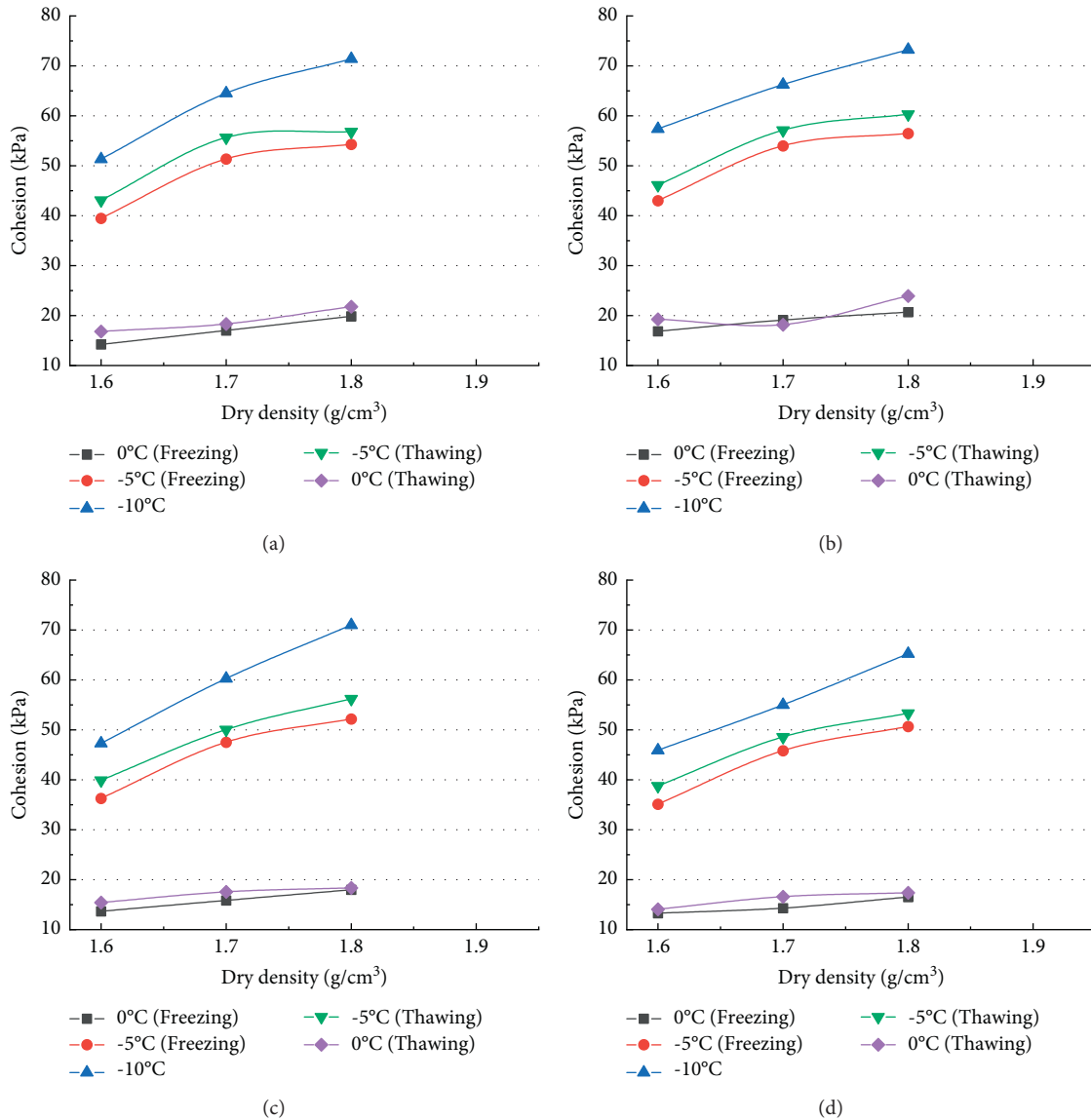


FIGURE 10: Relationship curve between cohesion  $c$  of sample group and dry density under freeze-thaw action. (a) Initial moisture content 12%. (b) Initial moisture content 15%. (c) Initial moisture content 18%. (d) Initial moisture content 20%.

significantly greater than the 0°C curve. While temperature varies from -5°C to -10°C, the back-end growth rate catches up with the front-end, the curve begins to show linear growth again, and the overall slope of the curve is greater than the 0°C curve.

The results above show the following. Firstly, the increase in sample density has a significant effect on the increase of cohesion at each temperature condition. Secondly, the cohesion growth rate corresponding to the dry density increases gradually as the temperature decreases, and the

growth rate of cohesion of low dry density samples is more easily influenced by temperature.

Similarly, for the internal friction angle, taking Figure 11(a) as an example, the internal friction angle curves grow linearly and parallel to each other at each temperature. Although the slopes of the other curves do not all increase linearly, the slope of each temperature curve at the same dry density remains unchanged, indicating that the freezing temperature does not affect the growth rate of the internal friction angle, which is different from the conclusion that the

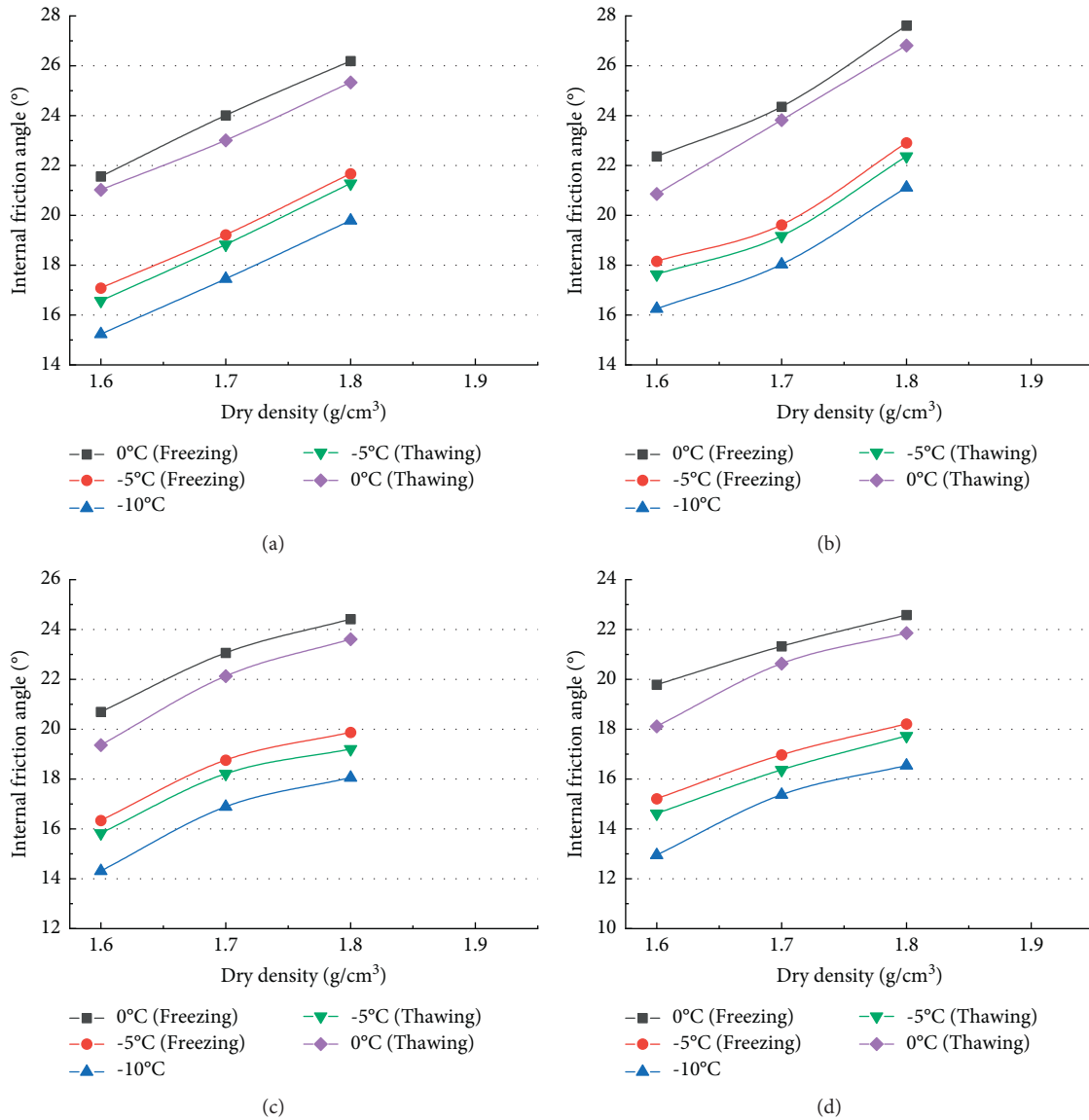


FIGURE 11: Relationship curve between internal friction angle  $\varphi$  and dry density of sample group under freeze-thaw action. (a) Initial moisture content 12%. (b) Initial moisture content 15%. (c) Initial moisture content 18%. (d) Initial moisture content 20%.

cohesion of the frozen soil with low dry density is more susceptible to temperature.

#### 4. Conclusion

In this work, the direct shear test of different dry density and moisture content samples at different temperatures during the freezing and thawing process of the frozen soil of the Qinghai-Tibet Railway between Tanggula South and Anduo section was carried out, and the influence of each test factor on the mechanical properties of the frozen soil during this process was analyzed, which produced the following main conclusions:

- (1) The cohesive force and internal friction angle are unchanged during the freezing and thawing process from 0 to 2°C. As the temperature decreases below

0°C and continues to decrease, the cohesive force of each sample shows a sharp increase (241%~295%). In contrast, the internal friction angle decreases slightly (23.5%~34.5%). The cohesive force obtained during the thawing process of the sample at the same shear temperature point is higher than that during the freezing process, whereas the internal friction angle shows an opposite property. When freezing and thawing are completed, the cohesion rises slightly (0.5%~21.1%) and the internal friction angle shows a slight decrease trend (2.1%~8.4%).

- (2) With the decrease in temperature and increase of cohesion, the corresponding slope within the temperature range can be divided into three stages due to the combined effect of pressure-thawing and ice-water phase change. In the range of 0~−2°C, a large

number of ice crystals exert their strength and cement the soil particles owing to the intense ice-water phase change, and the cohesive force increases rapidly. In the range of  $-2\sim-8^{\circ}\text{C}$ , for the reason that the water content is reduced and the pressure-thawing effect inhibits the generation of ice crystals, the growth rate slows down. In the range of  $-8\sim-10^{\circ}\text{C}$ , as the pressure-thawing effect disappears with the decrease of temperature, the inhibition vanishes and the cohesion begins to increase rapidly for the second time, and the decline rate of the internal friction angle also shows similar patterns.

- (3) The samples' cohesive force and internal friction angle show a climbing trend and then decline with the rising of the initial moisture content, the critical point of which is located at or near the optimal moisture content of 15%. In this case, both the cohesion and the internal friction angle obtain peak values.
- (4) Both the cohesion and the internal friction angle increase with the increase of dry density. And the cohesion growth rate corresponding to the dry density will gradually increase as the temperature decreases. Moreover, the growth rate of cohesion of low dry density samples is more susceptible to temperature, while the internal friction angle growth rate is exempt from such influence.

## Data Availability

The data used to support the findings of this study are included within the article.

## Conflicts of Interest

The authors declare no conflicts of interest.

## Acknowledgments

The authors gratefully acknowledge the support provided by the National Natural Science Foundation of China (nos. 51878571 and U2034205) and the Fundamental Research Funds for the Central Universities, CHD (30010220516).

## References

- [1] X. Xu and M. Qiu, *Advanced Soil Mechanics [M]*, Harbin Institute of Technology Press, Harbin, China, 2008.
- [2] S. E. Chadburn, E. J. Burke, P. M. Cox, P. Friedlingstein, G. Hugelius, and S. Westermann, "An observation-based constraint on permafrost loss as a function of global warming," *Nature Climate Change*, vol. 7, no. 5, pp. 340–344, 2017.
- [3] M. James, A. G. Lewkowicz, S. L. Smith, and C. M. Miceli, "Multi-decadal degradation and persistence of permafrost in the Alaska highway corridor, northwest Canada[J]," *Environmental Research Letters*, vol. 8, no. 4, Article ID 045013, 2013.
- [4] M. Johansson, J. Åkerman, F. Keuper, T. R. Christensen, H. Lantuit, and T. V. Callaghan, "Past and present permafrost temperatures in the a area: rb," *Ambio*, vol. 40, no. 6, pp. 558–565, 2011.
- [5] T. V. Callaghan, C. Jonasson, T. Thierfelder et al., "Ecosystem change and stability over multiple decades in the Swedish subarctic: complex processes and multiple drivers[J]," *Philosophical Transactions of the Royal Society B: Biological Sciences*, vol. 368, 2013.
- [6] G. Cheng and H. Jin, "Groundwater and its changes in permafrost regions of the Tibetan Plateau [J]," *Hydrogeological engineering geology*, vol. 40, no. 01, pp. 1–11, 2013.
- [7] Y. Feng, *Quantitative Analysis of Permafrost Changes in the Tibetan Plateau and its Ecological and Hydrological Significance [D]*, China University of Geosciences, Beijing, China, 2015.
- [8] S. Wei, *Mechanical Properties and Deformation Prediction of Subgrade Filling under Freeze-Thaw Action [D]*, Xi'an University of Science and Technology, Xi'an, China, 2020.
- [9] Di Zheng, *Study on Typical Geological Disasters in Permafrost Regions in the Hinterland of the Qinghai-Tibet Plateau [D]*, China University of Geosciences, Beijing, China, 2009.
- [10] O. J. Ferrians and R. Kachadoorian, *Permafrost and Related Engineering Problems in Alaska[R]*, USGS, Reston, Virginia, 1969.
- [11] S. Wang, F. Niu, J. Chen, and Y. Dong, "Permafrost research in China related to express highway construction," *Permafrost and Periglacial Processes*, vol. 31, no. 3, pp. 406–416, 2020.
- [12] S. Yao, L. Cai, and M. Hu Lin, "Discussion on geological disaster protection technology of pipelines in alpine permafrost regions [J]," *Petroleum and chemical equipment*, vol. 23, no. 5, pp. 90–92, 2020.
- [13] X. Dong and Z. Dang, "Briefly discussed the matters needing attention in the construction of catenary foundation in permafrost regions of the Gra section of Qinghai-Tibet Railway [J]," *Sichuan Cement*, no. 07, pp. 250–251, 2020.
- [14] J. Wu, S. Yu, Q. Wu, and Z. Wen, "The process and mode of permafrost degradation in the Qinghai-Tibet Plateau [J]," *Chinese Science (D: Geoscience)*, vol. 39, no. 11, pp. 1570–1578, 2009.
- [15] S. Li, Z. Nan, and L. Zhao, "Effect of freeze-thaw on energy exchange between system and environment," *Glacier permafrost*, vol. 24, no. 2, pp. 109–115, 2002.
- [16] S. Wang, *Research on Highway Subgrade Stability and Prediction Technology in Plateau Permafrost Region [D]*, Southeast University, Nanjing, China, 2005.
- [17] R. W. Van Klaveren, *Hydraulic Erosion Resistance of Thawing soil[D]*, Department of Agricultural Engineering, Washington State University, Washington, USA, 1987.
- [18] B. D. Alkire and J. M. Morrison, "Change in soil structure due to freeze-thaw and repeated loading[J]," *Transportation Research Record*, vol. 18, no. 9, pp. 15–21, 1983.
- [19] C. Song, J. Qi, and F. Liu, "The effect of freeze-thaw on the mechanical properties of Lanzhou loess [J]," *Geotechnical mechanics*, no. 04, pp. 1077–1080 + 1086, 2008.
- [20] X. Yao, J. Qi, and C. Song, "Effect of freeze-thaw action on engineering properties of Qinghai-Tibet clay [J]," *Glacier permafrost*, no. 01, pp. 165–169, 2008.
- [21] Li-X. Zhang, X.-Z. Xu, Z.-X. Zhang, and Y.-S. Deng, "Experimental study of the relationship between the unfrozen water content of frozen soil and pressure," *Journal of Glaciology and Geocryology*, vol. 2, pp. 28–31, 1998.
- [22] Z. Zhou, S. Zhong, and L. Han, "Test on the influence of freeze-thaw cycles on road performance of loess [J]," *Journal of Chang'an University (Natural Science Edition)*, vol. 33, no. 4, pp. 1–6, 2013.

- [23] A. Hotineanu, M. Bouasker, A. Aldaood, and M. Al-Mukhtar, "Effect of freeze-thaw cycling on the mechanical properties of lime-stabilized expansive clays," *Cold Regions Science and Technology*, vol. 119, no. 11, pp. 151–157, 2015.
- [24] D. Wang, W. Ma, X. Chang, Z. Sun, W. Feng, and J. Zhang, "The effect of freeze-thaw cycles on the physical and mechanical properties of Qinghai-Tibet clay [J]," *Rock mechanics and engineering*, no. 23, pp. 4313–4319, 2005.
- [25] T. Hu, J. Liu, and Q. Wang, "etc. Experimental study on undrained shear properties of silty clay under freeze-thaw cycles [J]," *Journal of Central South University*, vol. 49, no. 6, pp. 1481–1490, 2018.
- [26] He Wu, Ge Qi, and J. Bo Tian, "Study on the shear strength parameters under different freezing and thawing cycles of soil slope in China[J]," *Applied Mechanics and Materials*, vol. 454, p. 2818, 2014.
- [27] Y. Mu, T. Chen, G. Chen, F. Niu, J. Luo, and G. Bi, "Experimental study on the effect of freeze-thaw cycles on shear strength of clay coarse grained soil [J]," *Journal of Disaster Prevention and Reduction Engineering*, vol. 39, no. 03, pp. 375–386, 2019.

## Research Article

# Mechanical Behavior, Energy Release, and Crack Distribution Characteristics of Water-Saturated Phyllite under Triaxial Cyclic Loading

Yang Zhou , Shengrui Su , and Peng Li

*School of Geological Engineering and Geomatics, Chang'an University, Xi'an 710064, China*

Correspondence should be addressed to Shengrui Su; shengruisu@163.com

Received 28 July 2021; Revised 17 October 2021; Accepted 26 November 2021; Published 30 December 2021

Academic Editor: Guowen Xu

Copyright © 2021 Yang Zhou et al. This is an open access article distributed under the Creative Commons Attribution License, which permits unrestricted use, distribution, and reproduction in any medium, provided the original work is properly cited.

Many geological engineering hazards are closely related to the dynamic mechanical behaviors of rock materials. However, the dynamic mechanical behaviors of phyllite are less studied. In this study, we have carried out a series of triaxial cyclic tests on dry and water-saturated phyllite by employing the MTS 815 servohydraulic testing system and AE testing equipment to reveal the mechanical behavior, energy release, and crack distribution characteristics of phyllite. Results show that phyllite is a water-sensitive rock. Water and cyclic loading substantially affect the compressive strength, crack damage stress, deformation parameters, dilatancy, energy release, and crack distribution characteristics of phyllite. Furthermore, based on the dissipated energy, a new damage variable for phyllite is established. The critical damage variable for phyllite is approximately 0.80; this variable can be used as an index to predict the failure of phyllite. The water saturation effect of phyllite is very obvious; that is, it results in the weakness of mechanical properties of phyllite and changes the AE energy release and crack distribution characteristics of phyllite. This research can provide guidance for engineering construction and disaster prevention and control.

## 1. Introduction

Rock mass is often affected by mechanical excavation, blasting, earthquake, and other dynamic loads in engineering activities. The mechanical properties of rock materials under dynamic loading have a significant influence on engineering activities. Many geological engineering hazards (such as slope instability, cave collapse, and large deformation of surrounding rock) are closely related to the dynamic mechanical behaviors of rock materials. Therefore, it is of great significance to study the effect of dynamic loading on the mechanical behaviors and failure mechanism of rock materials for engineering construction and disaster prevention and control.

When tunnels and slopes are excavated, the rock mass undergoes very complicated stress path owing to the layered, segmented excavation and excavation between adjacent caverns. The rock mass is in a state of cyclic loading and unloading. Once the stress exceeds the ultimate bearing

capacity of the rock mass, geological engineering hazards may occur; these pose a great threat to the safety of engineering and field staff. At present, considerable research has been conducted on the mechanical behaviors of rocks under cyclic loading. Fuenkajorn and Phueakphum [1] studied the effect of cyclic loading on compressive strength and elastic modulus of rock salt. Duan and Yang [2] studied the fatigue deformation of sandstone under uniaxial cyclic loading and found that the energy dissipation curve can reflect the fatigue deformation of the sandstone. Liu et al. [3] studied the mechanical behaviors of intermittently jointed rock models under uniaxial cyclic loading. Xiao et al. [4] studied the damage evolution of sandstone under cyclic loading and found the three-stage evolution process of the damage. Fan et al. [5] conducted a series of discontinuous cyclic loading tests and studied the fundamental role of the loading history in the fatigue performance of salt. Sheng et al. [6] studied the mechanical damage characteristics of sandstone under triaxial cyclic loading. Ning et al. [7] studied the crack

initiation and propagation thresholds of coal specimens based on energy dissipation theory. The mechanical behaviors of rocks are closely related to the stress path, confining pressure, moisture condition, and rock type. However, the mechanical properties, energy release, and crack distribution characteristics of water-saturated rock materials under cyclic loading are less studied.

Phyllite is a type of metamorphic rock that is widely distributed on the surface of the Earth and is used for many engineering activities. During construction and later operation, the mechanical properties of phyllite directly affect the safety and stability of project. To date, many achievements have been made regarding the static mechanical properties of phyllite [8–15]. However, the mechanisms of damage, deformation, and failure of saturated phyllite under cyclic loading are still unclear. This study focuses on the mechanical behaviors and AE characteristics of dry and saturated phyllite under the influence of confining pressure and cyclic loading. The deformation parameters, dilatancy characteristic, damage stress, and damage variable of phyllite under confining pressures of 5, 10, and 20 MPa were analyzed. Degradation mechanism of water-saturated phyllite was discussed, and the energy release and crack distribution characteristics were revealed. The research results can provide guidance for the safe construction of slopes, tunnels, and foundations, as well as disaster prevention.

## 2. Materials and Methods

In this paper, slightly weathered phyllite obtained from the northwest part of Sichuan Province, China, was used as the research object. This phyllite is composed of quartz, plagioclase, calcite, mica, and chlorite. The average density and P-wave velocity of phyllite were  $2.70 \text{ g/cm}^3$  and  $2.48 \text{ km/s}$ , respectively. According to the recommendations of the International Society of Rock Mechanics (ISRM), the phyllite was processed into  $\phi 50 \times 100 \text{ mm}$  cylindrical specimens. The bedding plane of the phyllite specimen was nearly horizontal. The two ends of the specimens were polished. P-wave velocities and densities of all specimens were measured to remove the outliers. Selected specimens were placed in an oven with a constant temperature of  $105^\circ\text{C}$  until the mass was constant. At that time, the specimens were considered to be dry. Half of the dry specimens were first vacuumed for 8 h using vacuum pumping and then placed in an aqueous solution for 48 h; after this, the specimens were considered to be saturated. Before testing, the water-saturated specimens were placed in fresh-keeping bags to prevent water evaporation. The uniaxial compressive strength of the phyllite was approximately 75 MPa, and the elastic modulus and Poisson's ratio were approximately 22 GPa and 0.18, respectively. A series of cyclic loading and unloading tests were carried out using the MTS 815 servohydraulic testing system (Figure 1). The PCI-2 monitoring system produced by the American Physical Acoustics Corporation was used for the AE testing. Eight AE sensors were installed on the surface of the sample chamber to collect the AE signals (Figure 1).

Triaxial cyclic loading and unloading tests were conducted and controlled using axial displacement loading and axial stress unloading. The loading rate of axial displacement was  $0.005 \text{ mm/s}$  and the unloading rate of axial stress was  $0.5 \text{ MPa/s}$ . The triaxial cyclic loading and unloading tests were performed under confining pressures of 5, 10, and 20 MPa. First, the triaxial confining pressures were applied to the predetermined levels (5, 10, and 20 MPa) at a rate of  $0.5 \text{ MPa/s}$ . Second, the confining pressure remained constant. The axial displacement was first loaded to 0.3 mm at a rate of  $0.005 \text{ mm/s}$ ; then, the axial deviatoric stress was unloaded to 0.5 MPa at a rate of  $0.5 \text{ MPa/s}$ . Third, the loading and unloading cycles were carried out at 0.03 mm axial displacement interval. The triaxial cyclic loading and unloading tests were continued until the phyllite specimens failed.

## 3. Results

**3.1. Stress-Strain Curves.** The loading and unloading curves cannot coincide completely under triaxial cyclic loading (Figure 2). The loading curve is always above the unloading curve. Phyllite is a heterogeneous material that contains microcracks. Owing to the sliding and closing of the cracks during the loading process, the unloading curve cannot completely return to its original shape. The loading and unloading curves form a hysteresis loop. Hysteresis loops are sparse in the first several cycles and then densely distributed for a long time. When the rock specimen approaches failure, the hysteresis loops become sparse again. Each hysteresis loop consists of elastic strain and plastic strain. The elastic strain can be recovered during the unloading process, whereas the plastic strain is irreversible. With an increase in the number of cycles, the plastic strain accumulates until the specimen fails. In addition, the compressive strength of saturated phyllite is obviously lower than that of dry phyllite. Phyllite is a type of water-sensitive rock.

**3.2. Deformation Parameters.** The strain, elastic modulus, and Poisson's ratio are important deformation parameters of rock. Phyllite is a heterogeneous material that retains its residual strain (irreversible strain) after unloading. The calculation method for the irreversible strain is shown in Figure 3. In general, with the increase of axial stress, the irreversible strain increases exponentially under different confining pressures (Figure 4). During the early loading process, the axial and radial irreversible strains increase at a relatively stable rate. When the phyllite approaches failure, the irreversible strain increases rapidly, leading to the sudden failure of the phyllite specimen. When the axial stresses are the same, the axial and lateral irreversible strains of saturated phyllite are significantly larger than those of dry phyllite. With the increase in axial stress, the difference in irreversible strain between saturated phyllite and dry phyllite increases gradually. Water has a significant effect on the axial and lateral irreversible strain of phyllite. The softening effect of water on phyllite leads to an increase in the plastic deformation. In addition, when the axial stresses are the same,

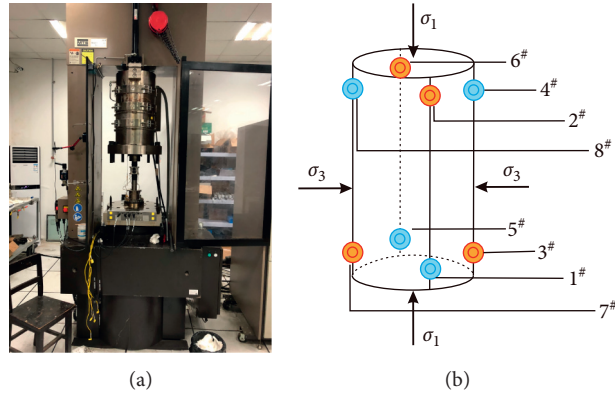


FIGURE 1: Experimental instruments: (a) MTS 815 servohydraulic testing system and (b) sketch of AE sensors arrangement.

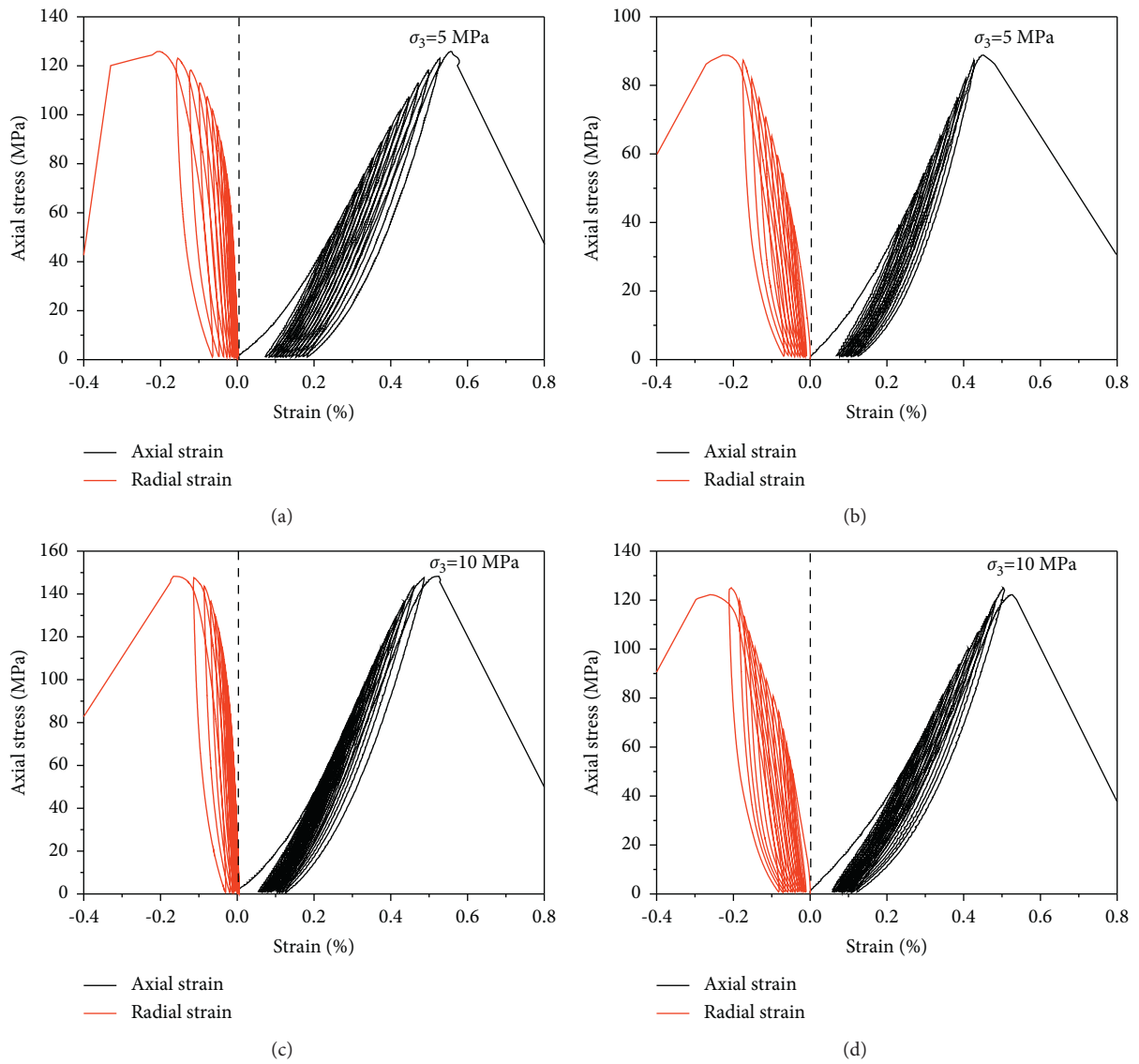


FIGURE 2: Continued.

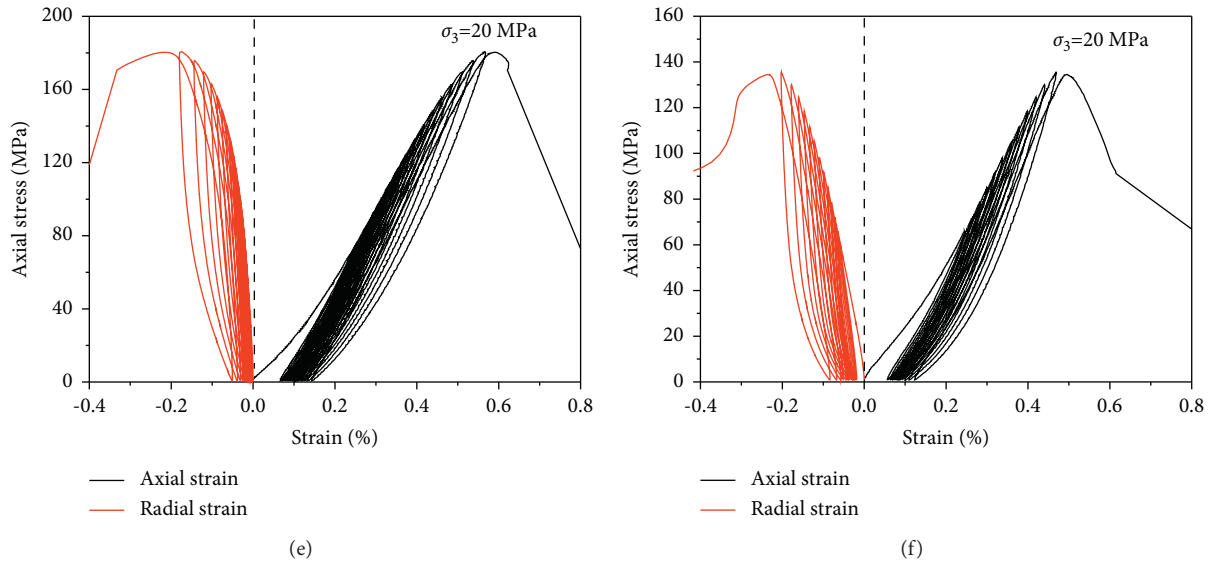


FIGURE 2: Stress-strain curves of phyllite under triaxial cyclic loading ( $\sigma_3$  is the confining pressure). (a) Dry sample. (b) Saturated sample. (c) Dry sample. (d) Saturated sample. (e) Dry sample. (f) Saturated sample.

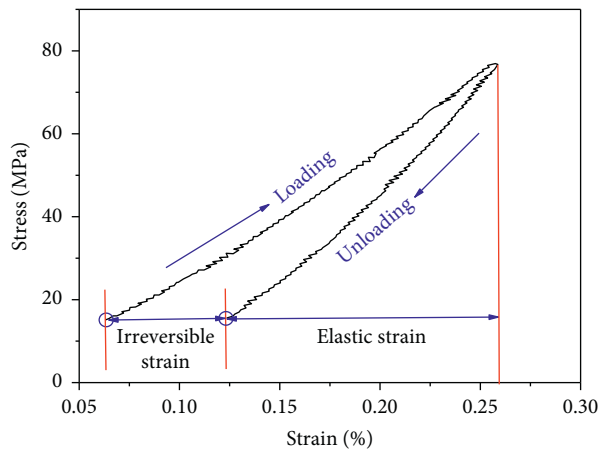


FIGURE 3: Sketch of irreversible strain.

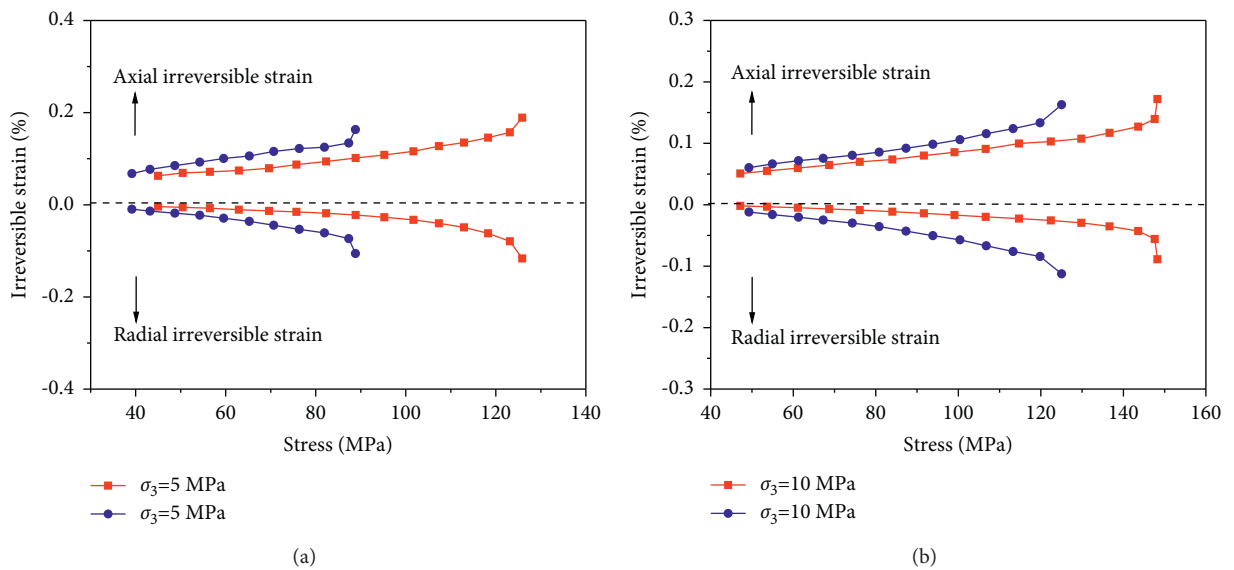


FIGURE 4: Continued.



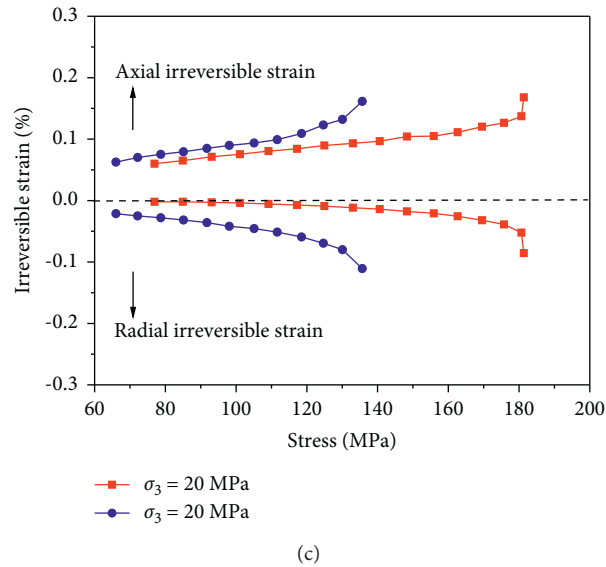


FIGURE 4: Relationship between irreversible strains and axial stress (blue denotes saturated phyllite and red denotes dry phyllite;  $\sigma_3$  is the confining pressure).

the axial and radial irreversible strains decrease with an increase in the confining pressure.

The straight parts of the loading curves were calculated to study the change law of the elastic modulus during cyclic loading. Figure 5 shows that the first loading has an obvious strengthening effect on phyllite, and the elastic modulus is greatly improved. With the increase of confining pressure, the elastic modulus of phyllite increases. The confining pressure improves the friction between crack surfaces, hinders the crack propagation and sliding, and improves the strength and elastic modulus of phyllite. The elastic modulus of dry phyllite is obviously larger than that of saturated phyllite. It may be that the softening effect of water reduces the ability of phyllite to resist deformation. Compared with confining pressure and water, the effect of the loading paths on the elastic modulus is more significant. With an increase in the number of cycles, the elastic modulus first increases, then tends to be constant, and finally decreases. The variation in the elastic modulus of phyllite is the same as that of gypsum [16]. That is because the preexisting microcracks in phyllite close, and the elastic modulus increases during the early cyclic loading. Then, the modulus is basically unchanged or increases slowly, a process which actually represents the competition between crack expansion and particle compaction. During the loading and unloading process, on the one hand, the disordered expansion microcracks in phyllite reduce the stiffness and modulus of the specimen. On the other hand, the mineral particles formed by crack cutting are recompacted, and the fracture is filled with detritus, which improves the stiffness and modulus of phyllite. The elastic modulus of phyllite remains constant or increases slowly under the influence of these two factors. During the last few cycles, the expansion cracks propagate and gather rapidly, and the elastic modulus decreases. However, the results of this study differ from those of Western granite and Etna basalt [16–18]. With an increase

in cycles, the elastic moduli of granite and basalt decrease. There is a significant difference between the elastic moduli of soft rock and hard rock under cyclic loading. This may be related to internal factors such as mineral composition and cementation type. Therefore, the expansion and distribution of cracks and the deformation characteristics of mineral particles under cyclic loading are the key to exploring the difference between the elastic moduli of soft rock and hard rock, which is worthy of further study.

Poisson's ratio of phyllite increases with an increase in cycles (Figure 5). This is because of the rapid increase in the lateral deformation (including crack expansion and fracture plane slip) during cyclic loading. In addition, Poisson's ratio of phyllite is very sensitive to water. Poisson's ratio of the saturated phyllite is almost twice that of dry phyllite. When the confining pressure is 5 MPa, the maximum Poisson's ratio of the saturated phyllite is 0.45. This is because phyllite contains clay minerals. The softening effect of water on phyllite promotes the lateral expansion. In addition, water reduces the friction coefficient between microcracks, which is conducive to the initiation and expansion of cracks and the sliding of fracture planes. This promotes an increase in Poisson's ratio.

**3.3. Dilatancy Characteristics.** The volume strain curves are shown in Figure 6. During the early cyclic loading (low stress level), the hysteresis loops are very narrow and dense. With the increase of cycles (high stress level), the hysteresis loops become wider, and the volume curves become sparse, which indicates that the volume of phyllite gradually changed from compaction-dominated to expansion-dominated. The confining pressure clearly inhibits the volume expansion of the phyllite. Furthermore, the volume expansion of saturated phyllite is different from that of dry phyllite. For example, when the confining pressure was 5 MPa, the volume of

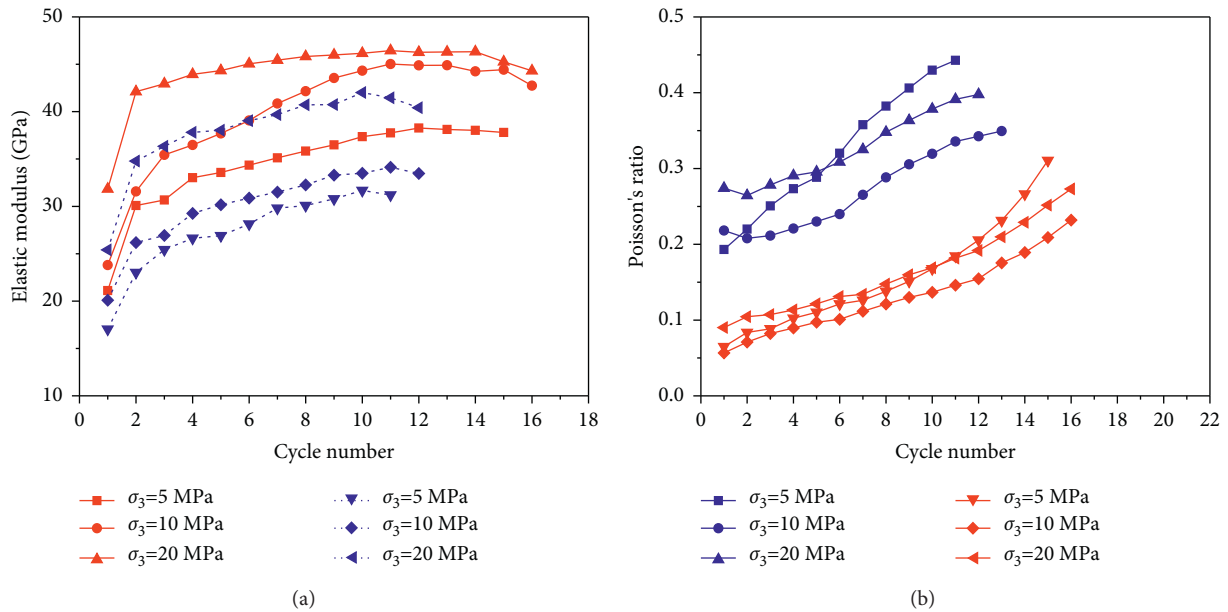


FIGURE 5: Elastic modulus and Poisson's ratio (blue denotes saturated phyllite and red denotes dry phyllite;  $\sigma_3$  is the confining pressure): (a) elastic modulus and (b) Poisson's ratio.

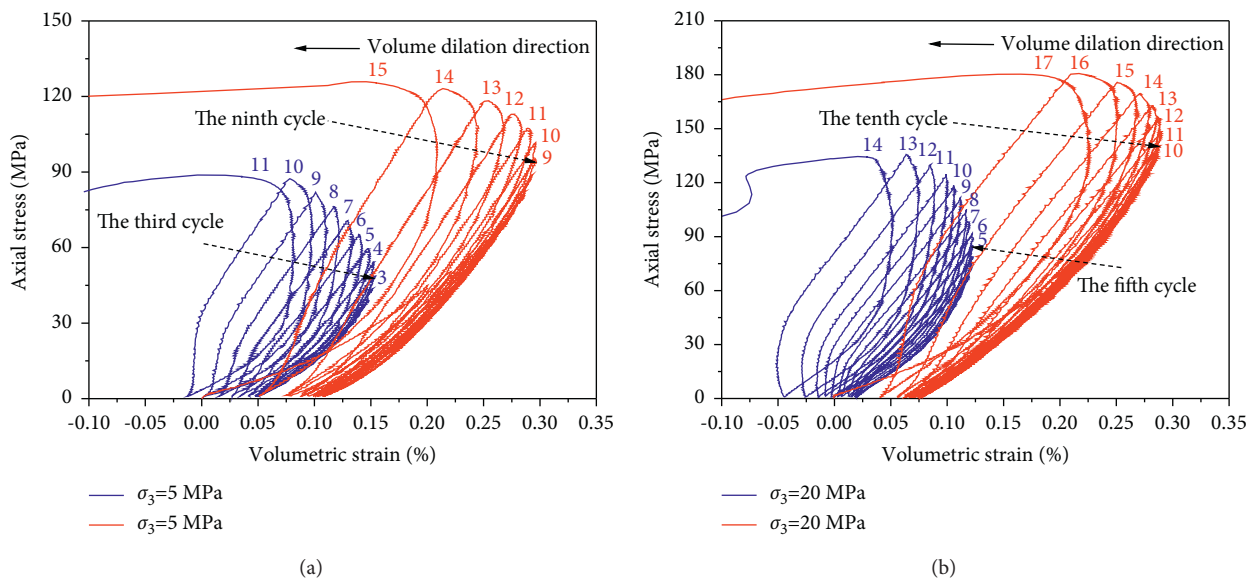


FIGURE 6: Typical volumetric strain of phyllite (blue denotes saturated phyllite and red denotes dry phyllite;  $\sigma_3$  is the confining pressure).

saturated phyllite changed from compaction-dominated to expansion-dominated in the third cycle, with a critical volume strain of 0.15. However, the volume of dry phyllite changed from compaction-dominated to expansion-dominated in the ninth cycle, with a critical volume of 0.30. When the confining pressure was 20 MPa, the volume of saturated phyllite changed from compaction-dominated to expansion-dominated in the fifth cycle, with a critical volume strain of 0.12. However, the volume of dry phyllite changed from compaction-dominated to expansion-dominated in the tenth cycle, with a critical volume strain of 0.29. Compared with dry phyllite, the volume expansion of

saturated phyllite starts earlier, and the compression deformation before volume expansion is smaller. Water accelerates the change of volume from compaction to expansion.

The stress-strain curves of rock materials in a triaxial compression test can be roughly divided into five stages (Figure 7): crack closure stage (I), elastic stage (II), stable crack growth stage (III), unstable crack growth stage (IV), and postpeak stage (V). Crack damage stress ( $\sigma_{cd}$ ) can be identified from laboratory test. Crack damage stress is the dividing point between stable crack growth stage and unstable crack growth stage. When the axial stress exceeds the crack damage

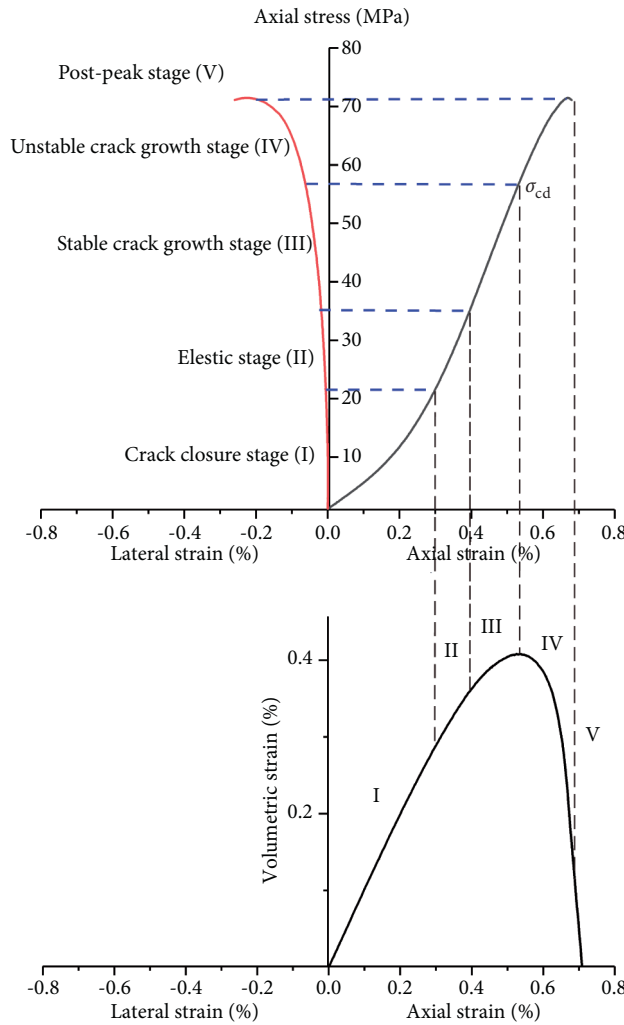


FIGURE 7: Stage division of rock failure process and schematic diagram of crack damage stress ( $\sigma_{cd}$ ) (adapted from Martin et al. [19]).

stress, the crack grows unsteadily and begins to coalesce. Crack damage stress is one of the key stresses in rocks, which corresponds to the long-term rock strength [19, 20]. The crack damage stress of a rock can be determined using the corresponding volume strain curve [21]. The relationship between the crack damage stress and cycle number is shown in Figure 8. When the cycle number is less than 3, the saturated phyllite does not change from compaction-dominated to expansion-dominated. The crack damage stress of the saturated phyllite cannot be obtained in this case. Similarly, when the cycle number is less than 7, the crack damage stress of the dry phyllite cannot be obtained. As shown in Figure 8, with an increase in the number of cycles, the crack damage stress of phyllite first increases and then decreases. For example, when the confining pressure was 10 MPa, the crack damage stress of dry phyllite first increases from 90.78 to 139.60 MPa. Then, the crack damage stress decreases from 139.60 to 130.63 MPa. With the increase of confining pressure, the crack damage stress of phyllite increases. The crack damage stress of saturated phyllite is lower than that of dry phyllite. This shows that water accelerates the change of volume from compaction to expansion.

**3.4. Energy Dissipation and Damage Variable.** For energy dissipation central to deformation and failure of rock materials [22, 23], damage is a process of accumulating dissipated energy. Ignoring the damping effect of the test system, the total energy ( $U$ ) generated by the external force is transformed into elastic energy ( $E_e$ ) and dissipative energy ( $E_d$ ). The elastic energy is released during unloading and is approximately equal to the negative work ( $E_r$ ) caused by the external force during unloading (Figure 9):

$$U = E_e + E_d = E_r + E_d, \quad (1)$$

where  $U$  is the total energy,  $E_e$  is the elastic energy,  $E_d$  is the dissipated energy, and  $E_r$  is the negative work done by the external force during unloading.

As shown in Figure 9, the area of the figure surrounded by “ABCF” represents the total input energy ( $U$ ), while the area surrounded by “CDEF” represents the negative work ( $E_r$ ) caused by the axial stress during unloading, which is approximately equal to the elastic energy ( $E_e$ ). The area surrounded by “ABCDE” represents the energy dissipated ( $E_d$ ) during one cyclic loading and unloading. The area

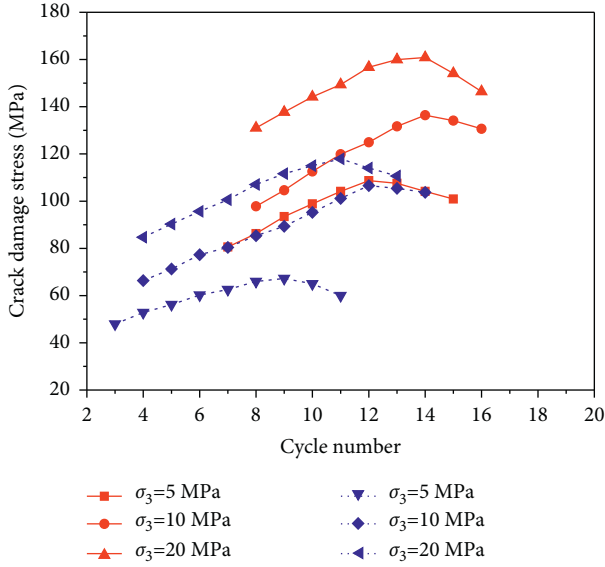


FIGURE 8: Relationship between crack damage stress and cycle number (blue denotes saturated phyllite and red denotes dry phyllite;  $\sigma_3$  is the confining pressure).

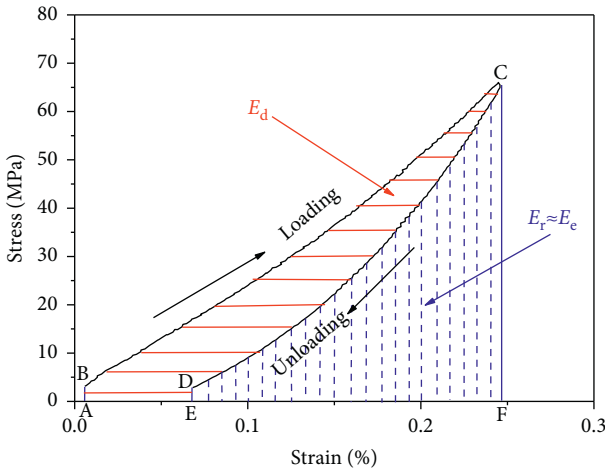


FIGURE 9: Schematic diagram of energy calculation during one cyclic loading and unloading.

surrounded by axial stress-strain curve can be calculated using calculus [24]. The accumulated dissipated energy ( $E^*d$ ) is equal to the sum of the dissipated energy ( $E_d$ ) of each cycle. As shown in Figure 10, the relationship between the cumulative dissipated energy ( $E^*d$ ) and axial stress can be expressed as

$$E_d^* = m \exp(n\sigma_1), \quad (2)$$

where  $E^*d$  is the accumulated dissipated energy,  $m$  and  $n$  are fitting parameters, and  $\sigma_1$  is the axial stress.

The cumulative dissipated energy ( $E^*d$ ) increases exponentially with an increase in axial stress (Figure 10).

To study the damage evolution of rocks under cyclic loading conditions, Peng et al. [24] proposed an expression for damage variable:

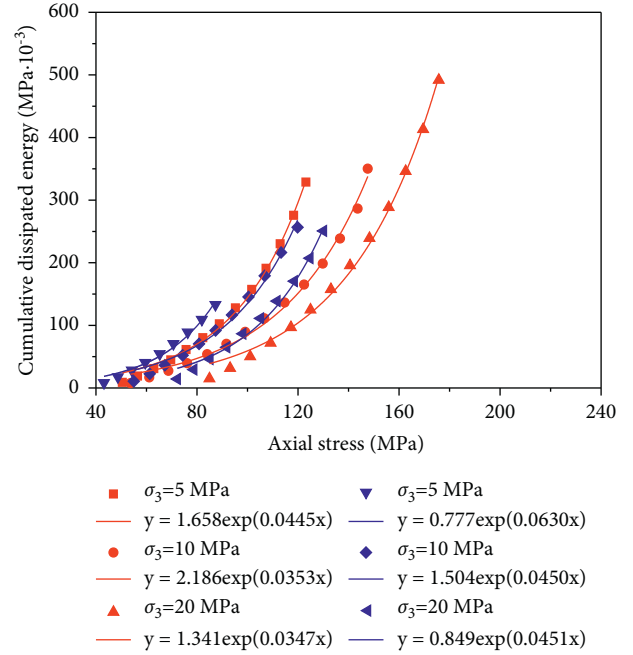


FIGURE 10: The relationship between cumulative dissipated energy and axial stress (blue denotes saturated phyllite and red denotes dry phyllite;  $\sigma_3$  is the confining pressure).

$$D = \frac{2}{\pi} \arctan \frac{E_d^*}{\sigma_1}, \quad (3)$$

where  $D$  is the damage variable,  $E^*d$  is the accumulated dissipated energy, and  $\sigma_1$  is the axial stress.

According to (2)-(3), we modify the damage variable  $D$ . The new damage variable ( $D_p$ ) of phyllite can be expressed as

$$D_p = \frac{2}{\pi} \arctan \frac{m \exp(n\sigma_1)}{\sigma_1}. \quad (4)$$

The damage variables of the saturated and dry phyllite were calculated according to (4). As shown in Figure 11, with the increase of axial stress, the damage variables of saturated and dry phyllite increase in an S-shape. The confining pressure and water have obvious effects on the damage variable. When the axial stresses are the same, the lower the confining pressure, and the larger the damage variable. This shows that the confining pressure can inhibit damage to phyllite. When the confining pressures are the same, the damage variable of saturated phyllite is larger than that of dry phyllite, as water aggravates the damage to phyllite. However, the evolution trend of the damage variable is unrelated to the confining pressure and water. There is a critical value for damage variable ( $D_0$ ). When  $D_p$  is larger than  $D_0$ , the phyllite sample is destroyed. The critical damage variables of the dry and saturated phyllite samples are between 0.745 and 0.841, with an average value of 0.80. The critical damage variable is independent of the confining pressure and water. This shows that the damage variable proposed in this paper is reasonable and can be used as an index to predict the failure of phyllite.

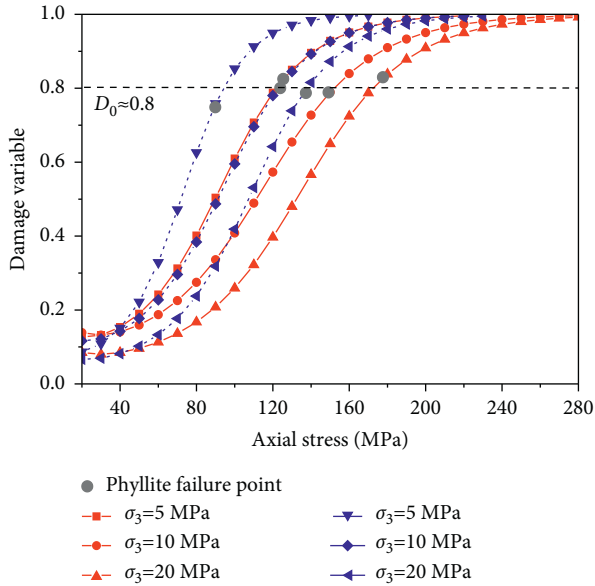


FIGURE 11: The relationship between the damage variable and axial stress (blue denotes saturated phyllite and red denotes dry phyllite;  $\sigma_3$  is the confining pressure;  $D_0$  is the critical damage variable).

**3.5. Failure Mode.** Failure mode is an important research topic in rock mechanics. Under triaxial cyclic loading conditions, the failure modes of the dry and saturated specimens are shear failures (Figures 12-13). The angle between the fracture plane and the horizontal plane is the fracture angle ( $\alpha$ ). When the confining pressure increases from 5 to 20 MPa, the fracture angle decreases from  $68^\circ$  to  $53^\circ$ . The fracture angle of phyllite decreases with the increase of confining pressure.

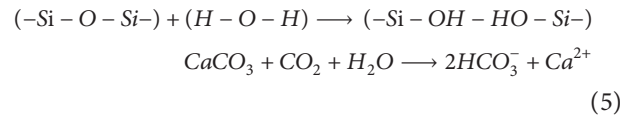
The fracture surfaces of phyllite under cyclic loading are shown in Figures 14-15. When the confining pressure is low ( $\sigma_3 = 5$  MPa), the U-shaped fractures are rough and uneven; furthermore, there are obvious slip marks and a significant amount of powder on the U-shaped fractures. This indicates that a large number of mineral particles slide and rotate on the shear plane, and the dilatancy effect is strong. With the increase of confining pressure ( $\sigma_3 = 10, 20$  MPa), the U-shaped fractures become smooth. There is a small amount of rock powder on the shear plane, and the dilatancy effect is weakened.

## 4. Discussion

**4.1. Degradation Mechanism of Water-Saturated Phyllite.** Phyllite is a type of water-sensitive rock. In this paper, the deterioration mechanism of water-saturated phyllite is discussed from two aspects: microstructure and micromechanics.

**4.1.1. Damage to Microstructure.** Phyllite contains clay minerals. During the saturation process, these minerals undergo swelling, nonuniform deformation, and shedding. To better analyze the changes in the microstructure of saturated phyllite, the dry and saturated phyllite were

analyzed using scanning electron microscopy. Figure 16(a) shows that the surfaces of the clay minerals are flat and smooth. The boundary of mineral particle is clear. Most of the clay minerals are in surface-to-surface contact and are some local microcracks. After water saturation (Figure 16(b)), the boundary between the mineral particles becomes blurred owing to the swelling deformation of the clay minerals and the dissolution of cement. Flaky clay minerals soften and shed, and the exfoliated material decomposes into small particles that adhere to the surfaces of large mineral particles. In a saturated state, the contact relationship between clay minerals gradually changes to point-to-surface contact. The structure of the samples tends to be loose, which leads to the deterioration of the saturated phyllite. In addition, the hydrolysis of quartz and the dissolution of calcite are also important factors for the degradation of phyllite. During saturation process, the microcracks are filled with free water. The crack tip is the most active area of the water-rock reaction [25]. Because of hydrolysis, the strong Si-O-Si bond is replaced by the weak Si-OH bond, which reduces the growth barrier and fracture toughness of microcracks [26, 27]. The mechanical properties of phyllite are further degraded. The reaction formulas can be expressed as



The physical and chemical reactions of clay minerals, quartz, and calcite with water damage the microstructure; this process is the basic factor for the deterioration of saturated phyllite.

**4.1.2. Micromechanical Analysis.** To study the effect of water on crack propagation, the sliding crack model [28] was used to analyze a single microcrack without considering the interaction between cracks (Figure 17). During the saturation process, the volume of clay minerals expands significantly, while the volume of quartz and feldspar remains almost unchanged, which leads to nonuniform expansion stress in phyllite. The expansion stress ( $P_{ew}$ ) can not only promote the propagation of the original cracks but also produce new microcracks. In addition to expansion stress, pore water pressure ( $P_{pw}$ ) may be another factor affecting the mechanical properties of phyllite. The pore water pressure is related not only to the volume deformation of the rock but also to the crack propagation rate. During volume compression, the pore water pressure increases with the increase of cyclic load. When the pore water pressure exceeds the tensile strength of the rock, it causes the propagation of microcracks [29]. During the volume expansion, the pore water pressure in a crack is mainly related to the distribution of water. Under triaxial cyclic loading conditions, the propagation speed of the crack is slow; free water can reach the crack tip in time [26, 30]. The free water at the crack tip will produce a water wedge effect and promotes crack

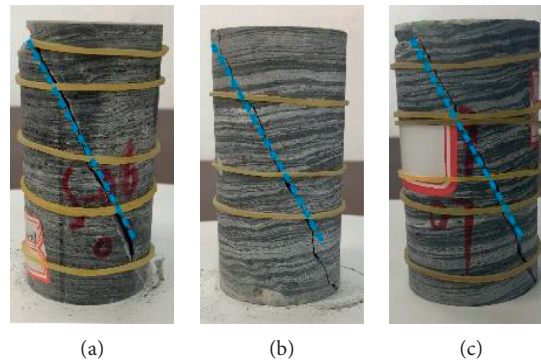


FIGURE 12: Failure modes of dry phyllite ( $\sigma_3$  is the confining pressure;  $\alpha$  is the fracture angle) (a)  $\sigma_3 = 5$  MPa,  $\alpha = 64^\circ$ ; (b)  $\sigma_3 = 10$  MPa,  $\alpha = 62^\circ$ ; and (c)  $\sigma_3 = 20$  MPa,  $\alpha = 61^\circ$ .

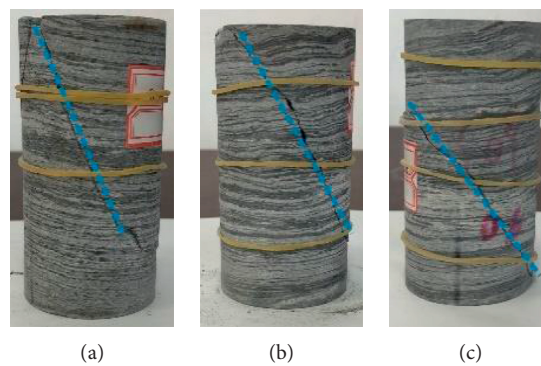


FIGURE 13: Failure modes of saturated phyllite ( $\sigma_3$  is the confining pressure;  $\alpha$  is the fracture angle) (a)  $\sigma_3 = 5$  MPa,  $\alpha = 68^\circ$ ; (b)  $\sigma_3 = 10$  MPa,  $\alpha = 62^\circ$ ; and (c)  $\sigma_3 = 20$  MPa,  $\alpha = 53^\circ$ .

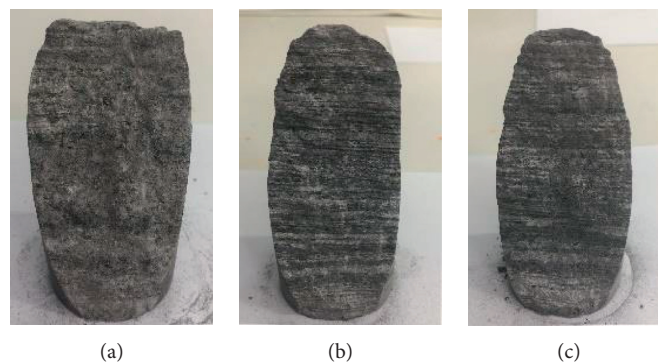


FIGURE 14: U-shaped fractures of dry phyllite specimens ( $\sigma_3$  is the confining pressure). (a)  $\sigma_3 = 5$  MPa, (b)  $\sigma_3 = 10$  MPa, and (c)  $\sigma_3 = 20$  MPa.

expansion [31]. In addition, (6) shows that pore water pressure ( $P_{pw}$ ) and expansion stress ( $P_{ew}$ ) can also reduce the effective normal stress ( $\sigma_w$ ) on the main crack, which promotes crack expansion and reduces the strength of phyllite. Under saturated conditions, the degree of loss of the friction coefficient of different minerals varies greatly. Quartz and feldspar have poor hydrophilicity; thus, the friction coefficients of quartz and feldspar do not change significantly [32]. This is because the surface charges of

quartz and feldspar are mostly neutral. There is little binding water on the particle surface; therefore, water has little effect on the friction coefficient of nonadsorbable minerals such as feldspar and quartz. However, the friction coefficients of illite, mica, chlorite, and other clay minerals decreases by 20–60% [32], which leads to the increase of the effective shear stress ( $\tau_w$ ) on the main crack (see (7)). This further promotes crack expansion and reduces the strength of phyllite.

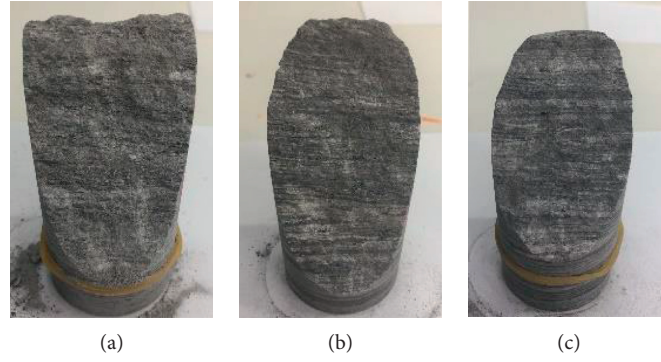


FIGURE 15: U-shaped fractures of saturated phyllite specimens ( $\sigma_3$  is the confining pressure) (a)  $\sigma_3 = 5$  MPa, (b)  $\sigma_3 = 10$  MPa, and (c)  $\sigma_3 = 20$  MPa.

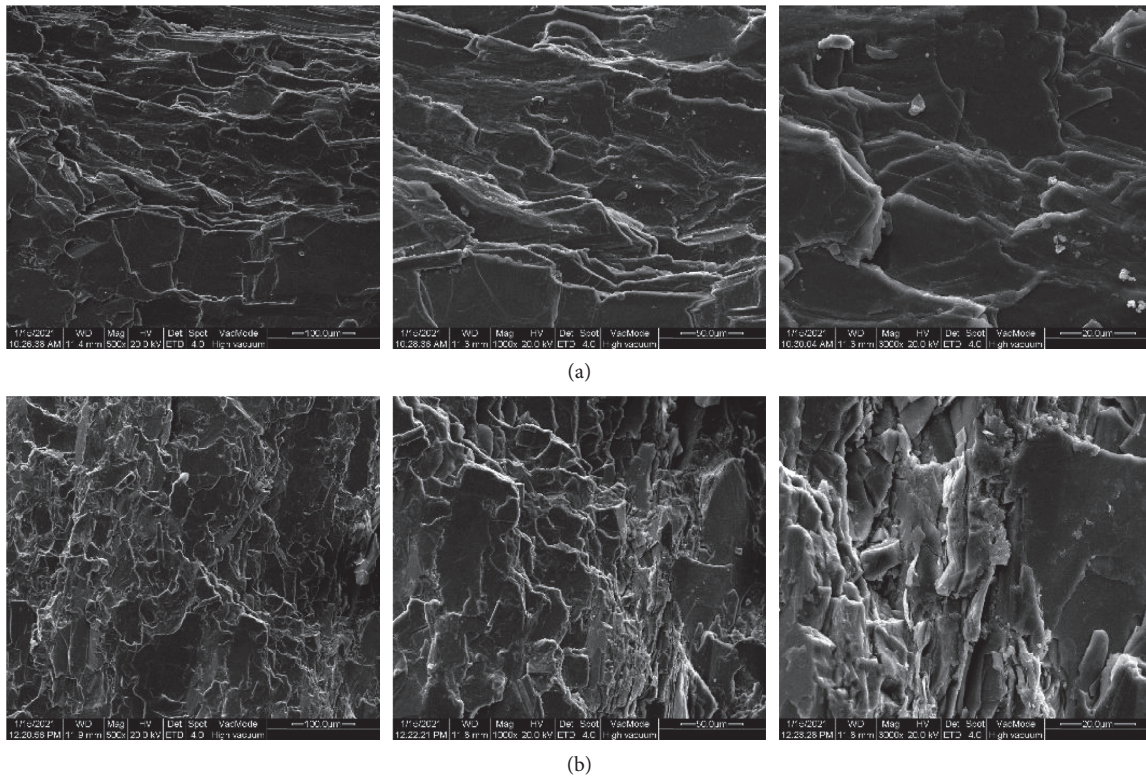


FIGURE 16: Scanning electron microscopy (SEM) photographs of phyllite: (a) dry phyllite and (b) saturated phyllite.

The effective normal stress ( $\sigma_w$ ) and the effective shear stress ( $\tau_w$ ) of the main crack can be approximately expressed as [33]

$$\sigma_w = \frac{1}{2} [(\sigma_1 + \sigma_3) + (\sigma_1 - \sigma_3)\cos 2\theta] - (P_{pw} + P_{ew}), \quad (6)$$

$$\tau_w = \frac{1}{2} (\sigma_1 - \sigma_3)\sin 2\theta - \mu_w \sigma_w, \quad (7)$$

where  $\sigma_1$  is the axial compressive stress,  $\sigma_3$  is the confining pressure,  $P_{pw}$  is the pore water pressure,  $P_{ew}$  is expansion force, the angle between the main crack and the horizontal axis is  $\theta$ ,  $\sigma_w$  is the effective normal stress,  $\tau_w$  is the effective shear stress, and  $\mu_w$  is the friction coefficient of the water-bearing crack.

**4.2. Energy Release and Crack Distribution Characteristics of Water-Saturated Phyllite.** During the cyclic loading process, AE signals can directly reflect the damage process of phyllite. The axial stress-time-AE energy curves of the phyllite are shown in Figure 18. The AE energy of phyllite can be divided into two modes. The first mode is the cluster mode. In this mode, during the early cyclic loading, the AE energy is very small, and the cumulative AE energy curve is relatively stable. However, during the last 1-2 cycles, the AE energy increases rapidly and distributes intensively. The AE energy of dry phyllite belongs to the cluster mode. This shows that there is little AE energy in the prepeak stage, and the input energy is almost all transformed into elastic energy. When the dry phyllite approaches failure, the accumulated energy

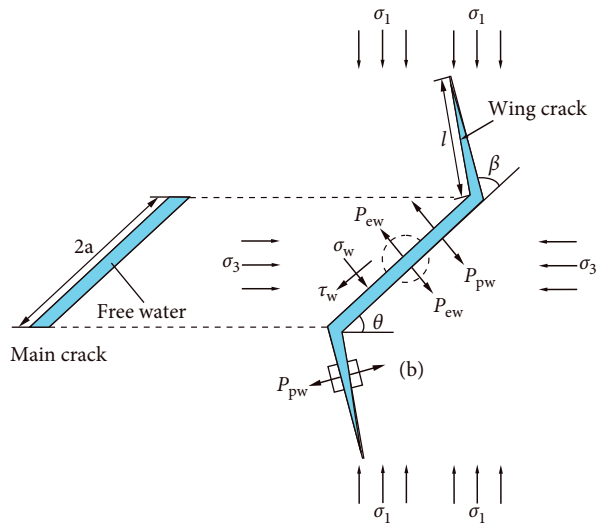


FIGURE 17: Sliding crack model.

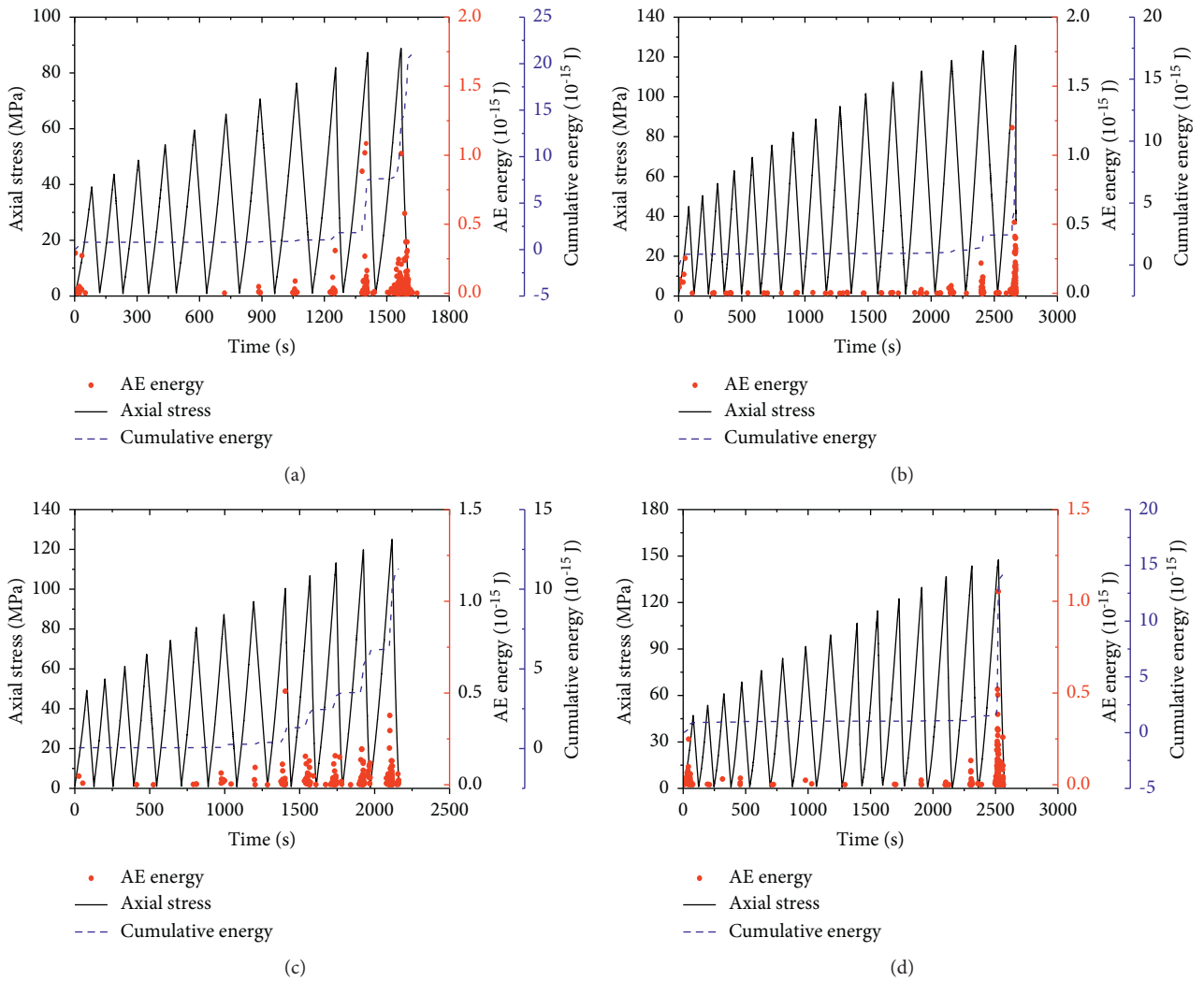


FIGURE 18: Continued.



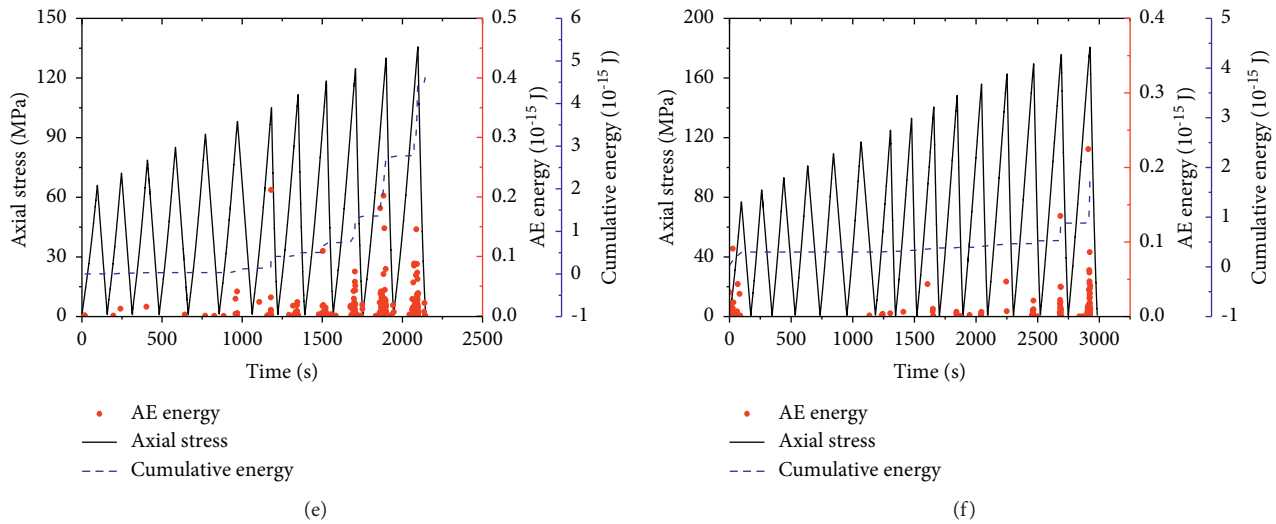


FIGURE 18: The axial stress-time-AE energy curves of phyllite ( $\sigma_3$  is the confining pressure). (a) Saturated sample,  $\sigma_3 = 5$  MPa. (b) Dry sample,  $\sigma_3 = 5$  MPa. (c) Saturated sample,  $\sigma_3 = 10$  MPa. (d) Dry sample,  $\sigma_3 = 10$  MPa. (e) Saturated sample,  $\sigma_3 = 20$  MPa. (f) Dry sample,  $\sigma_3 = 20$  MPa.

is rapidly released to form macro fracture plane. High-energy rupture events can be detected when only failure occurs. The second mode is the multipeak mode, which includes several peaks of AE energy during loading and unloading. Moreover, the cumulative energy curve exhibits obvious steps. The AE energy of saturated phyllite belongs to the multipeak mode (Figure 18). During the early cyclic loading (compaction and elastic stages), there is little difference in AE energy between saturated phyllite and dry phyllite. However, with the increase of cycles (plastic stage), the saturated phyllite produces a large number of AE energy by sliding friction. This indicates that water reduces the energy required for breakdown and promotes the sliding of shear cracks. The damage stress of saturated phyllite decreases. Therefore, the damage of water-saturated phyllite occurs at a lower stress level, and the microcracks initiate and expand continuously during cyclic loading. The AE energy curve of saturated phyllite exhibits obvious steps before failure, and high-energy shear rupture events can be detected repeatedly.

The evolution of AE events with axial stress is shown in Figures 19-20. Under early cyclic loading conditions (compaction and elastic stages), fewer AE events occur. The AE events mainly consist of the closure of primary cracks. With the increase of axial stress (more than  $0.7 \sigma_c$ ), the crack distribution characteristic of saturated phyllite becomes different from that of dry phyllite. Water reduces the strength of phyllite and accelerates the localization of damage. The cracks in saturated phyllite are relatively concentrated. There is an obvious nucleation region in the center of the saturated specimen (Figure 19). With the increase of cyclic loading, the nucleation region gradually diffuses from the center to the upper and lower ends of the specimen. However, there is no obvious nucleation area in the dry phyllite, and the microcracks are scattered (Figure 20). With the increase of cyclic loading, cracks increase sharply, forming a fracture zone.

**4.3. Potential Application for the Engineering.** With an increase in excavation depth, rock mass is inevitably affected by confining pressure and strong excavation disturbances, which induce a series of geological engineering hazards. When tunnels and slopes are excavated, the rock mass undergoes very complicated stress path owing to the layered, segmented excavation and excavation between adjacent caverns. The rock mass is in a state of cyclic loading and unloading. In addition, owing to the existence of water in engineering rock mass, the deformation and failure process of rocks become more complicated. The stability of rock mass is the key to engineering safety. In previous engineering applications, stability was evaluated on the basis of critical stress or deformation parameters. However, sometimes these parameters cannot reflect the actual damage of the rock mass under complex stress paths. For instance, the damage stresses and elastic modulus of phyllite first increased and then decreased under triaxial cyclic loading. Therefore, the appropriate damage variable is helpful to identify the actual damage in rock. The damage variable proposed in this paper can be used as an index to predict the failure of phyllite. According to the actual damage inside the rock, the reasonable and economical supporting schemes are adopted. Furthermore, AE can effectively monitor the internal damage of rock. It is helpful to explore the failure mechanism of rocks and provide a basis for disaster prevention. The results of this study reveal the AE energy release characteristics of dry and saturated phyllite during excavation, which can provide guidance for monitoring the deformation and damage of surrounding rock. In the process of excavation of the surrounding rock, water-bearing phyllite releases a lot of energy before failure and high-energy shear rupture events can be detected repeatedly. However, a large amount of AE energy and high-energy rupture events appear when only the dry phyllite approaches failure, which needs our special attention.

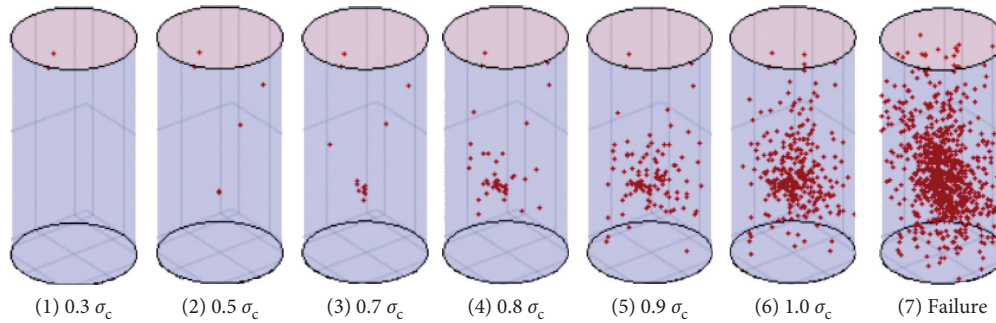


FIGURE 19: Spatial distribution of AE events at different stress levels for saturated phyllite ( $\sigma_3 = 20$  MPa;  $\sigma_c$  is the peak stress). (a)  $0.3 \sigma_c$ , (b)  $0.5 \sigma_c$ , (c)  $0.7 \sigma_c$ , (d)  $0.8 \sigma_c$ , (e)  $0.9 \sigma_c$ , (f)  $1.0 \sigma_c$ , and (g) failure.

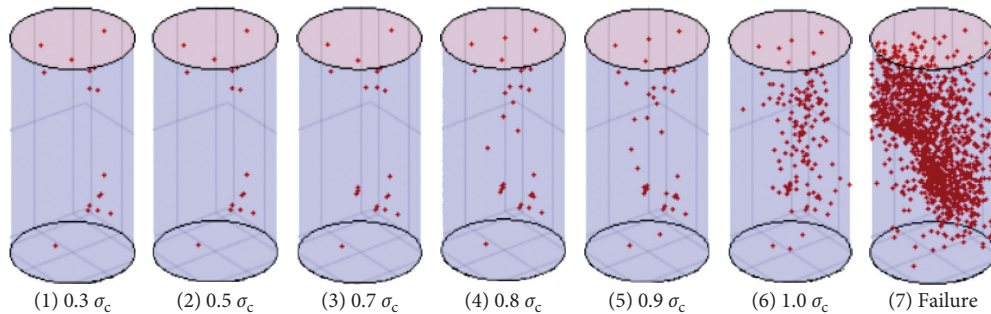


FIGURE 20: Spatial distribution of AE events at different stress levels for dry phyllite ( $\sigma_3 = 20$  MPa;  $\sigma_c$  is the peak stress). (a)  $0.3 \sigma_c$ , (b)  $0.5 \sigma_c$ , (c)  $0.7 \sigma_c$ , (d)  $0.8 \sigma_c$ , (e)  $0.9 \sigma_c$ , (f)  $1.0 \sigma_c$ , and (g) failure.

## 5. Conclusions

In this study, we have carried out a series of triaxial cyclic tests on dry and water-saturated phyllite by employing the MTS 815 servohydraulic testing system and AE testing equipment. The deformation parameters, damage stress, damage variable, AE characteristics, and failure mode of phyllite under confining pressures of 5, 10, and 20 MPa were analyzed. Degradation mechanism of water-saturated phyllite was discussed, and the energy release and crack distribution characteristics of phyllite was revealed. The main conclusions are as follows:

- (1) Phyllite is a type of water-sensitive rock. The compressive strength, damage stress, and elastic modulus of saturated phyllite decrease, while the irreversible strain and Poisson's ratio of saturated phyllite increase. Water accelerates the change of volume from compaction to expansion.
- (2) Stress path has an obvious influence on the deformation parameters of phyllite. The irreversible strain increases exponentially with the increase of axial stress. With the increase of cycles, the elastic modulus increases first, then tends to be constant, and then finally decreases. Poisson's ratio increases with the number of cycles. The crack damage stresses of phyllite specimens first increased and then decreased with an increase in the number of cycles.
- (3) Based on the dissipated energy, a new damage variable ( $D_p$ ) for phyllite was established. With the increase of axial stress, the damage variable of dry and saturated

phyllite increases in an S-shape. The critical damage variable ( $D_0$ ) of phyllite is approximately 0.80; this variable can be used as an index to predict the failure of phyllite.

- (4) The localization of damage is serious for saturated phyllite. The microcracks occur earlier and are relatively concentrated, and there is an obvious nucleation area. The AE energy curve exhibits obvious steps before failure, and high-energy shear rupture events can be detected repeatedly. The microcracks of dry phyllite are scattered. High-energy rupture events can be detected when only failure occurs.
- (5) The water saturation effect of phyllite is obvious. The effective normal stress on the crack surface decreases and the shear stress increases under the influence of expansion stress, pore water pressure, and friction coefficient. Water promotes crack initiation and propagation, reduces the strength of phyllite, accelerates the localization of damage, and changes the AE energy release and crack distribution characteristics of the phyllite.

## Data Availability

The data used to support the findings of the study are included within the article.

## Conflicts of Interest

The authors declare no conflicts of interest.

## Acknowledgments

This work was supported by the Fundamental Research Funds for the Central Universities, CHD (300102260708), the National Natural Science Foundation of China (41831286 and 42041006), and the Transportation Construction Science and Technology Program of Sichuan Province (no. 2015A1-3).

## References

- [1] K. Fuenkajorn and D. Phueakphum, "Effects of cyclic loading on mechanical properties of Maha Sarakham salt," *Engineering Geology*, vol. 112, no. 1-4, pp. 43–52, 2010.
- [2] H. Duan and Y. Yang, "Deformation and dissipated energy of sandstone under uniaxial cyclic loading," *Geotechnical & Geological Engineering*, vol. 36, no. 1, pp. 611–619, 2017.
- [3] Y. Liu, F. Dai, L. Dong, N. Xu, and P. Feng, "Experimental Investigation on the fatigue mechanical properties of intermittently jointed rock models under cyclic uniaxial compression with different loading parameters," *Rock Mechanics and Rock Engineering*, vol. 51, no. 1, pp. 47–68, 2018.
- [4] J.-Q. Xiao, D.-X. Ding, F.-L. Jiang, and G. Xu, "Fatigue damage variable and evolution of rock subjected to cyclic loading," *International Journal of Rock Mechanics and Mining Sciences*, vol. 47, no. 3, pp. 461–468, 2010.
- [5] J. Fan, J. Chen, D. Jiang, A. Chemenda, J. Chen, and J. Ambre, "Discontinuous cyclic loading tests of salt with acoustic emission monitoring," *International Journal of Fatigue*, vol. 94, pp. 140–144, 2017.
- [6] Y. Sheng-Qi, P. G. Ranjith, and H. Yan-Hua, "Experimental investigation on mechanical damage characteristics of sandstone under triaxial cyclic loading," *Geophysical Journal International*, vol. 201, pp. 662–682, 2015.
- [7] J. Ning, J. Wang, J. Jiang, S. Hu, L. Jiang, and X. Liu, "Estimation of crack initiation and propagation thresholds of confined brittle coal specimens based on energy dissipation theory," *Rock Mechanics and Rock Engineering*, vol. 51, no. 1, pp. 119–134, 2018.
- [8] J. Singh, T. Ramamurthy, and G. V. Rao, "Strength anisotropies in rocks," *Indian Geotechnical Journal*, vol. 19, pp. 147–166, 1989.
- [9] T. Ramamurthy, G. V. Rao, and J. Singh, "Engineering behaviour of phyllites," *Engineering Geology*, vol. 33, no. 3, pp. 209–225, 1993.
- [10] Z. Q. Chen, C. He, D. Wu, W. L. Gan, G. W. Xu, and W. B. Yang, "Mechanical properties and energy damage evolution mechanism of deep-buried carbonaceous phyllite," *Rock and Soil Mechanics*, vol. 39, pp. 1–12, 2018.
- [11] Y. S. Wu, Z. S. Tan, and Y. Yu, "Anisotropically mechanical characteristics of Maoxian group phyllite in northwest of Sichuan province," *Rock and Soil Mechanics*, vol. 39, pp. 207–215, 2018.
- [12] G. Xu, C. He, A. Su, and Z. Chen, "Experimental investigation of the anisotropic mechanical behavior of phyllite under triaxial compression," *International Journal of Rock Mechanics and Mining Sciences*, vol. 104, pp. 100–112, 2018.
- [13] A. Özbek, M. Gül, E. Karacan, and Ö. Alca, "Anisotropy effect on strengths of metamorphic rocks," *Journal of Rock Mechanics and Geotechnical Engineering*, vol. 10, no. 1, pp. 164–175, 2018.
- [14] K. Hu, Q. Feng, and X. Wang, "Experimental research on mechanical property of phyllite tunnel surrounding rock under different moisture state," *Geotechnical & Geological Engineering*, vol. 35, no. 1, pp. 303–311, 2017.
- [15] G. Xu, C. He, Z. Chen, and A. Su, "Transverse isotropy of phyllite under Brazilian tests: laboratory testing and numerical simulations," *Rock Mechanics and Rock Engineering*, vol. 51, no. 4, pp. 1111–1135, 2018.
- [16] F. Trippetta, C. Colletini, P. G. Meredith, and S. Vinciguerra, "Evolution of the elastic moduli of seismogenic Triassic Evaporites subjected to cyclic stressing," *Tectonophysics*, vol. 592, pp. 67–79, 2013.
- [17] M. J. Heap and D. R. Faulkner, "Quantifying the evolution of static elastic properties as crystalline rock approaches failure," *International Journal of Rock Mechanics and Mining Sciences*, vol. 45, no. 4, pp. 564–573, 2008.
- [18] M. J. Heap, S. Vinciguerra, and P. G. Meredith, "The evolution of elastic moduli with increasing crack damage during cyclic stressing of a basalt from Mt. Etna volcano," *Tectonophysics*, vol. 471, no. 1-2, pp. 153–160, 2009.
- [19] C. D. Martin, R. Christiansson, and J. Soderhall, *Rock Stability Considerations for Siting and Constructing a KBS-3 Repository. Based on Experiences from Aespoe HRL, AECL's URL, Tunneling and Mining [R]*, Swedish Nuclear Fuel and Waste Management Company, Stockholm, 2001.
- [20] C. D. Martin, "Seventeenth Canadian Geotechnical Colloquium: the effect of cohesion loss and stress path on brittle rock strength," *Canadian Geotechnical Journal*, vol. 34, no. 5, pp. 698–725, 1997.
- [21] M. Cai, P. K. Kaiser, Y. Tasaka, T. Maejima, H. Morioka, and M. Minami, "Generalized crack initiation and crack damage stress thresholds of brittle rock masses near underground excavations," *International Journal of Rock Mechanics and Mining Sciences*, vol. 41, no. 5, pp. 833–847, 2004.
- [22] H. Xie, L. Li, R. Peng, and Y. Ju, "Energy analysis and criteria for structural failure of rocks," *Journal of Rock Mechanics and Geotechnical Engineering*, vol. 1, no. 1, pp. 11–20, 2009.
- [23] P. Ruidong, Ju. Yang, J. G. Wang, H. P. Xie, F. Gao, and L. T. Mao, "Energy dissipation and release during coal failure under conventional triaxial compression," *Rock Mechanics and Rock Engineering*, vol. 48, pp. 509–526, 2015.
- [24] R. D. Peng, J. Yang, and G. Feng, "Energy analysis on damage of coal under cyclical triaxial loading and unloading conditions," *Journal of China Coal Society*, vol. 39, pp. 245–252, 2014.
- [25] G. H. Newman, "The effect of water chemistry on the laboratory compression and permeability characteristics of some North Sea Chalks," *Journal of Petroleum Technology*, vol. 35, no. 5, pp. 976–980, 1983.
- [26] E. Cadoni, K. Labibes, C. Albertini, M. Berra, and M. Giangrosso, "Strain-rate effect on the tensile behaviour of concrete at different relative humidity levels," *Materials and Structures*, vol. 34, no. 1, pp. 21–26, 2001.
- [27] S. W. Freiman, "Effects of chemical environments on slow crack growth in glasses and ceramics," *Journal of Geophysical Research: Solid Earth*, vol. 89, no. B6, pp. 4072–4076, 1984.
- [28] H. Horii and S. Nemat-Nasser, "Brittle failure in compression: splitting, faulting and brittle-ductile transition," *Philosophical Transactions of the Royal Society of London*, vol. 319, pp. 337–374, 1986.
- [29] C. L. Zhong, Z. Y. Zhang, G. R. Pathegama, Y. Y. Lua, and C. Xavier, "The role of pore water plays in coal under uniaxial cyclic loading," *Engineering Geology*, vol. 257, pp. 105–125, 2019.

- [30] P. Rossi and C. Boulay, "Influence of free water in concrete on the cracking process," *Magazine of Concrete Research*, vol. 42, no. 152, pp. 143–146, 1990.
- [31] Z. Zhou, X. Cai, D. Ma et al., "Water saturation effects on dynamic fracture behavior of sandstone," *International Journal of Rock Mechanics and Mining Sciences*, vol. 114, pp. 46–61, 2019.
- [32] C. A. Morrow, D. E. Moore, and D. A. Lockner, "The effect of mineral bond strength and adsorbed water on fault gouge frictional strength," *Geophysical Research Letters*, vol. 27, no. 6, pp. 815–818, 2000.
- [33] M. F. Ashpy and S. M. Hallam, "The failure of brittle solids containing small cracks under compressive stress states," *Acta Metallurgica*, vol. 34, pp. 497–510, 1986.

## Research Article

# Experimental Research on Key Factors Influencing the Expansion Performance of New Type Sealing Materials

Yaobin Li <sup>1</sup>, Xin Guo <sup>1</sup>, Sheng Xue <sup>1</sup>, Chun-Shan Zheng <sup>1</sup>, Maoliang Shen <sup>1</sup>,  
and Yang Xu <sup>2</sup>

<sup>1</sup>School of Safety Science and Engineering, Anhui University of Science and Technology, Huainan 232001, Anhui, China

<sup>2</sup>College of Horticulture Science and Engineering, Fujian Agricultural University, Fuzhou 350000, Fujian, China

Correspondence should be addressed to Xin Guo; guoxin190510@163.com

Received 8 September 2021; Accepted 15 December 2021; Published 30 December 2021

Academic Editor: Chunchi Ma

Copyright © 2021 Yaobin Li et al. This is an open access article distributed under the Creative Commons Attribution License, which permits unrestricted use, distribution, and reproduction in any medium, provided the original work is properly cited.

To improve the borehole sealing effect, especially that of coal seam with low permeability and micro fissures, this paper takes the expansion rate of the sealing material as the response value and establishes the quadratic model embracing the expansion rate and various experimental factors by designing orthogonal experiments. The response surface is used to further determine the significance order of each key factor according to the expansion rate and adjust the admixture content to obtain the optimal ratio of the sealing material. For the research investigating a sealing material, the optimal ratio of the sealing material is obtained: the content of water reducing agent of 0.5%, the content of retarder of 0.04%, water-cement ratio of 0.8, and the content of expansion agent of 10%. At this time, the expansion rate reaches 3.136%. Besides, a scanning electron microscope is used to observe the microscopic morphology of the material. According to the scanning electron microscopy analysis of new borehole sealing materials, the surface of the new borehole sealing material shows no holes and possesses compactness; and a large amount of ettringite is formed on the surface of the hydration product of hardened cement slurry. The ettringite improves the expansibility of the material. The new sealing material provides a new idea for gas sealing, which is of great significance to improve the efficiency of borehole extraction, improve the utilization rate of resources, and prevent gas accidents.

## 1. Introduction

Gas disasters and accidents frequently occur in China and seriously affect production safety in coal mines. With the consumption of coal resources, China is facing increasingly serious gas problems [1, 2]. Currently, the commonly used gas control measure is gas drainage, and the sealing material is one of the critical factors to ensure the drainage effect. The common sealing materials of coal mines in China include cement mortar and polyurethane materials. However, the cement mortar materials will shrink after curing, resulting in cracks and air leakage [3–6]. Polyurethane materials are expensive and toxic.

To solve these problems, many scholars have studied the optimization of sealing materials. Some scholars have developed a CF type expansive cement composed of ordinary Portland cement, aluminum powder, CaO, and gypsum. The

expansive cement with good fluidity and high compressive capacity optimizes the expansion performance of cement materials [7, 8]. Hogancamp and Grasley [9] have found that carbon nanofibers can increase the shrinkage and improve the expansion ratio of ultrafine cement mortar while maintaining the hardness. Wang et al. [10] have mixed ordinary cement, coal gangue powder, and clay in a certain proportion for a new type of grouting sealing material, whose compressive strength and expansion ratio can be significantly improved. Liu et al. [11] studied the effect of different expansive agents on the expansion properties of cement slurry. Ye et al. [12] have compared the effects of calcium sulfoaluminate-calcium oxide and magnesium oxide on the expansion rate of Portland cement and found that calcium sulfoaluminate-calcium oxide increases the early strength, while magnesium oxide improves the expansion rate at the middle and late stage. Some scholars have studied

the effect of sulfate on the early hydration and hardening of Portland cement. Sulfate accelerates the hydration at all times [13, 14]. Feng et al. [15] studied the effect of magnesium oxide expansive agent on self-healing of early cracks in concrete. Some scholars have studied the influencing factors of MgO expansive agent effect, which provides a direction for the improvement of expansion performance of sealing materials [16, 17]. Zhou and Wang [18] have studied the influence of the amount of dispersant and expansion agent on the new sealing material based on the compressive strength and expansion ratio and finally determined the optimal ratio of each factor.

At present, the research of improving sealing materials has made remarkable achievements but mostly focusing on enhancing the grouting effect on large fissures. There is little research on the grouting effect on micro fissures. This study focuses on curing cracking of cement materials and the poor grouting effect on micro fissures. Design-Expert software is used to design an orthogonal experiment, draw a response surface graph, and take the expansion rate of the material as the index to optimize the ratio of the sealing material. Finally, the scanning electron microscope is used to analyze the microstructure of the material and the expansion mechanism is studied.

## 2. Experimental Materials

The new type of borehole sealing material with a gray appearance is based on ultrafine Portland cement, and its composition is provided in Table 1. All technical parameters and indicators have met the requirements of "Superfine Portland Cement" (GB/T35161-2017). The expansion agent is HCSA with an appearance of off-white powder. The water-reducing agent is PCE with white powder. The retarder used in this experiment is seaweed powder with a white appearance.

## 3. Experimental Method

29 groups of experiments with four factors and three levels were designed using Box-Behnken experiment design function in Design-Expert 8.0.5 software. The value ranges of the experimental factors are shown in Table 2.

Firstly, the standard triple trial mold was prepared. Secondly, according to the ratio in Table 2, the dry material quality and water quality required for the production of the specimens were calculated. Thirdly, the ultrafine cement and the admixture were mixed thoroughly (as shown in Figure 1) by adding water. Finally, after molding and then demolding (as shown in Figure 2), the specimens were put into the curing box for curing (temperature of  $20 \pm 2^\circ\text{C}$ , humidity above 95%, as shown in Figure 3).

The well-mixed cement slurry was poured into the round mold in the fluidity test of sealing material. After the surface was scraped, the round mold was quickly lifted. The round mold is 60 mm in height with an upper mouth diameter of 36 mm and a low mouth diameter of 60 mm. After the

flowing of the cement slurry, the two diameters perpendicular to each other were measured, and the average value was used as the fluidity.

The measurement of setting time refers to the test method for water consumption of the material with standard cement consistency, setting time, and stability (GB/T1346-2011). The setting time was measured by the Vicat apparatus. Firstly, the Vicat apparatus was made zero. Then the mixed material was poured into the test mold. After that, the surface of the material was scraped and the material was put into the curing box for curing. Finally, the initial and final setting times were measured according to national standards.

The material's initial volume after molding and demolding was recorded as  $V_1$ , and then the volumes at intervals were recorded as  $V_n$ . The expansion rate of this experimental study is the expansion rate after curing for 60 days, according to the expansive Cement Expansion Rate Test Method (JC\_T 313-2009). The expansion rate was calculated according to the following formula:

$$\varepsilon_t = \frac{V_n - V_1}{V_1} \times 100\%, \quad (1)$$

where  $V_n$  is the volume of the specimen at a certain age and  $V_1$  is the initial volume of the specimen.

The compressive strength test of the sample utilizes the RMT uniaxial press to test the compressive strength of stones of different ages (Figure 4).

After obtaining the optimal ratio of admixtures through orthogonal experiments, firstly, the specimens with the ultrafine cement material and admixture are prepared according to the optimal ratio. Secondly, the ZEISS scanning electron microscope was used to analyze the hydration mineral composition, hydration degree, and microstructure of cement-based materials. Finally, the action mechanism of new sealing materials was studied.

## 4. Experimental Results and Discussion

*4.1. Orthogonal Experiment Results and Response Surface Analysis.* In the practical application, it is necessary to comprehensively consider the compressive strength, fluidity, and expansion rate and optimize the multiobjective nonlinear formula to determine the optimal ratio. According to the results of the orthogonal experiment in Table 3, water-cement ratio, retarder dosage, water reducer dosage, and expansion agent dosage were set as independent variables A, B, C, and D. The expansion ratio was taken as the objective function for multiple variables nonlinear regression fitting and response surface analysis.

The results of the orthogonal experiment (shown in Table 3) were inputted into the Design-Expert 8.0.5 Trial software to find the most suitable model. The fitting results are shown in Tables 4 and 5. It can be seen from Table 4 that the linear equation and the quadratic equation model have a larger  $F$  value and a smaller  $\text{Prob} > F$  value, indicating that the two fitting models are the most suitable ones. It can be seen from Table 5 that the sum of squares of prediction residuals is low in several models. The  $R^2$  value of the

TABLE 1: Chemical composition of raw materials.

Chemical composition	$w$ (SiO <sub>2</sub> )	$w$ (Al <sub>2</sub> O <sub>3</sub> )	$w$ (Fe <sub>2</sub> O <sub>3</sub> )	$w$ (CaO)	$w$ (MgO)	$w$ (SO <sub>3</sub> )	Loss	Total
HCSA expanding agent	4.96	8.52	0.99	64.18	2.67	16.97	1.19	99.48
Superfine Portland cement	20.57	9.89	3.08	57.65	2	2.7	2.6	98.49

TABLE 2: Range of factors in the orthogonal experiment.

Test group	Value range of each factor/%			
	Water-cement ratio	Retarder	Water-reducing agent	Expanding agent
ZJ1-29	0.8~1.0	0.03~0.05	0.3~0.5	8~10



FIGURE 1: Sealing material before and after mixing.

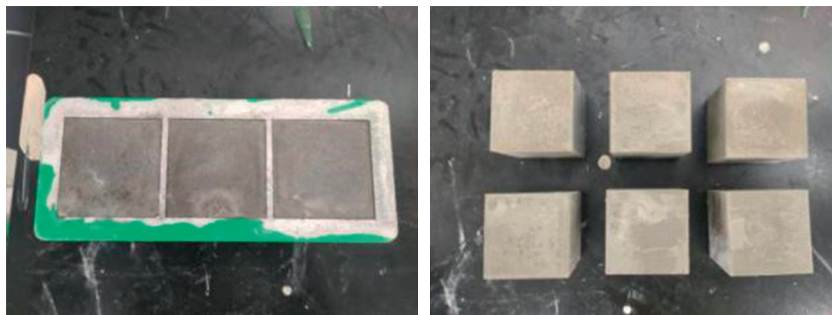


FIGURE 2: Preparation of specimens.



FIGURE 3: Curing of the specimens.

quadratic model (0.9052) is closer to 1. Besides, Adj.  $R^2$  of the linear model is smaller than that of the quadratic equation model, indicating that the linear model needs further improvement.

4.2. *Variance Results and Significance Tests.* From Table 6, it can be seen that the significance order of the factors is as follows: D (expansion agent) > A (water-cement ratio) > C (water-reducing agent) > B (retarder). The order of interaction of different factors is as follows: AD (water-cement ratio, expansion agent) > CD (water-reducing agent, expansion agent) > BD (retarder, expansion agent) > AC (water-cement ratio, water-reducing agent) > BC (retarder, water-reducing agent) > AB (water-cement ratio, retarder).

4.3. *Response Surface Analysis.* The interaction law was also obtained by analyzing the interaction of any two factors. Figure 5 shows the effect of retarder [19] and expansion agent [20] on the expansion rate. It can be seen that the



FIGURE 4: Compressive strength test.

TABLE 3: Results of orthogonal test.

No.	A	B/%	C/%	D/%	Expansion rate/%
1	0.8	0.03	0.4	9	1.897
2	0.8	0.04	0.5	9	2.032
3	0.8	0.04	0.4	10	3.281
4	0.8	0.04	0.3	9	1.931
5	0.8	0.04	0.4	8	1.593
6	0.8	0.05	0.4	9	1.821
7	0.9	0.03	0.5	9	1.898
8	0.9	0.03	0.4	10	2.471
9	0.9	0.03	0.4	8	1.614
10	0.9	0.03	0.3	9	1.521
11	0.9	0.04	0.4	9	2.053
12	0.9	0.04	0.4	9	2.053
13	0.9	0.04	0.3	10	2.329
14	0.9	0.04	0.4	9	2.053
15	0.9	0.04	0.5	8	1.589
16	0.9	0.04	0.5	10	2.809
17	0.9	0.04	0.3	8	1.621
18	0.9	0.04	0.4	9	2.053
19	0.9	0.04	0.4	9	2.053
20	0.9	0.05	0.3	9	1.621
21	0.9	0.05	0.5	9	1.812
22	0.9	0.05	0.4	10	2.597
23	0.9	0.05	0.4	8	1.531
24	1	0.04	0.3	9	1.986
25	1	0.03	0.4	9	1.778
26	1	0.04	0.4	10	2.093
27	1	0.05	0.4	9	1.803
28	1	0.04	0.4	8	1.302
29	1	0.04	0.5	9	1.889

contours of the ordinate are denser than those of the abscissa, indicating that the effect on the response value of the expansion agent is more significant than that of the water-cement ratio. The response surface is relatively steep, indicating that the interaction between the water-cement ratio and the expansive agent is prominent. The most obvious interaction occurs when the water-cement ratio

reaches the low limit, and the expansion agent reaches the upper limit, which is shown as the steepest response surface.

Figure 6 shows the effect of the water-reducing agent [21–23] and the expansion agent on the expansion rate. It can be seen that the ordinate contours are denser than the abscissa contours, indicating that the expansion agent has a



TABLE 4: Analysis of variance of different models.

Source	Sum of squares	df	Mean square	F value	p value	Prob > F
Mean versus total	112.36	1	112.36			
Linear	3.67	4	0.92	18.18	<0.0001	Suggested
2FI	0.30	6	0.050	0.98	0.4653	
Quadratic	0.45	4	0.11	3.40	0.0384	Suggested
Cubic	0.41	8	0.051	5.63	0.0247	
Residual	0.054	6	$9.061 \times 10^{-3}$			
Total	117.24	29	4.04			

TABLE 5: Comprehensive statistical analysis of multiple models.

Source	Std. dev	R-squared	Adjusted R-squared	Predicted R-squared	PRESS
Linear	0.22	0.7519	0.7106	0.6149	1.88
2FI	0.23	0.8131	0.7093	0.3961	2.95
Quadratic	0.18	0.9052	0.8105	0.4542	2.66
Cubic	0.095	0.9889	0.9480	-0.6049	7.83

TABLE 6: Response surface quadratic model and ANOVA results.

Source	Sum of squares	df	Mean square	F	Prob > F
Model	4.42	14	0.32	9.55	<0.0001
A	0.24	1	0.24	7.33	0.0170
B	$3.000 \times 10^{-6}$	1	$3.000 \times 10^{-6}$	$9.086 \times 10^{-5}$	0.9925
C	0.087	1	0.087	2.63	0.1274
D	3.34	1	3.34	101.13	<0.0001
AB	$2.550 \times 10^{-3}$	1	$2.550 \times 10^{-3}$	0.077	0.7851
AC	$9.801 \times 10^{-3}$	1	$9.801 \times 10^{-3}$	0.30	0.5944
AD	0.20	1	0.20	6.09	0.0271
BC	$8.649 \times 10^{-3}$	1	$8.649 \times 10^{-3}$	0.26	0.6168
BD	0.011	1	0.011	0.33	0.5743
CD	0.066	1	0.066	1.98	0.1807
A <sup>2</sup>	0.017	1	0.017	0.52	0.4819
B <sup>2</sup>	0.21	1	0.21	6.49	0.0232
C <sup>2</sup>	0.062	1	0.062	1.87	0.1931
D <sup>2</sup>	0.10	1	0.10	3.14	0.0981
Residual	0.46	14	0.033		
Lack of fit	0.46	10	0.046		
Pure error	0.000	4	0.000		
Cor total	4.88	28			

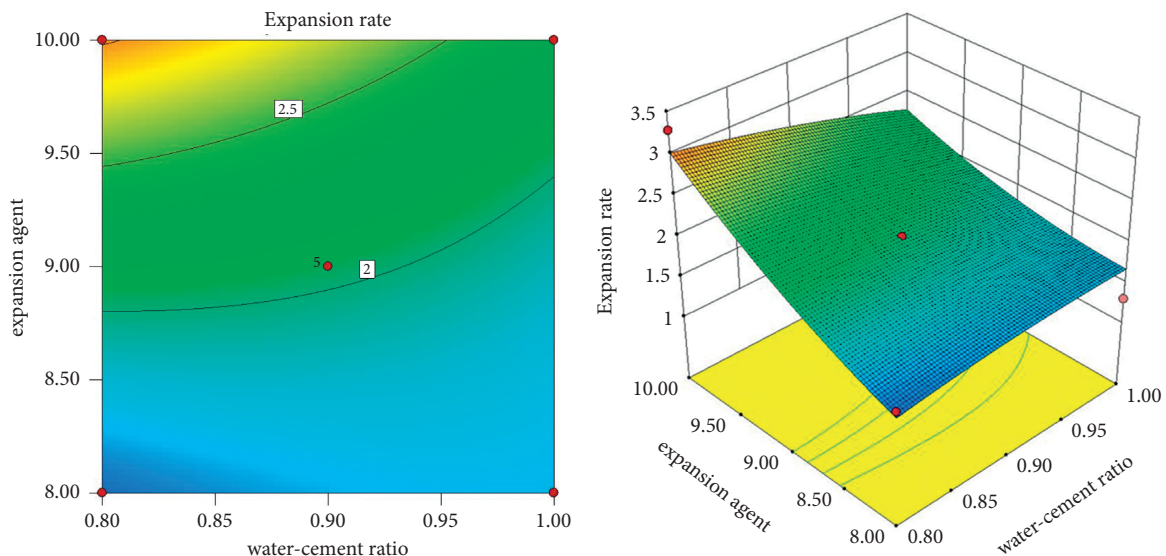


FIGURE 5: Effect of the water-cement ratio A and expansion agent D on the expansion rate.

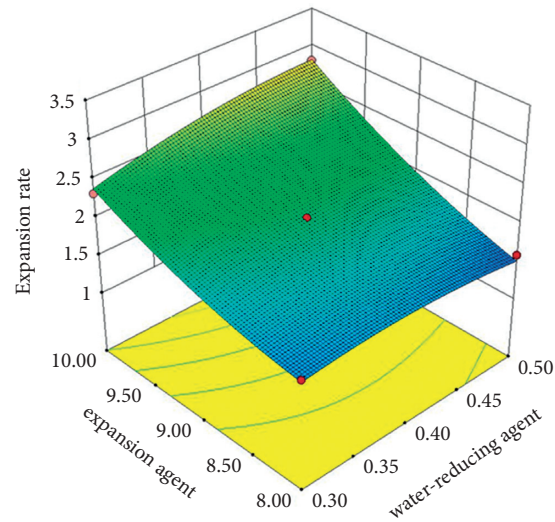
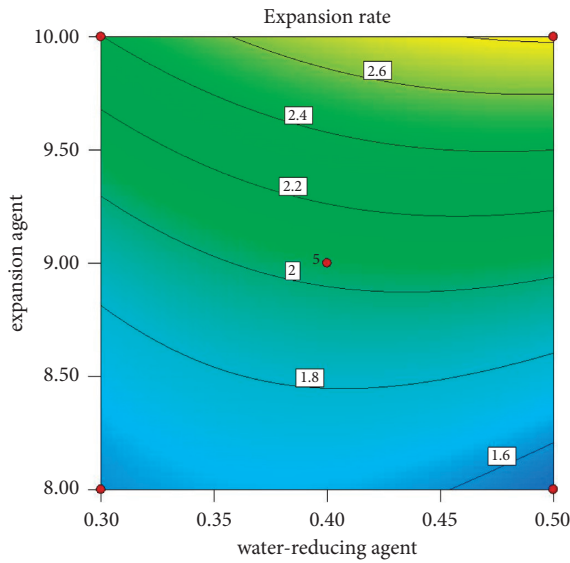


FIGURE 6: Effect of water-reducing agent C and expansion agent D on the expansion rate.

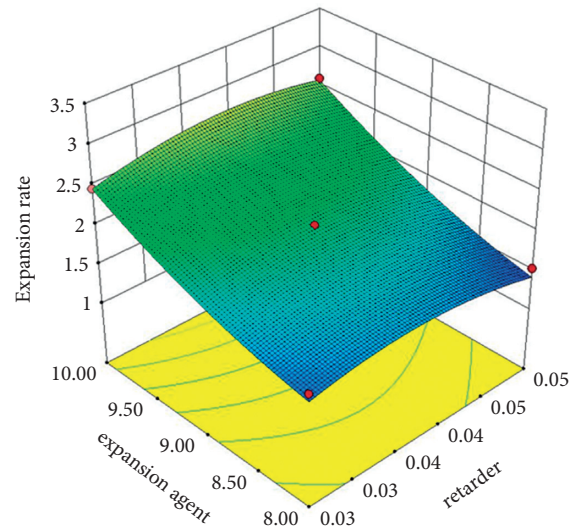
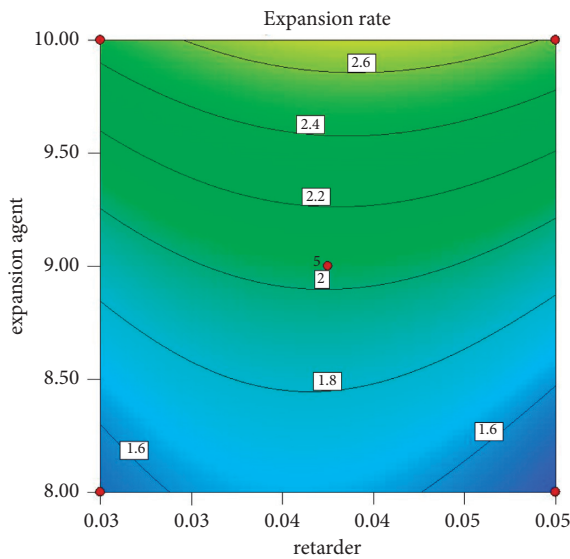


FIGURE 7: Effect of retarder B and expansion agent D on the expansion rate.

more significant influence on the response value than the water-reducing agent. The response surface is steep, indicating that the interaction between the two factors is obvious. When the values of water reducer and expansion agent reach the upper limit, the influence is the most significant.

Figure 7 shows the effect of retarder and expansion agent on the expansion rate. It can be seen that the ordinate contours are denser, indicating that the expansion agent has a higher effect on the expansion rate than the retarder, which is consistent with the results of the analysis of variance. When the value of the expansion agent is closer to the upper limit, the response surface is steeper, which shows that the interaction between the retarder and the expansion agent has a significant effect on the response value.

Figure 8 shows the effect of water-cement ratio and water-reducing agent on the expansion rate. It can be seen that the distributions of the ordinate contour and the abscissa contour are equivalent, showing that the effect of the water-cement ratio is close to that of the water-reducing agent on the response value. The contour distribution trend is related to the factor level, and the response surface graph has a certain distortion, which proves the certain interaction between the water-cement ratio and the water-reducing agent. However, the interaction between the two factors is weak, which is reflected in the small distortion of the surface graph.

Figure 9 shows the contours of the retarder and the water reducer are relatively sparse, and the response surface is relatively smooth, indicating that the two factors have a certain influence on the expansion rate, but the range of this influence is small.

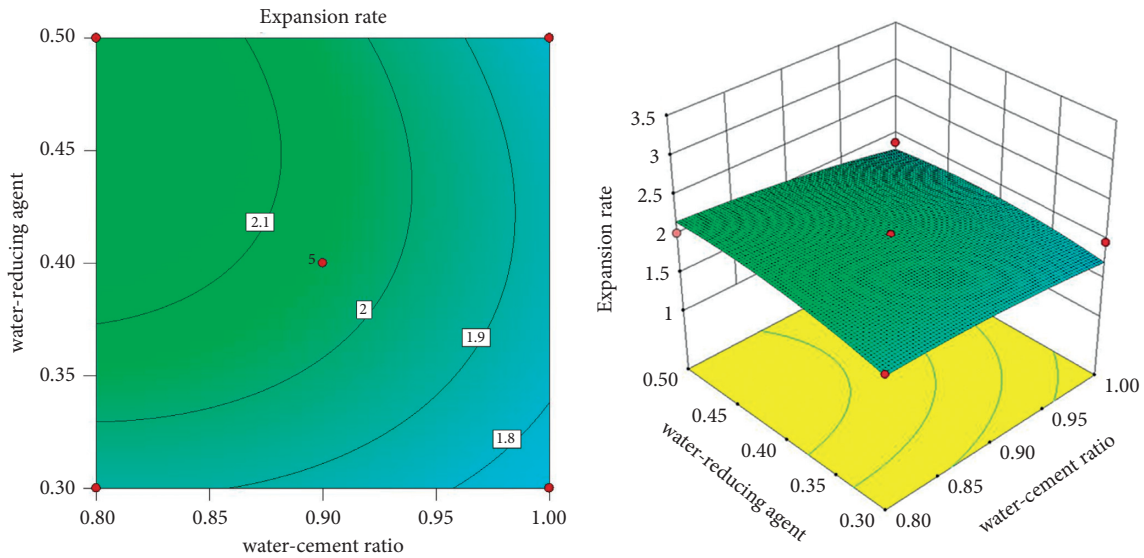


FIGURE 8: Effect of the water-cement ratio A and water reducer C on the expansion rate.

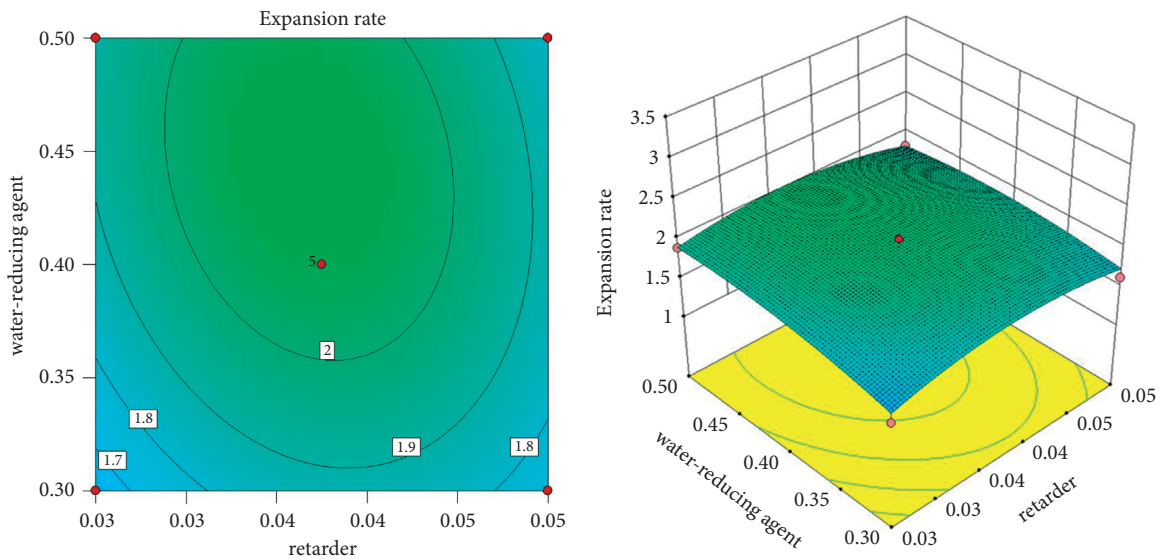


FIGURE 9: Effect of retarder B and water reducer C on the expansion rate.

Figure 10 shows the effect of the water-cement ratio and retarder on the expansion rate. It can be seen that the contours of water-cement ratio and retarder are sparse, and the response surface is relatively smooth, indicating that the two factors have a certain influence on the expansion rate, but the range of this influence is small, which is consistent with the results of the analysis of variance.

4.4. *Parameter Optimization and Result Verification.* The experimental results were further analyzed. The index was optimized with the expansion rate and the optimized experimental plan was obtained with the Design-Expert software. The first five groups of optimized experimental schemes were selected for verification, and the results are shown in Table 7.

It can be seen from Table 7 that, after the optimization of the ratio, the maximum absolute error between the predicted value of the material expansion rate and the actual measured value is only 1.601%, indicating that the model is relatively reliable. Given the operability and simplicity of on-site grouting, comprehensive expansion rate, fluidity, and strength, the best experimental conditions were selected as the water-reducing agent content of 0.5%, retarder content of 0.04%, water-cement ratio of 0.8, and expansion agent content of 10%.

4.5. *Micromorphology of Hydration Products.* The micromorphology of the new sealing material at different curing ages is shown in Figure 11. It can be seen that, when curing for 3 days, there are flocculent C-S-H gels wrapping around

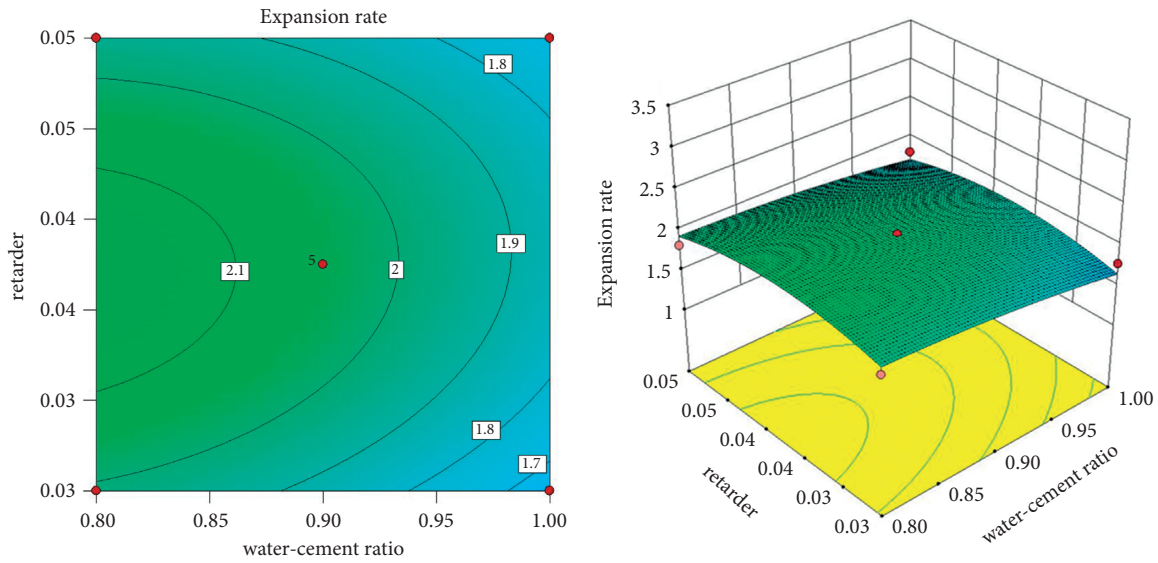


FIGURE 10: Effect of the water-cement ratio and retarder on the expansion rate.

TABLE 7: Optimum scheme and results.

No.	Experimental optimization ratio				Forecast expansion rate/%	Measured expansion rate/%	Error/%
	Water-cement ratio	Retarder/%	Water-reducing agent/%	Expansion agent/%			
1	0.8	0.04	0.5	10	3.18703	3.136	-1.601
2	0.8	0.04	0.49	10	3.17847	3.142	-1.147
3	0.8	0.04	0.5	9.95	3.13293	3.109	-0.764
4	0.82	0.04	0.5	10	3.12996	3.127	-0.095
5	0.84	0.04	0.48	10	3.0509	3.044	-0.226
6	0.8	0.03	0.44	9.91	2.92713	2.934	0.235

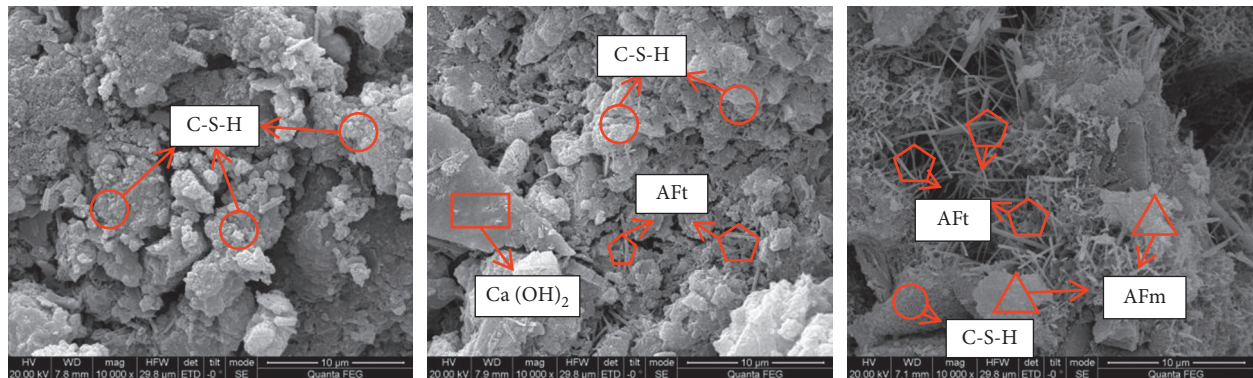


FIGURE 11: The micromorphology of the new material at different curing ages.

the cement particles, and a small amount of needle-shaped ettringite is generated. After curing for 7 days, the surface of cement particles is wrapped by hydration products and more ettringite is generated, which provides a certain strength for the material. After curing for 60 days, ettringite attached to the surface of cement particles is quite obvious, being longer and denser. A large flocculent C-S-H gel interacts with ettringite, which can absorb large amounts of water

molecules and then cause the cement particles to repel each other, bringing more expansion.

### 5. Conclusions

- (1) The influence of each component on the material expansion rate was tested by analysis of variance and significance test: D (expansion agent) > A (water-

cement ratio) > C (water-reducing agent) > B (retarder). According to the response surface drawn by the binomial polynomial regression equation, the interaction of any two factors to obtain the interaction law was analyzed: AD (water-cement ratio, expansion agent) > CD (water-reducing agent, expansion agent) > BD (retarder, expansion agent) > AC (water-cement ratio, water-reducing agent) > BC (retarder, water-reducing agent) > AB (water-cement ratio, retarder).

- (2) Ultrafine Portland cement is selected as the major ingredient and the expansion agent, water-reducing agent, and retarder were selected as the minor ingredients to produce a new kind of borehole sealing material. The optimal experimental conditions in this experiment were obtained by response surface analysis as water-reducing agent content of 0.5%, retarder content of 0.04%, water-cement ratio of 0.8, and expansion agent content of 10%, with an expansion rate reaching 3.136%.
- (3) The microstructures of the new materials are observed and analyzed. The amount of ettringite increases with the curing time. At 3 d hydration, a small amount of needle-shaped ettringite is generated. At 7 d hydration, more ettringite is generated, which provides a certain strength for the material. At 60 d hydration, almost no cement particles are observed in the hardened cement paste. A large amount of needle-shaped ettringite is produced on the surface of hydration products such as C-S-H gel and  $\text{Ca}(\text{OH})_2$  to provide power for the expansion of the material.

## Data Availability

The data used in the article can be obtained from the corresponding author.

## Conflicts of Interest

The authors declare no potential conflicts of interest with respect to the research, authorship, and/or publication of this article.

## Authors' Contributions

All the authors contributed to this paper. Xin Guo prepared and edited the manuscript. Sheng Xue and Yaobin Li made a substantial contribution to the data analysis and revised the article. Maoliang Shen and Yang Xu reviewed the manuscript and processed the results of numerical simulation during the research process. Chun-Shan Zheng provided the fund's support.

## References

- [1] L. Yuan, "Strategic thinking of simultaneous exploitation of coal and gas in deep mining," *Journal of China Coal Society*, vol. 41, no. 1, pp. 1–6, 2016.
- [2] L. Yuan and P. S. Zhang, "Development status and prospect of geological guarantee technology for precise coal mining," *Journal of China Coal Society*, vol. 44, no. 8, pp. 2277–2284, 2019.
- [3] C. A. Juarez, G. Fajardo, S. Monroy, A. Duran-Herrera, P. Valdez, and C. Magniont, "Comparative study between natural and PVA fibers to reduce plastic shrinkage cracking in cement-based composite," *Construction and Building Materials*, vol. 91, pp. 164–170, 2015.
- [4] M. Wyrzykowski, P. Trtik, B. Münch, J. Weiss, P. Vontobel, and P. Lura, "Plastic shrinkage of mortars with shrinkage reducing admixture and lightweight aggregates studied by neutron tomography," *Cement and Concrete Research*, vol. 73, pp. 238–245, 2015.
- [5] E. Boghssian and L. D. Wegner, "Use of flax fiber to reduce plastic shrinkage cracking in concrete," *Cement and Concrete Composites*, vol. 30, no. 10, pp. 929–937, 2008.
- [6] F. Pelisser, A. B. d. S. S. Neto, H. L. L. Rovere, and R. C. d. A. Pinto, "Effect of the addition of synthetic fibers to concrete thin slabs on plastic shrinkage cracking," *Construction and Building Materials*, vol. 24, no. 11, pp. 2171–2176, 2010.
- [7] T. J. Zhang, R. Y. Bao, S. G. Li, S. Zhang, L. Zhang, and K. Jiang, "Experimental study on expansion and creep characteristics of new CF sealing material," *Journal of Mining & Safety Engineering*, vol. 36, no. 1, pp. 175–183, 2019.
- [8] S. G. Li, J. F. Zhang, C. Zhang, and H. Yang, "Experimental study on expansion mechanism of new CF sealing material and the key influencing factors," *Journal of Mining & Safety Engineering*, vol. 35, no. 2, pp. 415–421, 2018.
- [9] J. Hogancamp and Z. Grasley, "The use of microfine cement to enhance the efficacy of carbon nanofibers with respect to drying shrinkage crack resistance of portland cement mortars," *Cement and Concrete Composites*, vol. 83, pp. 269–272, 2017.
- [10] H. T. Wang, X. C. Wang, M. H. Zhai et al., "Experiment and application of new material for grouting of gangue based aquifer," *Journal of China Coal Society*, vol. 42, no. 11, pp. 2981–2988, 2017.
- [11] Y. X. Liu, Y. Y. Chi, and W. Tian, "Effect of different expanders on properties of cement-based grouting," *Material Journal of Build Material*, vol. 1–13, 2021, <http://kns.cnki.net/kcms/detail/31.1764.TU.20210514.1112.024.html>.
- [12] X. Ye, W. X. Wu, W. H. Hou, S. Lei, and Z. Zhou, "Influence of expansion agent on the volume stability of high-strength grouting materials," *Journal of Building Materials*, vol. 21, no. 6, pp. 950–955, 2018.
- [13] C. Rossler, A. Eberhardt, H. Kucerova, and B. Moser, "Influence of hydration on the fluidity of normal Portland cement pastes," *Cement and Concrete Research*, vol. 38, no. 7, pp. 897–906, 2008.
- [14] B. Mota, T. Matschei, and K. Scrivener, "The influence of sodium salts and gypsum on alite hydration," *Cement and Concrete Research*, vol. 75, pp. 53–65, 2015.
- [15] J. J. Feng, P. Zhang, and W. Chen, "Self-healing behavior of early concrete cracks incorporating magnesium oxide expansive agent," *Journal of Building Materials*, vol. 21, no. 4, pp. 656–662, 2018.
- [16] F. Z. Cao and P. Y. Yan, "Effect of water-binder ratio on hydration degree and expansive characteristics of magnesium oxide expansive agents," *Journal of the Chinese Ceramic Society*, vol. 47, no. 2, pp. 171–177, 2019.
- [17] Z. Y. Liu, W. L. Bi, and Y. Guan, "Impact of expansive agent from calcined magnesite tailings on expansion performance of cement mortar," *Journal of Building Materials*, vol. 24, no. 3, pp. 466–472, 2021.

- [18] A. Zhou and K. Wang, "A new inorganic sealing material used for gas extraction borehole," *Inorganic Chemistry Communications*, vol. 102, pp. 75–82, 2019.
- [19] H. C. Du, Y. N. Wang, M. M. He, Z. Lin, and Z. Lyu, "Study on the effect of organic retarder on the performance of cement modified emulsified asphalt mastic," *Materials Review*, vol. 33, no. S2, pp. 254–260, 2019.
- [20] B. K. You and N. Z. Li, *Expansive Agent and Shrinkage Compensating Concrete*, China Building Materials Industry Press, Beijing, China, 2005.
- [21] X. Yu, C. Yu, Q. P. Ran, and J. Liu, "Retarding mechanism of hydroxy carboxylic acid retarder on cement hydration," *Journal of the Chinese Ceramic Society*, vol. 46, no. 2, pp. 181–186, 2018.
- [22] Y. Zhang and X. Kong, "Correlations of the dispersing capability of NSF and PCE types of superplasticizer and their impacts on cement hydration with the adsorption in fresh cement pastes," *Cement and Concrete Research*, vol. 69, no. 3, pp. 1–9, 2015.
- [23] L. Shui, Z. Sun, H. Yang, X. Yang, Y. Ji, and Q. Luo, "Experimental evidence for a possible dispersion mechanism of polycarboxylate-type superplasticisers," *Advances in Cement Research*, vol. 28, no. 5, pp. 287–297, 2016.

## Research Article

# Researches on the Influence of Blasting of Newly Built Tunnel on the Existing Tunnel Structure with Small Cross Angle

Xian Du,<sup>1</sup> Qinghua Xiao ,<sup>2</sup> Congming Li,<sup>2</sup> Qiang Xiong,<sup>2</sup> and Jianyou Yu<sup>1</sup>

<sup>1</sup>Yanchong Expressway Construction Office, Hebei Expressway Group Co., Ltd., Shijiazhuang 050000, China

<sup>2</sup>School of Civil Engineering, Southwest Jiaotong University, Chengdu 610031, China

Correspondence should be addressed to Qinghua Xiao; xqhb@swjtu.edu.cn

Received 23 July 2021; Revised 22 September 2021; Accepted 5 November 2021; Published 25 November 2021

Academic Editor: Qian Chen

Copyright © 2021 Xian Du et al. This is an open access article distributed under the Creative Commons Attribution License, which permits unrestricted use, distribution, and reproduction in any medium, provided the original work is properly cited.

In recent years, with the increasement of the railway expansion projects, the blasting damage has caused great threat to the safety of the existing tunnel structure. However, few researches are carried out on the influence of tunnel blasting construction on existing small-angle crossing tunnel structure. In this study, the dynamic response of existing tunnel structure to the blasting activities in newly built tunnel is analyzed by numerical simulation. From the comparison of vibration velocity, lining stress, and the displacement of the existing tunnel structure, the blasting methods, surrounding rock condition, cross angle, and clear distance are proven to be the highly correlated factors for the dynamic response of the existing tunnel to blasting. Then, combined with the analytic hierarchy process, the vibration velocity is selected as the optimal index to indicate the dynamic response to blasting activities.

## 1. Introduction

Nowadays, the railway has become one of the important modern transportations which is related to the national economy and people's livelihood [1, 2]. With the construction of the large-scale transport network, it is unavoidable to appear more and more spatially crossing railway tunnels with very small crossing angles, especially for the high-speed railways whose lines must be as straight as possible [3, 4], for example, in the new Guiyang-Guangzhou Railway, the Sizhai Tunnel goes under the Ruipo Tunnel, with a plane crossing angle of 22° and the minimum vertical clear distance of 23.0 m [5]. In the Wenzhou-Fuzhou Railway, the newly built Guantouling Tunnel goes under a tunnel of Wen-Fu Expressway, with a plane crossing angle of 36° and the minimum vertical clear distance of 2.91 m [6]. Under such extreme space conditions, the commonly used construction method will inevitably affect the surrounding structures [7, 8]. Hence, it is necessary to evaluate the influence of the blasting activities on the existing tunnel structures.

In the few decades, amounts of researches have been carried out to study the response of structure to the blasting

activities in tunnel constructions, such as the field tests, indoor experiments, numerical simulation, artificial intelligence [9–17]. Hong [18] studied the dynamic impact of cross section blasting excavation at intersections on the lining of existing tunnels, and the results showed that the maximum vibration velocity and the maximum tensile stress of each section of the lining were greatly reduced out of the range of  $\pm 8$  m at the cross section, and the lining structure was more sensitive to blasting within the range of  $\pm 8$  m around the blasting source. Liu et al. [19] established a finite element model of the upper and lower crossing tunnels and extracted the velocity-time history curve and equivalent stress-time history curve of each monitoring point, and the results indicated that the vibration velocity distribution of each point was basically consistent with the monitored vibration velocity; combined with the equivalent stress criterion, the vibration velocity of the critical mass point can be selected to ensure the safety of tunnel structure. Song et al. [20] studied the dynamic response law of the surrounding rock during the excavation of a large section tunnel by the virtue of portable electric spark source and found that the blasting process of the back tunnel has a greater impact on

the stability of the surrounding rock, while the surrounding rock at the oblique back of the tunnel is less sensitive to excavation and blasting vibration and is affected by the blasting process for longer time. In summary, the dynamic response characteristics of cross-tunnel blasting have attracted the attention of researchers, but most of them focus on the vibration velocity, without considering the stress and displacement of the existing railway tunnel. Therefore, to ensure the safety of the existing railway tunnel structure, it is necessary to comprehensively analyze the regular changes of its vibration velocity, displacement, and stress under different influencing factors.

Moreover, the partitioning methods also play vital role in the study of the impact of tunnel blasting [21, 22]. In the *Guidelines for the Approaching Construction of Existing Railway Tunnels* and the *Guidelines for the Approaching Construction of Highway Tunnels*, the problems of proximity construction were systematically discussed, and the concepts of proximity and influence zoning were clearly put forward. The latest Chinese monographs and specifications also contain relevant research content on the proximity construction of different building types. The *Code for Design of Highway Tunnels* clarifies the content of small clear distance tunnels and proposed the general process and methods of design and construction. Zhang et al. [23] established the tunnel construction impact zone of adjacent buildings according to the change trend of the stress state of the surrounding rock; based on the stress condition, the construction of new tunnels adjacent to the existing buildings can be divided into three types: strong, weak, and noninfluencing zones. Tian et al. [24] selected the ultimate shear strain as the criterion for instability of surrounding rock based on the existing problems of different criteria for instability of surrounding rock, by comparing the tunnels of a single tunnel and adjacent systems with existing urban roads, and taking the difference in safety factor as the threshold of the affected area, a mechanical calculation model for different tunnels near existing urban roads is established. However, the existing researches rarely studied the partitioning methods of dynamic impact zone of railway tunnels.

In this study, the response of existing tunnel structure to the blasting activities was studied by numerical simulation methods, various factors were incorporated into the model under different conditions, and finally various factors are compared to distinguish the optimal indicator for the dynamic response of existing tunnel. The framework of this paper is arranged as follows: Section 2 mainly describes the engineering background, Section 3 introduces the simulation methods blasting in tunnel excavation, Section 4 analyzes the simulation results in various conditions, Section 5 focuses on the determination of optimal indicator of dynamic response to blasting activities, and Section 6 summarizes the whole paper.

## 2. Engineering Background

The Tashi tunnel located in Longquan City (Zhejiang Province) is an important part of the Xianju-Qingyuan expressway. The starting point of the project line is on the left side of the Yuankengling tunnel in Tashi street and connected with the 322nd national highway. The terminal

point is located at the intersection of Fangye and Housha road, Jianchi Street. The newly built Tashi tunnel is designed according to the secondary highway standard with designed speed of 60 km/h. The geometries of tunnel are designed as follows: the length is 1825 m, the width is 12 m, and the clear height is 5 m. More significantly, the Tashi tunnel is located under the Yuankengling tunnel which belong to the existing Qujing Railway.

Considering the above complicated conditions, the newly built tunnel passes through the existing tunnel structure with small cross angle, the safety of existing tunnel structure is severely influenced by the excavation of the newly built tunnel, and the impact of the blasting construction of a new tunnel on the existing tunnel structure should be carefully evaluated during construction. Hence, in order to make the effective safety controlling methods, it is necessary to study the various influencing factors on the dynamic response of existing tunnel structure and distinguish the optimal indicator of dynamic response to blasting activities.

## 3. Numerical Simulation Methods

*3.1. Simulation of Material in Explosion.* Among many numerical simulation methods, ANSYS/LS-DYNA is widely used in blasting simulation because it can be used to calculate the large deformation dynamic response of nonlinear structural materials [25, 26]. Among them, the simulation of the three materials in the explosion problem, explosives, air, and rock materials, is particularly important.

*3.1.1. Explosive Model.* The JWL state equation is always used to describe the relationship between the pressure and volume of the detonation product of high-performance explosives, and the specific pressure  $P_{eos}$  of the explosive detonation product can be calculated using the following equation:

$$P_{eos} = A \left( 1 - \frac{\omega}{R_1 V} \right) e^{-R_1 V} + B \left( 1 - \frac{\omega}{R_2 V} \right) e^{-R_2 V} + \frac{\omega E_0}{V}, \quad (1)$$

where  $P_{eos}$  is the specific pressure,  $V$  is the relative volume,  $E_0$  is the specific internal energy, and  $A$ ,  $B$ ,  $R_1$ ,  $R_2$ , and  $\omega$  are constants determined by material. The above parameters of explosive used in the current study are listed in Table 1.

*3.1.2. Air Model.* The air is simulated by \*MAT\_NULL model, and its pressure can be calculated by the linear polynomial state equation EOS\_LINEAR\_POLYNOMIAL, as shown in the following equations:

$$p_0 = C_0 + C_1 \lambda + C_2 \lambda^2 + C_3 \lambda^3 + (C_4 + C_5 \lambda + C_6 \lambda^2) E_1, \quad (2)$$

$$\lambda = \frac{1}{V_0} - 1, \quad (3)$$

Where  $p_0$  is the pressure,  $E_1$  is the internal energy of unit volume,  $V_0$  is the initial relative volume, and  $C_0$ ,  $C_1$ ,  $C_2$ ,  $C_3$ ,



TABLE 1: Parameters of explosive in simulation.

Density $\rho_e$ (kg/m <sup>3</sup> )	Detonation velocity $D_H$ (m/s)	$A$ (GPa)	$B$ (GPa)	$R_1$	$R_2$	$\omega$	$P_{eos}$ (GPa)	$E_0$ (GPa)
1000	4200	211	0.18	4.20	0.90	0.15	9.70	4.19

$C_4$ ,  $C_5$ , and  $C_6$  are real constants of the state equation. The above parameters of simulated air are listed in Table 2.

**3.1.3. Rock Model.** The rock mass adopts \*MAT\_PLASTIC\_KINEMATIC isotropic followup plastic strengthening material mode. Compared with the condition of static load, the mechanical properties of the rock mass under the blasting load have also changed, and the strain rate has been greatly improved. Based on the Symonds–Cowper empirical formula, the model introduces the strain rate amplification factor, defines the element failure keyword \*MAT\_ADD\_EROSION, and defines the rock mass strength as the failure criterion to realize the damage and failure of the rock mass. The yielding stress  $\sigma_y$  of rock mass can be calculated by

$$\sigma_y = \left[ 1 + \left( \frac{\dot{\epsilon}}{C} \right)^{(1/P)} \right] (\sigma_0 + \beta E_p \varepsilon_p^{\text{eff}}), \quad (4)$$

$$E_p = \frac{E_0 E_{\text{tan}}}{E_0 - E_{\text{tan}}}, \quad (5)$$

$$\varepsilon_p^{\text{eff}} = \int_0^t d\varepsilon_p^{\text{eff}}, \quad (6)$$

$$d\varepsilon_p^{\text{eff}} = \sqrt{\frac{2}{3} d\varepsilon_{ij}^p d\varepsilon_{ij}^p}, \quad (7)$$

where  $\sigma_0$  is the initial yielding stress,  $E$  is Young's modulus,  $\dot{\epsilon}$  is the loading strain rate,  $C$  and  $P$  are the constants determined by the strain rate of the material,  $E_p$  is the plastic hardening modulus of rock mass,  $E_{\text{tan}}$  is the tangent modulus,  $\beta$  is the influence degree of hardening parameters on isotropic hardening and kinematic hardening,  $\varepsilon_p^{\text{eff}}$  is the effective plastic strain of rock mass,  $t$  is the duration of plastic strain, and  $\varepsilon_{ij}^p$  is the component of plastic strain deviation of rock mass. The above parameters are shown in Table 3.

**3.2. The Geometries of Models.** Considering the research target and the simplification of computational process, the numerical model is designed as follows. According to the influence of tunnel construction, the size of impact area is always regarded as 3 to 5 times the tunnel radius. That is, the existing tunnel influence area is 27.09 m to 45.15 m. Hence, 40 m is selected in the simulation. Similarly, the influence area of the new tunnel is calculated as 38.82 m to 64.70 m, and 50 m impact zone is considered in the model calculation. Consequently, the simulation model 140.00 m  $\times$  200.00 m  $\times$  124.52 m is established as shown in Figure 1. Figure 1(a) is the spatial structure diagram of the model, and Figure 1(b) is the constructed 3-dimensional element model.

As can be seen, the newly built tunnel is located under the existing tunnel, which is consistent with the cases in the practical engineering, and the distance  $D$  and cross angle  $\alpha$  are set as variables in the simulation, so as to distinguish the influence of the spatial relationship on the dynamic response of the existing tunnel.

**3.3. Design of Test Conditions.** According to the research purpose of the current study, the blasting methods of tunnel, the condition of surrounding rock, and the relative position (clear distance and angle of the spatial intersection) are selected as the main influencing factors of the dynamic response to the tunnel blasting. Therefore, based on the above influencing factors, the test conditions are designed as shown in Table 4, and the ANSYS/LS-DYNA blasting dynamic software is used to perform numerical simulation to analyze the sensitivity of each influencing factor, which will further provide parameter indicators for the indication of dynamic response. It should be noted that the values of maximum charge per delay of each blasting method are directly calculated from the blasting schemes. The simulation is implemented when the tunnel excavation face is located under the existing tunnel.

## 4. Results and Analysis

The above research simulates the blasting activities of new tunnel under various conditions, such as the blasting method, the surrounding rock condition, clear distance, and cross angle. It should be noted that the effectiveness of the adopted numerical methods has been proved in several published literatures, and the simulation results are consistent with the monitored results in practical engineering. Then the response of existing tunnel to the blasting is analyzed from the aspects of vibration velocity, lining stress, and structure displacement.

**4.1. Different Blasting Methods.** The full-section method and bench method are two frequently used construction methods for the excavation of mountainous tunnel. The main difference between such two methods is the maximum charge per delay, that is, the energy released in a short time.

Firstly, the vibration velocity-time history of different parts of the existing tunnel structure is extracted from the simulation results, as shown in Figure 2. The envelope diagram of the vibration velocity of existing tunnel is shown in Figure 3. It could be found that the maximum vibration velocity of the existing railway tunnel structure for full-section and bench method both appeared on the tunnel left foot, with the values of 8.08 cm/s and 5.30 cm/s, respectively. The minimum vibration velocity for such two methods appeared on the right arch waist of the tunnel, with the

TABLE 2: Parameters of air in simulation.

Density ( $\text{kg/m}^3$ )	$C_0$	$C_1$	$C_2$	$C_3$	$C_4$	$C_5$	$C_6$	$E_1$ (MPa)	$V_0$
1.29	0	0	0	0	0.40	0.40	0	0.25	1.00

TABLE 3: Parameters of rock in simulation.

$\rho_0$ ( $\text{kg/m}^3$ )	$E$ (GPa)	$\nu$	$\sigma_0$ (MPa)	$E_{\text{tan}}$ (GPa)	$C$ ( $\text{s}^{-1}$ )	$P$	$\sigma_c$ (MPa)	$\sigma_t$ (MPa)
2900	20.50	0.26	75.00	15	2.63	3.96	185.00	5.20

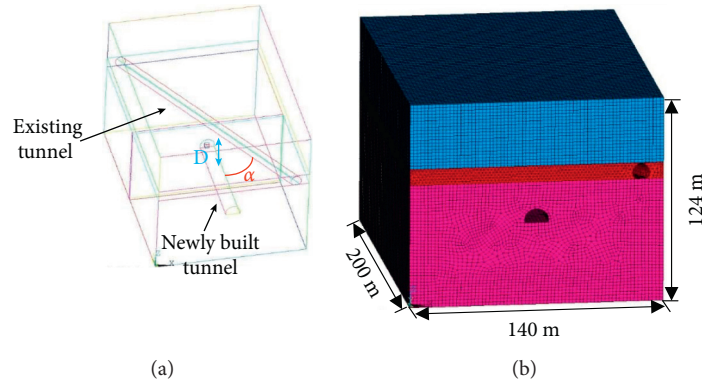


FIGURE 1: The geometries of the numerical model.

TABLE 4: The arrangement of testing conditions.

No.	Maximum charge per delay $Q$ (kg)	Surrounding rock	Clear distance $D$ (m)	Cross angle $\alpha$ ( $^\circ$ )	Blasting methods
1	26.50	III	16.90	$30^\circ$	Full-section method
2	13.14	III	16.90	$30^\circ$	Bench method
3	13.14	IV	16.90	$30^\circ$	Bench method
4	13.14	III	16.90	$15^\circ$	Bench method
5	13.14	III	16.90	$45^\circ$	Bench method
6	13.14	III	8.45	$30^\circ$	Bench method
7	13.14	III	25.35	$30^\circ$	Bench method

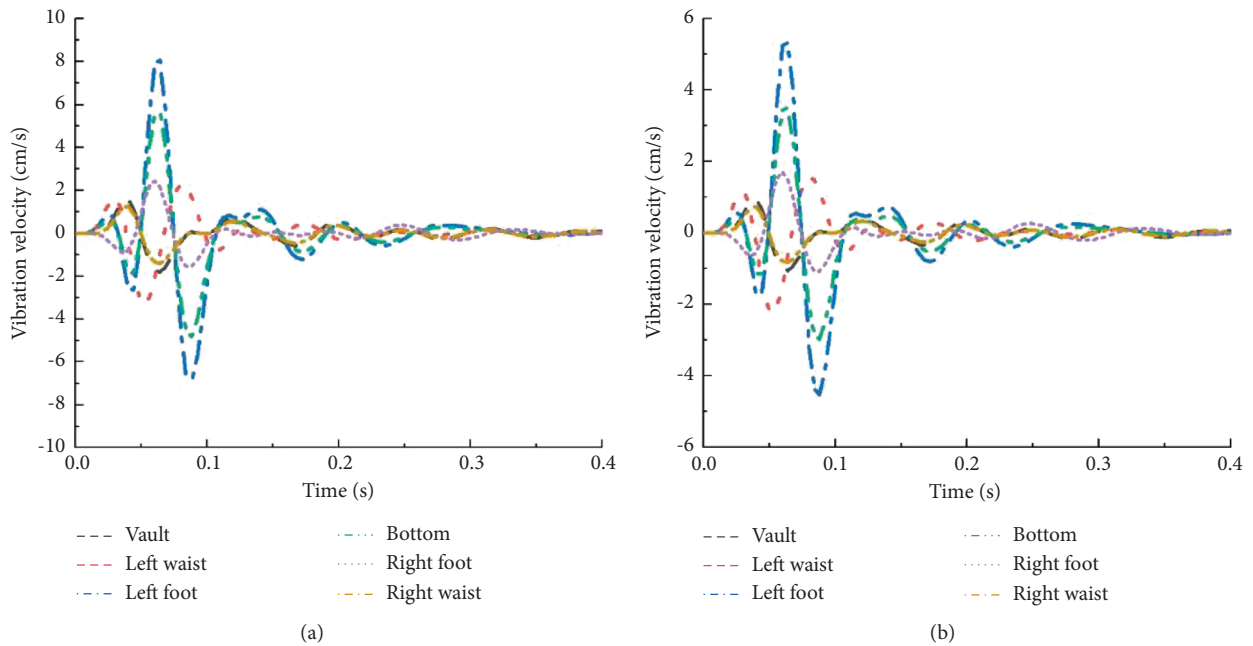


FIGURE 2: The vibration velocity-time history of different parts of the existing tunnel: (a) condition 1 and (b) condition 2.

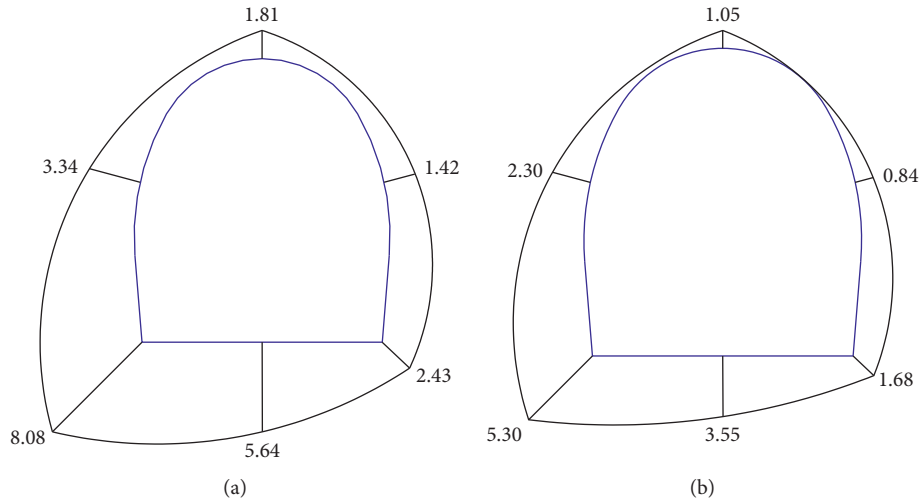


FIGURE 3: The envelope diagram of the vibration velocity of existing tunnel: (a) condition 1 and (b) condition 2.

values of 1.42 cm/s and 0.84 cm/s. This is due to the fact that the left arch of the existing railway tunnel is mainly located on the front side of the blasting, while the right arch waist is mainly located on the back side of the blasting. Moreover, compared with full-section method, an obvious decrease of vibration velocity could be observed in the existing railway tunnel structure constructed with the bench method.

After that, the stress nephogram is chosen to compare the response of existing tunnel to the different blasting methods applied in the newly built tunnel, as shown in Figure 4. When the full-section method and the bench method are used for cutting blasting, the maximum stress of the existing railway tunnel lining structure appears at the left arch waists, which are 5.43 MPa and 4.02 MPa, respectively. The minimum stress appears at the bottom of the tunnel lining structure, which are 0.25 MPa and 0.31 MPa, respectively. This is the effect of the redistribution of soil stress after the blasting action, and due to the principle of the arch effect of the Earth pressure, the tensile stress at the arch waists of the lining structure is the largest, and the tensile stress at the bottom of the tunnel is the smallest. The maximum stress value of different parts of the existing railway tunnel lining structure caused by the bench method cutting blasting is reduced by 25.97% compared with the full-section method, which is located on the left and right side of the tunnel. It can be found that the results obtained from the stress nephogram are consistent with the response law of vibration velocity.

Finally, the displacement nephograms of the lining structure are compared under different excavation methods, as shown in Figures 5 and 6. When the full-section method and the bench method are used for cutting blasting, the maximum displacement caused by the blasting effect appears in the Z direction, with the value of 5.92 mm and 5.85 mm, respectively. The maximum Y-direction displacement is 3.14 mm and 3.10 mm, and the maximum X-direction displacement is 0.73 mm and 0.88 mm. It can be concluded that the vertical displacement of tunnel lining structure is more sensitive to the

dynamic disturbance, but the influence of excavation methods is not so obvious.

**4.2. Different Surrounding Rock Conditions.** This section studies the influence of surrounding rock conditions on the response of existing tunnel to the blasting activities. The excavation method is specified as bench method, and the clear distance and cross angle between newly built and existing tunnels remain unchanged. Table 5 lists the vibration velocity, stress, and displacement of lining structure under different surrounding rock conditions. The similar law in the current simulation results could be found, the maximum vibration velocity and maximum stress both appear at the left arch foot, the minimum vibration velocity and stress appear at the right arch waist, and the maximum displacement occurs in the Z-direction. Compared with the IV-class surrounding rock, the tunnel built in the III-class surrounding rock tends to be more sensitive to the blasting activities in the newly built tunnel. This is because the III-class surrounding rock has better geological conditions and fewer joints and cracks in the stratum, the attenuation of blasting vibration waves is slower, and the adjacent tunnel structure responds more obviously to cutting blasting.

**4.3. Different Spatial Relations.** In this section, the effect of spatial relation (cross angles and clear distance) on the response of existing tunnel to the blasting activities is studied. The excavation method is specified as bench method, and the surrounding rock is specified as III-class. By the virtue of numerical simulation, the vibration velocity, stress, and displacement under different spatial relations are obtained.

The cross angles between the existing tunnel and newly built tunnel are set as 15°, 30°, and 45°, and then the vibration velocity, lining stress, and displacement of structure are collected as shown in Table 6. The maximum vibration velocity all appears at the left foot of the existing tunnel

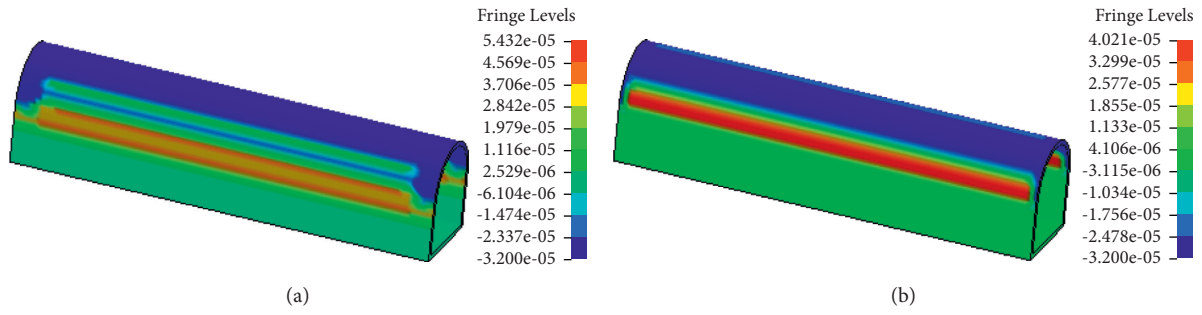


FIGURE 4: The lining stress of the existing tunnel: (a) condition 1 and (b) condition 2.

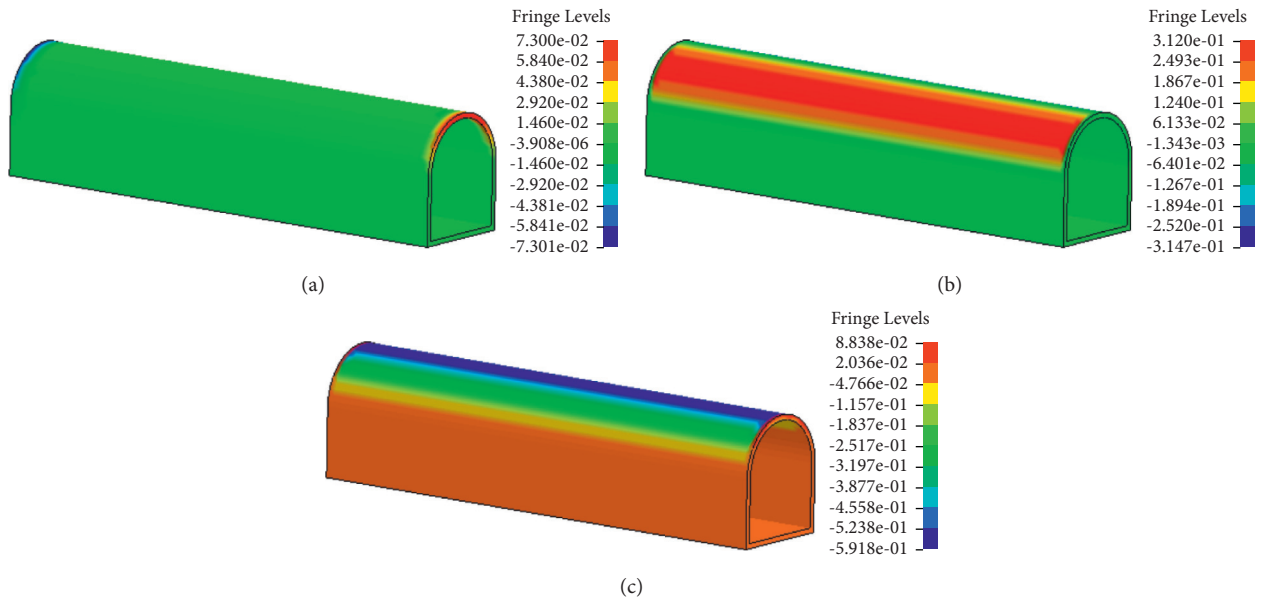


FIGURE 5: The displacement nephograms of the existing tunnel structure in condition 1.

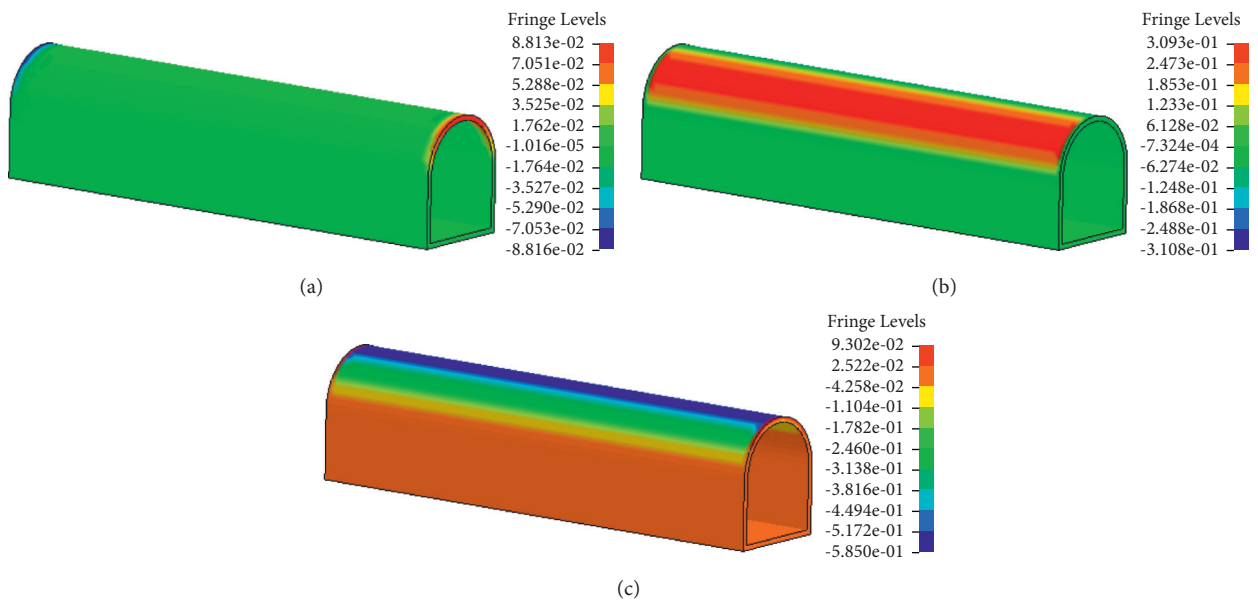


FIGURE 6: The displacement nephograms of the existing tunnel structure in condition 2.

TABLE 5: The dynamic response of the existing tunnel to blasting under different surrounding rock conditions.

Items	Vibration velocity (cm/s)		Lining stress (MPa)		Direction	Displacement (mm)	
	III	IV	III	IV		III	IV
Tunnel position							
Vault	1.05	0.90	-3.20	-3.20	X	0.88	0.96
Left waist	2.30	2.01	4.02	3.94			
Left foot	5.30	4.95	1.13	1.06	Y	3.10	3.09
Bottom	3.55	3.22	0.21	0.20			
Right foot	1.68	1.42	1.13	1.06	Z	5.85	5.82
Right waist	0.84	0.75	4.02	3.94			

TABLE 6: The dynamic response of the existing tunnel to blasting under different cross angle conditions.

Items	Vibration velocity (cm/s)			Lining stress (MPa)			Direction	Displacement (mm)		
	15	30	45	15	30	45		15	30	45
Tunnel position										
Vault	1.34	1.05	0.68	-3.20	-3.20	-3.20	X	0.80	0.88	1.30
Left waist	2.68	2.30	2.01	4.60	4.02	3.52				
Left foot	5.95	5.30	4.66	1.65	1.13	0.51	Y	3.10	3.10	3.15
Bottom	4.25	3.55	2.85	0.32	0.21	0.16				
Right foot	2.12	1.68	1.22	1.66	1.13	0.51	Z	5.88	5.85	5.83
Right waist	0.98	0.84	0.72	4.45	4.02	3.52				

structure under three conditions. When the cross angle increases from 15° to 45°, the maximum vibration velocity decreases by 22%. The considerable lining stress occurs at the left arch waist and right arch waist, and the obvious decrease can be also found for lining stress with the variation of cross angle. For the index of the displacement of tunnel structure, the maximum values occur in the Z-direction, but the cross angle has little influence on such index.

Then the effect of clear distance between the existing tunnel and newly built tunnel on the dynamic response of the existing tunnel structure is studied. In the current simulating process, the new tunnel is excavated by the bench method, the surrounding rock condition is set as III-class, the cross angle is set as 30°, the clear distance is set as 8.45 m, 16.90 m, and 25.35 m, respectively. After the calculation of the above numerical model under three different conditions, the vibration velocity, lining stress, and structure displacement were collected as shown in Table 7. It can be found that the distribution of three indexes is similar to the above research results, the maximum vibration velocity appears at the left foot, the maximum lining stress occurs at the arch waist, and the maximum displacement happens in Z-direction. Moreover, the clear distance is proved to be significant for weakening the dynamic response of the existing tunnel to the blasting activities.

## 5. Optimal Indicator of the Dynamic Response

In this section, the blasting methods, surrounding rock conditions, cross angle, and clear distance are selected to distinguish the optimal index to indicate the dynamic response of the existing tunnel to blasting activities. Hence, the analytic hierarchy process is applied to calculate the contribution weight of the vibration velocity  $P_1$ , the lining stress  $P_2$ , and the structure displacement  $P_3$  (scheme layer) to the dynamic response of existing tunnel (target layer). The

detailed analytic hierarchy process is arranged as follows [27–30].

**5.1. Establishment of Hierarchical Model.** The model is composed of three layers, as shown in Figure 7. The top layer is used to select the optimal indicator I. The bottom layer consists of the vibration velocity  $P_1$ , the lining stress  $P_2$ , and the structure displacement  $P_3$  of the existing tunnel. The intermediate layer consists of the blasting methods  $R_1$ , surrounding rock conditions  $R_2$ , cross angle  $R_3$ , and clear distance  $R_4$ .

**5.2. Construction of the Judgement Matrix.** The importance of the blasting methods  $R_1$ , surrounding rock conditions  $R_2$ , cross angle  $R_3$ , and clear distance  $R_4$  to the optimal indicator I is compared on the basis of the published literatures [20, 31–39]. Combined with Saaty's scale table, the judgement matrixes are constructed as follows:

$$A_{4 \times 4} = \begin{bmatrix} 1 & 5 & 5 & 3 \\ \frac{1}{5} & 1 & 1 & \frac{1}{5} \\ \frac{1}{5} & 1 & 1 & \frac{1}{5} \\ \frac{1}{3} & 5 & 5 & 1 \end{bmatrix}. \quad (8)$$

**5.3. Hierarchical Single Sorting and Consistency Check.** Through the transformation of matrix, the maximum eigenvalue is calculated to be 4.1545, and the corresponding

TABLE 7: The dynamic response of the existing tunnel to blasting under different clear distance conditions.

Items Tunnel position	Vibration velocity (cm/s)			Lining stress (MPa)			Direction	Displacement (mm)		
	8.45	16.90	25.35	8.45	16.90	25.35		8.45	16.90	25.35
Vault	1.45	1.05	0.26	-3.20	-3.20	-3.20	X	1.71	0.88	1.12
Left waist	3.54	2.30	1.29	5.32	4.02	2.90				
Left foot	8.64	5.30	3.10	1.48	1.13	0.46				
Bottom	5.76	3.55	2.06	0.35	0.21	0.08	Y	3.25	3.10	3.10
Right foot	2.45	1.68	0.91	1.48	1.13	0.46				
Right waist	1.26	0.84	0.38	5.32	4.02	2.90				

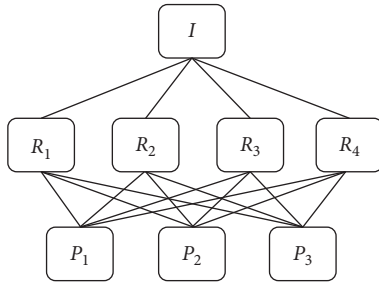


FIGURE 7: Hierarchical model of index for determining the optimal indicator of dynamic response.

eigenvector is extracted as  $W = [0.8564, 0.1246, 0.1246, 0.4853]^T$ ; after the normalization, the above vector is presented as  $w = [0.5383, 0.0783, 0.0783, 0.3050]^T$ . Hence, the consistency index is calculated as  $CI = (\lambda - n)/(n - 1) = (4.1545 - 4)/(4 - 1) = 0.0515$ , and the random consistency index  $RI$  is determined as 0.90. Consequently, the consistency rate of the hierarchical single arrangement of the order  $CR = CI/RI = 0.0515/0.90 = 0.0572 < 0.10$ , which means the order passes the consistency check.

**5.4. Hierarchical Total Sorting and Consistency Check.** Firstly, the importance of four factors,  $R_1, R_2, R_3$ , and  $R_4$ , in intermediate layer to the target  $I$  in top layer is assumed as  $r_1, r_2, r_3$ , and  $r_4$ , respectively, the importance of three factors,  $P_1, P_2$ , and  $P_3$ , to the target  $R_j$  in the intermediate layer is assumed as  $p_{1j}, p_{2j}, p_{3j}$  ( $j = 1, 2, 3, 4$ ). Hence, the hierarchical total sorting of the bottom layer can be calculated though the factors' contribution to the overall target ( $\sum_{j=1}^4 r_j p_{ij}$ ).

Then the consistency check is carried out following the step of consistency check in the single sorting. The importance of the vibration velocity  $P_1$ , the lining stress  $P_2$ , the structure displacement  $P_3$ , the factors  $R_1, R_2, R_3, R_4$  in intermediate layer, and, the judgement matrixes are listed as follows:

$$B_{3 \times 3}^1 = \begin{bmatrix} 1 & 5 & 3 \\ \frac{1}{5} & 1 & 1 \\ \frac{1}{3} & 1 & 1 \end{bmatrix},$$

$$B_{3 \times 3}^2 = \begin{bmatrix} 1 & 3 & 3 \\ \frac{1}{3} & 1 & 1 \\ \frac{1}{3} & 1 & 1 \end{bmatrix},$$

$$B_{3 \times 3}^3 = \begin{bmatrix} 1 & 3 & 3 \\ \frac{1}{3} & 1 & 1 \\ \frac{1}{3} & 1 & 1 \end{bmatrix},$$

$$B_{3 \times 3}^4 = \begin{bmatrix} 1 & 5 & 3 \\ \frac{1}{5} & 1 & 1 \\ \frac{1}{3} & 1 & 1 \end{bmatrix}.$$

(9)

After computing the maximum characteristic roots, the corresponding weight vectors are calculated as  $w_1^3 = [0.6586, 0.1562, 0.1852]^T$ ,  $w_2^3 = [0.6000, 0.2000, 0.2000]^T$ ,  $w_3^3 = [0.6000, 0.2000, 0.2000]^T$ , and  $w_4^3 = [0.6586, 0.1562, 0.1852]^T$ . Then the combined weight of  $P_1, P_2$ , and  $P_3$  to the target  $R_j$  in the intermediate layer is calculated as 0.6494, 0.1631, and 0.1875, and the corresponding weight vector is determined as  $[0.6494, 0.1631, 0.1875]^T$ . Consequently, the consistency rate of the hierarchical overall arrangement of the order  $CR = CI/RI = 0.0212 < 0.10$  means the assumed order meets the requirements of the consistency check. That is, the vibration velocity is the optimal index for indicating the dynamic response of existing tunnel to the blasting activities. Actually, the *Safety Technical Specification for Blasting Vibration of Railway Engineering* also adopts the vibration velocity as the safety index of existing structure and points out that the vibration velocity of single-line railway tunnel should be controlled lower than 6.0 cm/s, which is consistent with the methods adopted in the practical engineering.

## 6. Conclusions

In this study, the effect of the blasting activities on the existing tunnel structure is analyzed by the way of numerical simulation. The blasting methods, surrounding rock condition, cross angle, and clear distance are selected as four influence factors for the dynamic response of the existing

tunnel, and the vibration velocity, lining stress, and the displacement of structure are selected to evaluate the safety condition of the existing tunnel when suffering the blasting loads. After that, the analytic hierarchy process is adopted to choose the optimal index to indicate the dynamic response of the existing tunnel to blasting activities. The main conclusions can be summarized as follows:

- (1) From the results of the numerical simulation, the dynamic response of existing tunnel is proved to be highly relevant to the blasting methods, surrounding rock condition, cross angle, and clear distance. The dynamic response tends to be stronger with the increase of maximum charge per delay, the better surrounding rock condition, and the decrease of cross angle and clear distance.
- (2) Comparing the dynamic response of different parts of existing tunnel structure, the maximum vibration velocity always appears at the left foot, the maximum lining stress always occurs at the left and right arch waist, and the maximum displacement always appears in the Z-direction. Hence, the above results can be referred to for development of the protective guideline of tunnel structure which is near to the blasting activities.
- (3) Combined with the analytic hierarchy process and numerical simulation results, the vibration velocity is picked as the optimal index to indicate the dynamic response of the existing tunnel to blasting activities, which is consistent with most safety control specification of tunnel structure.

## Data Availability

The data used to support the findings of this study are included within the article.

## Conflicts of Interest

The authors declare that they have no conflicts of interest.

## Acknowledgments

This work was supported by the Science and Technology Project of Hebei Provincial Department of Transportation (YC201907).

## References







- [1] X. Zhang, W. Zhang, and P. T. W. Lee, "Importance rankings of nodes in the China railway express network under the belt and road initiative," *Transportation Research Part A: Policy and Practice*, vol. 139, pp. 134–147, 2020.
- [2] Q. Sun, X. Guo, W. Jiang, D. Haiying, L. Tingzhen, and X. Xingbo, "Exploring the node importance and its influencing factors in the railway freight transportation network in China," *Journal of Advanced Transportation*, vol. 2019, Article ID 1493206, 16 pages, 2019.
- [3] Z. Zhang, W. Xu, W. Nie, and L. Deng, "DEM and theoretical analyses of the face stability of shallow shield cross-river tunnels in silty fine sand," *Computers and Geotechnics*, vol. 130, Article ID 103905, 2021.
- [4] M. Wang, J. Guo, L. Luo et al., "Study of critical buried depth of large cross-section loess tunnel for high speed railway," *Rock and Soil Mechanics*, vol. 31, no. 4, pp. 1157–1162, 2010.
- [5] P. Tao, "Case study on design of a railway tunnel crossing underneath an existing highway tunnel with a small angle," *Tunnel Construction*, vol. 07, 2013.
- [6] B. L. Wei, "Construction technology for Wenfu railway Guantouling tunnel under crossing the highway tunnel," *Chinese Journal of Underground Space and Engineering*, vol. 4, 2007.
- [7] L. Wu, X. Zhang, Z. Zhang, and W. Sun, "3D discrete element method modelling of tunnel construction impact on an adjacent tunnel," *KSCE Journal of Civil Engineering*, vol. 24, no. 2, pp. 657–669, 2020.
- [8] P. Ye, X. Yang, B. L. Ling et al., "Vibration effects on existing tunnel induced by blasting of an adjacent cross tunnel," *Rock and Soil Mechanics*, vol. 32, no. 2, pp. 537–541, 2011.
- [9] Y. L. Gui, Z. Y. Zhao, L. B. Jayasinghe, H. Y. Zhou, A. T. C. Goh, and M. Tao, "Blast wave induced spatial variation of ground vibration considering field geological conditions," *International Journal of Rock Mechanics and Mining Sciences*, vol. 101, pp. 63–68, 2018.
- [10] A. De, T. F. Zimmie, and K. E. Vamos, "Centrifuge experiments to study surface blast effects on underground pipelines," in *Proceedings of the Pipeline Division Specialty Conference 2005*, pp. 362–370, TX, USA, August 2005.
- [11] J. B. Martino and N. A. Chandler, "Excavation-induced damage studies at the underground research laboratory," *International Journal of Rock Mechanics and Mining Sciences*, vol. 41, no. 8, pp. 1413–1426, 2004.
- [12] T. Wang, Z. Song, J. Yang, J. Wang, and X. Zhang, "Experimental research on dynamic response of red sandstone soil under impact loads," *Geomechanics and Engineering*, vol. 17, no. 4, pp. 393–403, 2019.
- [13] B. Duan, H. Xia, and X. Yang, "Impacts of bench blasting vibration on the stability of the surrounding rock masses of roadways," *Tunnelling and Underground Space Technology*, vol. 71, pp. 605–622, 2018.
- [14] W. Lu, J. Yang, M. Chen, and C. Zhou, "An equivalent method for blasting vibration simulation," *Simulation Modelling Practice and Theory*, vol. 19, no. 9, pp. 2050–2062, 2011.
- [15] S. G. Chen and J. Zhao, "A study of UDEC modelling for blast wave propagation in jointed rock masses," *International Journal of Rock Mechanics and Mining Sciences*, vol. 35, no. 1, pp. 93–99, 1998.
- [16] D. J. Armaghani, M. Hajihassani, E. T. Mohamad, A. Marto, and S. A. Noorani, "Blasting-induced flyrock and ground vibration prediction through an expert artificial neural network based on particle swarm optimization," *Arabian Journal of Geosciences*, vol. 7, no. 12, pp. 5383–5396, 2014.
- [17] M. Khandelwal and T. N. Singh, "Prediction of blast-induced ground vibration using artificial neural network," *International Journal of Rock Mechanics and Mining Sciences*, vol. 46, no. 7, pp. 1214–1222, 2009.
- [18] Z. Y. Hong, *Study on Dynamic Influence of Existing Highway Tunnel Caused by Blasting Construction of Diversion Tunnel Passing under it*, Chongqing Jiaotong University, Chongqing, China, 2018, in Chinese.
- [19] D. Z. Liu, Q. C. Gao, and X. Y. Wang, "Study on blasting vibration characteristics of up and down cross tunnels," *Transactions of Beijing Institute of Technology*, vol. 40, no. 12, pp. 1267–1274, 2020.

- [20] S. Song, S. Li, L. Li et al., "Model test study on vibration blasting of large cross-section tunnel with small clearance in horizontal stratified surrounding rock," *Tunnelling and Underground Space Technology*, vol. 92, Article ID 103013, 2019.
- [21] R. Nateghi, M. Kiany, and O. Gholipouri, "Control negative effects of blasting waves on concrete of the structures by analyzing of parameters of ground vibration," *Tunnelling and Underground Space Technology*, vol. 24, no. 6, pp. 608–616, 2009.
- [22] P. K. Singh and M. P. Roy, "Damage to surface structures due to blast vibration," *International Journal of Rock Mechanics and Mining Sciences*, vol. 47, no. 6, pp. 949–961, 2010.
- [23] J. H. Zhang, L. Guo, Y. C. Zheng et al., "Influence and countermeasure analysis on urban tunneling near buildings," *Journal of Railway Engineering Society*, vol. 33, no. 4, pp. 95–100, 2016.
- [24] M. Tian, D. Zhang, G. Qu et al., "Research on influence zoning of tunnel side crossing existing urban roads based on ultimate shear strain failure criterion," *IOP Conference Series: Materials Science and Engineering*, vol. 741, no. 1, 2020.
- [25] J. O. Hallquist, *LS-DYNA Keyword User's Manual*, Livermore Software Technology Corporation, Livermore, CA, USA, 2007.
- [26] J. Henrych and R. Major, *The Dynamics of Explosion and its Use*, Elsevier, Amsterdam, Netherland, 1979.
- [27] B. L. Golden, E. A. Wasil, and P. T. Harker, *The analytic hierarchy process*, Vol. 2, Applications and Studies, Berlin, Heidelberg, 1989.
- [28] T. L. Saaty, "How to make a decision: the analytic hierarchy process," *Interfaces*, vol. 24, no. 6, pp. 19–43, 1994.
- [29] O. S. Vaidya and S. Kumar, "Analytic hierarchy process: an overview of applications," *European Journal of Operational Research*, vol. 169, no. 1, pp. 1–29, 2006.
- [30] T. L. Saaty, "Decision making with the analytic hierarchy process," *International Journal of Services Sciences*, vol. 1, no. 1, pp. 83–98, 2008.
- [31] Z. Zhang, C. Zhou, A. Remennikov, T. Wu, S. Lu, and Y. Xia, "Dynamic response and safety control of civil air defense tunnel under excavation blasting of subway tunnel," *Tunnelling and Underground Space Technology*, vol. 112, Article ID 103879, 2021.
- [32] Z. G. Zhu, M. L. Sun, Y. Q. Zhu et al., "Field monitoring on blasting vibration and dynamic response of ultra-small spacing tunnels," *Rock and Soil Mechanics*, vol. 33, no. 12, pp. 3747–3752, 2012.
- [33] L. P. Li, S. C. Li, Q. S. Zhang et al., "Analysis of dynamic response on blasting excavation of close-spaced tunnel," *Journal of Highway and Transportation Research and Development*, vol. 7, no. 148, 2008.
- [34] B. Duan, W. Gong, G. Ta, Y. Xuxu, and Z. Xuewei, "Influence of small, clear distance cross-tunnel blasting excavation on existing tunnel below," *Advances in Civil Engineering*, vol. 2019, Article ID 4970269, 16 pages, 2019.
- [35] X. Xia, H. B. Li, J. C. Li, B. Liu, and C. Yu, "A case study on rock damage prediction and control method for underground tunnels subjected to adjacent excavation blasting," *Tunnelling and Underground Space Technology*, vol. 35, pp. 1–7, 2013.
- [36] R. Nateghi, "Prediction of ground vibration level induced by blasting at different rock units," *International Journal of Rock Mechanics and Mining Sciences*, vol. 48, no. 6, pp. 899–908, 2011.
- [37] F. Xue, C. Xia, G. Li, J. Baocheng, H. Yongwang, and F. Yapeng, "Safety threshold determination for blasting vibration of the lining in existing tunnels under adjacent tunnel blasting," *Advances in Civil Engineering*, vol. 2019, Article ID 8303420, 10 pages, 2019.
- [38] C. Dai, H. Sui, and C. Ma, "Study on the vibration effect of short footage blasting load on surrounding rock-support structure of tunnel," *Shock and Vibration*, vol. 2020, Article ID 8829349, 15 pages, 2020.
- [39] Z. S. Wu, G. Q. Chen, K. Zen, K. Kasama, and D. L. Wang, "Effect of blasting on the adjacent underground tunnels," *Applied Mechanics and Materials*, vol. 90-93, pp. 1870–1878, 2011.



## Research Article

# Water Inrush Risk Assessment Based on AHP and Advance Forecast Approach: A Case Study in the Micangshan Tunnel

Tao Song <sup>1,2</sup>, Jun Zeng <sup>1,2</sup>, Jiayi Ma <sup>1,2</sup>, Chunchi Ma <sup>1,2</sup>, Tianbin Li <sup>1,2</sup> and Tao Xia <sup>3</sup>

<sup>1</sup>College of Environment and Civil Engineering, Chengdu University of Technology, Chengdu 610059, Sichuan, China

<sup>2</sup>State Key Laboratory of Geohazard Prevention and Geoenvironment Protection, Chengdu University of Technology, Chengdu 610059, Sichuan, China

<sup>3</sup>The Civil Engineering Group Corporation of China Construction Second Engineering Bureau Ltd., Beijing, China

Correspondence should be addressed to Chunchi Ma; machunchi17@cdut.edu.cn

Received 8 May 2021; Revised 28 September 2021; Accepted 5 October 2021; Published 28 October 2021

Academic Editor: Angelo Aloisio

Copyright © 2021 Tao Song et al. This is an open access article distributed under the Creative Commons Attribution License, which permits unrestricted use, distribution, and reproduction in any medium, provided the original work is properly cited.

Water inrush is a serious geological disaster in tunnel. For the effective prevention and control of the occurrence of water inrush, a static-dynamic water inrush risk assessment method is proposed by considering the Micangshan tunnel as an example. First, four possible types of water inrush phenomenon are identified based on the geological and hydrogeological conditions of the tunnel: water inrush in water-bearing cracks, fault fracture zones, karst pipelines, and karst caves. Next, evaluation indexes that affect water inrush are determined. By combining the index weight value calculated by analytic hierarchy process (AHP) with the index quantitative value, the static water inrush disaster evaluation model is established, which provides a basis for tunnel design. Finally, with the combination of the static evaluation model and advanced forecast method, a dynamic risk prediction method of water inrush is established, which provides guidance for safe construction. The results confirm that the proposed method is a reliable theoretical basis for early assessment and prediction of tunnel water inrush disasters.

## 1. Introduction

Detection of anomalous geological structures such as fault zones, faults, aquifers, and karsts in the process of tunnel construction is challenging owing to their large buried depth and length of the tunnel [1–4]. In particular, during the construction of a tunnel in a complex karst area, high water pressure makes the surrounding rock unstable, resulting in a water gushing disaster, which in turn may cause delay in the construction, economic loss, and even serious casualties [5, 6]. Therefore, the prediction of the water gushing phenomenon in a tunnel is a key step in tunnel construction [7].

The analytic hierarchy process (AHP) by considering the several evaluation indexes of water inrush has been widely used as a decision support tool to solve complex decision-making problems [8]. Lyu et al. [9–12] applied remote sensing and GIS coupled with AHP techniques for delineating

potential groundwater zones in semiarid areas. A hierarchical structure of multilevel goals, standards, substandards, and alternatives has been established [13]. Wang et al. [14] used a fuzzy AHP to construct water inrush indices of coal seam floors based on geological, hydrogeological, floor aquitard, and mine-size factors for predicting water inrush through coal seam floors. Xue et al. [15] selected seven main factors, namely, the surrounding rock grade, rock integrity, overburden thickness, seawater thickness, tunnel section, permeability coefficient, and construction technology level, as risk assessment indicators for the evaluation model. Zhang et al. [16] considered the karst geological conditions and selected nine main factors such as ground water level, land form and physiology, attitude of rock formation, and unfavorable geological conditions as the evaluation indexes affecting water inrush in tunnels. However, the existing prediction models do not introduce factors affecting the types

of water inrush. First, rock roofs with different thickness have distinct failure patterns under complex pressure [17, 18]. Moreover, the uncertainty of the geological conditions in front of the tunnel face causes different hydrogeological conditions and types of water inrush phenomenon in different areas. Second, in the AHP, the consistency test of the judgment matrix is complicated and requires multiple adjustments, and most of the existing evaluation models lack quantitative indicators of evaluation factors to analyze the risk of water inrush and hazards [19]. Therefore, it is necessary to introduce evaluation indexes of the water inrush disaster types into the prediction model in order to establish a quantitative and qualitative water inrush prediction method.

Water inrush and mud inrush and their early warning system focusing on risk assessment and advanced prediction have been extensively researched. At present, advanced prediction methods of tunnels, such as tunnel seismic prediction (TSP), tunnel reflection tomography (TRT), ground penetrating radar (GPR) detection, infrared water detection, and advanced borehole detection, can determine different response characteristics with respect to the groundwater according to the specific characteristics of each detection method, and a follow-up dynamic prediction method is adopted to predict the location of water inrush disaster in the tunnel. For example, to prevent unforeseen unfavorable geological conditions, it is necessary to investigate the geological and hydrogeological conditions in front of tunnel excavation faces in the construction stage [20]. According to the properties of seismic waves, TSP is used as a long distance prediction method, and for this method, explosives are used as the seismic source to identify anomalies related to geological structures and aquifers [21–23]. Yamamoto et al. [24] developed a three-dimensional reflector tracking system, namely, TRT, which can detect the geological conditions at 100–150 m in front of the tunnel face. For the improvement of detection and interpretation, ground penetrating radar is used as a short-term prediction method [25, 26]. With the interpretation of GPR images, abundant useful information can be extracted for describing and distinguishing groundwater and its specific location [27]. Corbeau et al. [28] used GPR attributes to predict 3D fluid permeability and mudstone distribution in east-central Utah. GPR attributes have also been studied in the geological exploration of karst tunnels [27]. Advance drilling can detect the softness and hardness of formation rock, the integrity of rock mass, and the distribution location of possible faults and water inrush, through the analysis of the propulsion rate, rotation speed, and exposed lithology [29]. However, because the relationship between the interpretation standard of advanced prediction methods and geological structure is nonlinear, widespread uncertainty and multiple results exist in the interpretation of geological advanced prediction [30, 31]. Therefore, it is necessary to deeply understand the response characteristics of various advanced prediction methods for groundwater, establish a dynamic risk assessment system, and predict the risk of water inrush disaster in the construction process.

In this study, we established a static-dynamic risk assessment method to predict water inrush hazards taking

the Micangshan tunnel as the research object. First, the types of water inrush disasters were classified based on engineering geological and hydrogeological conditions. According to the analytic hierarchy process and the scoring method, a quantitative and qualitative static evaluation method was established to quantify the risk of water inrush hazard, thereby providing a basis for the design stage. Second, according to the static evaluation method, three dynamic prediction methods corresponding to the water inrush disaster in the construction process were established. Finally, the reliability and applicability of the method were verified with an example for the tunnel water inrush disaster prediction, prevention, and control to provide reference.

## 2. Engineering Profile

*2.1. Site and Geology.* The Micangshan tunnel connects the Shanxi Province with the Sichuan Province as shown in Figure 1. It is a separated deep-buried super-long twin tunnel and is a major engineering structure in the Taoba Expressway. Its beginning-ending mileage is K39 + 733–K53 + 527; it is 13.8 km long and has the maximum buried depth of approximately 1055 m. The tunnel entrance is located in the Nanzheng County of Hanzhong City, Shaanxi Province. The distribution of precipitation in this area is uneven, mainly concentrated from July to September, accounting for 53% of the whole year, with an average annual precipitation of 920 mm. The exit of the tunnel is located in the Nanjiang County of Bazhong City, Sichuan Province. This area has abundant precipitation, with an average precipitation of 1828 mm for many years. The surface water body in the geological area of the tunnel is well developed, with most of the gullies developing into tree shape and most of the smaller gullies having only seasonal water. The groundwater in the tunnel area is mainly divided into clastic rock fissure water, karst fissure water, and bedrock fissure water.

*2.2. Geological Structure.* The geological structure of the Micangshan tunnel is shown in Figure 2. Based on the borehole Z1–Z4 data, the lithology mainly comprises argillaceous siltstone, argillaceous limestone, dolomite, and quartz diorite. This well-developed structure consists of two syncline structures, i.e., Xiaoba and Neutron Mountain, and one anticline structure, i.e., Daba, as well as six fault fracture zones (F1–F6). Based on the borehole Z1 data, the axial strata of the Xiaoba syncline structures are severely crumpled, having the characteristics of karst. According to the exposure of borehole Z4, the Daba anticline structure is located in the concave valley, and the rock masses at its two wings and core are magmatic rocks with massive structure. The limestone section belongs to the regional karst section, with weak to medium karst development, relatively well-developed fissures, abundant water content, and high water head that bears high pressure. There are surface karst caves, shafts, and funnels in some sections.

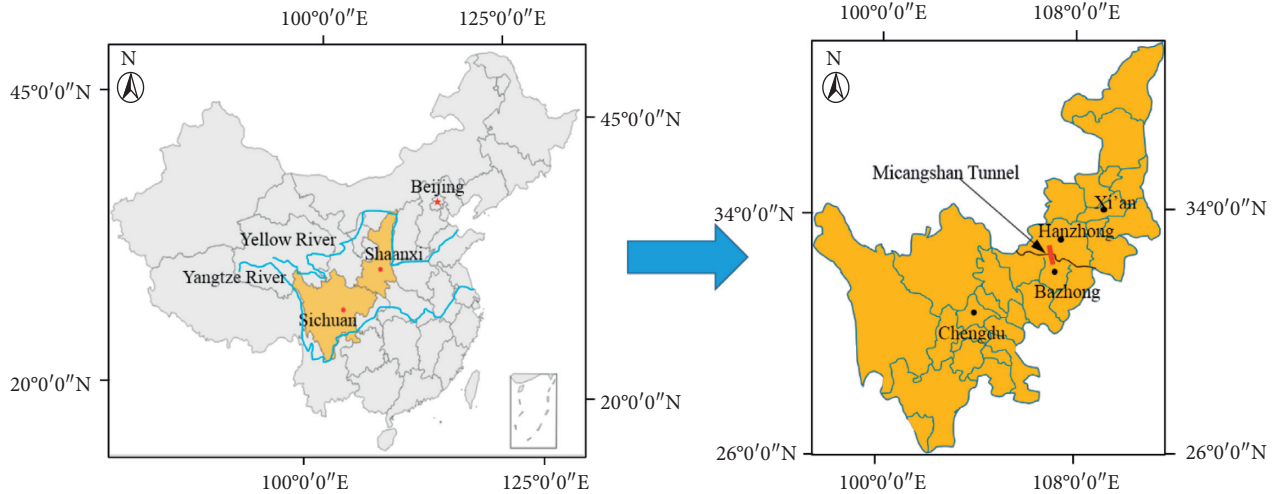


FIGURE 1: Location of the Micangshan tunnel.

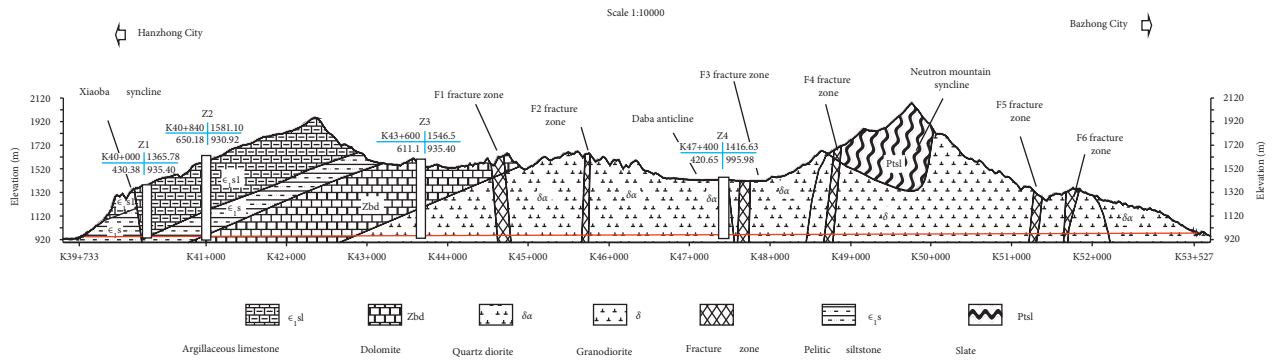


FIGURE 2: Overview of the geological structure of the Micangshan tunnel.

There is a joint dense zone in the position of the rock contact zone, syncline structure, and fault fracture zone. Tectonics and waterproofing effect make the soluble rocks in the region beneficial to the recharging of groundwater and the dissolution of soluble rock components, resulting in a strong degree of karst development and various dissolution forms in this area.

**2.3. Prediction of Types of Water Inrush.** The water inrush of the tunnel involves three aspects: the disaster source, water inrush channel, and antioutburst structure. The disaster source is the most important source of power and material basis for the water inrush. The possibility and states of water inrush in the Micangshan tunnel are predicted according to its underlying geological and hydrogeological conditions. Four main types of water inrush are identified: water inrush in water-bearing cracks, fault fracture zones, karst pipelines, and karst caves [32, 33].

**2.3.1. Water Inrush in Water-Bearing Cracks.** As shown in Figure 3, when excavating in rock strata with poor permeability, the stress around the surrounding rock constantly changes because the disturbance caused by tunnel excavation destroys the original seepage balance system.

Under the combined action of high groundwater pressure head and surrounding rock stress, the groundwater weakens the fractured rock mass and forms water wedges in it. When the groundwater pressure in the fracture plane exceeds the ultimate strength of the fracture expansion in the rock mass, the water-bearing fracture may expand and split gradually [32, 33]. The scouring and enlarging effect of groundwater will expand the water inrush channel continuously, which leads to the groundwater directly gushing into the tunnel or infiltrating into the tunnel from the cracks, forming a water gushing channel and causing the water inrush phenomenon.

**2.3.2. Water Inrush in Fault Fracture Zones.** As shown in Figure 4, the special tectonic action of the fault leads to the formation of a large number of fracture zones in the rock mass, and most of the fillers in the fault zone are angular and of different sizes. Because the water permeability of the fault fracture zone is higher than that of the aquifer rock mass, strong tangential stress and circumferential stress may appear in the fault fracture zone, leading to the relaxation of the original fault zone, further expansion of the original fracture, and even formation of new cracks. At the same time, groundwater can collect between two rock masses in the

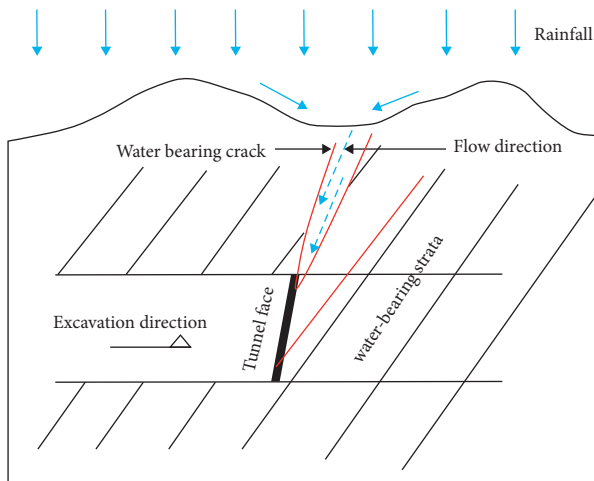


FIGURE 3: Diagram of water inrush in a water-bearing crack.

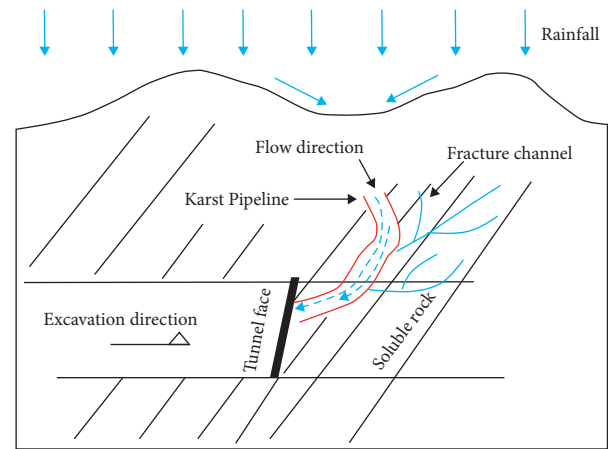


FIGURE 5: Diagram of water inrush in a karst pipeline.

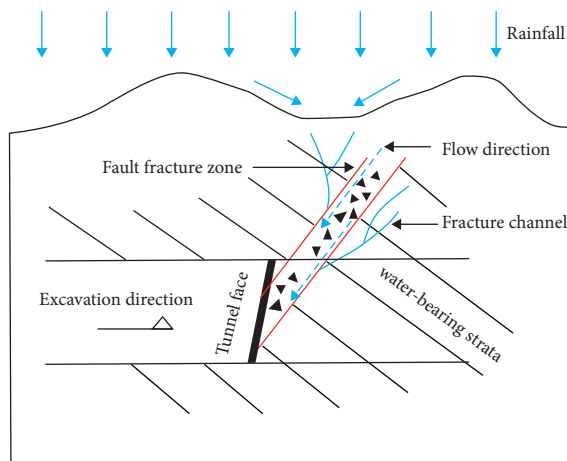


FIGURE 4: Diagram of water inrush in a fault fracture zone.

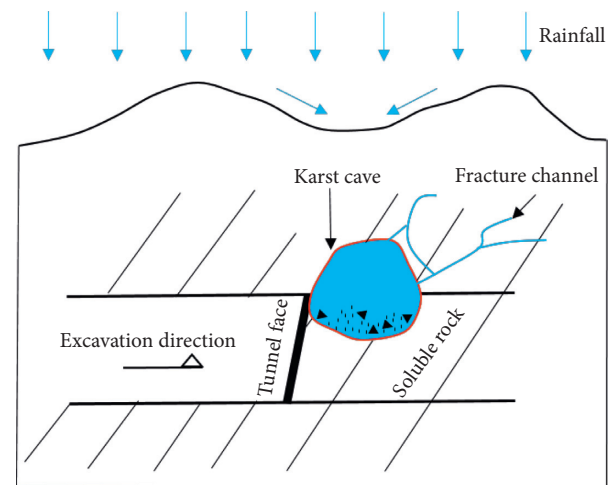


FIGURE 6: Diagram of water inrush in a karst cave.

faults, providing space and channels for the storage and migration of groundwater. When tunnel excavation is performed at such faults, the amount of water gushing may be considerably large [32, 33].

**2.3.3. Water Inrush in Karst Pipelines.** As shown in Figure 5, the topographical and lithological effects cause low-lying areas to easily form basins and become recharge areas of karst groundwater. Owing to the long-term action of surface water or groundwater, the rock is eroded, and the presence of water-bearing pipes with good connectivity, strongly permeable water-bearing strata, fissures, or other water-bearing structures with good permeability in the surrounding rock results in the formation of karst pipelines [32, 33]. The excavation of the tunnel in the areas with karst pipelines directly reveals the water-bearing structure in the surrounding rock, which leads to the water inrush phenomenon in the tunnel.

**2.3.4. Water Inrush in Karst Caves.** As shown in Figure 6, due to geological tectonics, the fissures and interlayer sliding spaces formed in the soluble rock strata create the original

space for the formation and expansion of karst caves. Under the action of chemical dissolution for a long time, the groundwater carries sediment, debris, and other materials into the karst cave through the fracture channel, forming a filling medium in the karst cave, together with the source rock, gravel, breccia, and other materials. During the construction of the tunnel, the karst caves are disturbed and they directly push over the waterproof layer; when they reach the critical state, because of the strong water pressure, the previously deposited materials are flushed out, forming a geological hazard of water and mud inrush into the tunnel [32, 33].

### 3. Scoring Method and Analysis of Static Water Inrush Disasters

A static water inrush disaster assessment model is a risk assessment system of the water inrush phenomenon based on the AHP and the scoring method. First, the evaluation indexes affecting the water inrush risk are determined. Based on the AHP, each evaluation index is further

divided into several evaluation factors, and the weight of each index is determined. Second, the disaster risk value is associated with the quantitative score of each evaluation index by a certain method, and the quantitative value that can accurately reflect the characteristics of environmental factors is input. According to the scoring method, the effect of the quantitative standard of each basic evaluation index or evaluation factor on the development of things is scored. Finally, a numerical model is established using the reverse-order superposition method, and the actual analysis is combined with it to determine the final judgment.

**3.1. AHP Analysis Method.** The AHP, which was recommended by Saaty [34], is a hierarchical weighting multi-objective comprehensive evaluation decision analysis method based on the network system theory. This combined quantitative-qualitative analysis is used for multiobjective decision-making and evaluation for complex problems. It involves the following major steps.

*Step 1.* Establish AHP structure model.

In this step, the overall goal is established, the decision-making problem is decomposed in detail, hierarchical and organized characteristics are formed, and a multilevel gradient structure model is developed. In the developed model, the elements are divided into the top, middle, and lower layers according to their attributes and interrelationships. The elements of the upper layer are composed of the elements of the lower layer, and they play a dominant role in determining the relevant elements of the subsequent layer. A linear series connection is adopted to build a hierarchical level of characteristics.

*Step 2.* Establish the comparative judgment matrix.

In this step, a certain factor  $U$  is considered the standard of the judgment matrix, based on which the factors of the lower layer are compared, and the  $n$ -order judgment matrix is obtained as shown in the following equation:

$$U = \begin{bmatrix} a_{11} & a_{12} & \cdots & a_{1n} \\ a_{21} & a_{22} & \cdots & a_{2n} \\ \cdots & \cdots & \cdots & \cdots \\ a_{n1} & a_{n2} & \cdots & a_{nn} \end{bmatrix}, \quad (1)$$

where  $a_{ij} = 1/a_{ji}$  ( $i \neq j$ ),  $a_{ii} = 1$  ( $i = j$ ).

Suppose there are  $n$  factors ( $U_1, U_2, \dots, U_n$ ) in the same layer; then all the factors are compared in pairs; for example,  $U_i$  is compared with  $U_j$  and the relative importance is evaluated on a scale of 1–9; the implications of the scales are shown in Table 1.

*Step 3.* Calculate the relative weights of elements following the single criterion and its consistency check.

According to the judgment matrix, the eigenvector corresponding to the maximum eigenvalue of  $Z$  is obtained by using linear algebra. The eigenvector obtained is the order

of importance of each evaluation factor, and then the normalized factors give the weight distribution. In this paper, the approximate solution technique of the sum-product method is adopted.

- (1) Each column is normalized by the judgment matrix, as shown in the following equation:

$$\bar{u}_{ij} = \frac{u_{ij}}{\sum_{k=1}^m u_{kj}}, \quad ij = 1, 2, \dots, m. \quad (2)$$

- (2) Each column of the normalized judgment matrix is added by row, as shown in the following equation:

$$\bar{W}_i = \sum_{i=1}^m \bar{u}_{ij}, \quad ij = 1, 2, \dots, m. \quad (3)$$

- (3) As shown in equation (4), the vector  $\bar{W} = (\bar{W}_1, \bar{W}_2, \dots, \bar{W}_m)^T$  is normalized:

$$a_i = \frac{\bar{W}_i}{\sum_{j=1}^m \bar{W}_j}, \quad ij = 1, 2, \dots, m, \quad (4)$$

$A = (a_1, a_2, a_1)$  obtained in turn is the eigenvector.

- (4) As shown in equation (5), the maximum eigenvalue  $\lambda_{\max}$  is calculated:

$$\lambda_{\max} = \frac{1}{m} \sum_{i=1}^m \frac{(TA)_i}{a_i}. \quad (5)$$

- (5) Consistency judgment: to verify whether the judgment matrix results have satisfactory consistency, the value of consistency ratio (CR) is used for judgment, as shown in the following equation:

$$\text{CR} = \frac{\text{CI}}{\text{RI}}, \quad (6)$$

$$\text{CI} = \frac{\lambda_{\max} - n}{n - 1},$$

where CI is the consistency indicator; RI is the random index determined by the number of evaluation factors in the judgment matrix (Table 2);  $\lambda_{\max}$  is the maximum eigenvalue of the judgment matrix; and  $n$  is the number of indicators. When  $\text{CR} < 0.1$ , the measures of the consistency levels of the judgment matrix-based results are satisfactory, which signifies that the weight distributions are reasonable and reliable. Otherwise, the matrix must be restructured until the consistency is satisfied.

*Step 4.* Calculate the element relative weights following the total criterion and its consistency check.

With the hierarchical ranking, the weight of each influencing factor relative to the overall goal is calculated, generally by using the top-down method. Subsequently, the consistency of the final synthesized results is checked to judge the overall consistency.

TABLE 1: Meaning of 1–9 scales.

Scale	Meaning
1	$i$ has the same importance, or $i$ or $j$ compares to itself
3	$i$ is slightly more important than $j$
5	$i$ is obviously more important than $j$
7	$i$ is much more important than $j$
9	$i$ is extraordinarily more important than $j$
2, 4, 6, 8	Scales between two consecutive scales given above
Reciprocal	Contrast to the above condition, namely, $j$ is more important than $i$

TABLE 2: Values of RI.

$N$	1	2	3	4	5	6	7	8	9
RI	0	0	0.58	0.94	1.12	1.24	1.32	1.41	1.45

3.2. *The Scoring Method.* The scoring method is used to calculate the comprehensive evaluation score of water inrush and determine the risk level of water inrush. First, the factors that affect the development of things are decomposed into a number of evaluation indexes ( $U_1, U_2, \dots, U_n$ ). Second, each evaluation index is divided into several basic evaluation factors ( $C_1, C_2, \dots, C_n$ ), and the scores of the impact of each basic evaluation index or evaluation factor on the development of things are determined according to the quantitative criteria. Finally, the risk value of the water inrush is obtained with the reverse-order superposition method, which is a linear combination relationship; the final evaluation is performed in combination with the actual analysis. The specific methods of the reverse-order superposition method are given by equations (7) and (8):

$$\text{TRV} = \sum_{n=1}^{\infty} W_{un} * f(U_n), \quad (7)$$

$$f(U_n) = \sum_{n=1}^{\infty} W_{cn} * f(C_n), \quad (8)$$

where the risk value of the water inrush (i.e., TRV) is the comprehensive evaluation index of the water inrush phenomenon; the higher the TRV value, the greater the possibility of water inrush in the tunnel;  $U_n$  is the quantitative score of each evaluation index;  $W_{un}$  is the weight of each evaluation index;  $C_n$  is the quantitative score of the basic evaluation factors;  $W_{cn}$  is the weight of each basic evaluation factor.

3.3. *Model Analysis.* More than 100 cases of water inrush in tunnels in China have been systematically summarized and analyzed mainly based on the variation characteristics and occurrence conditions of water inrush in the tunnel [16, 35–38]. The tunnel water inrush disaster is caused by the effect of tunneling engineering and its interaction with the groundwater environment. Formation lithology is the basis of groundwater storage. The level of the surrounding rock and the lithology of the stratum in which it is located are different. Topography conditions play an important role in groundwater recharge, runoff, and discharge and serve as an

important factor affecting the alternation of the groundwater cycle. Geological structure conditions are the dominant factor controlling the direction of groundwater burial, distribution, and movement. Because the location of the tunnel section in the geological structure varies, the stratigraphic production and catchment area in the tunnel sections also significantly vary. The length and burial depth of the tunnel are external factors affecting the formation of the disaster; the longer the tunnel extends in the construction process, the more hydrogeological units and rock layers it traverses; the deeper the tunnel, the larger the catchment area, runoff, and recharge area of the tunnel site. Karst development is an intrinsic factor affecting the water inrush phenomenon.

In this paper, a static water inrush disaster evaluation model of the Micangshan tunnel is established taking into consideration the engineering geological conditions, tunnel section characteristics, and hydrogeological conditions of the tunnel, as well as the statistical analysis of the type of water inrush development. These characteristics are mainly classified as formation lithology ( $U_1$ ), topography conditions ( $U_2$ ), geological structure conditions ( $U_3$ ), tunnel length and buried depth ( $U_4$ ), and karst development ( $U_5$ ). These are further divided into five evaluation indicators and 12 evaluation factors ( $C_1, C_2, C_3, C_4, C_5, C_6, C_7, C_8, C_9, C_{10}, C_{11}, C_{12}$ ). The AHP hierarchical structure model of the water inrush disaster is shown in Figure 7. The level of water inrush disaster is divided into five types, namely, very low risk (risk level I), low risk (risk level II), medium risk (risk level III), high risk (risk level IV), and extremely high risk (risk level V).

Experts' judgment questionnaire is a key point of AHP. There are two approaches to do experts questionnaire: (1) one is the pairwise comparison, proposed by Saaty [34], improved by Li et al. [39]; (2) another method to do questionnaire is to use table comparison proposed by Lyu et al. [40]. The paper used the second method to conduct the questionnaire, which can not only get the appropriate experts' reply but also determine the fuzzy number based on experts' replies. The authors selected six experienced experts with expertise in hydrogeological geological and tunnel engineering to assess the water inrush risk of Micangshan tunnel.

As shown in Tables 3–8, the judgment matrix of the index layer can be calculated. The largest eigenvalue ( $\lambda_{\max}$ ) of the judgment matrix can be calculated by equation (5), and the CR can be calculated and verified by equation (6). The other judgment matrices of the subindex layer to the index

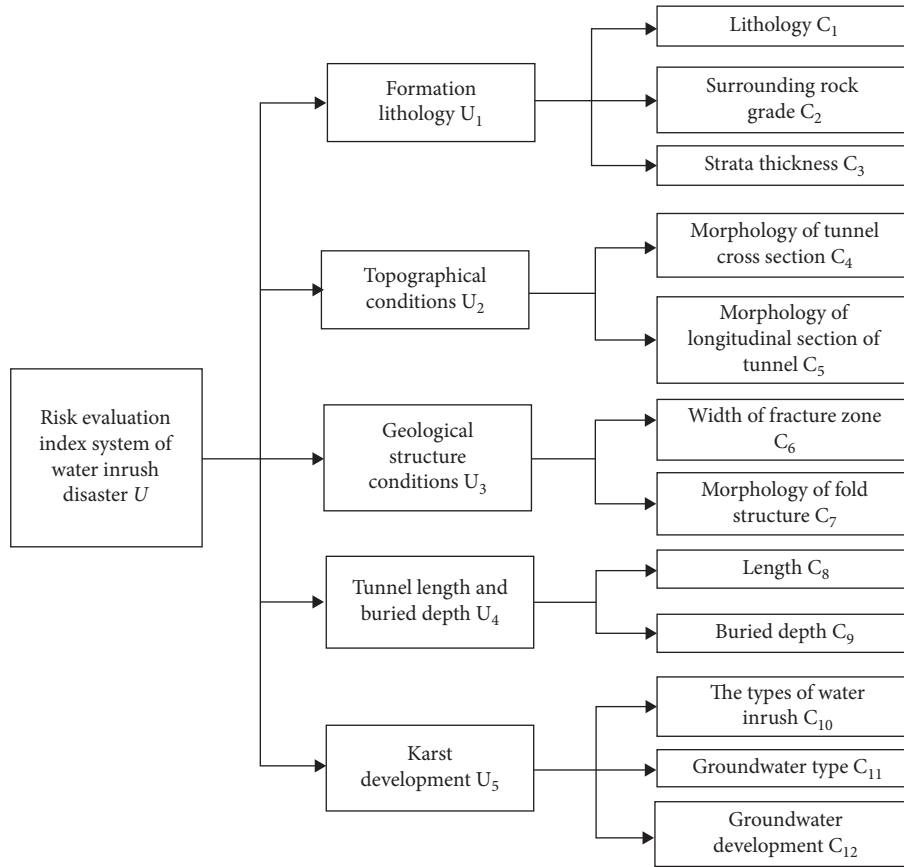


FIGURE 7: AHP structure model of inrush water intensity.

TABLE 3: Primary index judgment matrix in  $U$ .

	$U_1$	$U_2$	$U_3$	$U_4$	$U_5$
$U_1$	1	7	3	9	5
$U_2$	1/7	1	1/5	3	1/3
$U_3$	1/3	5	1	7	5
$U_4$	1/9	1/3	1/7	1	1/5
$U_5$	1/5	3	1/5	5	1

layer can also be obtained. In addition, the weight of each judgment matrix can be calculated using the aforementioned method. As shown in Tables 9 and 10, the weight values of the primary and secondary evaluation indexes in this level are calculated separately, and the rationality of the CR is calculated and verified. The CR is less than 0.1, which indicates that the judgment matrix is consistent.

According to the degree and range of disaster causing factors in the evaluation index, the quantitative value of disaster causing factors is determined (see Table 11) [41–43]. At least five tunnel engineering experts are selected for scoring based on the field geological and hydrogeological conditions. The average score of each evaluation index is calculated based on the scores of all the experts, which can improve the accuracy of the final score of each index. Using equations (7) and (8) and the determined weights of the evaluation indexes, the risk value of the water inrush (TRV) is calculated using the scoring method as follows:

$$TRV = 5 * (0.5 * U_1 + 0.06 * U_2 + 0.29 * U_3 + 0.03 * U_4 + 0.12 * U_5),$$

$$\begin{cases} U_1 = 0.63C_1 + 0.11C_2 + 0.26C_3, \\ U_2 = 0.83C_4 + 0.17C_5, \\ U_3 = 0.25C_6 + 0.75C_7, \\ U_4 = 0.5C_8 + 0.5C_9, \\ U_5 = 0.65C_{10} + 0.07C_{11} + 0.28C_{12}. \end{cases} \quad (9)$$

The maximum score of  $U_n$  is 20. This score must be increased by five times to meet the target TRV value of 100. According to the THR value, the risk grade can be divided into five grades; the higher the score, the higher the level of risk of the disaster, as shown in Table 12.

#### 4. Method of Dynamic Risk Prediction of Water Inrush Phenomenon

The dynamic prediction of the water inrush phenomenon is based on the risk grade of static water inrush, and the advance prediction method is used to determine and analyze the location of the water inrush position in the construction stage. The dynamic prediction of the tunnel water inrush disaster is realized through an integrated advanced prediction method that combines the long distance (e.g., TSP, TRT) and short distance (e.g., GPR, TEM, infrared water detection method, advanced drilling) prediction methods.

TABLE 4: Secondary index judgment matrix in  $U_1$ .

	$C_1$	$C_2$	$C_3$
$C_1$	1	5	3
$C_2$	1/5	1	1/3
$C_3$	1/3	3	1

TABLE 5: Secondary index judgment matrix in  $U_2$ .

	$C_4$	$C_5$
$C_4$	1	5
$C_5$	1/5	1

TABLE 6: Secondary index judgment matrix in  $U_3$ .

	$C_6$	$C_7$
$C_6$	1	1/3
$C_7$	3	1

TABLE 7: Secondary index judgment matrix in  $U_4$ .

	$C_8$	$C_9$
$C_8$	1	1
$C_9$	1	1

TABLE 8: Secondary index judgment matrix in  $U_5$ .

	$C_{10}$	$C_{11}$	$C_{12}$
$C_{10}$	1	7	3
$C_{11}$	1/7	1	1/5
$C_{12}$	1/3	5	1

TABLE 9: Calculation results of hierarchical single sorting.

Sorting layer	$W$			$\lambda_{\max}$	CI	RI	CR		
V-U	0.50	0.06	0.29	0.03	0.12	5.3537	0.0884	1.12	0.079
$U_1$ -C	0.63	0.11	0.26			3.0385	0.01925	0.58	0.033
$U_2$ -C	0.83	0.17				2	0	0	0
$U_3$ -C	0.25	0.75				2	0	0	0
$U_4$ -C	0.50	0.5				2	0	0	0
$U_5$ -C	0.65	0.07	0.28			3.065	0.0325	0.58	0.056

TABLE 10: Hierarchical total sorting weights.

$U$ -C	$U_1$	$U_2$	$U_3$	$U_4$	$U_5$	Total sorting weight
V-U	0.50	0.06	0.29	0.03	0.12	
$C_1$	0.63	0	0	0	0	0.32
$C_2$	0.11	0	0	0	0	0.05
$C_3$	0.26	0	0	0	0	0.13
$C_4$	0	0.83	0	0	0	0.05
$C_5$	0	0.17	0	0	0	0.01
$C_6$	0	0	0.25	0	0	0.073
$C_7$	0	0	0.75	0	0	0.217
$C_8$	0	0	0	0.50	0	0.015
$C_9$	0	0	0	0.50	0	0.015
$C_{10}$	0	0	0	0	0.65	0.078
$C_{11}$	0	0	0	0	0.07	0.008
$C_{12}$	0	0	0	0	0.28	0.034

Note. CI=0.0139, RI=0.3596, and CR=0.038.



TABLE 11: Risk grade system evaluation of the water inrush disaster index.

First-grade evaluation index	Second-grade evaluation index	Quantitative value of disaster causing factors				
U <sub>1</sub>	C <sub>1</sub>	No fissure hard rock	Mudstone, sandstone, shale	Argillaceous siltstone, sandy mudstone, shale	Dolomite, argillaceous limestone, and other soluble rocks	Dolomitic limestone, dolomite,
	Score	0-4	4-8	8-12	12-16	16-20
	C <sub>2</sub>	I, II	III	IV	V	VI
	Score	0-4	4-8	8-12	12-16	16-20
U <sub>2</sub>	C <sub>3</sub> (cm)	Thick layer	Middle-thick layer	Middle layer	Thin layer	Unconsolidated layers
	Score	0-8	8-12	12-15	15-18	18-20
U <sub>2</sub>	C <sub>4</sub>	Convex type	Flat type	Single slope type	Parallel type below the side of the valley	Parallel type below the valley
	Score	0-8	8-12	8-12	15-18	18-20
	C <sub>5</sub>	Convex type	Flat type	Mixed type	Depression type	River crossing type
U <sub>3</sub>	Score	0-6	6-10	10-14	14-17	17-20
	C <sub>6</sub> (m)	< 1.5	1.5-3	3-5 or contact surfaces of different rock	5-8	> 8
	Score	0-6	6-10	10-14	14-17	17-20
	C <sub>7</sub>	Other parts of fold structure	Wing of the gently dipping fold structure	Wing of the steep fold structure	Core of the gently dipping fold structure	Core of the steep fold structure
U <sub>4</sub>	Score	0-3	3-6	6-10	10-15	15-20
	C <sub>8</sub> (m)	< 200	200-500	500-1000	1000-1500	> 1500
	Score	0-2	2-6	6-14	14-16	16-20
	C <sub>9</sub> (m)	< 100	100-300	300-500	500-700	> 700
U <sub>5</sub>	Score	14-20	10-14	6-10	4-6	0-4
	C <sub>10</sub>	No water inrush	Water inrush in water-bearing crack	Water inrush in fault fracture zone	Water inrush in karst pipeline	Water inrush in karst cave
	Score	0-4	4-12	12-16	16-18	18-20
	C <sub>11</sub>	Bedrock fissure water	Clastic rock fissure water	Clastic rock fissure water, bedrock fissure water	Karst fissure water, clastic rock fissure water	Karst fissure water, clastic rock fissure water, bedrock fissure water
U <sub>5</sub>	Score	0-6	6-10	10-14	14-17	17-20
	C <sub>12</sub>	Dry	Humid	Dripping	Rainy	Downpour, local inrush water
	Score	0-2	2-8	8-12	12-16	16-20

TABLE 12: Risk value assessment of water inrush disaster.

Value of TRV	0-20	20-40	40-50	50-70	>70
Risk level	I (very low risk)	II (low risk)	III (medium risk)	IV (high risk)	V (extremely high risk)

TABLE 13: Conventional advanced geological forecast methods and characteristics.

Category	Method	Distance (m)	Analysis of the characteristics of groundwater detection	Advantage
Geological analysis method	Geological analysis of tunnel face	—	According to the situation of the tunnel face, the water outlet location and flow rate are recorded	Accurate observation of the location and volume of the effluent
	Advanced drilling	10-20	To judge whether there is a water-bearing body in front of the tunnel face by observing whether the borehole is out of water and determining the amount of water flowing out of it	Accurate observation of the water output and water pressure

TABLE 13: Continued.

Category	Method	Distance (m)	Analysis of the characteristics of groundwater detection	Advantage
Seismic wave method	Tunnel seismic prediction (TSP)	100–150	In the reflection layer, the shear wave velocity ( $V_s$ ) tends to decrease, the ratio of longitudinal wave velocity to shear wave velocity ( $V_s/V_p$ ) increases, or Poisson's ratio suddenly increases	Accurate recognition and location of anomalous geological bodies in front of the tunnel face (such as faults, underground rivers, and caves)
	Tunnel reflection tomography (TRT)	100–150		Properties, size, and 3D holographic imaging of faults, fractured zones, karst caves, underground rivers, and other anomalous geological bodies in front of the tunnel face
Electromagnetic method	Ground penetrating radar (GPR)	15–30	Frequency of electromagnetic wave decreases, resulting in multiple strong reflection interfaces, scattering, and diffraction, resulting in cluttered reflection waveforms	Sensitive to fracture zone, lithology, and water-bearing state changes
	Transient electromagnetic method (TEM)	50–80	The resistivity of surrounding rock is obviously lower than that of surrounding rock	Sensitive to low resistor fracture zones filled with water
Other methods	Infrared water detection method	20–30	The detection instrument shows that the curve has a sudden change	Sensitive to water-bearing rock

TABLE 14: Dynamic risk prediction method of water inrush in tunnel.

Dynamic prediction method	Primary dynamic prediction	Secondary dynamic prediction	Tertiary dynamic prediction
Risk level	I (extremely low-risk area)    II (low-risk area)	III (moderate-risk area)	IV (high-risk area)    V (extremely high-risk area)
Dynamic risk prediction methods	Geological analysis of the tunnel face; TSP or TRT detection	Geological analysis of the tunnel face; TSP or TRT detection; GPR or TEM or infrared water detection method	Geological analysis of the tunnel face; TSP or TRT detection; GPR or TEM or infrared water detection method; advanced drilling

The long distance means that the predicted distance from the tunnel face is about 100 m, and the short distance means that the predicted distance from the tunnel face is about 30 m. According to the characteristics of each advance prediction method, the diversity of solutions can be reduced and the reliability of detection results can be improved.

#### 4.1. Advanced Prediction Method of the Tunnel.

Conventional prediction methods are geological analysis methods (e.g., palm-top geological analysis, advanced drilling), seismic wave methods (e.g., TSP, TRT), electromagnetic methods (e.g., GPR, TEM), and other methods (e.g., infrared water detection method). Each detection method is based on the difference in some properties of the geological medium (such as elasticity, resistivity, and wave velocity). Owing to the limitations and constraints of factors such as the complexity of geological conditions in the crossing area of long and deep-buried tunnels and the multiple solutions of geophysical methods, each advanced prediction method has its own advantages and limitations (see, for example, Table 13). Using only a single advanced prediction method, it is difficult to accurately detect the geological conditions in front of the tunnel. In particular, under the complex geological and hydrogeological conditions such as those in the

Micangshan tunnel, it is more important to determine a scientific, effective, and accurate advance geological prediction method [44, 45].

4.2. *Dynamic Prediction Method.* According to the static evaluation results of water inrush risk in different sections of Micangshan tunnel, the risk levels of different water inrush disasters are determined. Then, the dynamic water inrush disaster prediction method is adopted, with different advanced prediction methods for different risk levels of water inrush disasters to predict the position of water inrush disasters in the construction process. Therefore, three dynamic water inrush prediction methods are divided, namely, primary dynamic prediction, secondary dynamic prediction, and terminal dynamic prediction (Table 14). Based on this, a comprehensive advanced geological prediction system suitable for tunnel engineering is constructed, and the process of dynamic prediction is formed.

## 5. Model Verification

The buried depth of the K41 + 440–K43 + 080 mileage section of the Micangshan tunnel is 751 m, the lithology mainly comprises dolomite, and the rock is formed in the middle

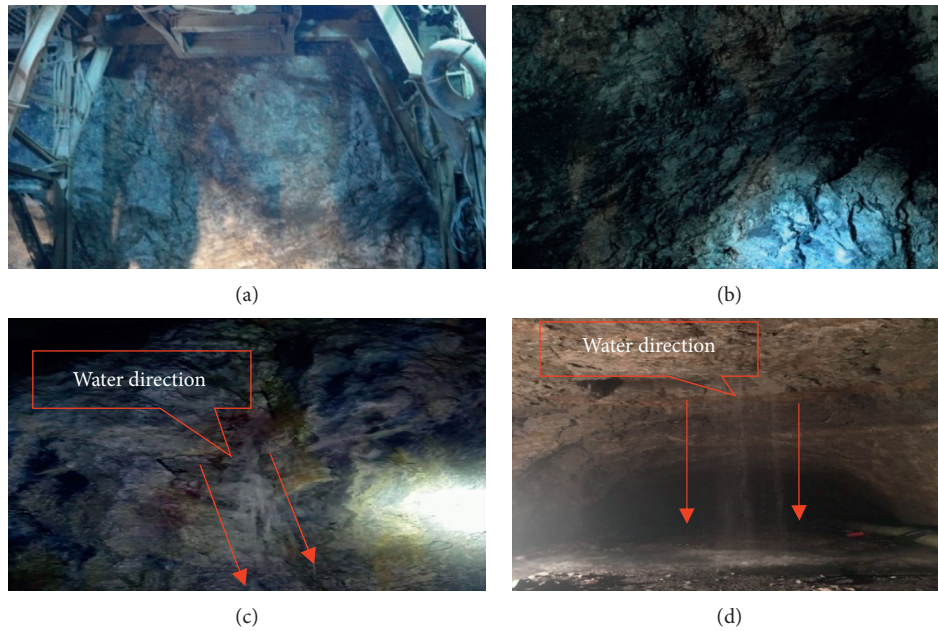


FIGURE 8: Geological analysis of the tunnel face. (a) Overall drawing of the tunnel face. (b) Right side of the tunnel face. (c) Water gushing from cracks on the left side of the tunnel face. (d) Water pouring downward from the crown.

layer. The sectional view indicates that it is a parallel type below the valley, and the groundwater is karst fissure water, with local water inrush, occurring in water-bearing cracks. The face of the tunnel excavated in the K42 + 480 section is shown in Figure 8. The surrounding rock is mainly dolomite, and the bedding plane is slightly bent and partially broken because of tectonic movement. The joints in the tunnel face are nonuniformly distributed, the source of the vault is rain, and water gushes from the cracks on the left side of the face of the tunnel. According to the specifications for design of highway tunnels, the surrounding rock is of level V. The quantitative and qualitative analysis of the static evaluation model provides a TRV value of 75, implying that this tunnel area has grade-V risk. As shown in Table 14, tertiary dynamic prediction is adopted in the area, including geological analysis of the tunnel face analysis, TSP detection, the GPR water detection method, and advanced drilling.

In the TSP method, seismic waves are generated by an artificially excited source and propagated in front of the tunnel along the tunnel axis. When unfavorable geological bodies (such as karst caves or fissures) are encountered in front of the tunnel face, the waves are reflected, which are received by highly sensitive sensors. According to the reflection time, propagation speed, and waveform of the reflected waves, different data characteristics are processed by TSPwin Light software to predict the location of the unfavorable geological bodies. As shown in Figure 9(a), the physical and mechanical parameter results obtained by TSP for the K42 + 510–K42 + 540 section clearly show that the velocities of both P and S waves decrease and the waveforms are abnormal. The ratio of P to S waves increases, while the elastic modulus and density decrease. The reflection layer produced by TSP in the corresponding section indicates the significant enhancement of the negative reflection region

(Figure 9(b)). The prediction results obtained by TSP for the K42 + 510–K42 + 540 section clearly indicate that there is considerable fracture development and a large amount of water content in this section.

In the GPR method, the distribution law of rock mass media is determined by transmitting pulsed electromagnetic waves in a certain frequency range. Through the comprehensive analysis and processing of radar data and complex meteorological elements, various characteristic parameters of disaster sources can be obtained, and adverse geological structures such as caves and faults in tunnels can be detected. According to the key water inrush areas predicted by the TSP method, SIR3000 GPR is used to detect geological structures in the K42 + 510–K42 + 540 section. Two measuring lines are used for measurement to ensure high detection accuracy. The radar is moved from left to right in uniform motion during implementation while avoiding the phenomena of disengaging, stagnation, and sudden drive as much as possible. The velocity and position of the two lines are consistent. The GPR interpretation results for the K42 + 510–K42 + 540 section show that the radar-reflected wave amplitude increases significantly and the strong reflection interface is clear (see Figure 10). This indicates broken rock mass in the cave section, likely containing voids and cavernous geological structures. The K42 + 492 section is mainly composed of medium dolomite, and advanced drilling is used in this section. The advanced drilling results indicate that the drilling speed increases to a large value and remains constant. Water gushes out from the pipe core, with a jet distance of approximately 1 m (Figure 11). This area has well-developed joints and fissures and high water pressure, and the groundwater gushes out through boreholes.

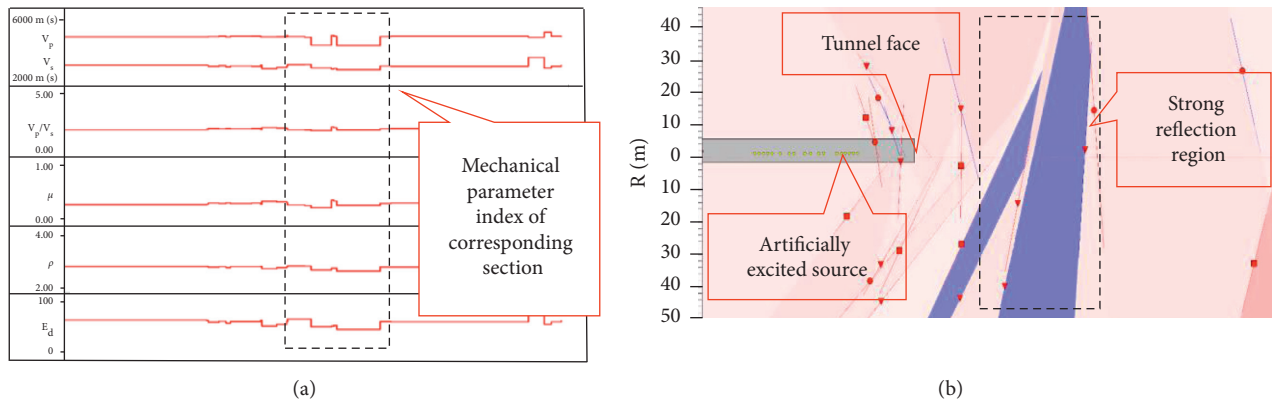


FIGURE 9: TSP advanced prediction interpretation. (a) TSP physical and mechanical parameters result map. (b) TSP reflective layer map.

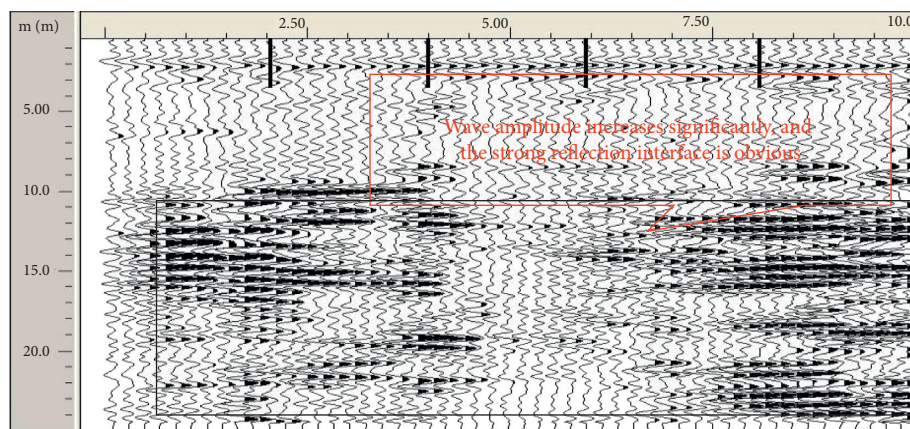


FIGURE 10: Ground penetrating radar interpretation map of the K42 + 510–K42 + 540 section.



FIGURE 11: Water gushing during advanced drilling.

When the tunnel is excavated to the K42 + 530 mileage section, the tunnel face mainly comprises dolomite, which is relatively weak and the cracks are developed as a whole. According to the static evaluation results of water inrush and the interpretation of the dynamic evaluation results, high risk of water inrush is considered highly likely to occur in this section. The surrounding rock is easy to deform after excavation and unloading, and the unloading fissure gradually expands to form a seepage or outburst channel for groundwater discharge. As shown in Figure 12, a large

amount of water gushes out of the boreholes and cracks, and water inrush continuously increases at approximately  $800 \text{ m}^3/\text{h}$  on average. As a result, the tunnel is flooded 60 m behind the work face. During advanced drilling, to release high-pressure water stored in the surrounding rock beforehand, emergency evacuation of workers and equipment was carried out and timely drainage measures were undertaken in the tunnel, avoiding any catastrophic water gushing accident. The static-dynamic water inrush risk assessment method realizes the accurate prediction of water inrush risk in karst tunnels. It



FIGURE 12: Photos of water gushing from actual excavation to K42 + 530.

would considerably reduce the possibility of water inrush and provide the design basis for the treatment.

## 6. Conclusions

- (1) Based on the geological and hydrogeological conditions of the Micangshan tunnel, four types of water inrush were identified: water inrush in water-bearing cracks, fault fracture zones, karst pipelines, and karst caves.
- (2) By considering the qualitative and quantitative factors, 5 first-level evaluation indexes and 12 second-level evaluation indexes were extracted, which form the tunnel water inrush risk assessment indexes. Based on these indexes, a static water inrush disaster risk assessment model was established. The risk of the water inrush disaster in terms of the TRV values was graded as I (very low risk), II (low risk), III (medium risk), IV (high risk), and V (extremely high risk). To accurately identify occurrence characteristics and the damage level of the water-bearing body, the sensitivity of the advanced prediction method to groundwater was summarized and analyzed, and the following three dynamic prediction methods were established: primary dynamic prediction, secondary dynamic prediction, and terminal dynamic prediction methods.
- (3) The excavation of the K42 + 510–K42 + 540 mileage section of the Micangshan tunnel was assessed using the static water inrush risk assessment method and was judged as high risk. Based on the dynamic evaluation model and using the terminal dynamic prediction method in the construction process, it can be inferred that rich fissure water develops before the tunnel face, and the connectivity between the tunnel face and groundwater is good. The accuracy of the static-dynamic water inrush disaster risk assessment and prediction method was verified and the rationality and applicability of the method were proved.

## Data Availability

The underlying data supporting the results of our study are unavailable.

## Conflicts of Interest

The authors declare that they have no conflicts of interest.

## Acknowledgments

This research was financially supported by the National Natural Science Foundation of China (nos. 41807255, 41772329, and U19A20111), the research fund of the State Key Laboratory of Geohazard Prevention and Geo-environment Protection Independent Research Project (SKLGP2020Z010), and Sichuan Science and Technology Project (no. 2019YJ0465).

## References

- [1] K. Suzuki, E. Nakata, M. Minami et al., “Estimation of the zone of excavation disturbance around tunnels, using resistivity and acoustic tomography,” *Exploration Geophysics*, vol. 35, no. 1, pp. 62–69, 2004.
- [2] M. Taromi, A. Eftekhari, J. K. Hamidi, and A. Aalianvari, “A discrepancy between observed and predicted NATM tunnel behaviors and updating: a case study of the Sabzkuh tunnel,” *Bulletin of Engineering Geology and the Environment*, vol. 76, no. 2, pp. 713–729, 2016.
- [3] A. Kaya, K. Karaman, and F. Bulut, “Geotechnical investigations and remediation design for failure of tunnel portal section: a case study in northern Turkey,” *Journal of Mountain Science*, vol. 14, no. 6, pp. 1140–1160, 2017.
- [4] D.-X. Liang, Z.-Q. Jiang, S.-Y. Zhu, Q. Sun, and Z.-W. Qian, “Experimental research on water inrush in tunnel construction,” *Natural Hazards*, vol. 81, no. 1, pp. 467–480, 2016.
- [5] D. Huang, Z. Liu, and W. Wang, “Evaluating the impact of coal mining on ordovician karst water through statistical methods,” *Water*, vol. 10, no. 10, pp. 1409–1425, 2018.
- [6] D. Mao, Z. Liu, W. Wang et al., “An application of hydraulic tomography to a deep coal mine: combining traditional pumping tests with water inrush incidents,” *Journal of Hydrology*, vol. 567, pp. 1–11, 2018.
- [7] Y.-H. Chen, S. Cheng, L.-P. Li, J.-y. Yang, H.-l. Liu, and W.-f. Tu, “Applicability analysis of microseismic technology in tunnel water inrush monitoring,” *KSCE Journal of Civil Engineering*, vol. 25, no. 7, pp. 2737–2747, 2021.
- [8] N. Dastanboo, X.-Q. Li, and H. Gharibdoost, “Investigation on the accuracy of ground penetrating radar in the tunnel based on improved analectic hierarchy process,” *International Nano Letters*, vol. 11, no. 1, pp. 69–83, 2021.

- [9] H.-M. Lyu, W.-J. Sun, S.-L. Shen, and A. Arulrajah, "Flood risk assessment in metro systems of mega-cities using a gis-based modeling approach," *The Science of the Total Environment*, vol. 626, pp. 1012–1025, 2018.
- [10] H.-M. Lyu, S.-L. Shen, A.-N. Zhou, and W.-H. Zhou, "Flood risk assessment of metro systems in a subsiding environment using the interval FAHP-FCA approach," *Sustainable Cities and Society*, vol. 50, Article ID 101682, 2019.
- [11] H.-M. Lyu, W.-H. Zhou, S.-L. Shen, and A.-N. Zhou, "Inundation risk assessment of metro system using AHP and TFN-AHP in Shenzhen," *Sustainable Cities and Society*, vol. 56, Article ID 102103, 2020.
- [12] H.-M. Lyu, S.-L. Shen, A. Zhou, and J. Yang, "Risk assessment of mega-city infrastructures related to land subsidence using improved trapezoidal FAHP," *The Science of the Total Environment*, vol. 717, Article ID 135310, 2020.
- [13] A.-T. Li and J.-W. Lin, "Constructing core competency indicators for clinical teachers in Taiwan: a qualitative analysis and an analytic hierarchy process," *BMC Medical Education*, vol. 14, no. 1, p. 75, 2014.
- [14] Y. Wang, W. Yang, M. Li, and X. Liu, "Risk assessment of floor water inrush in coal mines based on secondary fuzzy comprehensive evaluation," *International Journal of Rock Mechanics and Mining Sciences*, vol. 52, no. 6, pp. 50–55, 2012.
- [15] Y. Xue, Z. Li, S. Li et al., "Water inrush risk assessment for an undersea tunnel crossing a fault: an analytical model," *Marine Georesources & Geotechnology*, vol. 37, no. 7, pp. 816–827, 2018.
- [16] K. Zhang, W. Zheng, C. Xu, and S. Chen, "An improved extension system for assessing risk of water inrush in tunnels in carbonate karst terrain," *KSCCE Journal of Civil Engineering*, vol. 23, no. 5, pp. 2049–2064, 2019.
- [17] H. Wu, D. Ma, A. J. S. Spearing, and G.-Y. Zhao, "Fracture response and mechanisms of brittle rock with different numbers of openings under uniaxial loading," *Geomechanics and Engineering*, vol. 25, no. 6, pp. 481–493, 2021.
- [18] D. Ma, J.-J. Wang, X. Cai et al. "Effects of height/diameter ratio on failure and damage properties of granite under coupled bending and splitting deformation," *Engineering Fracture Mechanics*, vol. 220, Article ID 106640, 2019.
- [19] Q. Li and W. Sui, "Risk evaluation of mine-water inrush based on principal component logistic regression analysis and an improved analytic hierarchy process," *Hydrogeology Journal*, vol. 29, no. 3, pp. 1299–1311, 2021.
- [20] M. A. M. Ismail, T. A. Majid, C. O. Goh, S. P. Lim, and C. G. Tan, "Geological assessment for tunnel excavation under river with shallow overburden using surface site investigation data and electrical resistivity tomography," *Measurement*, vol. 144, pp. 260–274, 2019.
- [21] K.-I. Song, G.-C. Cho, and S.-B. Chang, "Identification, remediation, and analysis of karst sinkholes in the longest railroad tunnel in South Korea," *Engineering Geology*, vol. 135–136, pp. 92–105, 2012.
- [22] S. C. Li, Z. Q. Zhou, Z. H. Ye, L. P. Li, Q. Q. Zhang, and Z. H. Xu, "Comprehensive geophysical prediction and treatment measures of karst caves in deep buried tunnel," *Journal of Applied Geophysics*, vol. 116, pp. 247–257, 2015.
- [23] A. Alimoradi, A. Moradzadeh, R. Naderi, M. Z. Salehi, and A. Etemadi, "Prediction of geological hazardous zones in front of a tunnel face using TSP-203 and artificial neural networks," *Tunnelling and Underground Space Technology*, vol. 23, no. 6, pp. 711–717, 2008.
- [24] T. Yamatoto, S. Shirasagi, Y. Yokota, and Y. Koizumi, "Imaging geological conditions ahead of a tunnel face using three-dimensional seismic reflector tracing system," *International Journal of the JCRM*, vol. 6, no. 1, pp. 23–31, 2011.
- [25] R. Ahmadi, N. Fathianpour, and G.-H. Norouzi, "Detecting physical and geometrical parameters of some common geotechnical targets through their effects on GPR responses," *Arabian Journal of Geosciences*, vol. 8, no. 7, pp. 4843–4854, 2015.
- [26] S.-H. Baek, S.-S. Kim, J.-S. Kwon, and E. S. Um, "Ground penetrating radar for fracture mapping in underground hazardous waste disposal sites: a case study from an underground research tunnel, South Korea," *Journal of Applied Geophysics*, vol. 141, pp. 24–33, 2017.
- [27] M.-M. Liu, Z.-H. Liu, D. Zhou, R.-Y. Lan, and H. Wu, "Recognition method of typical anomalies during karst tunnel construction using GPR attributes and Gaussian processes," *Arabian Journal of Geosciences*, vol. 13, no. 16, pp. 4843–4854, 2020.
- [28] R. M. Corbeanu, G. A. McMechan, R. B. Szerbiak, and K. Soegaard, "Prediction of 3-D fluid permeability and mudstone distributions from ground-penetrating radar (GPR) attributes: example from the Cretaceous Ferron Sandstone Member, east-central Utah," *Geophysics*, vol. 67, no. 5, pp. 1495–1504, 2002.
- [29] L. Liu, Z.-M. Shi, M. Peng et al., "A borehole multifrequency acoustic wave system for karst detection near piles," *Journal of Applied Geophysics*, Article ID 104051, 2020.
- [30] S. Li, B. Liu, X. Xu et al., "An overview of ahead geological prospecting in tunneling," *Tunnelling and Underground Space Technology*, vol. 63, pp. 69–94, 2017.
- [31] E. Forte, M. Pipan, D. Casabianca, R. Di Cuia, and A. Riva, "Imaging and characterization of a carbonate hydrocarbon reservoir analogue using GPR attributes," *Journal of Applied Geophysics*, vol. 81, pp. 76–87, 2012.
- [32] S.-C. Li, K. Wang, L.-P. Li, Z. Q. Zhou, S. Shi, and S. Liu, "Mechanical mechanism and development trend of water-inrush disasters in karst tunnels," *Chinese Journal of Theoretical and Applied Mechanics*, vol. 49, no. 1, pp. 22–30, 2017, in Chinese.
- [33] Y.-G. Xue, F.-M. Kong, S.-C. Li et al., "Water and mud inrush hazard in underground engineering: genesis, evolution and prevention," *Tunnelling and Underground Space Technology*, vol. 114, Article ID 103987, 2021.
- [34] T. L. Saaty, "A scaling method for priorities in hierarchical structures," *Journal of Mathematical Psychology*, vol. 15, no. 3, pp. 234–281, 1977.
- [35] S.-C. Li, Z.-Q. Zhou, L.-P. Li, Z.-h. Xu, Q.-q. Zhang, and S.-s. Shi, "Risk assessment of water inrush in karst tunnels based on attribute synthetic evaluation system," *Tunnelling and Underground Space Technology*, vol. 38, pp. 50–58, 2013.
- [36] S. C. Li, J. Wu, Z. H. Xu, L. Zhou, and B. Zhang, "A possible prediction method to determine the top concealed karst cave based on displacement monitoring during tunnel construction," *Bulletin of Engineering Geology and the Environment*, vol. 78, no. 1, pp. 341–355, 2019.
- [37] X. Huang, S.-C. Li, Z.-H. Xu, M. Guo, and Y.-C. Chen, "Assessment of a concealed karst cave's influence on karst tunnel stability: a case study of the huaguoshan tunnel, China," *Sustainability*, vol. 10, no. 7, p. 2132, 2018.
- [38] S. Wang, S. Li, L. Li et al., "Study on early warning method for water inrush in tunnel based on fine risk evaluation and hierarchical advance forecast," *Geosciences*, vol. 9, no. 9, pp. 392–412, 2019.
- [39] F. Li, K. K. Phoon, X. Du, M. Zhang, and M.-J. Zhang, "Improved AHP method and its application in risk

- identification,” *Journal of Construction Engineering and Management*, vol. 139, no. 3, pp. 312–320, 2013.
- [40] H.-M. Lyu, S. M. Asce, W.-J. Sun, A. M. Asce, S.-L. Shen, and A.-N. Zhou, “Risk assessment using a new consulting process in fuzzy AHP,” *Journal of Construction Engineering and Management*, ASCE, vol. 146, no. 3, Article ID 04019112, 2020.
- [41] Y.-C. Wang, X. Yin, H.-W. Jing, R. Liu, and H. Su, “A novel cloud model for risk analysis of water inrush in karst tunnels,” *Environmental Earth Sciences*, vol. 75, Article ID 103987, 2016.
- [42] T. Song, *Study on Prediction and Treatment Measures of Water Inrush in Micangshan Tunnel*, Chengdu University of Technology, Chengdu, China, 2015, in Chinese.
- [43] Y.-X. Peng, L. Wu, Q.-J. Zuo, C.-H. Chen, and Y. Hao, “Risk assessment of water inrush in tunnel through water-rich fault based on AHP-Cloud model,” *Geomatics, Natural Hazards and Risk*, vol. 11, no. 1, pp. 301–317, 2017.
- [44] L.-C. Nie, Y.-H. Zhang, M.-X. Su et al., “Comprehensive ahead prospecting of tunnels in severely weathered rock mass environments with high water inrush risk: a case study in Shaanxi Province,” *Advances in Civil Engineering*, vol. 2020, Article ID 8867382, 10 pages, 2020.
- [45] L. Bu, S. Li, S. Shi et al., “Application of the comprehensive forecast system for water-bearing structures in a karst tunnel: a case study,” *Bulletin of Engineering Geology and the Environment*, vol. 78, no. 1, pp. 357–373, 2019.

## Research Article

# Deformation and Mechanical Properties of a Constant-Friction-Force Energy-Absorbing Bolt

Tao Song <sup>1,2</sup>, Tianbin Li <sup>1,2</sup>, Lubo Meng<sup>1,2</sup>, Chunchi Ma <sup>1,2</sup>, Chaofei Li<sup>1,2</sup>, and Feng Peng<sup>1,2</sup>

<sup>1</sup>State Key Laboratory of Geohazard Prevention and Geoenvironment Protection, Chengdu University of Technology, Chengdu 610059, China

<sup>2</sup>College of Environment and Civil Engineering, Chengdu University of Technology, Chengdu 610059, China

Correspondence should be addressed to Tianbin Li; [lbt@cduet.edu.cn](mailto:lbt@cduet.edu.cn)

Received 11 June 2021; Revised 19 September 2021; Accepted 24 September 2021; Published 16 October 2021

Academic Editor: Quoc-Bao Bui

Copyright © 2021 Tao Song et al. This is an open access article distributed under the Creative Commons Attribution License, which permits unrestricted use, distribution, and reproduction in any medium, provided the original work is properly cited.

The conventional bolts used in surrounding rock tunnels with large deformation often fail. As a solution to this problem, we developed an extensible bolt with energy-absorbing and constant-friction-force (EACF) characteristics. The EACF bolt mainly comprises a damping device, a hollow threaded bolt, a tightening nut, and a face plate. To reveal its working mechanism, the bolt was tested in terms of its friction, displacement, and energy absorption through a modified tensile test device in a laboratory. The static pull-out test results showed that the axial force-displacement curve of the bolt can be mainly divided into three stages: a conical extrusion stage, an elongation stage, and an elastic failure stage. The EACF bolts exhibited stable energy absorption behaviors when subjected to static loading. The maximum constant friction force could be adjusted by increasing the size and diameter of the straight section of the damping block, and the maximum elongation could be adjusted by increasing the length of the damping cylinder. When the properties of the bolt materials are kept constant, increasing the diameter of the damping block can help achieve a high constant resistance. The proposed EACF bolt has reliable deformation and energy-absorption properties, which ensure its stability when employed in tunnels under the combined action of support and surrounding rocks.

## 1. Introduction

Rock bolts are employed in civil and underground engineering projects (e.g., tunneling excavation and roadway supports). With the increasing complexity of geological conditions, a surrounding rock is mainly characterized by large deformation [1], which can be divided into two cases. In the first case, the rock mass is soft. The self-stability of a soft rock roadway is poor, and soft rocks typically exhibit a creeping behavior, wherein the rock deformation increases with time. In the second case, after roadway excavation, the surrounding rock under a high in situ stress is mostly in the overload state and exhibits a large deformation [2]. In such cases, conventional bolts are easily damaged in advance under the excessive load, causing pull-out and fracture of the bolt [3]. The root causes of this problem are the low elongation and easy yielding of the bolt. Hence, it is

necessary to improve the elongation and bearing capacity of bolt-support systems [4]. Under a high stress, with the deformation of the surrounding rock bolt quickly reaching or approaching its ultimate load, the deformation continues for a sufficient distance while maintaining a high load. Therefore, an ideal energy-absorbing or pressure-yielding bolt should have both sufficient strength and good deformation characteristics [5].

Existing large-deformation energy-absorbing bolts can be classified into two categories based on the working principle. In the first category, we have extensible and sliding extensible bolts with structural elements. Examples include rod extensible bolts, such as D bolts [6], J energy-releasing bolts [7], energy absorption bolts [8], and TCC yielding rock bolts [9]. The bolt structure or the elongation of the performance material is changed to provide anchor displacement; however, it is difficult to control the amount of CE



elongation. The D bolt is made of a round steel with a certain number of anchorage points at certain intervals; however, because the threaded part of the bolt is weak [10], the amount of deformation between adjacent anchorage units is small, and damage can be easily induced [11].

In the other category, we have sliding and extensible anchor bolts with structural elements, including cone bolts [12], Garford bolts [13], Roofex bolts [14], He-bolts [15], and AIEA-T bolts [16]. In these bolts, sliding elongation occurs mainly through a mechanical structure. However, this specific structure increases the number of processing steps required for the anchor, particularly in terms of material selection, and also increases the cost. A Garford bolt is made of round steel and has an anchor head and a threaded steel sleeve. Because of the large diameter of anchor rods, large-diameter anchor holes are required, and the installation cost is high. He-bolts are prepared by incorporating a constant-resistance device into the common anchor rod to achieve a constant resistance and pressure function, and the constant-resistance value is typically in the range of 150–200 kN in the test. However, the Ti sleeve tube is expensive [17].

Because anchor bolts have various drawbacks in terms of the constant friction force, maximum displacement, stability, and production cost, these energy-absorbing bolts cannot sufficiently adapt to the characteristics of large deformation of surrounding rocks under high stress conditions. Therefore, this study developed an extensible bolt with energy-absorbing and constant-friction-force (EACF) characteristics. In the rest of this paper, we introduce the structural composition and working mechanism of the proposed EACF bolt, report its mechanical characteristics analyzed by conducting static tensile experiments, and present the effects of damping block size on the constant resistance, tensile displacement, and energy absorption. EACF bolts are expected to provide a new and reliable means of support for the large deformation observed in tunnel surrounding rocks.

## 2. Structure and Working Mechanism of EACF Bolt

**2.1. Structural Composition of EACF Bolt.** The EACF bolt comprises a threaded hollow bolt, a damping device (including a damping cylinder, a damping block, and a damping tube), a sealing steel ring, a tightening nut, and a face plate (Figure 1). The outer diameter and thickness of the damping cylinder are 50 and 5 mm, respectively. The outer diameter and thickness of the threaded hollow anchor bolt are 25 and 7 mm, respectively. The damping block comprises straight and tapered sections and is connected to the threaded hollow bolt as a single unit by the tightening nut. The damping device can be located inside the anchor hole or outside. The EACF bolt described in this paper is equipped with a damping device at the end and a face plate and tightening nut at the front. The interaction between the components in the damping device not only generates a constant friction force to achieve energy absorption but also determines the constant-resistance displacement by changing the length of the damping cylinder. The strength of

the damping tube is lower than that of the damping block; this helps prevent frictional failure of the block. Therefore, the constant friction force provided by the EACF bolts can be adjusted to meet the different requirements of practical engineering applications, making them more applicable.

**2.2. EACF Bolt-Surrounding Rock Interaction.** In the EACF bolt, the sliding of the damping block in the damping device helps achieve the yield. During the sliding process, the mutual friction between the damping block, damping cylinder, and damping tube provides a constant load-bearing capacity; after the set reserved deformation is released, the EACF bolt is transformed into a normal bolt, at which time the load-bearing capacity will be the same as that of a normal bolt. To achieve an ideal operation of the EACF bolt and ensure that it starts to slip at the nodes before yielding, the following requirements should be met: the maximum static friction of the bolt should be less than the yield strength of the normal bolt.

Since the drill hole of a conventional bolt has an aperture range of 28–32 mm, installing the damping device inside the hole will expand the hole diameter, which requires more procedures, special machine, and more time. For example, an NPR anchor cable requires a special reaming drill to enlarge the drilled hole to install a constant-resistance device [18]. Therefore, we installed the damping device of the EACF bolt outside the hole. The installation of the EACF bolt was the same as that of the conventional rock bolt.

Figure 2 shows the working process. The EACF bolt is driven into the surrounding rock area, and the fixed length of the hollow threaded bolt is anchored by grouting. The bolt can reserve a certain length of the displacement through the damping device, as shown in Figure 2(a). When the surrounding rock deformation is large at the free length, the bolt will be subjected to the pulling force of the tunnel's critical surface. The damping block and anchor will slide outward along the inner side of the damping cylinder. When the straight section of the damping block enters the inner part of the damping cylinder, the conical section of the damping block continuously compresses the damping tube, and the damping tube will be squeezed into the thin plate, thereby generating a frictional force. At the same time, friction is generated between the straight section of the damping block and the inner wall of the damping cylinder. The interaction between the two generates a constant friction force in the damping cylinder. When the reserved deformation is released, the damping block and the sealing steel ring are in contact with each other, and the axial force is borne by the threaded hollow bolt, as shown in Figure 2(b).

Figure 3 illustrates the interaction relationship between the EACF bolt support and the surrounding rock. Curve 1 is the characteristic curve of the surrounding rock of the tunnel under unsupported conditions. Curve 2 is the normal bolt support with the same support stiffness and material. The characteristic curve of the support of the EACF bolt (Curve 3) has an additional yielding process, i.e., the displacement of  $\Delta u$ . The intersection points "a" and "b" in Curve 1 and Curves 2 and 3 are the equilibrium points of the ordinary

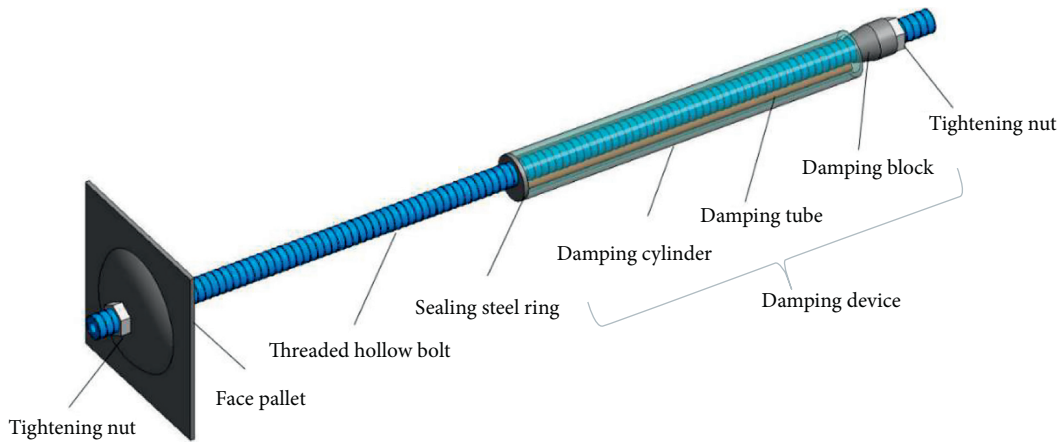


FIGURE 1: Schematic of EACF bolt.

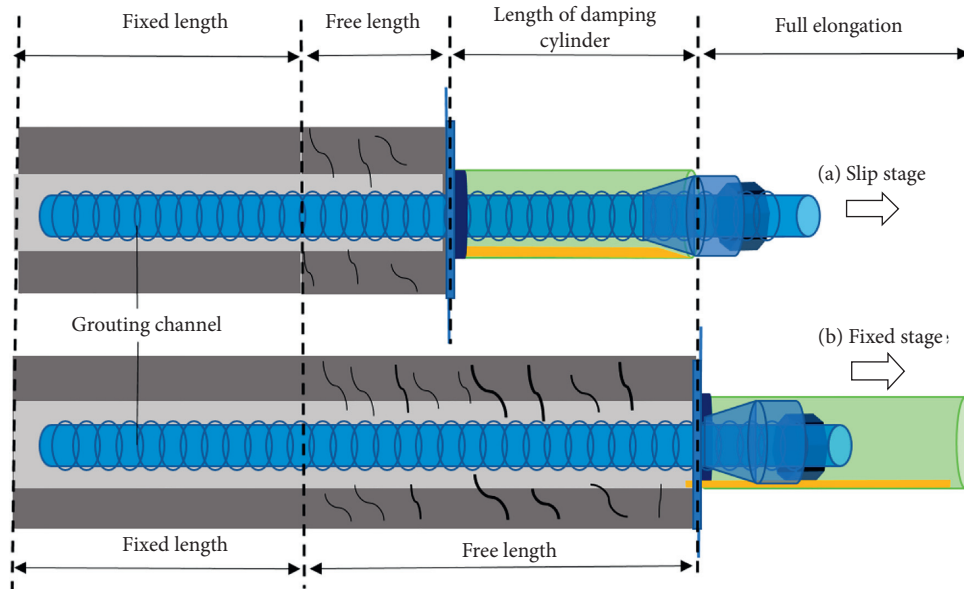


FIGURE 2: Working process of EACF bolt.

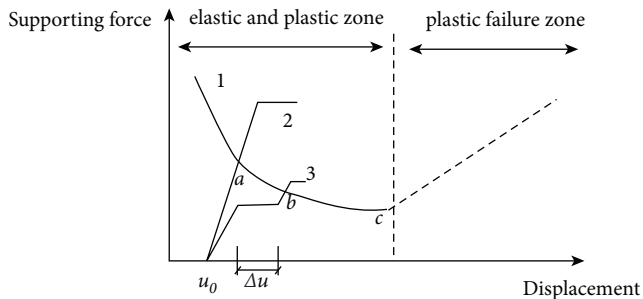


FIGURE 3: Convergence-confinement curves for different supporting concepts.

bolt and EACF bolt support, and they are both in the elastic stage of support, and the support system has good safety. Point c is the stable equilibrium point of the surrounding rock. When the supporting structure cannot work normally

in the loosening failure zone, the action point of the supporting structure should be near the left side of point c. The normal bolt (Curve 2) can reduce the deformation of the roadway surrounding rock by increasing the support stiffness and the support resistance; however, because of the high position of the balance point between the surrounding rock and the anchor bolt support, the support structure will be in a high internal force state, the normal bolt support structure will be under a higher stress, and the support resistance corresponding to point “a” will be much greater than the support resistance at point “b.”

Therefore, the EACF bolt exhibits constant resistance and yield, whereby a certain amount of constant-resistance displacement is released to adapt to the deformation of the surrounding rock. It can also ensure the stability of the surrounding rock with a relatively low working resistance, effectively prevent the bolt from entering the yielding stage prematurely, and ensure that the bolt will not be destroyed

prematurely during the support duration, which not only improves the support life but also contributes to the long-term stability of the rock mass. Hence, the EACF bolt represents a reasonable solution for large-deformation support of soft rocks.

### 3. Static Pull-Out Test Analysis

**3.1. Test Plan and Equipment.** To study the energy absorption performance and extensibility of the EACF bolt, the constant friction force of the bolt was analyzed by varying the diameter and length of the linear section of the damping block with the same material properties of the damping device.

Nine different combinations of dimensions with diameters of 38, 38.5, and 38.7 mm and straight segment lengths of 20, 25, and 30 mm were prepared, denoted by BG-1 to BG-9. The test equipment was improved to meet the test requirements with a maximum load of 500 kN, a maximum displacement of 150 mm, a loading rate of 0.1 to 20 kN/min, a displacement rate of 0.5 to 100 mm/min, a damping cylinder length of 100 mm, and a tensile displacement of 100 mm. The constant speed set in the tensile test was 10 kN/min.

Considering the special characteristics of the damping device, the damping cylinder and the damping tube were made of fixed size and fixed material to ensure that they exhibited good strength and ductility. The outer diameter/thickness of the damping cylinder, damping tube, and anchor bolt were 50/5, 12/2, and 25/7 mm, respectively. The modulus of elasticity of the damping cylinder material was 5000 MPa. The high load-bearing damping block was made of 20# steel, which is much harder than the damping cylinder. The modulus of elasticity and Poisson's ratio of the 20# steel were 200 GPa and 0.3, respectively. The hollow threaded bolt was made of Q345 steel. The yield strength and ultimate strength were 360 and 510 MPa, respectively.

Test data were obtained through a modified tensile test system designed for the EACF bolt (Figure 4). This specialized monitoring system was welded to both sides of the monitoring system to help transmit and record the pulling forces. The EACF bolt was passed through the hollow ring to provide an opposite reaction force during the test, and a linear displacement transducer was fixed to the test equipment to monitor the tensile length of the bolt (Figure 5). In addition, the top steel bar of the monitoring system and the bottom of the bolt were fixed and adjusted using the tensile test equipment; this ensured that the monitoring system and the EACF bolt were in the same plane. However, the steel ring at the bottom of the damping cylinder was not considered in the test. Therefore, the test was stopped when the bolt was completely pulled out of the damping cylinder.

**3.2. Experimental Procedure.** As shown in Figure 6, the pull-out tests on BG-1, BG-2, and BG-3 indicate that the test process can be divided into two stages: an axial force rise stage and an axial force balance stage. During the 0–60 mm

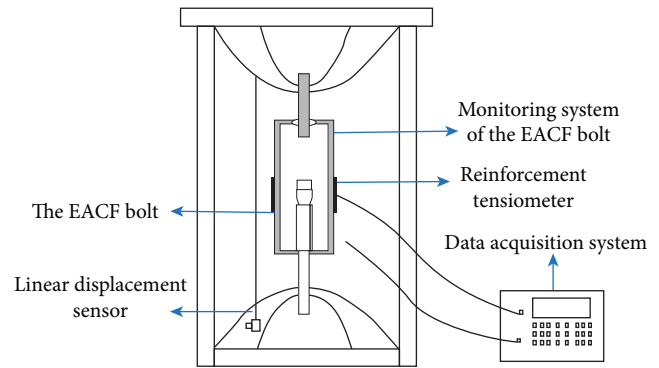


FIGURE 4: Schematic of a modified tensile test device.

stroke, the resistance gradually increases with some fluctuations, and when the damping block completely slides into the damping cylinder, the tension value stabilizes. The constant-friction-force strokes of BG-1, BG-2, and BG-3 are 39.4, 39.2, and 39.6 mm, respectively. The average constant resistances are 60, 63, and 67 kN.

As shown in Figure 7, the pull-out tests of BG-4, BG-5, and BG-6 indicate that the test process can be divided into a resistance rise stage and a resistance balance stage. During the 0–60 mm stroke, the resistance gradually increases with some fluctuations, and when the damping block completely slides into the damping cylinder, the tension value stabilizes. The constant-resistance strokes of BG-4, BG-5, and BG-6 are 39.7, 39.7, and 39.8 mm, respectively. The average constant resistances are 72, 75, and 78 kN.

As shown in Figure 8, from the pull-out tests on BG-7, BG-8, and BG-9, the conditions of the previous specimens are similar during the test. The constant-resistance strokes of BG-7, BG-8, and BG-9 are 39.6, 39.8, and 39.5 mm, respectively. The average constant resistances are 80, 83, and 87 kN.

In summary, as listed in Table 1, different damping block sizes have a certain effect on the constant resistance of the EACF bolt. The test showed that the static friction is the main force at the beginning of the test, and there is no relative displacement between the damping block, the damping tube, and the damping cylinder. With the continuation of the test process, the friction force and displacement increase. When the damping block completely enters the damping cylinder, the EACF bolt reaches the maximum friction force, which gradually stabilizes with the fluctuation, which is a constant friction force until the end of the reserved displacement.

**3.3. Mechanical Analysis of EACF Bolt.** As shown in the figure, the mechanical properties of the normal and EACF bolts are evidently different. The deformation damage stage of the ordinary bolt is the O-A'-B'-C'-D' stage, whereas that of the EACF bolt is the O-A-B-C-D stage. The main difference between the normal and EACF bolts is the yielding-energy absorbing platform of AB; therefore, this study mainly focuses on the elongation stage of the constant friction force. Based on the mechanical curve of the tensile

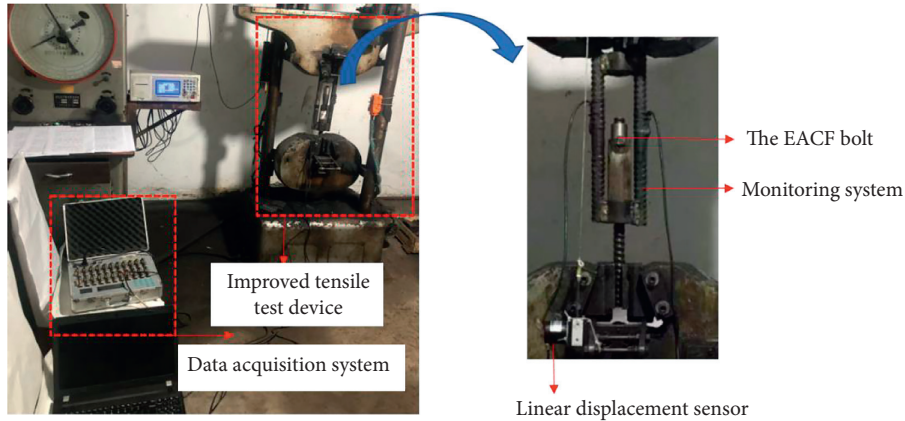


FIGURE 5: Monitoring device of the EACF bolt.

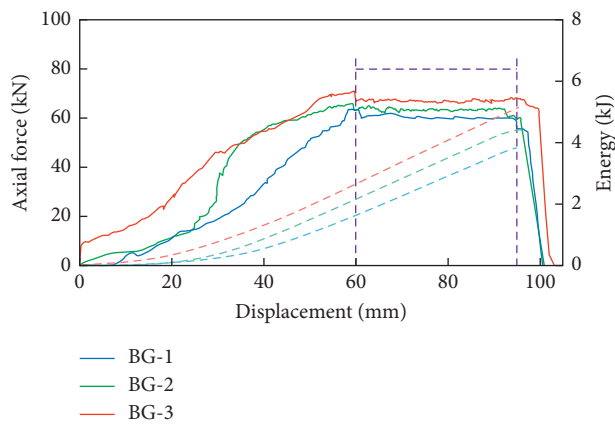


FIGURE 6: Energy and displacement diagrams of BG-1, BG-2, and BG-3.

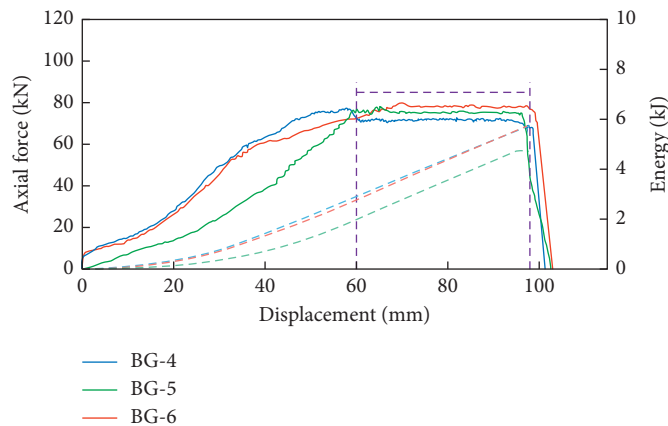


FIGURE 7: Energy and displacement diagrams of BG-4, BG-5, and BG-6.

test, the mechanism of the EACF bolt can be analyzed. The stress process of the EACF bolt includes three stages: a conical extrusion stage, an elongation stage of constant resistance, and an elastoplastic failure stage.

The conical extrusion stage corresponds to the OA stage shown in Figure 9. In the initial stage, there is a relative displacement between the damping block, the damping tube, and the damping cylinder. When the

damping block squeezes the damping tube and damping cylinder, the tension increases linearly. Over time, the friction and displacement increase rapidly. However, the ordinary bolt is mainly in the elastoplastic stage in the OA' stage. As the pressure increases, the deformation of the bolt is not evident, and it shows a linear increase. Here, the curves of the two bolts have the same characteristics.

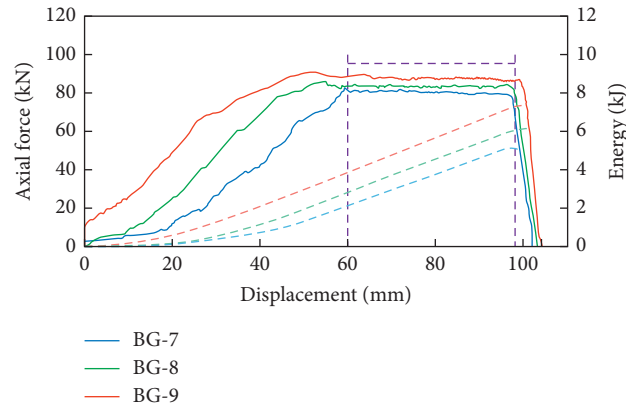


FIGURE 8: Axial force, energy, and displacement diagrams of BG-7, BG-8, and BG-9.

TABLE 1: Tensile test results of the EACF bolt.

Types of EACF bolts	Diameter of the straight section of the damping block (mm)	Straight line length of the damping block (mm)	Average constant-friction force (kN)	Constant displacement (mm)	Absorbed energy (J)
BG-1	38	20	60	39.4	3806
BG-2	38	25	63	39.2	4407
BG-3	38	30	67	39.6	5215
BG-4	38.5	20	72	39.7	4687
BG-5	38.5	25	75	39.7	5064
BG-6	38.5	30	78	39.8	5746
BG-7	38.7	20	80	39.6	5116
BG-8	38.7	25	83	39.8	6097
BG-9	38.7	30	87	39.5	7340

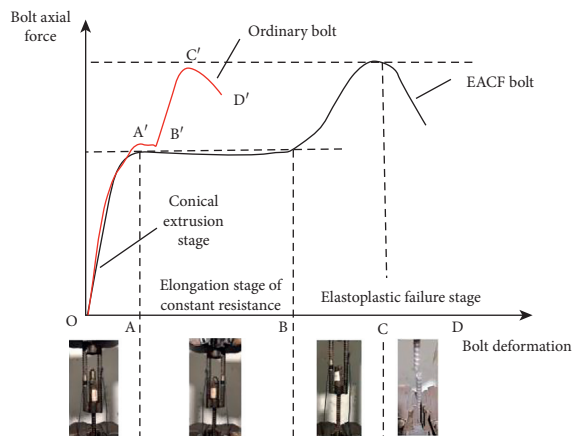


FIGURE 9: Mechanical property curves of EACF and normal bolts.

The elongation stage of the constant resistance corresponds to the AB stage shown in Figure 9. At this stage, as the straight part of the damping block completely enters the damping cylinder, the EACF bolt produces a constant friction force. This stage produces a platform. Compared with the A'B' stage of the normal bolt, this stage is a controllable elongation displacement, and the proposed bolt evidently outperforms the normal bolt. The reason for this stage is that the constant friction force produced by the damping device is lower than the yield load of the bolt itself,

which improves the deformation performance of the support system. Moreover, in terms of the energy absorption, the damping device of the EACF bolt absorbs most of the energy generated by tension and displacement, which is equivalent to absorbing the energy of the surrounding rock deformation. Therefore, the constant friction force and displacement are key factors that reflect the mechanical properties and energy absorption efficiency of the EACF bolt.

The elastoplastic failure stage corresponds to the BCD stage shown in Figure 9. When the damping block is fixed by the steel ring at the bottom of the damping cylinder, it no longer slides. The EACF bolt is now transformed into a normal bolt, and as the axial force of the bolt further increases, the bolt body reaches the yielding stage until the bolt breaks. This stage is similar to the B'C'D' stage of the ordinary bolt.

## 4. Discussion

**4.1. Effect of Damping Block Size on Constant Resistance.** When the diameter of the linear section of the damping block remains constant, the constant friction force increases with the increase in the linear section length of the damping block, from 6 to 8 kN. Compared with the initial constant friction force, its increase is 8% to 10%. As shown in Figure 10, when the straight section length of the damping block

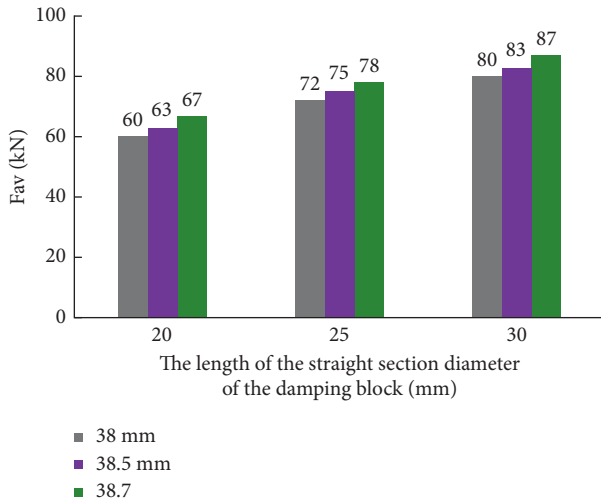


FIGURE 10: Effect of damping block size on energy-absorbing and constant-friction-force bolt.

remains constant, increasing the diameter of the damping block can help significantly increase the constant friction force. The increase is within 12–20 kN. Compared with the initial constant friction force, the maximum increase is 30%–33%. Therefore, when the size of the damping device is constant, increasing the diameter of the damping block can produce a more evident constant friction force.

**4.2. Effect of Damping Block Size on Constant Tensile Displacement.** The damping block size has little effect on the constant tensile displacement. As shown in Figures 6–8, the axial force increases rapidly to a peak at a displacement of approximately 60 mm, i.e., the damping block completely enters the damping cylinder, indicating that the bolt can resist the deformation of the rock in a short extension range under static loading. Since the dimension of the conical section in the damping block is constant, the constant tensile displacement is mainly controlled by the length of the damping cylinder. More specifically, it is determined by the length of the damping cylinder minus the length of the damping block; therefore, the effect of constant tensile displacement is not significant in the stretching process. In soft rocks, the support length should be calculated to mitigate the hazard of large tunnel deformation through energy absorption.

**4.3. Energy Absorption Capacity of EACF Bolt under Different Damping Block Sizes.** The EACF bolt has a good energy absorption capacity. The energy absorption capacity is the area under the axial force-displacement curve based on the static tensile test. Therefore, the total energy absorption depends on the level of the bearing capacity and displacement. The length of the damping cylinder is the same as that of the tensile displacement of the EACF bolt. When the length of the damping cylinder is increased, the energy absorbed by the EACF bolt increases.

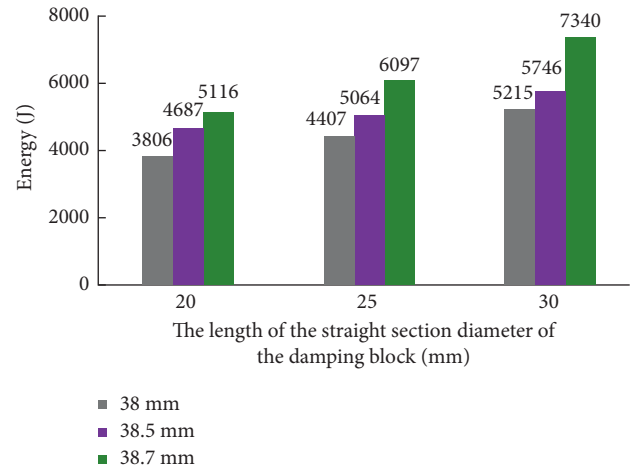


FIGURE 11: Effect of constant straight section length of the damping block on the energy-absorbing and constant-friction-force bolt.

From Figure 11, we find that the energy absorption capacity increases when increasing the diameter of the straight section of the damping block with the length of the straight section of the damping block being constant, and the range of increase is 34%–42% compared with the initial increase. When the diameter of the straight section of the damping block remains constant, the energy absorption capacity increases when increasing the straight section length of the block, with a range of 22%–39% compared with the initial increase. Therefore, the energy absorption increases with the increase in the damping block size; however, the increase in the energy absorbed by the EACF bolt is more evident with the increase in the damping block diameter.

The static load tensile test shows that the EACF bolt has the characteristics of constant-resistance displacement and constant resistance. The maximum constant force of 60–87 kN reported in this paper meets the application requirements of highway tunnels through field investigation and literature research; the maximum constant force is generally in the range of 40–60 kN [19, 20]. Compared with the installation of a damping device in the borehole, installing the damping device outside the borehole could help optimize the construction process in practical applications. Hence, the EACF bolt has certain application value, and we will further study its practical applications.

## 5. Conclusions

- (1) We developed an extensible bolt with energy-absorbing and constant-friction-force characteristics, with functions such as constant friction force, variable displacement, and energy absorption. The constant support resistance is provided through the squeezing and sliding of the damping cylinder, damping block, and damping tube. The adjustable constant friction force ranges from 60 kN to 87 kN, and the maximum extensible displacement is determined by the damping cylinder. Through static pull-out tests, we found that by adjusting the length of the damping device, the tensile displacement of

the EACF bolt could be varied, the deformation energy of the surrounding rock due to the high ground stress could be absorbed, and the large deformation of the surrounding rock could be effectively supported. The dynamic performance for hard rocks will be investigated in the future.

- (2) The tensile test results showed that increasing the diameter and length of the straight section of the damping block can help increase the constant friction force and energy absorption under the condition that the material performance of the damping device remains unchanged. When the diameter of the damping block is increased, the maximum increase range of the constant resistance is 30%–33%; the range of increase in the energy absorption capacity is 22%–39% compared with the initial increase. Therefore, increasing the diameter of the damping block can help produce a more evident supporting effect.
- (3) The experimental analysis showed that the elongation stage of the EACF bolt is evidently different from that of the normal bolt. The mechanical properties of the EACF bolt are mainly reflected in three stages: a conical extrusion stage, an elongation stage of the constant friction force, and an elastoplastic failure stage. The development of EACF bolts can release the internal energy of the surrounding rock, can effectively maintain its stability, and has a good reference value for the prevention and control of large deformation of tunnels.

## Data Availability

The data used to support the findings of this study are available from the corresponding author upon request.

## Conflicts of Interest

The authors declare that they have no conflicts of interest.

## Acknowledgments

This study was supported by the National Natural Science Foundation of China (nos. U19A20111 and 41772329), the Research Fund of the State Key Laboratory of Geohazard Prevention and Geoenvironment Protection (nos. SKLGP2018Z009 and SKLGP2018Z016), and the Sichuan Science and Technology Planning Project (no. 2019YJ0538).

## References

- [1] K. Skrzypkowski, W. Korzeniowski, K. Zagórski, and A. Zagórska, "Flexibility and load-bearing capacity of roof bolting as functions of mounting depth and hole diameter," *Energies*, vol. 12, no. 19, p. 3754, 2019.
- [2] Z. Chen, C. He, G. Xu, G. Ma, and W. Yang, "Supporting mechanism and mechanical behavior of a double primary support method for tunnels in broken phyllite under high geo-stress: a case study," *Bulletin of Engineering Geology and the Environment*, vol. 78, no. 7, pp. 5253–5267, 2019.
- [3] H. Kang, Y. Wu, F. Gao et al., "Mechanical performances and stress states of rock bolts under varying loading conditions," *Tunnelling and Underground Space Technology*, vol. 52, no. 2, pp. 138–146, 2016.
- [4] C. C. Li, "Principles of rockbolting design," *Journal of Rock Mechanics and Geotechnical Engineering*, vol. 9, no. 3, pp. 396–414, 2017.
- [5] M. Ghorbani, K. Shahriar, M. Sharifzadeh, and R. Masoudi, "A critical review on the developments of rock support systems in high stress ground conditions," *International Journal of Mining Science and Technology*, vol. 30, no. 5, pp. 557–572, 2020.
- [6] C. Li, "A new energy-absorbing bolt for rock support in high stress rock masses," *International Journal of Rock Mechanics and Mining Sciences*, vol. 47, pp. 396–404, 2010.
- [7] X. D. Zhao, Q. K. Zhu, J. A. Niu, X. Yang, S. Zhang, and Y. Chen, "Mechanical mechanism analyses and dynamic impact experimental tests of a kind of novel J energy-releasing bolts," *Chinese Journal of Rock Mechanics and Engineering*, vol. 39, pp. 13–21, 2020.
- [8] A. W. Wang, Y. S. Pan, B. Y. Zhao, and J. Sheng, "Static and dynamic mechanical properties of energy absorption bolts (cable) and field tests," *Chinese Journal of Geotechnical Engineering*, vol. 39, no. 7, pp. 1292–1301, 2017.
- [9] X. Wu, Y. Jiang, G. Wang, B. Gong, Z. Guan, and T. Deng, "Performance of a new yielding rock bolt under pull and shear loading conditions," *Rock Mechanics and Rock Engineering*, vol. 52, no. 9, pp. 3401–3412, 2019.
- [10] B. Zhao, J. Li, A. Wang, and H. Xiang, "Theoretical and numerical analysis of a new energy-absorbing rock bolt with controllable constant resistance and large displacement," *Tunnelling and Underground Space Technology*, vol. 106, 2020.
- [11] X. Z. Wu, G. Wang, Y. J. Jiang, B. Gong, and B. Li, "Mechanism of CTC-yield bolts and its experimental research," *Chinese Journal of Geotechnical Engineering*, vol. 37, no. 1, pp. 139–147, 2015.
- [12] A. J. Jager, "Two new support units for the control of rockburst damage," in *Proceedings of the International Symposium Rock Support in Mining and Underground Construction*, pp. 621–631, Rotterdam: Balkema, 1992.
- [13] R. Varden, R. Lachenicht, J. Player, and A. Thompson, "Development and implementation of the Garford dynamic bolt at the kanowna belle mine," in *Proceedings of the 10th Underground Operators' Conference*, pp. 14–16, Launceston, Australia, 2008.
- [14] E. Neugebauer, "Ready for roofex—a new way to tackle safety in underground operations," *Min Construct*, vol. 3, pp. 12–13, 2008.
- [15] M. He, W. Gong, J. Wang et al., "Development of a novel energy-absorbing bolt with extraordinarily large elongation and constant resistance," *International Journal of Rock Mechanics and Mining Sciences*, vol. 67, pp. 29–42, 2014.
- [16] L. Dai, Y. Pan, A. Wang, Y. Xiao, and X. Ma, "Experimental study on the self-protection performance of anchor bolts with energy-absorbing tails," *Rock Mechanics and Rock Engineering*, vol. 53, no. 5, pp. 2249–2263, 2020.
- [17] Y. Hao, Y. Wu, P. G. Ranjith, and K. Zhang, "A novel energy-absorbing rock bolt with high constant working resistance and long elongation: principle and static pull-out test," *Construction and Building Materials*, vol. 243, 2020.
- [18] X. M. Sun, B. Zhang, G. Li, T. Zhigang, and Z. Chengwei, "Application of constant resistance and large deformation anchor cable in soft rock highway tunnel," *Advances in Civil Engineering*, vol. 2019, Article ID 4347302, 2019.
- [19] B. Zhang, Z. Q. Zhang, B. Wang, and L. Zhou, "Experimental study of application of yielding bolt to large deformation tunnel," *Rock And Soil Mechanics*, vol. 37, no. 7, pp. 2047–2055, 2016.

- [20] L. X. Kong, K. Gu, and S. Zhang, "Experimental study of application of yielding bolt to large deformation tunnel," *Chinese Journal of Underground Space and Engineering*, vol. 16, no. S01, pp. 55-58, 2020.



## Research Article

# Viscoelastoplastic Displacement Solution for Deep Buried Circular Tunnel Based on a Fractional Derivative Creep Model

Yi-Hang Gao,<sup>1,2</sup> Zhou Zhou,<sup>1,2</sup> Hang Zhang,<sup>1,2</sup> Shuang Jin ,<sup>3</sup> Wen Yang,<sup>3</sup>  
and Qing-Hua Meng<sup>4</sup>

<sup>1</sup>State Key Laboratory of Geohazard Prevention and Geoenvironment Protection (Chengdu University of Technology), Chengdu 610059, China

<sup>2</sup>College of Environment Geology and Civil Engineering, Chengdu University of Technology, Chengdu 610059, China

<sup>3</sup>Fifth Geological Brigade, Hebei Bureau of Geology and Mineral Resources, Tangshan 063000, China

<sup>4</sup>Tianjin Center, China Geological Survey, Tianjin 300000, China

Correspondence should be addressed to Shuang Jin; jinshuang19870202@gmail.com

Received 22 July 2021; Revised 15 August 2021; Accepted 16 August 2021; Published 16 September 2021

Academic Editor: Guowen Xu

Copyright © 2021 Yi-Hang Gao et al. This is an open access article distributed under the Creative Commons Attribution License, which permits unrestricted use, distribution, and reproduction in any medium, provided the original work is properly cited.

Time-dependent deformation of surrounding rock is a common phenomenon for tunnels situated in soft rock stratum or hard rock stratum with high geo-stress. To describe this phenomenon, a creep model combining the Abel dashpot and a non-Newton viscous element was adopted, and the analytical solution about the viscoelastoplastic deformation for circular tunnel was obtained based on this creep model. Then, the auxiliary tunnel of Jinping II hydropower station was taken as an example to reveal the influence of creep parameters on the creep deformation. The research shows that (1) the creep model can well describe the whole creep stage of rocks, that is, the decay, constant, and accelerated creep stages, (2) the creep deformation has a positive relation with the value of fractional order of Abel dashpot and the order of the non-Newton viscous element, and (3) the creep curves between test results and analytical solutions are well consistent with each other, which demonstrate the validity of the analytical solution.

## 1. Introduction

The rheological deformation of surrounding rock is a common issue encountered in the excavation of soft rock tunnels under the conditions of high in situ stress. When the rheological deformation exceeds a certain level, the surrounding rock will be squeezed, which causes the failure of supporting structures and adversely affects the safety of tunnel constructions and long-term operations [1]. Therefore, the analysis regarding the rheological effect of surrounding rock and its influence on the viscoelastic-plastic process of tunnel deformation has important theoretical and practical significance.

Researchers have conducted a lot of analytical studies on the creep features of tunnels. Hong et al. [2] obtained the rheological deformation solution of an axisymmetric circular roadway tunnel based on the Nishihara model. Tang et al. [3] derived the time-dependent displacement solution

of deep-buried tunnels considering the effects of strain strengthening and dilation of surrounding rock using a viscoelastic-plastic creep model which is comprised of Burgers body and Drucker-Prager yield criterion. Zhang et al. [4] adopted the improved Nishihara model to derive the viscoelastic-plastic creep displacement of seepage tunnels under the influence of the expansion strain of the surrounding rock. Gu and Yan [5] studied the creep behavior of surrounding rock under the action of seepage with the improved Burgers model. Deleruyelle et al. [6] used the Norton-Hoff criterion to describe the creep effect of surrounding rock and derived an analytical solution for tunnel displacement considering the postpeak effect of surrounding rock.

In former research, the creep behavior of surrounding rock is generally described by viscoelastic constitutive models. However, none of these models can well reflect the accelerated deformation stage of rocks [7, 8]. Few

researchers have done pioneer work in deriving the closed-form solution of tunnel displacement using viscoelasto-plastic models [9, 10]. Therefore, in this article, a creep model, which consists of an elastic element, a non-Newtonian viscous element, an Abel element based on the fractional calculus theory, and a plastic element, is adopted to simulate the whole creep deformation stage of rocks. Then, the viscoelastic displacement solution of the deep-buried tunnel is derived based on this creep model. Finally, taking the auxiliary tunnel of Jinping II Hydropower Station as an example, the influence of rheological parameters on the tunnel deformation is discussed.

## 2. Creep Constitutive Model

**2.1. Abel Element Based on Fractional Theory.** Fractional calculus operation refers to that the order of integration or differentiation of a function is any real or complex number [11]. Among all relevant definitions, the Riemann–Liouville definition is most suitable for studying the viscosity characteristics of materials. The integral of function  $f(t)$  with an order of  $\gamma$  is

$$\frac{d^{-\gamma}[f(t)]}{dt^{-\gamma}} = {}_{t_0}D_t^{-\gamma}f(t) = \frac{1}{\Gamma(\gamma)} \int_{t_0}^t (t-\tau)^{\gamma-1} f(\tau) d\tau. \quad (1)$$

The corresponding differentiation is

$$\frac{d^\gamma[f(t)]}{dt^\gamma} = {}_{t_0}D_t^\gamma f(t) = \frac{d^n [{}_{t_0}D_t^{-(n-\gamma)} f(t)]}{dt^n}, \quad (2)$$

where  $\gamma > 0$  and  $n-1 < \gamma \leq n$  ( $n$  is the smallest positive integer which is larger than  $\gamma$ ) and  $\Gamma(\gamma)$  is the Gamma function with expression of  $\int_0^\infty e^{-t} t^{\gamma-1} dt$ .

The Abel dashpot based on the theory of fractional calculus can well describe the viscous characteristics of the viscous body between the ideal elastic body and the ideal fluid, and its expression is

$$\sigma(t) = \eta \frac{d^\gamma \varepsilon(t)}{dt^\gamma}. \quad (3)$$

When  $\sigma(t)$  is a constant, its creep equation is

$$\varepsilon(t) = \frac{\sigma}{\eta^\gamma} \frac{t^\gamma}{\Gamma(1+\gamma)} \quad (0 \leq \gamma \leq 1). \quad (4)$$

**2.2. Non-Newtonian Viscous Element.** The NVPB element [12] is put forward to describe the accelerated deformation process of rock after it enters the plastic stage, and its creep equation is

$$\varepsilon(t) = \frac{H(\sigma_0 - \sigma_s)}{\eta} \frac{t^n}{t_0^{n-1}} = \frac{H(\sigma_0 - \sigma_s)}{\eta} t^n, \quad (5)$$

where  $t_0$  is reference time with a value of 1,  $n$  is the creep index,  $\sigma_s$  is the long-term strength of rock, and  $H(\sigma)$  is unit step function:

$$H(\sigma_0 - \sigma_s) = \begin{cases} 0, & \sigma_0 \leq \sigma_s, \\ \sigma_0 - \sigma_s, & \sigma_0 > \sigma_s. \end{cases} \quad (6)$$

**2.3. The Creep Model.** A creep model (Figure 1) combining the Abel dashpot and a non-Newton viscous element was adopted to simulate the whole creep deformation stage of rocks.

The stress-strain relation of each element under the condition of viscoelastic state is [9]

$$\begin{cases} \sigma_1 = E_1 \varepsilon_1, \\ \sigma_2 = \eta_2^\gamma \frac{d^\gamma \varepsilon_2}{dt^\gamma}, \sigma_0 < \sigma_s, \\ \sigma = \sigma_1 = \sigma_2, \\ \varepsilon = \varepsilon_1 + \varepsilon_2. \end{cases} \quad (7)$$

The stress-strain relation of each element under the condition of viscoplastic (the plastic behavior of rocks is described by the Hoke–Brown criterion) state is

$$\begin{cases} \sigma_1 = E_1 \varepsilon_1, \\ \sigma_2 = \eta_2^\gamma \frac{d^\gamma \varepsilon_2}{dt^\gamma}, \\ \sigma_3 = \sigma_s + \eta_2 \frac{\dot{\varepsilon}_3}{(nt^{n-1})}, \sigma_0 \geq \sigma_s, \\ \sigma = \sigma_1 = \sigma_2 = \sigma_3, \\ \varepsilon = \varepsilon_1 + \varepsilon_2 + \varepsilon_3, \end{cases} \quad (8)$$

where  $\sigma$  and  $\varepsilon$  are the total stress and strain, respectively,  $\sigma_1$ ,  $\sigma_2$ , and  $\sigma_3$  are the stress of element 1, 2, and 3, respectively,  $\varepsilon_1$ ,  $\varepsilon_2$ , and  $\varepsilon_3$  are the strain of element 1, 2, and 3, respectively, and  $E_1$  the elastic modulus of element 1.

(1) The stress-strain relationship of the elastic element:

$$\varepsilon_1 = \frac{\sigma}{E_1}. \quad (9)$$

(2) The stress-strain relationship of the Abel dashpot [9]:

$$\varepsilon_2 = \frac{\sigma}{\eta^\gamma} \frac{t^\gamma}{\Gamma(1+\gamma)}. \quad (10)$$

(3) The stress-strain relationship of the NVPB element [12]:

$$\varepsilon_3 = \frac{\sigma - \sigma_s}{\eta_3} t^n. \quad (11)$$

Thus, the constitutive model of the creep model is

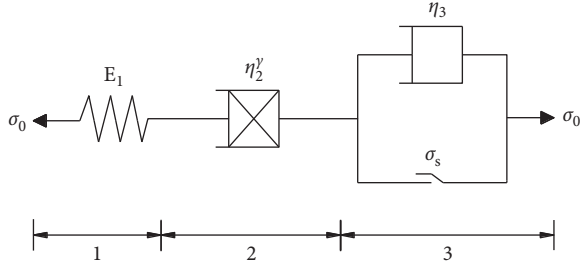


FIGURE 1: Creep constitutive model.

$$\varepsilon(t) = \frac{\sigma}{E} + \frac{\sigma}{\eta_2^\gamma} \frac{t^\gamma}{\Gamma(1+\gamma)} \quad (\sigma < \sigma_s), \quad (12)$$

$$\varepsilon(t) = \frac{\sigma}{E} + \frac{\sigma}{\eta_2^\gamma} \frac{t^\gamma}{\Gamma(1+\gamma)} + \frac{\sigma - \sigma_s}{\eta_s} t^n \quad (\sigma \geq \sigma_s).$$

2.4. *The Validation of the Creep Model.* Chen et al. [13] conducted uniaxial compression creep test to study the creep behavior of marble. The result showed that the long-term strength of marble is 130.1 MPa, and it underwent evident three-stage creep deformation when the axial compression stress exceeds 135.7 MPa. Thus, the creep curve at 135.7 MPa is chosen to validate this creep model.

The calibrated parameters and simulated creep curves are shown in Table 1 and Figure 2, respectively. It reveals that the calculated results agree well with the test results, which shows that the creep model can describe the whole creep deformation stage of rock.

### 3. Visco-elastoplastic Displacement of Tunnels

3.1. *Basic Assumption.* The derivation of the visco-elastoplastic displacement of tunnels is based on the following assumptions (Figure 3):

- (1) The radius of deep-buried tunnel is  $R_0$ . The hydrostatic pressure is  $p_0$  and the tunnel is in the plane strain state.
- (2) The creep deformation of surrounding rock occurs after the tunnel excavation. At this time, the stress redistribution of surrounding rock has been completed, and the secondary stress field of the surrounding rock is constant.

3.2. *The Initial Stress Field before Creep Deformation of Tunnels.* The surrounding rock of deep tunnels has non-linear characteristics. Therefore, the Hoek–Brown criterion is suitable to describe the nonlinearity of rock mass. Its constitutive formula is

$$\sigma_1 = \sigma_3 + \sqrt{m\sigma_3\sigma_c + s\sigma_c^2}, \quad (13)$$

where  $\sigma_1$  and  $\sigma_3$  are the maximum and minimum principal stress after the rock mass enters into the yield failure (MPa),  $\sigma_c$  is the uniaxial compression strength of intact rock (MPa),

TABLE 1: Creep parameters of marble.

$E_1$ (GPa)	$\eta_2^\gamma$ (GPa·h $^\gamma$ )	$\eta_3$ (GPa·h)	$\gamma$	$n$
43.6	2465	3543	0.4	1.5

and  $m$  and  $s$  are parameters related to the quality of rock mass.

The stress in the elastic zone after tunnel excavation is [10]

$$\left\{ \begin{array}{l} \sigma_r^e = p_0 - \frac{R_0^2}{r^2} N e^{2M}, \\ \sigma_\theta^e = p_0 + \frac{R_0^2}{r^2} N e^{2M}, \\ \sigma_z^e = p_0, \\ M = \frac{\sqrt{m^2 + 16m p_0 / \sigma_c + 16s} - 4\sqrt{s} - m}{2m}, \\ N = p_0 - \sqrt{s} \sigma_c M - \frac{m\sigma_c}{4} M^2. \end{array} \right. \quad (14)$$

The stress in the plastic zone is [10]

$$\left\{ \begin{array}{l} \sigma_r^p = \frac{m\sigma_c}{4} \left( \ln \frac{r}{R_0} \right)^2 + \sqrt{s} \sigma_c \ln \frac{r}{R_0}, \\ \sigma_\theta^p = \frac{m\sigma_c}{4} \left( \ln \frac{r}{R_0} \right)^2 + \left( \sqrt{s} \sigma_c + \frac{m\sigma_c}{2} \right) \ln \frac{r}{R_0} + \sqrt{s} \sigma_c, \\ \sigma_z^p = \frac{(1 + \sin \psi) \sigma_\theta^p + (1 - \sin \psi) \sigma_r^p}{2}, \\ R_p = R_0 e^M, \end{array} \right. \quad (15)$$

where  $\sigma_r^e$ ,  $\sigma_\theta^e$ , and  $\sigma_z^e$  are the radial, tangential, and normal elastic stress, respectively,  $\sigma_r^p$ ,  $\sigma_\theta^p$ , and  $\sigma_z^p$  are the radial, tangential, and normal plastic stress, respectively,  $R_p$  is the radius of plastic zone,  $r$  is the distance between any point within the surrounding rock and the circle center, and  $\psi$  is the dilation angle.

#### 3.3. Creep Deformation

3.3.1. *Viscoelastic Zone.* Figure 1 shows that the NVPB plastic element does not contribute to the creep deformation of tunnels when the surrounding rock is at the viscoelastic state. Thus, the creep model degrades into a creep model in which the elastic element connects with the Abel dashpot. The creep feature of surrounding rock at the elastic zone is described using this degraded model.

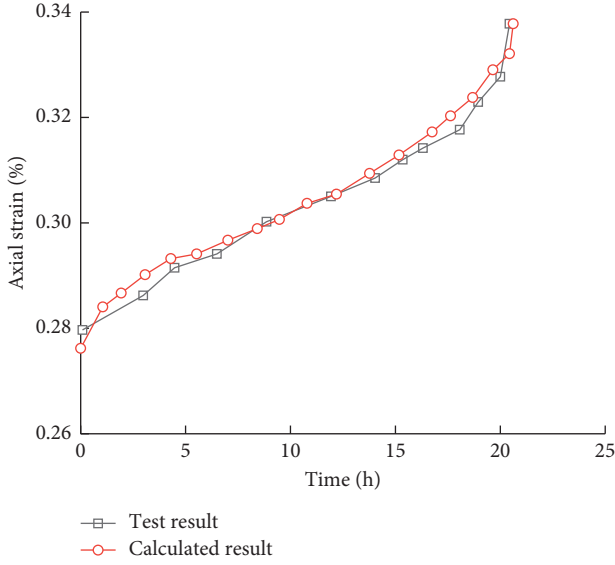


FIGURE 2: Validation of the creep model.

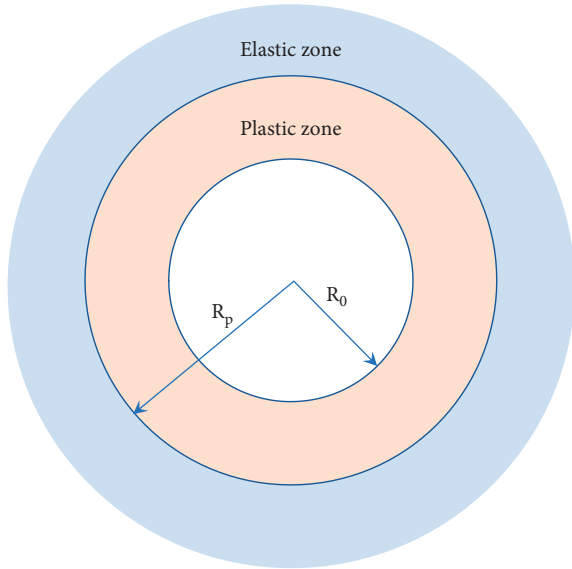


FIGURE 3: Calculation model.

The relationship between deformation and strain of surrounding rock at the viscoelastic zone is

$$\begin{cases} \varepsilon_\theta = \frac{u}{r}, \\ \varepsilon_r = \frac{du}{dr}, \end{cases} \quad (16)$$

where  $\varepsilon_\theta$  and  $\varepsilon_r$  are the tangential and radial strain of surrounding rock and  $u$  is the radial deformation of surrounding rock.

Thus, the creep deformation is

$$u_r^{\eta_e} = \frac{R_0^2}{2Er} Ne^{2M} + \frac{R_0^2}{r} Ne^{2M} \frac{t^\gamma}{\eta^\gamma \Gamma(1+\gamma)}. \quad (17)$$

3.3.2. *Viscoplastic Zone.* The nonassociated rule is adopted to calculate the deformation at the viscoplastic zone:

$$\frac{du_r^{\eta_p}}{dr} + k_\psi \frac{u_r^{\eta_p}}{r} = \varepsilon_r^{\eta_p} + k_\psi \varepsilon_\theta^{\eta_p}, \quad (18)$$

where  $u_r^{\eta_e}$  is the radial displacement at the viscoplastic zone and  $k_\psi$  is the dilated coefficient:

$$k_\psi = \frac{\tan(\pi/4 + \varphi/2)}{\tan(\pi/4 + \varphi/2 - \psi)}, \quad (19)$$

where  $\varphi$  is the frictional angle of rock mass.

Substituting equation (15) into equation (18) yields

$$\begin{aligned} \frac{du_r^{\eta_p}}{dr} + k_\psi \frac{u_r^{\eta_p}}{r} &= \frac{1}{6} \left[ \frac{1}{2E} + \frac{1}{\eta^\gamma} \frac{t^\gamma}{\Gamma(1+\gamma)} + \frac{t^n}{\eta_3} \right] \\ &\cdot \left[ (k_\psi (3 - \sin \varphi) - (3 + \sin \varphi)) \right. \\ &\cdot \left. \left( \frac{m\sigma_c}{2} \ln \frac{r}{R_0} + \sqrt{s} \sigma_c \right) \right] \\ &- (1 + k_\psi) \frac{\sigma_s t^n}{\eta_3}. \end{aligned} \quad (20)$$

The displacement at the boundary between the viscoelastic and viscoplastic zone meets the following relation:

$$\begin{aligned} u_r^{\eta_p}(R_p, t) &= u_r^{\eta_e}(R_p, t), \\ &= \frac{R_0^2}{2ER_p} Ne^{2M} + \frac{R_0^2}{R_p} Ne^{2M} \frac{t^\gamma}{\eta^\gamma \Gamma(1+\gamma)}. \end{aligned} \quad (21)$$

Thus, the displacement at the viscoplastic zone,  $u_r^{\eta_p}$ , is

$$\begin{aligned} u_r^{\eta_p} &= \frac{1}{6} \left[ \frac{m\sigma_c}{2(k_\psi + 1)} g_1(r) + \left( r - R_p \left( \frac{R_p}{r} \right)^{k_\psi} \right) \sqrt{s} \sigma_c \right] \\ &\cdot [k_\psi (3 - \sin \psi) - (3 + \sin \psi)] \\ &\cdot \left[ \frac{1}{2E} + \frac{1}{\eta^\gamma} \frac{t^\gamma}{\Gamma(1+\gamma)} + \frac{t^n}{\eta_3} \right] + \left( r - R_p \left( \frac{R_p}{r} \right)^{k_\psi} \right) \frac{\sigma_0 t^n}{\eta_3} \\ &+ \left( \frac{R_p}{r} \right)^{k_\psi - 1} \left[ \frac{R_0^2}{2ER_p} Ne^{2M} + \frac{R_0^2}{R_p} Ne^{2M} \frac{t^\gamma}{\eta^\gamma \Gamma(1+\gamma)} \right], \end{aligned} \quad (22)$$

where  $g_1(r)$  is

$$\begin{aligned} g_1(r) &= \ln \left( \frac{r}{R_0} \right)^r - \left( \frac{R_p}{r} \right)^{k_\psi} \ln \left( \frac{R_p}{R_0} \right)^{R_p} \\ &- \frac{1}{k_\psi + 1} \left( r - R_p \left( \frac{R_p}{r} \right)^{k_\psi} \right). \end{aligned} \quad (23)$$

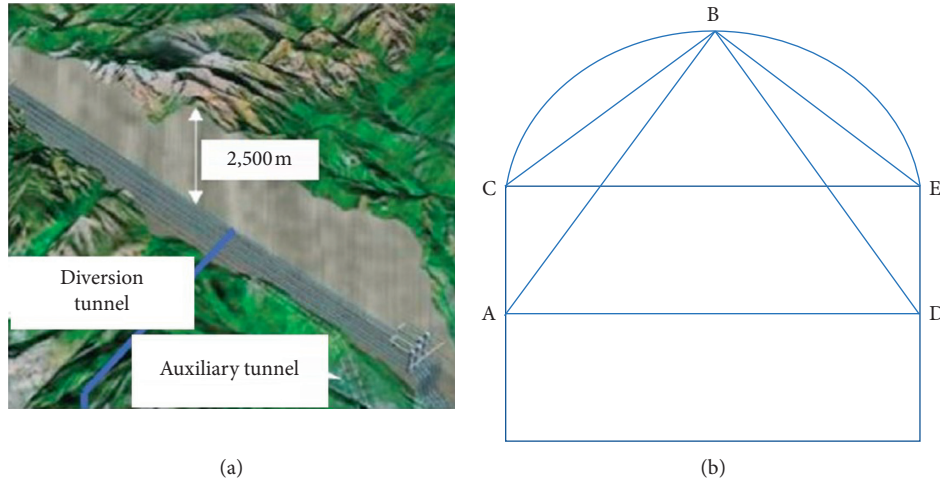


FIGURE 4: Jinping II hydropower station. (a) The position of tunnels [13]. (b) Measuring lines of the auxiliary tunnel [14].

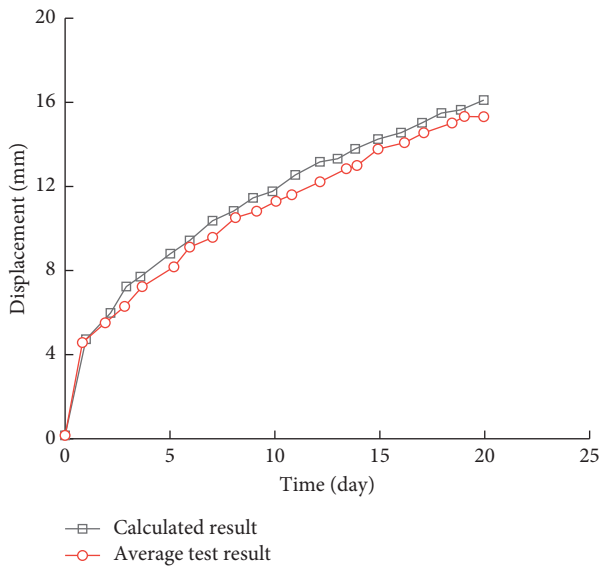


FIGURE 5: Comparison between analytical and test curves.

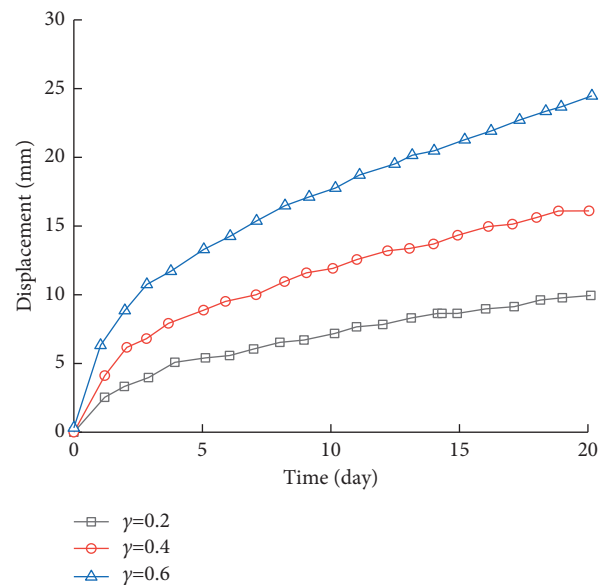


FIGURE 6: Influence of fractional order of Abel dashpot on the deformation.

## 4. Engineering Application

**4.1. Validation of the Closed-Form Solution.** The Jinping number II hydropower station was built on the Jinping Dahe Bay in Sichuan Province (Figure 4(a)). This project consists of 4 diversion tunnels, 2 auxiliary tunnels, and 1 construction drainage tunnel. The average length of the tunnel is about 16.8 km, and the average buried depth is between 1500 and 2000 m.

The stratum that the auxiliary tunnel passes through is mainly composed of marble, and its uniaxial compressive strength is 141.17 MPa, GSI = 50, and  $m_i = 9$ . According to the test results, the rock rheological parameters obtained by inversion are shown in Table 1. The initial in situ stress field of the tunnel site is simplified to the hydrostatic pressure field, that is,  $p_0 = 40$  MPa. The arrangement of the measurement points of the convergence monitoring section is shown in Figure 4(b).

The displacement curves of field monitoring and theoretical calculation is shown in Figure 5. It can be seen that the average value of the monitoring curve is in good agreement with the theoretical calculation result, which verifies the validity of the theoretical solution in this paper.

### 4.2. Parametric Study

**4.2.1. The Influence of Fractional Order.** The relationship between the order  $\gamma$  of the Abel dashpot and the displacement of surrounding rock is shown in Figure 6. It shows that there is a positive correlation between the displacement of the surrounding rock and the magnitude of  $\gamma$ . This is because that, as the value of  $\gamma$  increases, the viscous characteristic of the Abel dashpot becomes more and more

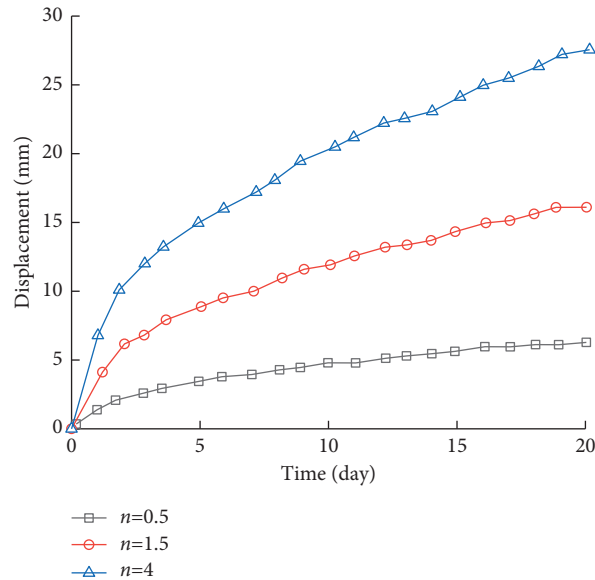


FIGURE 7: Influence of the creep index of NVPB element on the deformation.

obvious, which leads to an increase in the creep displacement of the surrounding rock.

#### 4.2.2. Influence of the Rheological Index of NVPB Element.

The influence of the rheological index of NVPB element on surrounding rock displacement is shown in Figure 7. It reveals that the displacement of surrounding rock increases with the increase of the rheological index. This is because, with the increase of the rheological index, the accelerating rheological process of the surrounding rock becomes more obvious, leading to an increase in the creep displacement of surrounding rock.

## 5. Conclusion

A creep model combining the Abel dashpot and a non-Newton viscous element was adopted, and the analytical solution about the visco-elastoplastic deformation for circular tunnel was derived based on this creep model. Major conclusions are as follows:

- (1) The creep model can well describe the whole creep stage of rocks, that is, the decay, constant, and accelerated creep stages.
- (2) The creep deform has a positive relation with the value of fractional order of Abel dashpot and the order of the non-Newton viscous element.
- (3) The creep curves between test results and analytical solutions are well consistent with each other, which demonstrates the validity of the analytical solution.

## Data Availability

The data used to support the findings of this study are available from the corresponding author upon request.

## Conflicts of Interest

The authors declare that they have no conflicts of interest regarding the publication of this paper.

## Acknowledgments

The research was supported by the National Natural Science Foundation of China (Grant no. 41977226).

## References

- [1] G. Xu, C. He, Y. Wang, and Y. Wang, "Study on the safety performance of cracked secondary lining under action of rheological load," *China Civil Engineering Journal*, vol. 49, no. 12, pp. 114–123, 2016.
- [2] G. Y. Hong, J. J. Li, B. Qiu, and J. J. Li, "Solving equation of rheological deformation in axisymmetric round well under dead load," *Rock and Soil Mechanics*, vol. 32, no. 2, pp. 341–346, 2011.
- [3] S. L. Tang, H. Wang, J. Yu, J. Zhang, and Y. Cai, "Time-varying displacement analytical solution of deep soft rock tunnel considering strain-hardening and dilatation of surrounding rock," *Tunnel Construction*, vol. 37, no. 1, pp. 72–78, 2017.
- [4] Z. J. Zhang, J. Yu, Y. Y. Cai, S.-H. Chen, and C.-M. Lin, "Viscoelastic-plastic creep solutions and deformation properties of tunnels in swelling rocks under seepage," *Chinese Journal of Geotechnical Engineering*, vol. 36, no. 12, pp. 2195–2202, 2014.
- [5] X. B. Gu and L. Yan, "Visco-elasto-plastic creep solutions to circular tunnels considering seepage force," *Electronic Journal of Geotechnical Engineering*, vol. 18, pp. 2231–2241, 2013.
- [6] F. Deleruyelle, T. A. Bui, H. Wong, N. Dufour, D. K. Tran, and X. S. Zhang, "Analytical study of the post-closure behaviour of a deep tunnel in a porous creeping rock mass," *Comptes Rendus Mecanique*, vol. 344, no. 9, pp. 649–660, 2016.
- [7] H. Lin, X. Zhang, Y. Wang et al., "Improved nonlinear Nishihara shear creep model with variable parameters for rock-like materials," *Advances in Civil Engineering*, vol. 2020, pp. 1–15, 2020.

- [8] H. Lin, X. Zhang, R. Cao, and Z. Wen, "Improved nonlinear Burgers shear creep model based on the time-dependent shear strength for rock," *Environmental Earth Sciences*, vol. 79, no. 6, p. 149, 2020.
- [9] J.-Z. Zhang, X.-P. Zhou, and P. Yin, "Visco-plastic deformation analysis of rock tunnels based on fractional derivatives," *Tunnelling and Underground Space Technology*, vol. 85, pp. 209–219, 2019.
- [10] Y. Cai, J. Z. Zhang, J. Yu, and S.-H. Chen, "Nonlinear displacement solutions for deep tunnels considering whole process of creep and dilatation of surrounding rock," *Rock and Soil Mechanics*, vol. 36, no. 7, pp. 1831–1839, 2015.
- [11] A. A. Kilbas, H. M. Srivastava, and J. J. Trujillo, *Theory and Applications of Fractional Differential Equations*, Elsevier, Amsterdam, Netherlands, 2006.
- [12] W. Y. Xu, S. Q. Yang, and W. J. Chu, "Nonlinear viscoelastoplastic rheological model (HOHAI MODEL) of rock and its engineering application," *Chinese Journal of Rock Mechanics and Engineering*, vol. 25, no. 3, pp. 433–447, 2006.
- [13] B. R. Chen, X. J. Zhao, X. T. Feng, and H. Zhao, "Time-dependent damage constitutive model for the marble in the Jinping II hydropower station in China," *Bulletin of Engineering Geology and the Environment*, vol. 73, pp. 499–515, 2014.
- [14] B. R. Chen and X. T. Feng, "Universal viscoelastoplastic combination model and its engineering application," *Chinese Journal of Rock Mechanics and Rock Engineering*, vol. 27, no. 5, pp. 1028–1035, 2008.

## Research Article

# Numerical Study of Wave- and Current-Induced Oscillatory Seabed Response near a Fully Buried Subsea Pipeline

Lunliang Duan,<sup>1,2,3</sup> Meiling Fan,<sup>1</sup> Duoyin Wang,<sup>1</sup> Caixia Meng,<sup>1</sup> and Lei Xing<sup>1</sup> 

<sup>1</sup>National Engineering Research Center for Inland Waterway Regulation, Chongqing Jiaotong University, Chongqing 400074, China

<sup>2</sup>State Key Laboratory of Bridge Structure Dynamics,

China Merchants Chongqing Communications Research & Design Institute Co., Chongqing 400074, China

<sup>3</sup>Department of Bridge Engineering, Southwest Jiaotong University, Chengdu 610031, China

Correspondence should be addressed to Lei Xing; 622180081001@mails.cqjtu.edu.cn

Received 1 April 2021; Accepted 17 July 2021; Published 5 August 2021

Academic Editor: Guowen Xu

Copyright © 2021 Lunliang Duan et al. This is an open access article distributed under the Creative Commons Attribution License, which permits unrestricted use, distribution, and reproduction in any medium, provided the original work is properly cited.

To investigate the wave- and current-induced seabed response near a fully buried subsea pipeline, a two-dimensional coupled model for fluid-seabed-pipeline interaction (FSPI-2D) is developed within the framework of COMSOL multiphysics. Different from previous studies, both the wave-current interaction and the nonlinear pipeline-soil contacts are considered in the present model. In this paper, Biot's consolidation mode is used to govern the fluid-induced seabed response, and combined Reynolds averaged Navier–Stokes (RANS) equation with the  $k$ - $\epsilon$  turbulence model is employed to simulate the fluid propagation. Meanwhile, the pipeline is treated as a linear elasticity. Firstly, the effectiveness of the new model is verified by laboratory experiments from previous reports. Then, the numerical model is employed to examine the effects of nonlinear pipeline-seabed contacts and fluid characteristics on the seabed response around the structure. Finally, the momentary liquefaction near the fully buried pipeline is studied based on the 2D coupled model.

## 1. Introduction

Subsea pipeline is an engineering facility for long-distance transportation of oil and gas, and it is the main component of the offshore oil (gas) production system. At present, in situ stability of subsea pipeline due to the seabed dynamic response has become the main focus for engineers in the field of offshore geotechnical engineering [1–4]. In the marine environment, the wave-induced cyclic pressures at the seabed surface might lead to the seabed liquefaction [5–9]. Once the seabed liquefies, it will lose bearing capacity and show fluid-like properties, which could cause the sinking or flotation [10] of the subsea pipeline due to the seabed liquefaction caused by pore pressure variations [11, 12]. Therefore, investigating the fluid-induced seabed dynamic response near the structure is very significant for offshore geotechnical engineers to predict the stability of the subsea pipeline.

Over the past few decades, many efforts have been devoted to the problem of wave-seabed interactions. Based on Biot's consolidation model [13], Yamamoto et al. proposed the analytical solution to wave-induced dynamic response of an isotropic, poro-elastic, and infinite seabed [14]. Whereafter, Hsu and Jeng further extended the analytical solution to an unsaturated, isotropic seabed with finite thickness due to three-dimensional, short-crested wave loadings [15]. As an extension of Biot's poro-elastic theory, Zienkiewicz et al. proposed the  $u$ - $p$  approximate solution for one-dimensional wave propagation in porous media [16]. Later, Jeng et al., Jeng and Rahman, and Ulker et al. further extended the  $u$ - $p$  approximation to the two-dimensional cases to examine the dynamic response of porous seabed [17–19]. Meanwhile, Ulker et al. summarized the application scope of three different Biot's fluid-structure coupled models [19]. Using the finite element model, Ye and Jeng studied the influences of fluid shear stress on the seabed dynamic response and



concluded that the fluid shear stress can greatly affect the stresses and pore pressure developments within the seabed [20]. In recent years, relevant researchers further investigated the dynamic response of seabed caused by wave loadings using laboratory experiments [21, 22], analytical methods [23], and numerical models [24, 25].

In real oceanic environment, the wave and current normally co-exist, and their interaction process is very complex, which can bring great difficulty to the analysis of fluid-induced seabed response. However, some investigations have still been carried out through different methods. Among these, Zhou et al. studied the wave- and current-induced seabed dynamic response through flume experiments and found that the current could aggravate the liquefaction of the sandy seabed [26]. Ye and Jeng investigated the seabed dynamic response due to combined wave and current loadings and concluded that the maximum error of the pore pressure can reach 25% unless the wave-current interaction is not considered [27]. Liao et al. proposed the analytical solution to the pore pressure response within the infinite seabed and derived that current would change the dynamic response of a near-saturated soil, under the wave loadings with a long wave period and shallow water depth. With the three-dimensional numerical model [28], Wen et al. studied the wave- and current-induced seabed response and found that the existence of following current would increase the pore pressure response in the seabed [29]. Based on the flume tests, Qi et al. studied the seabed response induced by wave and current loadings and clarified that the fluid-induced pore pressure increased for the following-current case, but reduced for the opposing-current case [30].

The phenomenon of wave-structure-seabed interactions (WSSI) has attracted great attention in the field of offshore geotechnical engineering involving the design of subsea pipelines [31]. In the 1980s, Wagner et al. firstly proposed the pipeline-soil interaction model [32, 33]. Similarly, Brennodden et al. proposed an energy-based pipe-soil interaction model based on physical experiments [34]. Later, based on Biot's model [13], Magda and Jeng employed the finite element model to investigate the wave-induced pore pressure around buried pipelines [35, 36]. Teh et al. and Sumer et al. conducted Flume experiments to investigate the wave-induced seabed response and the stability of subsea pipeline [37, 38]. By means of finite element model, the influences of pipeline-seabed contact effects and inertial effects on the wave-induced seabed response near the pipeline were examined by [39]. Later, Fredsøe reviewed the research process of pipeline-seabed interaction and pointed out the future research direction for pipeline stability in marine environment [2]. Recently, Gao revealed the coupled mechanism of fluid-pipeline-seabed [40]. Chen et al. studied the pipeline-soil interaction using the finite element model and concluded that the existence of pipeline can accelerate the accumulation of pore pressure at the top and side of pipeline [41]. The aforementioned studies can deepen the understanding of seabed response near the buried pipeline. However, most of the existing studies did not consider the effects of fluid shear stress at the seabed surface while examining the seabed dynamic response. Moreover, previous

studies normally used different numerical methods to solve fluid submodel and seabed submodel, respectively, which may affect the accuracy of the numerical results.

The purpose of this study is to investigate the fluid-induced dynamic response of seabed near the fully buried pipeline. Therefore, a two-dimensional fully coupled model for fluid-seabed-structure interaction is proposed within the framework of COMSOL multiphysics, where both the wave-current interaction and the fluid shear stress at the seabed surface are considered. Using the new model, the effects of the nonlinear pipeline-seabed contacts and the fluid characteristics on seabed dynamic response near the fully buried subsea pipeline are studied.

## 2. Methods

This paper mainly studies the fluid-induced transient dynamic response of seabed near the fully buried subsea pipeline, based on a two-dimensional numerical model built in the framework of COMSOL multiphysics, where the dynamic calculation is adopted. The quadrilateral mesh is used and the minimum size of the mesh is 0.01 m in this study. The new model mainly includes the fluid submodel, the seabed submodel, and the pipeline submodel. The fluid submodel and the seabed submodel are adopted to govern the fluid motions and the seabed dynamic response near the subsea pipeline. Meanwhile, the pipeline submodel is employed to describe the fluid-induced pipeline dynamic response.

The diagram of fluid-seabed-pipeline interaction (FSPI-2D) is shown in Figure 1, where  $L_s$  is the length of the calculated area,  $h$  is the depth of the seabed,  $L$  is the wave length,  $d$  is the depth of the water,  $e$  is the thickness of the pipeline cover,  $U$  is the current velocity,  $D$  is the pipeline diameter, and  $B$  is a point at the pipeline bottom.

*2.1. Fluid Submodel.* In the fluid submodel, the Reynolds averaged Navier–Stokes (RANS) equations with the  $\kappa$ - $\epsilon$  turbulence model is adopted to simulate the fluid propagations, and the level set method (LSM) is adopted to track the free water surface. As for a two-dimensional problem, the RANS equations can be expressed as follows:

$$\frac{\partial \langle \bar{\mu}_i \rangle}{\partial x_i} = 0, \quad (1)$$

$$\frac{\partial \langle \bar{\mu}_i \rangle}{\partial t} + \frac{\partial \langle \bar{\mu}_i \rangle \langle \bar{\mu}_j \rangle}{\partial x_j} = - \left( \frac{1}{p_w} \frac{\partial \langle P_w \rangle}{\partial x_i} + \frac{1}{p_w} \frac{\partial \tau_{ij}}{\partial x_j} \right) + g_i + S_i, \quad (2)$$

where  $x_i$  is the Cartesian coordinate,  $u_i$  and  $u_j$  are the ensemble averaged velocity,  $p_w$  is the water pressure,  $\rho_w$  is the water density.  $g_i$  is the component of gravity acceleration,  $t$  is time, and  $S_i$  is a source term related to wave characteristics, which is used to generate waves. Since the model in this study is two-dimensional, thus,  $S_y = 0$ ;  $\tau_{ij}$  is the shear stress tensor including the viscous stress and the Reynolds stress, which can be expressed as

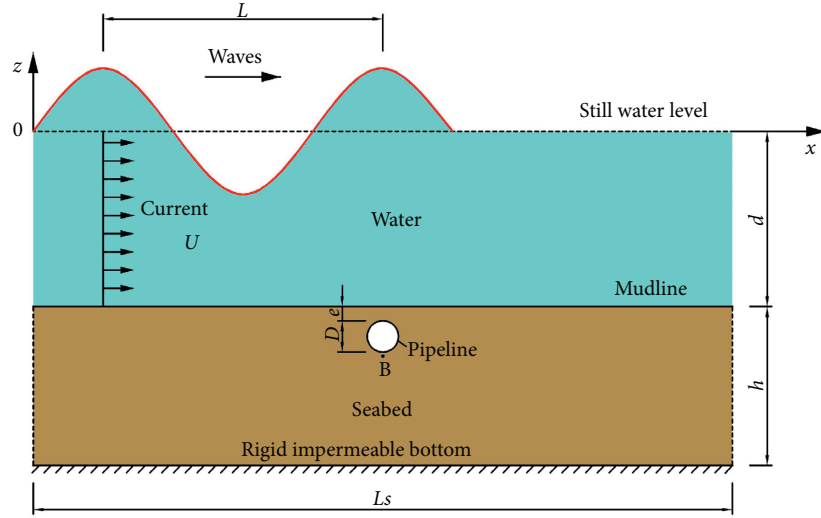


FIGURE 1: Diagram of the model for fluid-seabed-pipeline interactions.

$$\tau_{ij} = \mu_f \left[ \frac{\partial \bar{u}_i}{\partial x_j} + \frac{\partial \bar{u}_j}{\partial x_i} \right] - \rho \bar{u}'_i \bar{u}'_j, \quad (3)$$

$$-\rho \bar{u}'_i \bar{u}'_j = \mu_t \left[ \frac{\partial \bar{u}_i}{\partial x_j} + \frac{\partial \bar{u}_j}{\partial x_i} \right] - \frac{2}{3} \rho_w \delta_{ij} \kappa, \quad (4)$$

where  $\mu_f$  is the dynamic viscosity,  $\rho \bar{u}'_i \bar{u}'_j$  is the Reynolds stress term,  $\kappa$  is the turbulence kinetic energy,  $\delta_{ij}$  is Kronecker Delta's sign,  $\mu_t$  is the turbulent viscosity, and  $\varepsilon$  is dissipation rate of the turbulent kinetic energy. Based on (3) and (4), (2) can be written as

$$\left( \frac{\partial \rho_w \bar{u}_i}{\partial t} + \frac{\partial \rho_w \bar{u}_i \bar{u}_j}{\partial x_j} \right) = -\frac{\partial}{\partial x_i} \left[ p_w + \frac{2}{3} \rho_w \kappa \right] + \frac{\partial}{\partial x_j} \left[ \mu_{eff} \left( \frac{\partial \bar{u}_i}{\partial x_j} + \frac{\partial \bar{u}_j}{\partial x_i} \right) + \frac{2}{3} \rho_w g_i \right], \quad (5)$$

where  $\mu_{eff} = \mu_f + \mu_t$  is the total effective viscosity.

The  $\kappa$ - $\varepsilon$  turbulence model used in this study can be expressed as

$$\begin{aligned} \frac{\partial \rho_w \kappa}{\partial t} + \frac{\partial \rho_w \bar{u}_i \kappa}{\partial x_j} &= \frac{\partial}{\partial x_j} \left[ \left( \mu_f + \frac{\mu_t}{\sigma_\kappa} \right) \frac{\partial \kappa}{\partial x_j} \right] + G_\kappa - \rho_w \varepsilon, \\ \frac{\partial \rho_w \varepsilon}{\partial t} + \frac{\partial \rho_w \bar{u}_j \varepsilon}{\partial x_j} &= \frac{\partial}{\partial x_j} \left[ \left( \mu_f + \frac{\mu_t}{\sigma_\varepsilon} \right) \frac{\partial \varepsilon}{\partial x_j} \right] + \frac{\varepsilon}{\kappa} (C_{\varepsilon 1} G_\kappa - C_{\varepsilon 2} \rho_w \varepsilon), \\ G_\kappa &= \mu_t \left( \frac{\partial \bar{u}_i}{\partial x_j} + \frac{\partial \bar{u}_j}{\partial x_i} \right) \frac{\partial \bar{u}_i}{\partial x_j}, \end{aligned} \quad (6)$$

where  $C_\mu = 0.09$ ,  $\sigma_\kappa = 1.00$ ,  $\sigma_\varepsilon = 1.30$ ,  $C_{\varepsilon 1} = 1.44$ , and  $C_{\varepsilon 2} = 1.92$

The governing equation of the level set method can be expressed as

$$\frac{\partial \Phi}{\partial t} + \nabla(u_j \Phi) = \gamma \nabla \left( \varepsilon_{ls} \nabla \Phi - \Phi (1 - \Phi) \frac{\nabla \Phi}{|\nabla \Phi|} \right), \quad (7)$$

where  $\Phi$  is the level set function,  $\varepsilon_{ls}$  is the parameter that controls the interface thickness, and  $\gamma$  is the reinitialization parameter.

**2.2. Seabed Submodel.** In this paper, Biot's poro-elastic equation is taken to govern the seabed response induced by the wave and current loadings. The governing equation should be expressed as

$$\begin{aligned} \left( \frac{\partial^2 u_e}{\partial x^2} + \frac{\partial^2 u_e}{\partial z^2} \right) - \frac{\gamma_w n_s \beta_s}{k_s} \frac{\partial u_e}{\partial t} &= \frac{\gamma_w}{k_s} \frac{\partial \varepsilon_s}{\partial t}, \\ G \nabla^2 u_s + \frac{G}{1 - 2\mu} \frac{\partial \varepsilon_s}{\partial x} &= \frac{\partial u_e}{\partial x}, \\ G \nabla^2 w_s + \frac{G}{1 - 2\mu} \frac{\partial \varepsilon_s}{\partial z} &= \frac{\partial u_e}{\partial z}, \end{aligned} \quad (8)$$

where  $u_s$  and  $w_s$  are the soil displacements along  $x$ - and  $z$ -directions, respectively,  $u_e$  is wave-induced pore water

pressure,  $Y_w$  is the unit weight of water,  $n_s$  is the soil porosity,  $k_s$  is the soil permeability,  $\varepsilon_s$  is the soil volume strain,  $\beta_s$  is the compressibility of the pore fluid, and  $G$  is the shear modulus. The definition of  $\varepsilon_s$ ,  $\beta_s$ , and  $G$  can be expressed as follows:

$$\begin{aligned}\varepsilon_s &= \left( \frac{\partial u_s}{\partial x} + \frac{\partial w_s}{\partial z} \right), \\ \beta_s &= \frac{1}{K_w} + \frac{(1 - S_r)}{P_{w0}}, \\ G &= \frac{E}{2(1 + \mu)},\end{aligned}\quad (9)$$

where  $K_w$  is the true elastic modulus of water, which is taken as 2.0 GPa in this study,  $S_r$  is the degree of seabed saturation,  $P_{w0}$  is the absolute water pressure,  $E$  is Young's modulus, and  $\mu$  is Poisson's ratio.

**2.3. Pipeline Submodel.** In the pipeline submodel, the pipeline is assumed to be a linear elastomer. In other words, the relationship between the stress and strain follows Hook's law, which can be expressed as follows:

$$\begin{aligned}\{\sigma\} &= [D]\{\varepsilon\} \\ &= [D][B]\{\delta\}^e,\end{aligned}\quad (10)$$

where  $[D]$  is the elastic matrix,  $[B]$  is the element strain matrix, and  $\{\delta\}^e$  is the element node displacement matrix.

**2.4. Boundary Condition.** In the numerical study, the boundary conditions can significantly affect the accuracy of the numerical results. The new model of this paper includes five boundary conditions, which are the water surface boundary condition, the seabed surface boundary condition, the seabed bottom boundary condition, the pipeline-seabed interface, and the seabed lateral sides boundary condition.

**2.4.1. Water Surface Boundary Condition.** The relative pressure at the free surface of water is zero at the water surface.

**2.4.2. Seabed Surface Boundary Condition.** As mentioned previously, one of the new contributions in this study is that the fluid shear stress is considered while examining the seabed dynamic response. Therefore, at the seabed surface, the shear stress of the soil ( $\tau_{szx}$ ) is equal to the fluid shear stress ( $\tau_w$ ) and the pore pressure ( $u_e$ ) is equal to the wave pressure acting on the seabed surface ( $p_a$ ). Meanwhile, the normal effective stress ( $\sigma'_z$ ) is equal to zero:

$$\begin{aligned}u_e &= p_a, \\ \tau_{szx} &= \tau_w, \\ \sigma'_z &= 0.\end{aligned}\quad (11)$$

**2.4.3. Seabed Bottom Boundary Condition.** In this study, the seabed is assumed to be placed on a rigid bedrock. Therefore, the pore pressure gradient as well as the soil displacements are set to be  $z \partial u_e / \partial z = 0$  and  $u_s = w_s = 0$ , at  $z = 0$ .

**2.4.4. Pipeline-Seabed Interface Boundary Condition.** In this paper, the interaction between the pipeline and the surrounding seabed is simulated through the pipeline-seabed interface constitutive equation, which can be expressed as follows:

$$T_t = \nu_f T_n + T_c, \quad (12)$$

where  $T_t$  is the traction force,  $T_n$  is the contact pressure,  $T_c$  is the coherent sliding resistance, which is taken as  $1 \times 10^4$  Pa, and  $\nu_f$  is the static frictional coefficient, which is taken as 0.213 [42]. Once the traction force ( $T_t$ ) exceeds the coherent sliding resistance, the sliding will occur. In this study, the seabed is considered to be cohesive;  $T_c$  is taken as  $1 \times 10^4$  Pa, and  $\nu_f$  is taken as 0.213. It should be noted that the contact pressure ( $T_n$ ) in the above equation should be determined considering gravity of the soil, while the gravity is not considered in the governing equation of seabed response, which would be one shortcoming of this study.

**2.4.5. Seabed Lateral Sides' Boundary Condition.** The left and right sides of the seabed are assumed to be roller boundaries, and the pore pressure gradient should be zero:

$$\begin{aligned}u_s &= 0, \\ \frac{\partial u_e}{\partial n} &= 0.\end{aligned}\quad (13)$$

**2.5. Model Validation.** In this section, two model verifications are conducted to check the accuracy of the present numerical model, which are fluid model validation and fluid-seabed-pipeline interaction model validation.

**2.5.1. Fluid Model Validation.** In this section, the laboratory results from Qi and Gao [43] are selected to validate the wave-current model. The schematic diagram of the experiment is shown in Figure 2 and the input data are listed in Table 1. Meanwhile, Figure 3 illustrates the comparison results of pore pressure ( $u_e$ ) on the seabed surface with time between the present model and laboratory experiments. As shown in above figure 3, the numerical results are nearly in accordance with the laboratory results.

**2.5.2. Fluid-Seabed-Pipeline Interaction Model Validation.** The experimental data from Zhai et al. [44] are applied to validate the new model in simulating fluid-induced seabed response around the pipeline. Figure 4 shows the schematic diagram of this experiment, and Figure 5 illustrates the comparison results of wave-induced dynamic pore pressure at the bottom of the pipeline with time between the present model and laboratory experiments, where the input data are

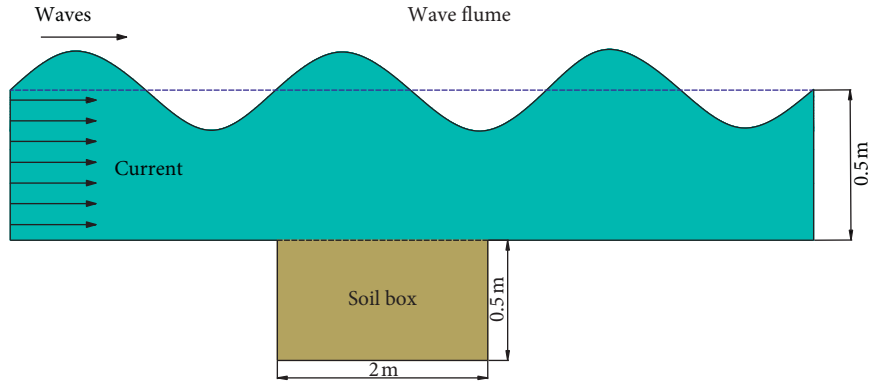


FIGURE 2: The schematic diagram of the experiment from Qi and Gao [43].

TABLE 1: Parameters used in the first validation.

Wave height ( $H$ )	0.085 m
Water depth ( $d$ )	0.5 m
Wave period ( $T$ )	1.4 s
Wave length ( $L$ )	2.57 m
Current velocity ( $U$ )	0.23 m/s
Seabed thickness ( $h$ )	0.5 m
Void ratio ( $e$ )	0.771
Buoyant unit weight of soil ( $\gamma'$ )	9.03 kN/m <sup>3</sup>
Relative density ( $D_r$ )	0.352
Soil permeability ( $k_s$ )	$1.88 \times 10^{-4}$ m/s

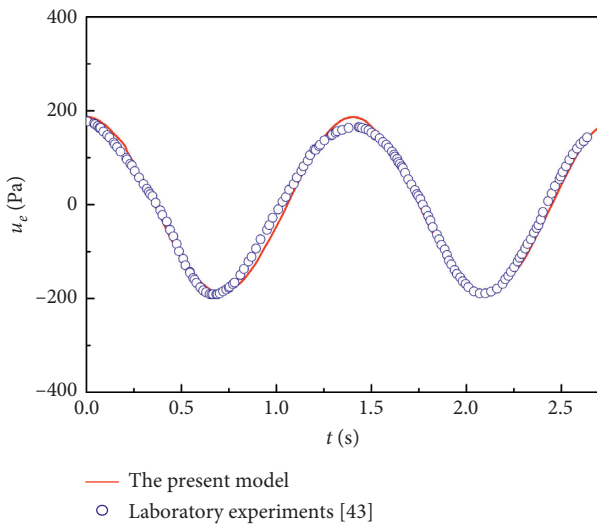


FIGURE 3: Comparison results of pore pressure at the surface of the seabed between the present model and the laboratory experiments [43].

listed in Table 2. It can be observed from Figure 5 that the simulated pore pressures agree well with laboratory measurements.

Based on the above two model validation results, it can be concluded that the present numerical model can effectively simulate the wave-current-seabed-pipeline interaction process.

### 3. Results and Discussion

As reported in previous studies, the fluid-induced soil dynamic response is a key factor to determine the seabed stability, which has been thoroughly studied in the past. However, most previous studies ignores the fluid shear stress at the seabed surface and pipeline-seabed contact effects when examining the seabed response, although Ye and Jeng [27] pointed out that the fluid shear stress may affect the maximum of the pore pressure in the case involving wave-current interaction. To examine the effects of fluid shear stress on seabed dynamic response, Figure 6 illustrates the comparison results of the wave- and current-induced pore pressure response at the bottom of the buried pipeline over a complete wave period between the model considering the fluid shear stress and the model without considering the fluid shear stress. It can be observed from Figure 6 that the pore pressure at the bottom of the pipeline is larger for the case considering the fluid shear stress onto the seabed surface.

In this section, the effects of pipeline-seabed contacts on fluid-induced seabed response are studied first. Then, the effects of fluid characteristics on seabed response and momentary liquefaction near the pipeline are fully checked. Finally, the momentary liquefaction around the buried pipeline is examined. The parameters used in the following study could refer to Table 3 unless specifically specified.

In this study, the criteria proposed by Zen and Yamazaki [45] are used to judge whether the seabed liquefies. As for these criteria, when the initial effective stress of the seabed is less than or equal to excess pore water pressure, the seabed will be considered to be liquefied:

$$\sigma'_0 \leq p, \quad (14)$$

where  $\sigma'_0$  is the initial effective stress in the soil and  $p$  is the excess pressure ( $p = u_e - p_a$ ).

*3.1. The Effects of the Pipeline-Soil Contact on Seabed and Pipeline Response.* The pipeline-soil interaction process is very complex, which belongs to nonlinear interface contact problem. In this section, the effects of the pipeline-soil

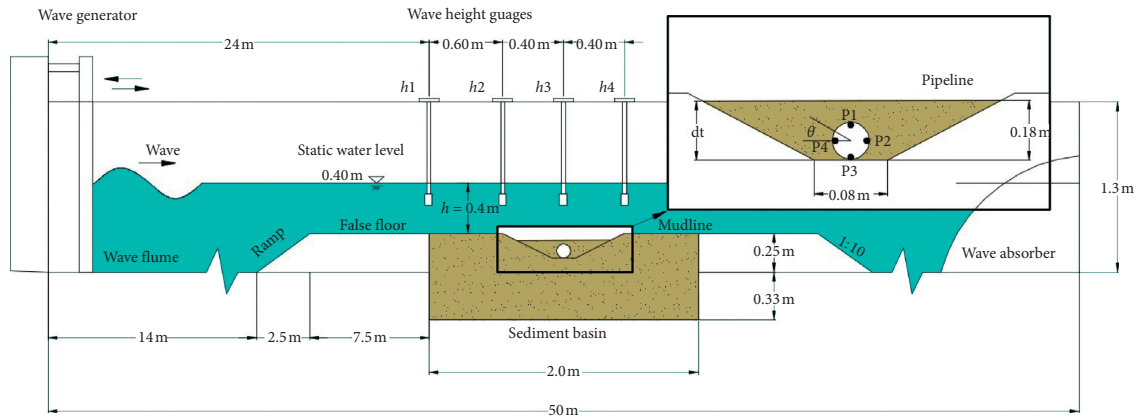


FIGURE 4: The schematic diagram of the experiment from Zhai et al. [44].

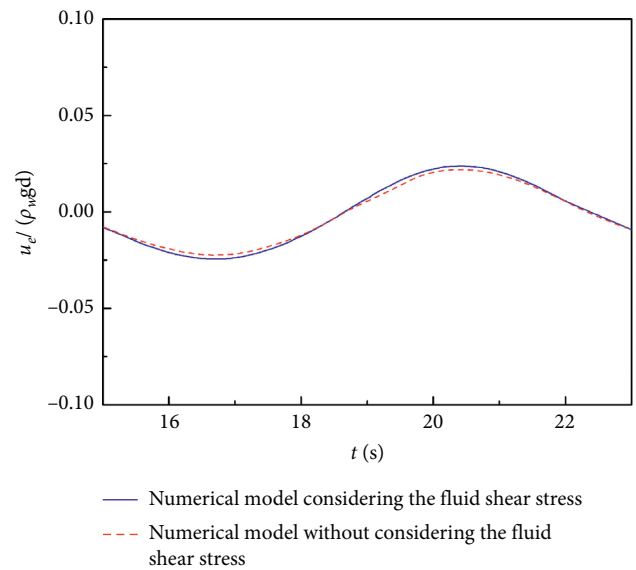
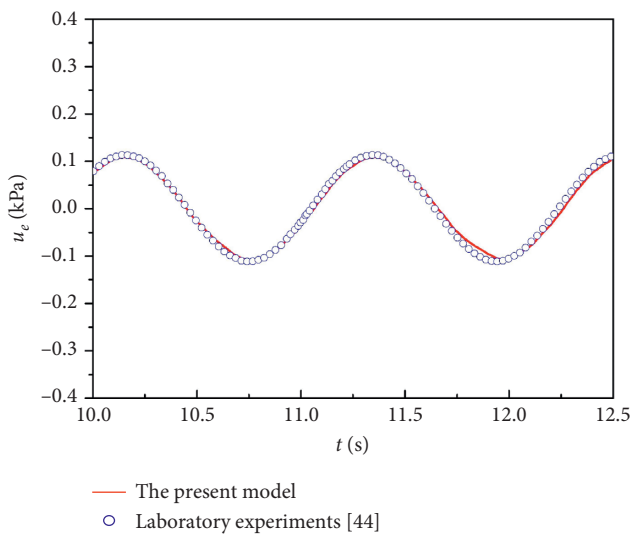


FIGURE 5: Comparison results of wave-induced pore pressure at the bottom of the pipeline between the present model and the experiments [44].

FIGURE 6: Comparison results of the pore pressure response at the bottom of the buried pipeline between the model considering the fluid shear stress and the model without considering the fluid shear stress.

TABLE 2: Parameters used in the second validation.

Wave period ( $T$ )	1.2 s
Wave height ( $H$ )	0.1 m
Soil permeability ( $k_s$ )	$3.75 \times 10^{-5}$ m/s
Shear modulus ( $G$ )	$8.28 \times 10^6$ Pa
Poisson's ratio ( $\mu$ )	0.3
Soil porosity ( $n$ )	0.369
Degree of saturation ( $S_r$ )	0.98

TABLE 3: Parameters used in the numerical examples.

Wave height ( $H$ )	4 m or various
Water depth ( $d$ )	7 m or various
Wave period ( $T$ )	8 s or various
Wave length ( $L$ )	61.39 m
Current velocity ( $U$ )	0.4 m/s or various
Seabed thickness ( $h$ )	20 m
Shear modulus ( $G$ )	$10^7$ N/m <sup>2</sup>
Poisson's ratio ( $\mu$ )	0.333
Soil permeability ( $k_s$ )	$1.5 \times 10^{-3}$ m/s
Degree of saturation ( $S_r$ )	0.98
Seabed porosity ( $n$ )	0.333
Density of soil ( $\rho$ )	1600 kg/m <sup>3</sup>
Density of water ( $\rho_w$ )	1000 kg/m <sup>3</sup>
Acceleration of gravity ( $g$ )	9.82 m/s <sup>2</sup>
Burial depth of pipeline ( $e$ )	0.5 m
Pipeline diameter ( $D$ )	1.2 m
Thickness of pipeline	0.01 m

contacts on fluid-induced seabed and pipeline responses are examined. Therefore, Figure 7 and Figure 8 display the distribution of the wave-current-induced seabed liquefaction and the pipeline dynamic response, where the wave trough is just passing over the pipeline.

It should be noted that the liquefaction zone, according to the criterion [45], has been removed when drawing the figures in this paper. Therefore, the white zone at the seabed surface and around the pipeline is the liquefaction zone. As shown in Figure 7, the liquefaction zone of the conode model

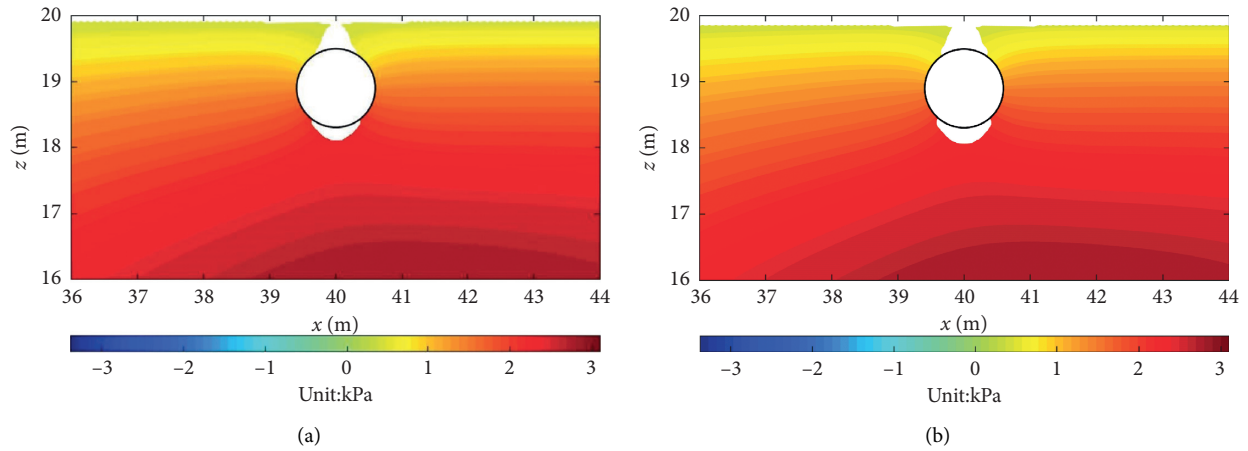


FIGURE 7: Distribution of the wave-current-induced liquefaction near the pipeline during the wave trough ( $H = 1$  m,  $T = 8$  s,  $d = 7$  m, and  $U = 0.4$  m/s): (a) the conode model; (b) the nonlinear contact model.

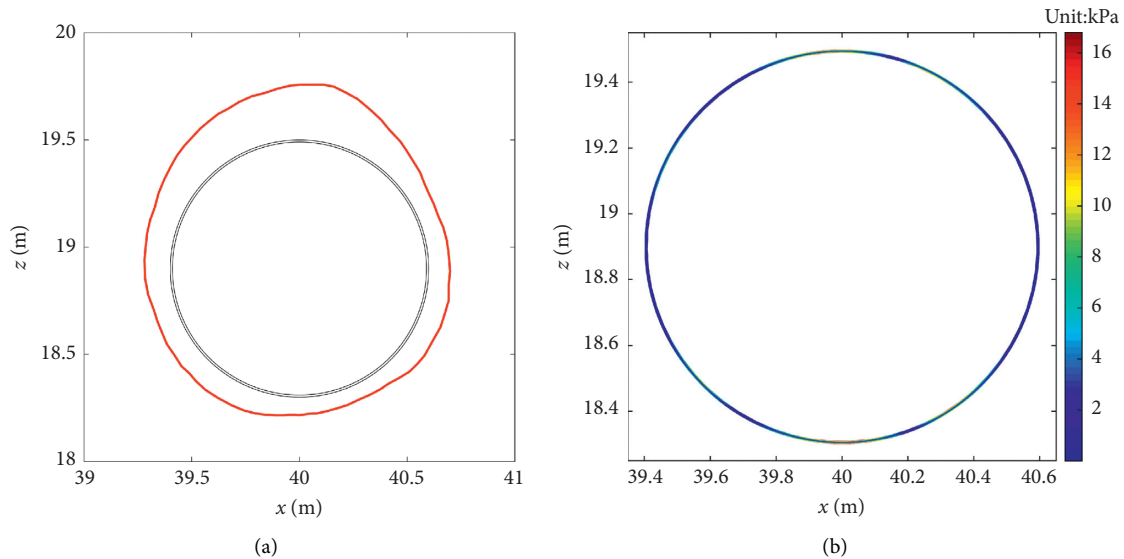


FIGURE 8: Dynamic response of the pipeline during the wave trough: (a) deformation profile of pipeline (magnified by 1000 times); (b) the distribution of stress of pipeline ( $H = 1.0$  m,  $T = 8$  s,  $d = 7$  m, and  $U = 0.4$  m/s).

near the pipeline is larger than that of the nonlinear contact model. Moreover, the liquefaction depth at the bottom of the pipeline in the conode model is 0.031 m greater than that in the nonlinear contact model (the liquefaction depth in the nonlinear contact model is 1.955 m). This phenomenon should be attributed to the over constraints of the pipeline on the surrounding seabed, which can increase the pore water pressure and enlarge the liquefaction region near the pipeline. Therefore, the nonlinear pipeline-soil contacts should be considered in the estimation of seabed response around the structure.

Based on the previous studies, the nonlinear interface contacts can greatly influence the structure dynamic response. As shown in Figure 8, the stresses of pipeline are larger at the top and the bottom of pipeline when the nonlinear pipeline-soil contact is considered. Notably, the

vertical displacement of the pipeline is large. Thus, emphasis should be placed on vertical pipeline displacement in the estimation of pipeline stability.

**3.2. Effects of Current Velocity on Pore Pressure Response near the Pipeline.** In the marine environment, the wave and current may co-exist and affect each other. Hence, the effects of wave-current interaction on the fluid-induced seabed response near the pipeline are investigated in this section. Thus, Figure 9 displays the pore water pressure over time at the surface of seabed and at the bottom of pipeline (in which  $U < 0$  means opposing current,  $U = 0$  represents no current, and  $U > 0$  means following current). As shown in Figure 9(a), the amplitude of pore pressure at the surface of seabed increases with the increasing current velocity. It is

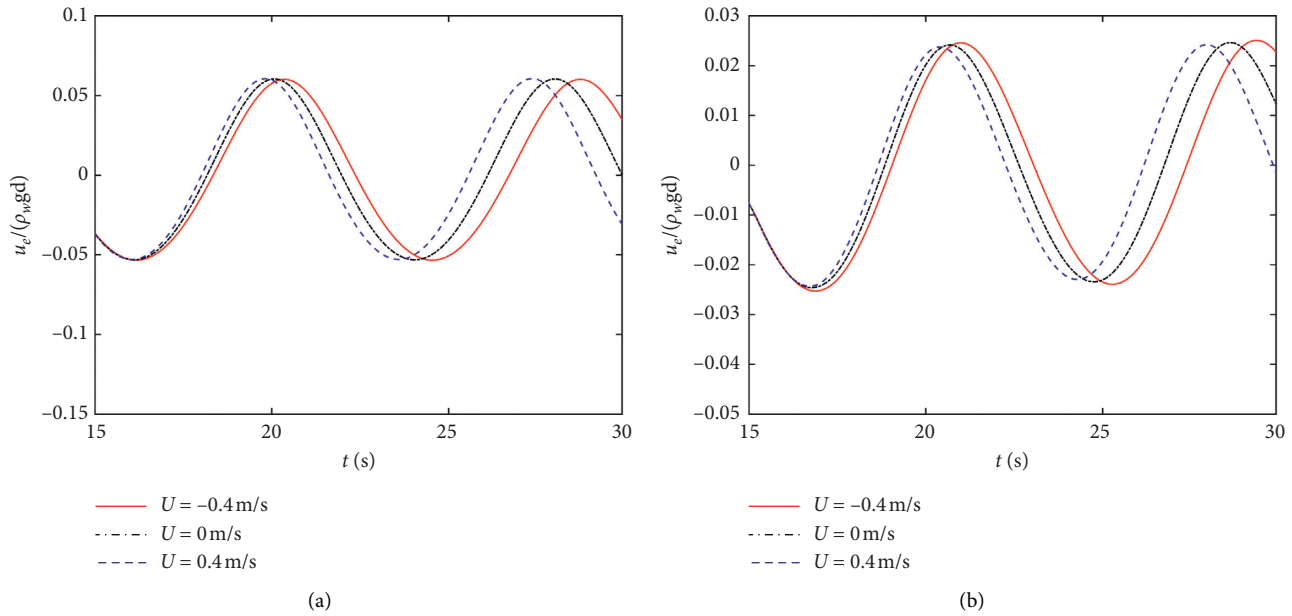


FIGURE 9: Variation of the wave-current-induced pore pressure over time at the surface of seabed and at the bottom of the pipeline ( $H = 1.0$  m,  $d = 7$  m, and  $T = 8$  s): (a) at surface of seabed; (b) at bottom of pipeline.

worth noting that the phase of waves decreases with increase of current velocity and the phase differences increase over time at different velocities. This phenomenon is due to the fact that the following current will accelerate the wave's propagation and opposing current will reduce the wave's propagation. Besides, the effect of currents on waves will increase with the amplitude of current velocity. It can be observed from Figure 9(b) that the amplitude of pore water pressure at the bottom of the pipeline increases with the increase of current velocity. Overall, the variation trend in Figure 9(a) is similar to that in Figure 9(b). Notably, the pore water pressure at the bottom of the pipeline for following currents is overall greater than that of the pore water pressure for opposing currents. In other words, the following current can aggravate the instability of seabed around a pipeline.

In addition, seven current velocities ( $U = -1.2$  m/s,  $-0.8$  m/s,  $-0.4$  m/s,  $0$  m/s,  $+0.4$  m/s,  $+0.8$  m/s,  $+1.2$  m/s) are selected to examine the effects of current on the fluid-induced oscillatory pore water pressure responses near the pipeline. Figures 10 and 11 illustrate the distribution of pore pressure in seabed around the pipeline and the amplitude of fluid-induced pore water pressure along the outer surface of the pipeline for different current velocities, where the wave trough is just passing over the pipeline. As shown in Figure 10, the pore water pressure near a pipeline continuously increases with the increase of current velocities. Furthermore, the pore water pressure around a pipeline when  $U = 1.2$  m/s improved by 15% compared to that when  $U = 0$  m/s and the pore water pressure around a pipeline when  $U = -1.2$  m/s reduced by 11% relative to that when  $U = 0$  m/s, respectively. Notably, the distribution of pore water pressure around the pipeline is dis-symmetric and this trend increases with the increase of amplitude of current

velocity. This phenomenon is due to the fact that the following currents may aggravate the wave-induced seabed response and the opposing currents may reduce the wave-induced seabed response. Meanwhile, the wave-current interaction can change the phase of wave, which can further induce the phase lags of the pore pressure within the seabed.

As shown in Figure 11, the amplitude of pore water pressure at the top of the pipeline is overall larger than that at the bottom of the pipeline, and the pore water pressure at the top of the pipe increases faster than that at the bottom of the pipeline as the current velocity increases. Moreover, the pore water pressure around the pipeline increases faster with the increase of the current velocity for the case with the following current. At the top ( $\theta = 90^\circ$ ), the lift side ( $\theta = 180^\circ$ ), and the bottom of pipeline ( $\theta = 270^\circ$ ), the difference of pore water pressure between when  $U = 1.2$  m/s and when  $U = 0$  m/s can reach up to 16.3%, 17.8%, and 14.6%, respectively, while the difference of the pore pressure between the case of  $U = -1.2$  m/s and the case of  $U = 0$  m/s only reaches up to 10.3%, 9.1%, and 12.4%, respectively. Consequently, the following current has a greater influence on fluid-induced seabed response near the pipeline than that of the opposing current.

**3.3. Effects of Wave Parameters on Pore Pressure Response near the Pipeline.** It is known that wave parameters can affect the fluid-induced dynamic pressure along the seabed surface, which may further influence the seabed instability. Among the wave parameters, the wave height ( $H$ ) can directly affect the fluid-induced dynamic pressure on the seabed surface. The wave period ( $T$ ) and the water depth ( $d$ ) can indirectly affect the wave-induced dynamic pressure on the seabed surface by changing wavelength ( $L$ ). Therefore, the effects of

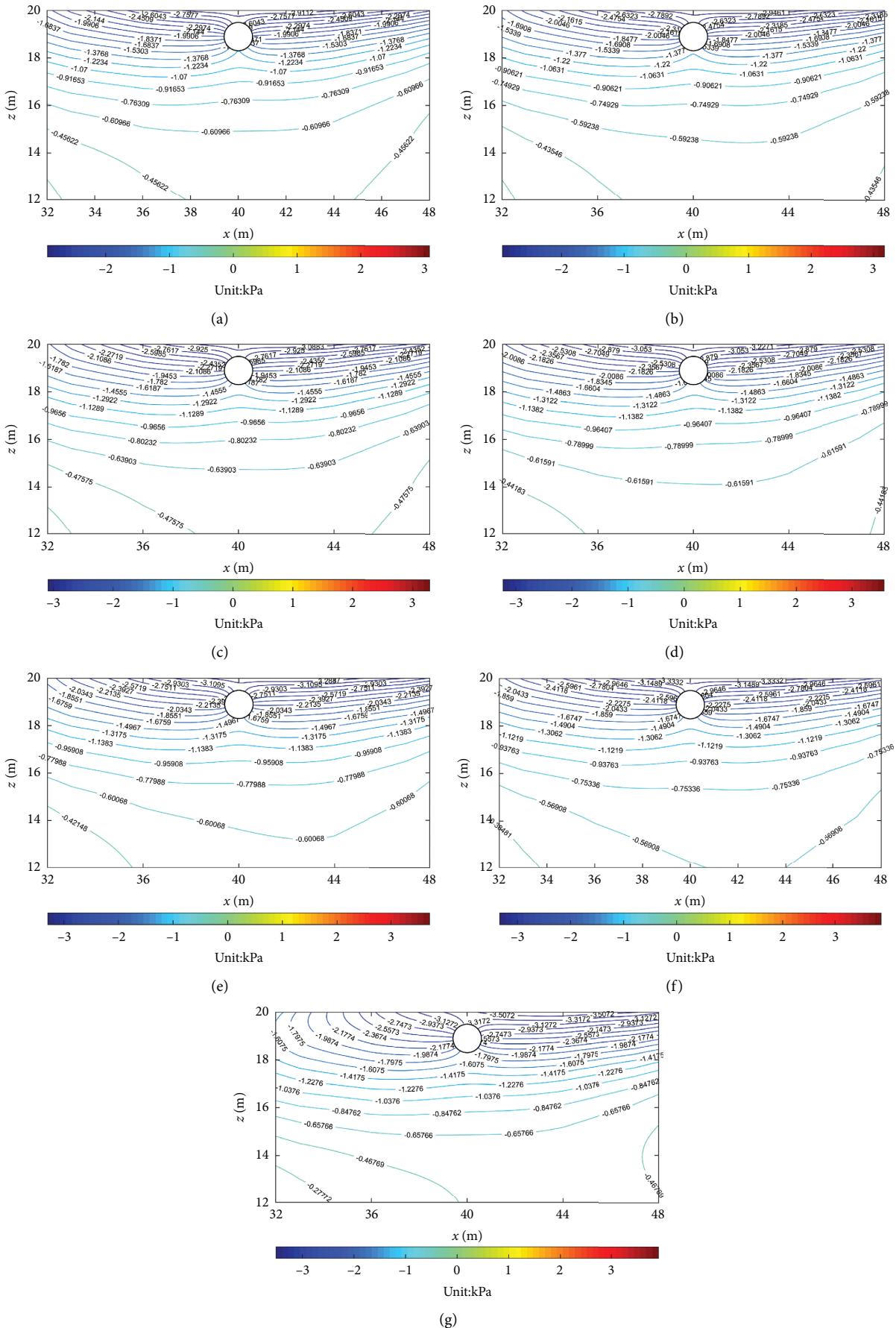


FIGURE 10: Distribution of pore pressure in seabed around the pipeline under different current velocities during the wave trough ( $H = 1$  m,  $T = 8$  s, and  $d = 7$  m): (a)  $U = -1.2$  m/s; (b)  $U = -0.8$  m/s; (c)  $U = -0.4$  m/s; (d)  $U = 0$  m/s; (e)  $U = 0.4$  m/s; (f)  $U = 0.8$  m/s; (g)  $U = 1.2$  m/s.



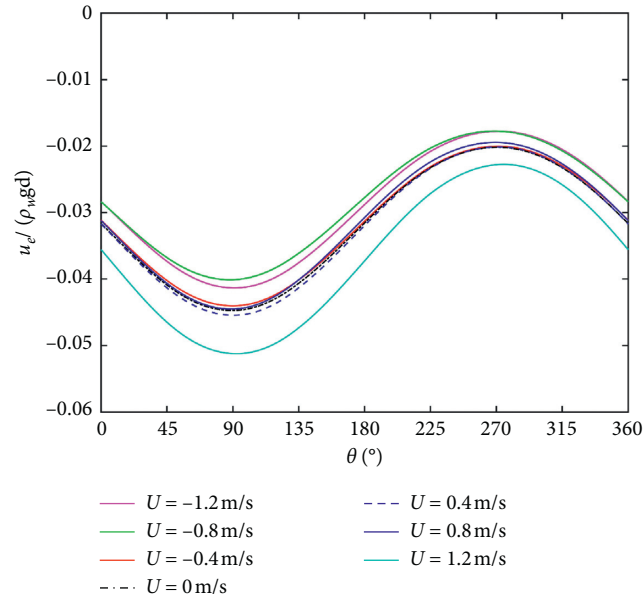


FIGURE 11: Distribution of amplitude of fluid-induced pore pressure along the pipeline outer surface under various current velocities ( $H = 1\text{ m}$ ,  $T = 8\text{ s}$ , and  $d = 7\text{ m}$ ).

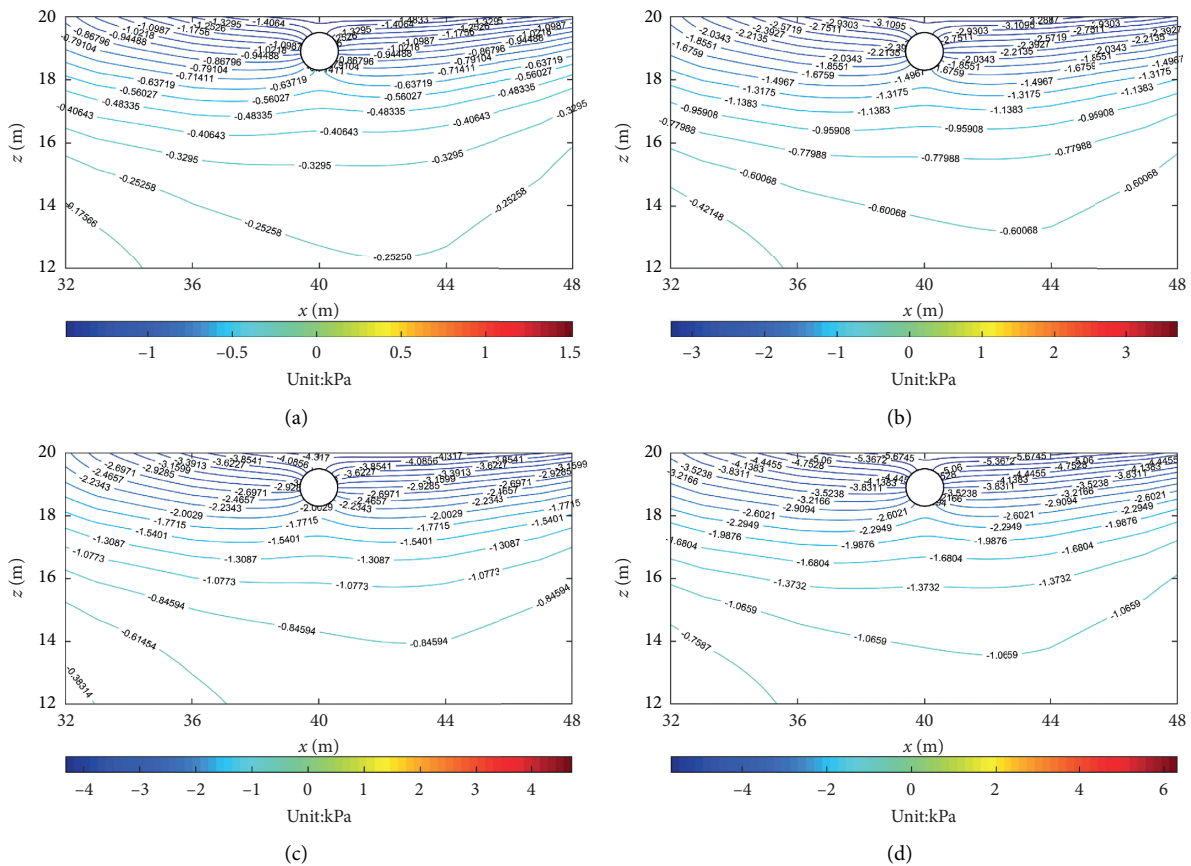


FIGURE 12: Distribution of pore pressure in seabed around a pipeline under different wave heights during the wave trough ( $T = 8\text{ s}$ ,  $d = 7\text{ m}$ , and  $U = 0.4\text{ m/s}$ ): (a)  $H = 0.5\text{ m}$ ; (b)  $H = 1\text{ m}$ ; (c)  $H = 1.5\text{ m}$ ; (d)  $H = 2\text{ m}$ .

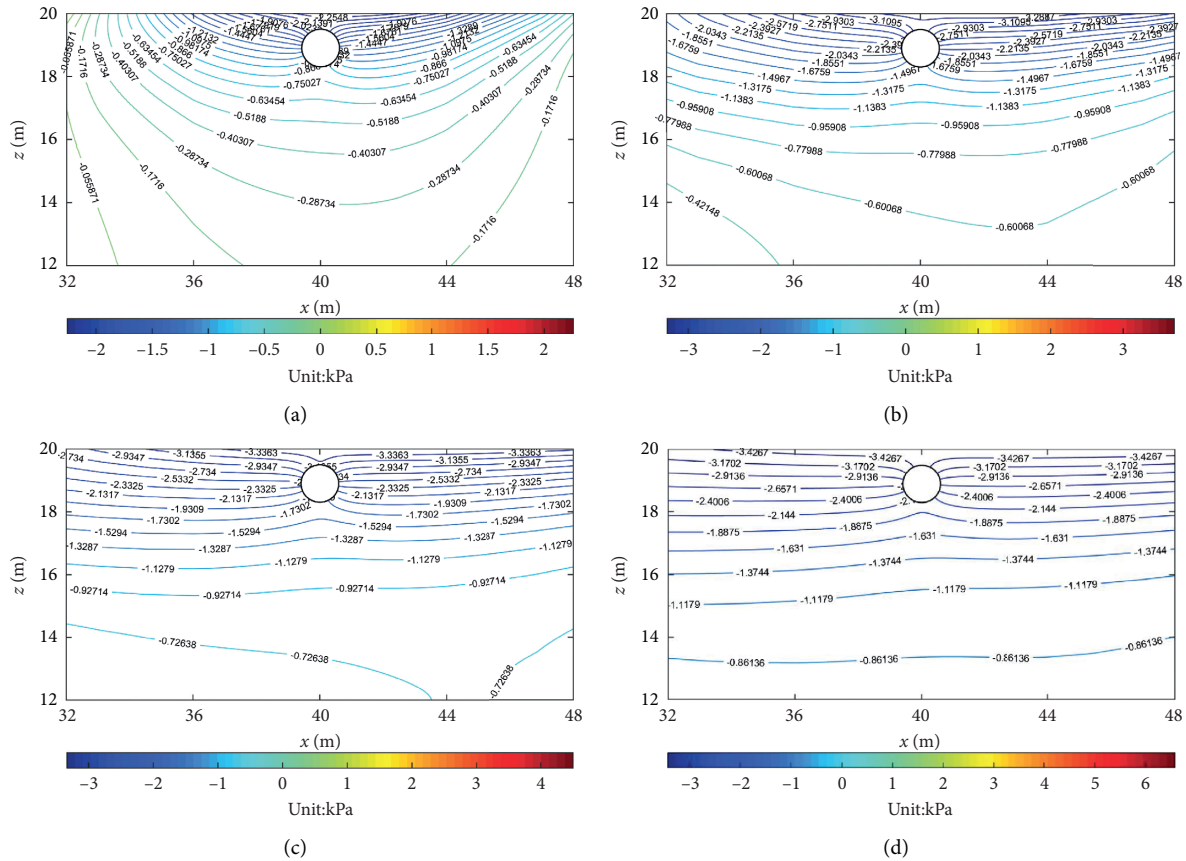


FIGURE 13: Distribution of pore pressure in seabed around a pipeline under different wave periods during the wave trough ( $H = 1\text{ m}$ ,  $d = 7\text{ m}$ , and  $U = 0.4\text{ m/s}$ ): (a)  $T = 5\text{ s}$ ; (b)  $T = 8\text{ s}$ ; (c)  $T = 11\text{ s}$ ; (d)  $T = 14\text{ s}$ .

wave height, wave period, and water depth on the fluid-induced pore water pressure are checked thoroughly based on the fully coupled model. In this section, the wave height ( $H$ ) ranges from 0.5 m to 2.0 m with an interval of 0.5 m, the wave period ( $T$ ) varies from 5 s to 14 s with an interval of 3 s, and the wave depth ( $d$ ) varies from 7 m to 16 m with an interval of 3 m. Figures 12–14 shows the distribution of pore water pressure in seabed around a pipeline with different wave heights ( $H$ ), different wave periods ( $T$ ), and different water depths ( $d$ ), respectively, where the wave trough is just passing over the pipeline. Figure 15 displays the distribution of amplitude of wave- and current-induced pore water pressure along the pipeline outer surface.

As shown in Figure 12, the pore water pressure near the subsea pipeline overall increases as the wave height increases. At the top ( $\theta = 90^\circ$ ), the lift side ( $\theta = 180^\circ$ ), and the bottom ( $\theta = 270^\circ$ ) of the pipeline, the pore water pressure increases linearly with the increase of the wave height, while the difference of pore water pressure at three locations can reach up to 47.6%, 46.3%, and 45.4% when  $H = 1.0\text{ m}$ , respectively. In addition, it can also be observed that the increase of pore water pressure at the top of the pipeline is larger than that at the bottom of the pipeline under the combined wave and current loadings. The difference of pore water pressure between the top ( $\theta = 90^\circ$ ) and the bottom ( $\theta = 270^\circ$ ) of the pipeline increases with the increase of the

wave height. Therefore, the potential instability of seabed around the subsea pipeline will enhance with the increase of wave height. As shown from Figure 13, with the wave periods' increase, the pore water pressure near the pipeline increases rapidly at first and then slows down. At the top ( $\theta = 90^\circ$ ), the lift side ( $\theta = 180^\circ$ ), and the bottom ( $\theta = 270^\circ$ ) of the pipeline, the differences of pore water pressure at three different locations are 17.3%, 22.5%, and 27.2% when  $T = 8.0\text{ s}$ , respectively. Figure 14 shows that the pore pressure around the pipeline decreases overall as the wave depth increases. At the top ( $\theta = 90^\circ$ ), the lift side ( $\theta = 180^\circ$ ), and the bottom of the pipeline ( $\theta = 270^\circ$ ), the decreased amplitude of pore water pressure can reach up to 12.1%, 9.4%, and 7.7% compared to that when  $d = 7.0\text{ m}$ , respectively.

**3.4. Fluid-Induced Momentary Seabed Liquefaction near the Pipeline.** Based on the new coupled model (FSPI-2D), the momentary liquefaction around the pipeline is examined in this section. Thus, Figure 16 illustrates the variation of fluid-induced momentary liquefaction around the pipeline in a complete wave period. As shown in Figure 16, the liquefaction zone, near the pipeline, changes constantly over the time. It is worth noting that the liquefaction region near the pipeline is greatest when the wave trough is over the pipeline head ( $t = 1/4 T$ ), and liquefaction mainly occurs at the

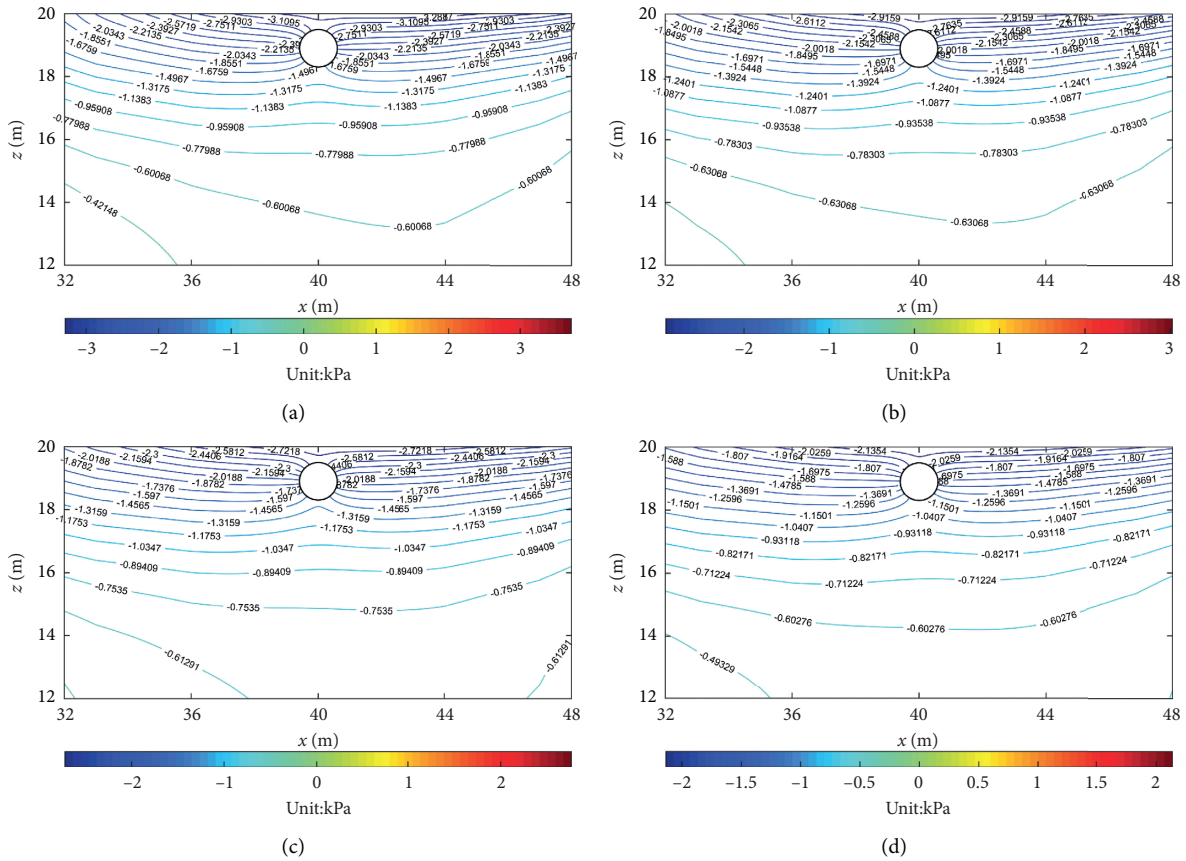


FIGURE 14: Distribution of pore pressure in seabed around the pipeline under different water depths during the wave trough ( $H=1$  m,  $T=8$  s, and  $U=0.4$  m/s): (a)  $d=7$  m; (b)  $d=10$  m; (c)  $d=13$  m; (d)  $d=16$  m.

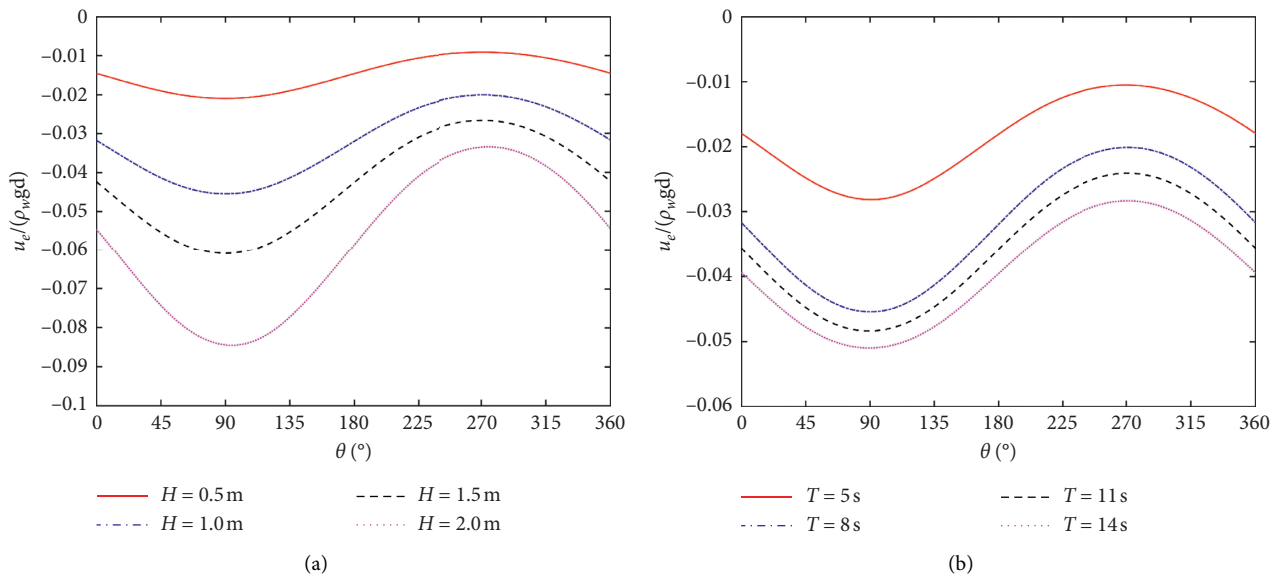


FIGURE 15: Continued.

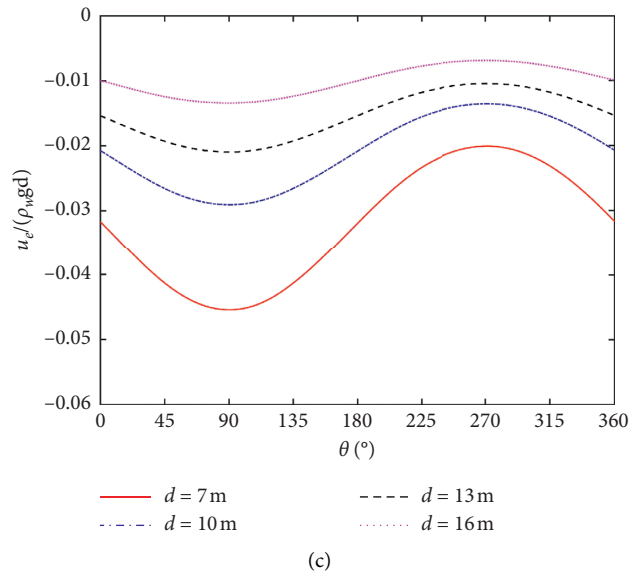


FIGURE 15: Distribution of the amplitude of the wave- and current-induced pore water pressure along the pipeline outer surface: (a)  $H=0.5\text{ m}, 1.0\text{ m}, 1.5\text{ m}, 2.0\text{ m}$  ( $T=8\text{ s}, d=7\text{ m}$ , and  $U=0.4\text{ m/s}$ ); (b)  $T=5\text{ s}, 10\text{ s}, 15\text{ s}, 20\text{ s}$  ( $H=1\text{ m}, d=7\text{ m}$ , and  $U=0.4\text{ m/s}$ ); (c)  $d=7\text{ m}, 10\text{ m}, 13\text{ m}, 16\text{ m}$  ( $H=1\text{ m}, T=8\text{ s}$ , and  $U=0.4\text{ m/s}$ ).

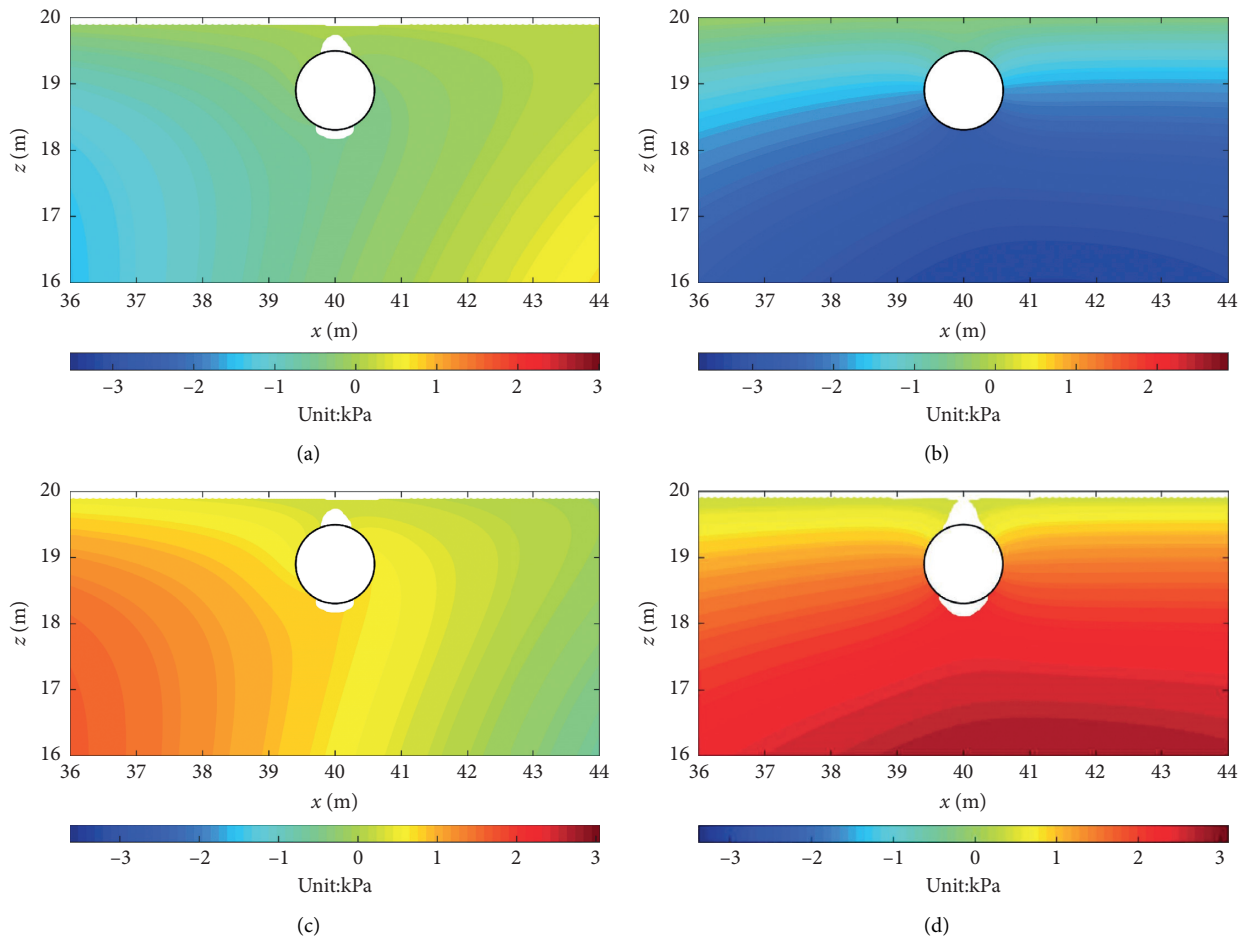


FIGURE 16: Variation of the wave- and current-induced momentary liquefaction around the pipeline in a complete wave period ( $H=1\text{ m}, T=8\text{ s}, d=7\text{ m}$ , and  $U=0.4\text{ m/s}$ ): (a)  $t=0$ , (b)  $t=1/4 T$ , (c)  $t=1/2 T$ , and (d)  $t=3/4 T$ .

surface of seabed and the top and bottom of the pipeline, which may cause the sinking or flotation of the pipeline.

#### 4. Conclusions

In this paper, the fluid-induced oscillatory seabed response and momentary liquefaction around the fully buried pipeline are thoroughly studied based on a 2D coupled model (FSPI-2D), where both the fluid shear stress at the seabed surface and the pipeline-seabed contact effects are considered. The new model is first validated with previous experimental reports, and then, the effects of fluid characteristics on seabed dynamic response are investigated in detail. The main findings of this study can be concluded as follows:

- (1) The pipeline-soil interaction and the fluid shear stress can enhance the fluid-induced oscillatory pore water pressure response near the structure
- (2) The fluid-induced stress response of the pipeline is small while the vertical displacement is large
- (3) The oscillatory seabed response can be enhanced with the increases of the current velocity when the wave travels following the current
- (4) The wave with a large wave height, a long time period, and a shallow depth may increase the liquefaction potential of the porous seabed

#### Data Availability

The data used to support the findings of this study are available from the corresponding author upon request.

#### Conflicts of Interest

The authors declare that they have no conflicts of interest.

#### Acknowledgments

The financial support of the China Postdoctoral Science Foundation (2020M683228), the Youth Project of Science and Technology Research Program of Chongqing Education Commission of China (KJQN-201900709), and the National Natural Science Foundation of China (51979017) are gratefully acknowledged. Meanwhile, the first author acknowledged the support of Fund of State Key Laboratory of Bridge Engineering Structural Dynamics and Key Laboratory of Bridge Earthquake Resistance Technology, Ministry of Communications, PRC.

#### References

- [1] M. F. Randolph, C. Gaudin, S. M. Gourvenec, D. J. White, N. Boylan, and M. J. Cassidy, "Recent advances in offshore geotechnics for deep water oil and gas developments," *Ocean Engineering*, vol. 38, no. 7, pp. 818–834, 2011.
- [2] J. Fredsøe, "Pipeline-seabed interaction," *Journal of Waterway, Port, Coastal, and Ocean Engineering*, vol. 142, no. 6, Article ID 03116002, 2016.
- [3] H.-Y. Zhao, J.-F. Zhu, J.-H. Zheng, and J.-S. Zhang, "Numerical modelling of the fluid-seabed-structure interactions considering the impact of principal stress axes rotations," *Soil Dynamics and Earthquake Engineering*, vol. 136, Article ID 106242, 2020.
- [4] T. Sui, L. H. Staunstrup, S. Carstensen, and D. R. Fuhrman, "Span shoulder migration in three-dimensional current-induced scour beneath submerged pipelines," *Coastal Engineering*, vol. 164, Article ID 103776, 2021.
- [5] E. Yamazaki, T. Kurasawa, S. Kakimoto, Y. Sumino, and I. Nakatsui, "Characteristics of acid urease from *Streptococcus mitior*," *Agricultural & Biological Chemistry*, vol. 54, no. 9, pp. 2433–2435, 1990.
- [6] B. M. Sumer and J. Fredsøe, *The Mechanics of Scour in the marine Environment*, World Scientific, Singapore, Asia, 2002.
- [7] D. S. Jeng, *Porous Models for Wave-Seabed Interactions*, Springer, Heidelberg, Germany, 2013.
- [8] L. Duan, C. Liao, D. Jeng, and L. Chen, "2D numerical study of wave and current-induced oscillatory non-cohesive soil liquefaction around a partially buried pipeline in a trench," *Ocean Engineering*, vol. 135, pp. 39–51, 2017.
- [9] Z. Liang and D.-S. Jeng, "PORO-FSSI-FOAM model for seafloor liquefaction around a pipeline under combined random wave and current loading," *Applied Ocean Research*, vol. 107, Article ID 102497, 2021.
- [10] J. Ye and K. He, "Dynamics of a pipeline buried in loosely deposited seabed to nonlinear wave & current," *Ocean Engineering*, vol. 232, Article ID 109127, 2021.
- [11] G. Yang and J. Ye, "Nonlinear standing wave-induced liquefaction in loosely deposited seabed," *Bulletin of Engineering Geology and the Environment*, vol. 77, no. 1, pp. 205–223, 2017.
- [12] G. Yang and J. Ye, "Wave & current-induced progressive liquefaction in loosely deposited seabed," *Ocean Engineering*, vol. 142, pp. 303–314, 2017.
- [13] M. A. Biot, "General theory of three-dimensional consolidation," *Journal of Applied Physics*, vol. 12, no. 2, pp. 155–164, 1941.
- [14] T. Yamamoto, H. L. Koning, H. Sellmeijer, and E. V. Hijum, "On the response of a poro-elastic bed to water waves," *Journal of Fluid Mechanics*, vol. 87, no. 1, pp. 193–206, 1978.
- [15] J. R. C. Hsu and D. S. Jeng, "Wave-induced soil response in an unsaturated anisotropic seabed of finite thickness," *International Journal for Numerical and Analytical Methods in Geomechanics*, vol. 18, no. 11, pp. 785–807, 1994.
- [16] O. C. Zienkiewicz, C. T. Chang, and P. Bettess, "Drained, undrained, consolidating and dynamic behaviour assumptions in soils," *Géotechnique*, vol. 30, no. 4, pp. 385–395, 1980.
- [17] D. S. Jeng, M. S. Rahman, and T. L. Lee, "Effects of inertia forces on wave-induced seabed response," *International Journal of Offshore and Polar Engineering*, vol. 9, no. 4, pp. 307–313, 1999.
- [18] D. S. Jeng and M. S. Rahman, "Effective stresses in a porous seabed of finite thickness: inertia effects," *Canadian Geotechnical Journal*, vol. 37, no. 6, pp. 1383–1392, 2000.
- [19] M. B. C. Ulker, M. S. Rahman, and D.-S. Jeng, "Wave-induced response of seabed: various formulations and their applicability," *Applied Ocean Research*, vol. 31, no. 1, pp. 12–24, 2009.
- [20] J. Ye and D.-S. Jeng, "Effects of bottom shear stresses on the wave-induced dynamic response in a porous seabed: PORO-WSSI (shear) model," *Acta Mechanica Sinica*, vol. 27, no. 6, pp. 898–911, 2011.

- [21] B. Liu, D.-S. Jeng, G. L. Ye, and B. Yang, "Laboratory study for pore pressures in sandy deposit under wave loading," *Ocean Engineering*, vol. 106, pp. 207–219, 2015.
- [22] L. Tong, J. Zhang, K. Sun, Y. Guo, J. Zheng, and D.-S. Jeng, "Experimental study on soil response and wave attenuation in a silt bed," *Ocean Engineering*, vol. 160, pp. 105–118, 2018.
- [23] M. B. C. Ülker, "Semianalytical solution to the wave-induced dynamic response of saturated layered porous media," *Journal of Waterway, Port, Coastal, and Ocean Engineering*, vol. 141, no. 1, Article ID 06014001, 2015.
- [24] Z. Guo, D.-S. Jeng, H. Zhao, W. Guo, and L. Wang, "Effect of seepage flow on sediment incipient motion around a free spanning pipeline," *Coastal Engineering*, vol. 143, pp. 50–62, 2019.
- [25] K. Li, Z. Guo, L. Wang, and H. Jiang, "Effect of seepage flow on shields number around a fixed and sagging pipeline," *Ocean Engineering*, vol. 172, pp. 487–500, 2019.
- [26] C. Zhou, G. Li, P. Dong, J. Shi, and J. Xu, "An experimental study of seabed responses around a marine pipeline under wave and current conditions," *Ocean Engineering*, vol. 38, pp. 226–234, 2013.
- [27] J. H. Ye and D.-S. Jeng, "Response of porous seabed to nature loadings: waves and currents," *Journal of Engineering Mechanics*, vol. 138, no. 6, pp. 601–613, 2012.
- [28] C. C. Liao, D.-S. Jeng, and L. L. Zhang, "An analytical approximation for dynamic soil response of a porous seabed due to combined wave and current loading," *Journal of Coastal Research*, vol. 315, no. 5, pp. 1120–1128, 2015.
- [29] F. Wen, J. H. Wang, and X. L. Zhou, "Response of saturated porous seabed under combined short-crested waves and current loading," *Journal of Coastal Research*, vol. 32, no. 2, pp. 286–300, 2016.
- [30] W.-G. Qi, C.-F. Li, D.-S. Jeng, F.-P. Gao, and Z. Liang, "Combined wave-current induced excess pore-pressure in a sandy seabed: flume observations and comparisons with theoretical models," *Coastal Engineering*, vol. 147, pp. 89–98, 2019.
- [31] B. M. Sumer, "Flow-structure-seabed interactions in coastal and marine environments," *Journal of Hydraulic Research*, vol. 52, no. 1, pp. 1–13, 2014.
- [32] D. A. Wagner, J. D. Murff, H. Brennodden, and O. Svegggen, "Pipe-soil interaction model," in *Proceedings of the The 8th Offshore Technical Conference (OTC 5504)*, pp. 181–190, Houston, TX, USA, May 1987.
- [33] D. A. Wagner, J. D. Murff, H. Brennodden, and O. Svegggen, "Pipe-soil interaction model," *Journal of Waterway, Port, Coastal, and Ocean Engineering*, vol. 115, no. 2, pp. 205–220, 1989.
- [34] H. Brennodden, J. T. Lieng, T. Sotberg, and R. L. P. Verley, "An energy-based pipe-soil interaction model," in *Proceedings of the 10th Offshore Technical Conference (OTC 6057)*, pp. 147–158, Houston, TX, USA, May 1989.
- [35] W. Magda, "Wave-induced uplift force on a submarine pipeline buried in a compressible seabed," *Ocean Engineering*, vol. 24, no. 6, pp. 551–576, 1997.
- [36] D. S. Jeng, "Numerical modeling for wave-seabed-pipe interaction in a non-homogeneous porous seabed," *Soil Dynamics and Earthquake Engineering*, vol. 21, no. 8, pp. 699–712, 2001.
- [37] T. C. Teh, A. C. Palmer, and J. S. Damgaard, "Experimental study of marine pipelines on unstable and liquefied seabed," *Coastal Engineering*, vol. 50, no. 1-2, pp. 1–17, 2003.
- [38] B. M. Sumer, C. Truelsen, and J. Fredsøe, "Liquefaction around pipelines under waves," *Journal of Waterway, Port, Coastal, and Ocean Engineering*, vol. 132, no. 4, pp. 266–275, 2006.
- [39] M. Luan, P. Qu, D.-S. Jeng, Y. Guo, and Q. Yang, "Dynamic response of a porous seabed-pipeline interaction under wave loading: soil-pipeline contact effects and inertial effects," *Computers and Geotechnics*, vol. 35, no. 2, pp. 173–186, 2008.
- [40] F.-p. Gao, "Flow-pipe-soil coupling mechanisms and predictions for submarine pipeline instability," *Journal of Hydrodynamics*, vol. 29, no. 5, pp. 763–773, 2017.
- [41] R. Chen, L. Wu, B. Zhu, and D. Kong, "Numerical modelling of pipe-soil interaction for marine pipelines in sandy seabed subjected to wave loadings," *Applied Ocean Research*, vol. 88, pp. 233–245, 2019.
- [42] H. Kishida and M. Uesugi, "Tests of the interface between sand and steel in the simple shear apparatus," *Géotechnique*, vol. 37, no. 1, pp. 45–52, 1987.
- [43] W.-G. Qi and F.-P. Gao, "Physical modeling of local scour development around a large-diameter monopile in combined waves and current," *Coastal Engineering*, vol. 83, pp. 72–81, 2014.
- [44] Y. Zhai, R. He, J. Zhao, J. Zhang, D.-S. Jeng, and L. Li, "Physical Model of wave-induced seabed response around trenched pipeline in sandy seabed," *Applied Ocean Research*, vol. 75, pp. 37–52, 2018.
- [45] K. Zen and H. Yamazaki, "Mechanism of wave-induced liquefaction and densification in seabed," *Soils and Foundations*, vol. 30, no. 4, pp. 90–104, 1990.

## Research Article

# An Analysis of Relationship between the Microfracture Features and Mineral Morphology of Granite

Meiben Gao <sup>1,2</sup>, Tianbin Li <sup>2</sup>, Junxun Zhu,<sup>3</sup> Hongyu Yin,<sup>2</sup> and Yongyi Yang<sup>1,4</sup>

<sup>1</sup>School of Emergency Science, Xihua University, Chengdu, Sichuan 610039, China

<sup>2</sup>State Key Laboratory of Geohazard Prevention and Geoenvironment Protection, Chengdu University of Technology, Chengdu, Sichuan 610059, China

<sup>3</sup>Shandong Construction Engineering Quality Inspection and Testing Center Co., Ltd., Jinan, Shandong 250031, China

<sup>4</sup>The Center of National Railway Intelligent Transportation System Engineering and Technology, China Academy of Railway Sciences Corporation Limited, Beijing 100081, China

Correspondence should be addressed to Tianbin Li; [lbt@cdut.edu.cn](mailto:lbt@cdut.edu.cn)

Received 25 June 2021; Accepted 27 July 2021; Published 31 July 2021

Academic Editor: Guowen Xu

Copyright © 2021 Meiben Gao et al. This is an open access article distributed under the Creative Commons Attribution License, which permits unrestricted use, distribution, and reproduction in any medium, provided the original work is properly cited.

Using the techniques of X-ray diffraction, polarizing microscopy, uniaxial compression, and scanning electron microscopy (SEM), the relationships between the microfracture features and mineral morphology of granite were studied. The results showed that feldspar, quartz, and biotite are the main components of the granite samples in this study. Biotite has a self-shaped flake structure with perfect cleavage. K-feldspar has a lattice double crystal structure with two groups of cleavage. Plagioclase has a semi-self-shaped plate structure with two groups of cleavage. Quartz is prismatic or granular and exhibits noncleavage. The microfracture features of biotite are flaky with exfoliation, and flake cleavage fracture is mainly determined by its peculiar flaky cleavage. Feldspar (K-feldspar and plagioclase) is plate, layered, or two groups of cleavage and is also mainly determined by its peculiar two groups of cleavage. The microfracture features of quartz are highly irregular, with many randomly distributed intergranular and transgranular cracks, small particles or granule bulges, similar to quartz crystal, and this is due to the noncleavage feature of quartz itself. It is demonstrated that microfractures are preferentially ruptured along cleavage planes for these granite minerals under the action of external forces.

## 1. Introduction

The study of rock micromorphology is of great importance for understanding the failure mechanisms and mechanical behaviour of rock. In recent years, many achievements have been made in rock microresearch based on the scanning electron microscope (SEM) technique [1–4]. For example, according to rock failure morphology under dry and saturated conditions, Zhang et al. found that water had little influence on the crack development direction, but promoted the development of microcracks [5]. Through the study of crack and microstructure characteristics of shale, Zhong et al. revealed the micro-macro mechanism of shale [6]. Li and Ni concluded that macrofatigue damage of granite was caused by the propagation and coalescence of cracks at the microscale [7]. Zhang and Zhao and Liang

et al. analysed the effect of loading rate on rock failure and found that more transgranular cracks occurred with increasing strain rate [8, 9]. Yao et al. analysed the correlation between the geometrical characteristic and fracture energy of marble [10].

In contrast, some researchers also investigated the microbehaviours of rocks by using model tests and numerical methods. In this field, Jiang et al. established a perfect microcementation model by the systemic study of model tests [11] and then used the model to simulate the cementation between rock particles [12]. With the combination of models of bonded particles and smooth joints, an equivalent crystal model was employed to reveal the fracture mechanism and strength of granite from a microscopic view [13]. In addition, according to the microfeatures visible through SEM, the characteristic image of the granite

microstructure can be obtained through a digital image processing method. Furthermore, with the development of numerical methods, the micromechanical characteristics and kinematic behaviours of rock grains can be analysed by those numerical methods, and these results reveals that cracks first generate at the interface, then in mica, and finally in feldspar and quartz [14, 15].

These findings, obtained from SEM, model tests, and numerical methods, focus predominantly on rock composition, natural microstructures, fracture morphology, microcrack fracturing, micromechanism, and micro-macro relationships, which are helpful in understanding rock mechanics. While rock is a natural assemblage of various mineral grains with different sizes, the size and morphology of each mineral grains undoubtedly affect their physical and mechanical properties [16]. Subsequently, grain size research studies on rocks were carried out [17]. Wong et al. found the peak strength decreased with the inverse square root of the mean grain size [18]. Hatzor et al. demonstrated that grain size alone cannot be used in correlation with ultimate strength; rather, the combination of both grain size and porosity controls the mechanical response of the rock [19]. Eberhardt et al. found that grain size had only a minor effect on new crack initiation, but did have a significant effect on crack propagation. Furthermore, they pointed out that rock strength decreased with increasing grain size, not by inducing crack initiation at lower stresses, but through a process where longer cracks propagating along longer planes of weakness coalesced at lower stresses [20]. Besides, Lan et al. found that the grain size distribution in brittle rocks was a good index to represent the microheterogeneity [21].

Certain types of rocks, such as granites, have similar composition minerals. Although their distribution and grain size differ, their mineral morphology is certain. Links between microfracture features and mineral morphology are rarely reported. In this research, granite compositions were measured using X-ray diffraction. The microfeatures of the granite after uniaxial compression were observed by scanning electron microscopy (SEM). This paper aims to explore the relationships between the microfracture features and mineral morphology of granite.

## 2. Experimental Tests

**2.1. Description of Rock Specimens.** Granite is an important raw material in industrial applications and is a widely distributed rock in the Earth's crust. It has applications in areas such as metallurgy, building materials, chemical industry, and agriculture. The granite used in this research was collected from the Gaoligongshan tunnel at a depth of 680 m in Baoshan city, Yunnan province, China. These specimens are grey in nature. Testing specimens have uniform texture, their average density is  $2.65 \text{ g/cm}^3$ , and the mean uniaxial compressive strength is 90 MPa.

**2.2. Testing Facilities and Testing Procedure.** The facilities used in this study involve an X-ray diffractometer (DMAX-3C made in Japan), polarizing microscope (Nikon

LV100POL, shown in Figure 1(a)), scanning electron microscope (Hitachi S-3000N, shown in Figure 1(b)), and uniaxial compression test machine (MTS815, shown in Figure 1(c)).

Firstly, we checked the original features of granite by X-ray diffraction and polarizing microscope experiment. The general morphological characteristics and arrangement of particles were determined using a polarizing microscope with a rock sheet (area  $22 \times 22 \text{ mm}$  and thickness  $0.03 \text{ mm}$ ). Meanwhile, to determine the mineral composition accurately, three small blocks were collected from different rock samples and ground into powder of approximately  $5 \text{ mm}$ . Then, we placed the powder in the diffractometer groove and covered it with a glass sheet to initiate this test.

Secondly, uniaxial compression tests were conducted using a stiff load frame with a closed-loop servo-control system (MTS815) at the Rock Mechanics Laboratory at the State Key Laboratory of Geohazard Prevention and Geo-environment Protection at the Chengdu University of Technology. The loading procedure in these experiments followed the International Society of Rock Mechanics (ISRM) guidelines. Specifically,  $1 \text{ kN}$  force was preloaded to make the rock sample fixed; then, axial loading was carried out at the loading rate of  $0.1 \text{ mm/min}$  until the specimen attains failure.

Finally, the SEM tests were carried out. The specimens for the SEM tests were typical blocks selected from the rock samples after the uniaxial compression tests. The microfracture features were observed by a set of rock sheets (area  $10 \times 10 \text{ mm}$  and thickness  $3 \text{ mm}$ ) after the process of cutting, grinding, and coating.

## 3. Mineral Characteristics of Granite

**3.1. Mineral Composition.** The constituent mineralogical components of granite and the composition of the granite are listed in Table 1. The mean components are feldspar (plagioclase 31% and K-feldspar 11%), quartz (25%), biotite (25%), chlorite (4%), tremolite (4%), and pyrite (2%).

**3.2. Mineral Morphology Features.** According to the polarizing microscope flake experiment results (Figure 2 and Table 2), biotite is self-shaped flake, with a set of perfect cleavage, yellowish brown-brownish green, with late chloritization, and a grain size in the range of  $0.4\text{--}1.0 \text{ mm}$ . Quartz has an aggregate distribution (prismatic and granular), mainly around feldspar, with a grain size in the range of  $0.2\text{--}0.7 \text{ mm}$ , which can reach up to  $1.5 \text{ mm}$ . Alkali feldspar (K-feldspar) exhibits a lattice double crystal structure or perthitic texture, with the grain size of most grains below  $2 \text{ mm}$ , in the range of  $1\text{--}5 \text{ mm}$ . Some creep metasomatism distribute around the local edge. The secondary alteration in the later stage is mainly characterized by sodium feldspar and weak kaolinite. Plagioclase (mainly, oligoclase-andesine) is a semi-self-shaped plate, with a cluster twin and girdle structure and a grain size in the range of  $0.5\text{--}2.0 \text{ mm}$ , which can reach up to  $3.0 \text{ mm}$ . The secondary alteration in the later stage is mainly weak chloritization or clay, and sericitization of a few grains is obvious.



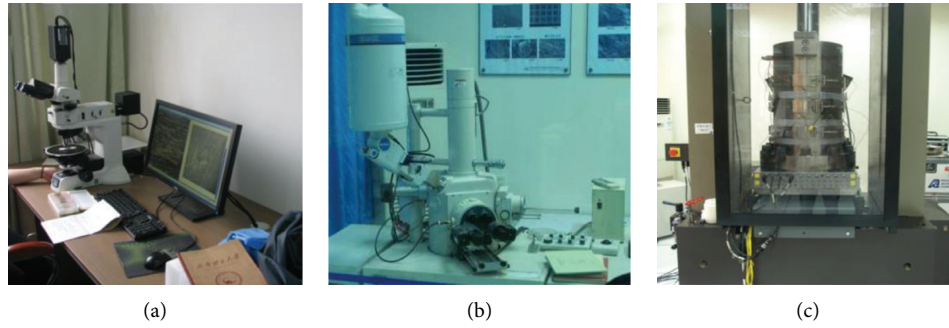


FIGURE 1: Testing facilities. (a) Nikon LV100POL polarizing microscope. (b) Hitachi S-3000N scanning electron microscope. (c) MTS815 rock mechanics testing machine.

TABLE 1: Mineralogical composition of the tested material (weight %).

Sample ID	Biotite	Quartz	K-feldspar	Plagioclase	Chlorite	Tremolite	Pyrite
G1	22	25	14	29	4	4	2
G2	27	22	9	32	3	4	3
G3	25	23	10	32	4	4	2
Mean	25	23	11	31	4	4	2

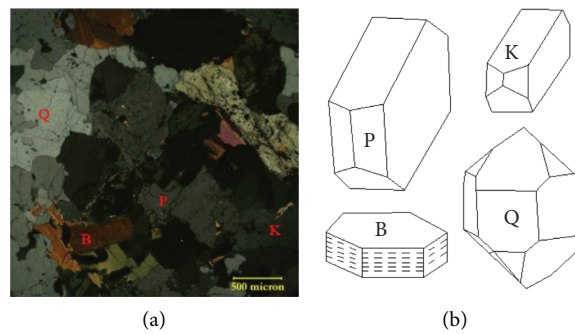


FIGURE 2: Microfeatures of granite. (a) Polarizing microscope features. (b) Mineral morphology (B: biotite, Q: quartz, K: K-feldspar, and P: plagioclase).

TABLE 2: Main mineral morphology features of granite.

Mineral	Particle size (mm)	Particle structure	Crystal form	Cleavage	Mohs hardness
Biotite	0.4–1.0	Self-shaped flake structure, perfect cleavage	Flake	Perfect cleavage	2.5
Quartz	0.2–1.5	Aggregate distribution, noncleavage	Prismatic and granular	Noncleavage and conchoidal fracture	7
K-feldspar	1.0–5.0	Lattice double crystal structure and perthitic texture	Thick plate and short columnar	Two groups of cleavage	6
Plagioclase	0.5–3.0	Semi-self-shaped plate, cluster twin, and girdle structure	Plate	Two groups of cleavage	6–6.5

#### 4. Microfeature and Analysis

4.1. *Microfeatures of Black Mica.* As shown in Figure 3(a), the mineral structure is loose, with pores and microcracks. The fracture is flaky, and the outer edge is uneven. A large number of transgranular cracks cut the mineral crystals into sheet-like crystal slices of different sizes, which are randomly distributed.

As shown in Figure 3(b), the contact state of mineral particles is good. The fracture is flaky, and the outer edge is

uneven. On the right side of the picture, the fracture characteristics are obviously flaky, and there is some grain particles' debris on the surface. The fracture on the upper left side is smooth and flat and is presumed to be a cleavage fracture along feldspar.

As shown in Figure 3(c), the contact state of mineral particles is good. The fracture surface is flat, and some biotite minerals show exfoliation fracture or parallel distortion along cleavage. The interface cracks develop well along the

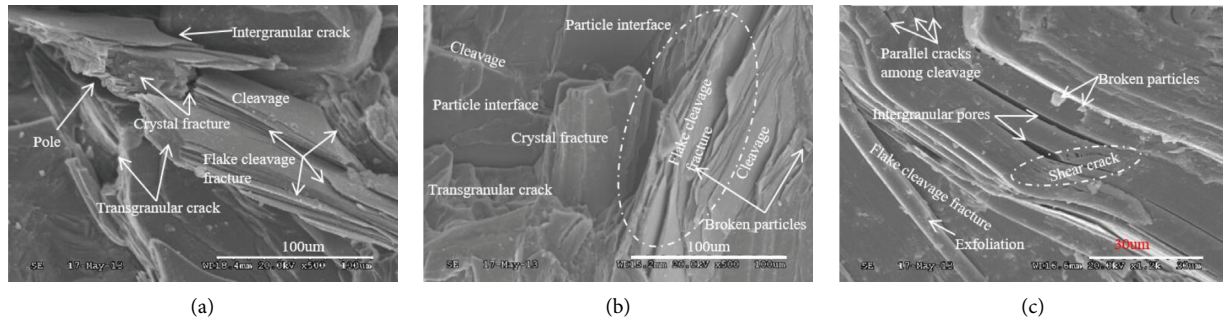


FIGURE 3: Main microfeatures of biotite. (a–c) Flaky fractures in granite samples.

long axis direction of the crack. Parts of the cracks terminate in the interior of the grains, forming an in-crystal crack. Moreover, parts of the cracks penetrate the whole mineral grains, forming a through-crystal crack resulting in flaky peeling. The surfaces of the in-crystal cracks and through-crystal cracks are smooth and flat. There is some grain particles' debris on the surface.

According to Figure 3, the microfracture features are flaky, exfoliation, and exhibits flake cleavage fracture. The combination of this and the mineral morphology show that only biotite is flake; feldspar is thick plate, plate, or short columnar; and quartz is prismatic or granular; thus, flaky rupture may only occur in flaky biotite minerals. Furthermore, the cleavage characteristics of granite minerals show that feldspar and quartz are two groups of cleavage and noncleavage or conchoidal fracture, respectively, which is inconsistent with the flake. In contrast, biotite is characterized by extreme perfect cleavage and flake and undergoes flaky damage under loading.

It is concluded that these flaky fractures in these granite samples may only occur in biotite mineral particles. On the basis of these features, the rupture characteristics of the biotite can be determined.

**4.2. Microfeatures of Feldspar.** As shown in Figure 4(a), the structure is relatively compact. Pores have not developed, and the original cracks are mostly in a closed state. The contact state of the mineral particles is good. The fracture is mainly transgranular, which is plate-like and the outer edge is rough rather than smooth. The particle interface is flat. Some cracks crack along the cleavage plane, and the surface is smooth. A number of tiny broken grain particles are distributed over the surface.

As shown in Figure 4(b), the structure is compact with limited pores and original cracks. The fracture is mainly along the cleavage with a smooth, layered, or plate surface. There are some small broken particles.

As shown in Figure 4(c), the structure is compact. There are no pores and original cracks. The contact state of mineral particles is good. Two main shear cracks may fracture along the two groups of cleavage, and their outer edge is uneven but smooth. The surface is without scratches and has no small particles. It is assumed that these fractures occurred within the feldspar particles along the cleavage.

According to Figure 4, the microfracture features are plate, layered, or two groups of cleavage, which is largely different from the fracture feature of biotite (flaky, exfoliated, and flake cleavage fracture). Compared with biotite flaky, these fractures have a certain thickness, and the fracture surface along the cleavage plane is flat and smooth, with good extension and plate-like rupture. The fracture features show the peculiar properties related to the two groups cleavage. These features, combined with the mineral morphology and cleavage characteristics of granite minerals, show that only feldspar has the two groups of cleavage, biotite is flaky, and quartz is prismatic or granular; thus, the plate, layered, or two groups of cleavage ruptures, with two-way extension, may only occur in feldspar minerals.

It is concluded that the plate, layered, or two groups of cleavage rupture fractures in these granite samples may only occur in feldspar mineral particles, and on the basis of these features, the rupture characteristics of the feldspar can be determined accordingly.

**4.3. Microfeatures of Quartz.** As shown in Figure 5(a), the mineral structure is loose, with many randomly distributed microcracks. The fracture surface is extremely uneven. Microcracks developed well, and they are mainly transgranular cracks with an uneven but relatively smooth surface. The right side of the picture shows a large number of messy small mineral particles.

As shown in Figure 5(b), a large number of small particles of different sizes are distributed irregularly over the surface. The presence of numerous intergranular and transgranular cracks causes breakage of the mineral crystals.

As shown in Figure 5(c), the fracture surface is extremely uneven, and there is a certain lamination phenomenon in the upper left corner, which is presumed to be a peculiar fracture in the biotite. There are many intergranular and transgranular cracks with uneven outer edges. The granule bulge in the middle, which has a smooth surface, is similar to the quartz crystal in Figure 2(b), and there is no obvious cleavage fracture surface.

According to Figure 5, the microfracture features are highly irregular, with many randomly distributed intergranular and transgranular cracks, small particles, or granule bulges, showing limited links to the regular cleavage. These fractures are not closely related to the exfoliation and flaky

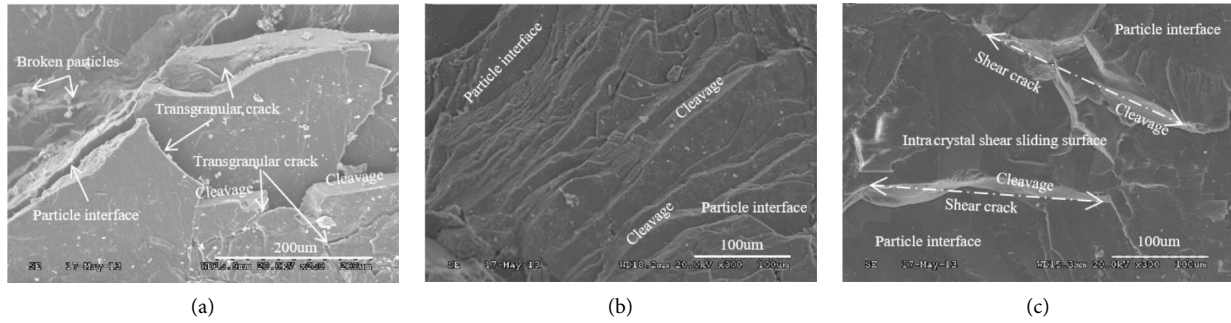


FIGURE 4: Main microfeatures of feldspar. (a, b) Plate or layered rupture fractures in granite samples. (c) Two groups of cleavage. Rupture fractures in granite samples.

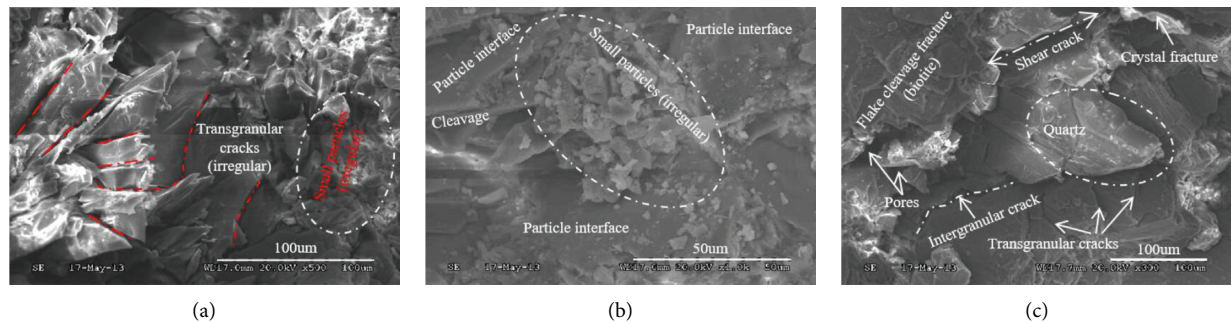


FIGURE 5: Main microfeatures of quartz. (a) Irregular, with many randomly distributed intergranular and transgranular cracks in granite samples. (b) Irregularly distributed particles in granite samples. (c) Granule bulges rupture fractures in granite samples.

characteristics of biotite and the characteristics of feldspar plate, layered, or two groups of cleavage fracture. Combining with the mineral morphology and cleavage characteristics of granite minerals, only quartz is prismatic, granular, and noncleavage; biotite is flaky; feldspar is thick plate, plate, or short columnar. Thus, these fractures that are not based on inherent cleavage may occur only in prismatic and noncleavage quartz minerals.

Above all, it is concluded that these fractures that are not based on inherent cleavage in these granite samples may only occur in quartz mineral particles, and on the basis of these features, the rupture characteristics of the quartz can be determined accordingly.

## 5. Conclusions

To study the relationship between the microfracture features and mineral morphology of granite, X-ray diffraction, polarizing microscopy, uniaxial compression, and SEM tests were conducted. Based on the experimental results and observations of the microfracture features and mineral morphology, the following findings are obtained. The main components and the compositions of the granite samples in this study are feldspar (plagioclase 31% and K-feldspar 11%), quartz (25%), and biotite (25%). Biotite has a self-shaped flake structure, flake, with perfect cleavage. K-feldspar has a lattice double crystal structure and perthitic texture, thick plate, or short columnar, with two groups of cleavage. Plagioclase has a semi-self-shaped plate, cluster twin and

girdle structure, plate, with two groups of cleavage. Quartz has an aggregate distribution, prismatic, and granular, with noncleavage or conchoidal fracture. The SEM results show that the microfracture features of biotite are flaky, exfoliation, and flake cleavage fracture, and these flaky fractures are the peculiar characteristics of biotite determined mainly by its cleavage. Feldspar (K-feldspar and plagioclase) has a plate structure, layered or two groups of cleavage, and these fracture features are also the peculiar characteristics of feldspar that are determined mainly by its cleavage. The microfracture features of quartz are highly irregular, with many randomly distributed intergranular and transgranular cracks, small particles, or granule bulging similar to quartz crystal; however, this is due to the noncleavage feature of quartz itself. These analyses demonstrate that microfractures are preferentially ruptured along cleavage planes for granite minerals under the action of external forces. The results of this study provide some reference value for the analysis of rock fracture mechanisms.

It is necessary to point out that the relationship between microfracture features and mineral morphology is the primary work for rock mechanics in terms of grain size. The final fracture and fracture pattern of rock samples are related to many factors, such as mineral composition, mineral morphology, mineral size, mineral distribution, mineral content, and interaction between mineral particles. Further research can be carried out from these two aspects: the fracture sequence of minerals and fracture process in terms of grain size.

## Data Availability

All the data used to support the findings of this study are included within the article.

## Conflicts of Interest

The authors declare no conflicts of interest.

## Acknowledgments

This research was supported by the National Natural Science Foundation of China (nos. U19A20111, 41772329, and 41230635), the On-Campus Talent Introduction Project in Xihua University (no. Z201125), and the Center of National Railway Intelligent Transportation System Engineering and Technology, China Academy of Railway Sciences (contract no. RITS2021KF04).

## References

- [1] M. L. Batzle, G. Simmons, and R. W. Siegfried, "Microcrack closure in rocks under stress: direct observation," *Journal of Geophysical Research*, vol. 85, no. B12, pp. 7072–7090, 1980.
- [2] X. Y. Wu, P. Baud, and T. F. Wong, "Micromechanics of compressive failure and spatial evolution of anisotropic damage in Darley Dale sandstone," *International Journal of Rock Mechanics and Mining Sciences*, vol. 37, no. 1, pp. 143–160, 2000.
- [3] M. J. Heap and D. R. Faulkner, "Quantifying the evolution of static elastic properties as crystalline rock approaches failure," *International Journal of Rock Mechanics and Mining Sciences*, vol. 45, no. 3, pp. 564–573, 2008.
- [4] W. Zhu, P. Baud, S. Vinciguerra, and T. F. Wong, "Micro-mechanics of brittle faulting and cataclastic flow in Alban Hills tuff," *Journal of Geophysical Research Atmospheres*, vol. 116, no. B6, pp. 1–23, 2011.
- [5] Y. B. Zhang, P. Liang, X. X. Liu, S. J. Liu, and B. Z. Tian, "Microstructure characteristics of rock burst fracture," *Journal of Liaoning Technical University: Natural Science*, vol. 34, no. 5, pp. 561–566, 2015.
- [6] J. H. Zhong, S. X. Liu, Y. S. Ma, C. M. Yin, C. L. Liu, and Z. X. Li, "Macro-fracture mode and micro-fracture mechanism of shale," *Petroleum Exploration and Development*, vol. 42, no. 9, pp. 242–250, 2015.
- [7] X. J. Li and X. H. Ni, "Test on meso-damage characteristic of granite mineral crystals under cyclic load," *Bulletin of Science and Technology*, vol. 31, no. 4, pp. 83–87, 2015.
- [8] Q. B. Zhang and J. Zhao, "Effect of loading rate on fracture toughness and failure micromechanisms in marble," *Engineering Fracture Mechanics*, vol. 102, no. 2, pp. 288–309, 2013.
- [9] C. Y. Liang, S. R. Wu, and X. Li, "Research on micro-meso characteristics of granite fracture under uniaxial compression at low and intermediates strain rates," *Chinese Journal of Rock Mechanics and Engineering*, vol. 34, no. s1, pp. 2977–2986, 2015.
- [10] S. F. Yao, Z. N. Zhang, X. R. Ge, Y. P. Qiu, and J. M. Xu, "Correlation between fracture energy and geometrical characteristic of mesostructure of marble," *Rock and Soil Mechanics*, vol. 37, no. 8, pp. 2341–2346, 2016.
- [11] M. J. Jiang, Y. G. Sun, L. Q. Li, and H. H. Zhu, "Contact behavior of idealized granules bonded in two different interparticle distances: an experimental investigation," *Mechanics of Materials*, vol. 55, pp. 1–15, 2012.
- [12] M. J. Jiang, Y. G. Sun, and Q. J. Yang, "A simple distinct element modeling of the mechanical behavior of methane hydrate-bearing sediments in deep seabed," *Granular Matter*, vol. 15, no. 2, pp. 209–220, 2013.
- [13] Y. Zhou, Y. T. Gao, S. C. Wu, Q. Yan, and H. Sun, "An equivalent crystal model for mesoscopic behaviour of rock," *Chinese Journal of Rock Mechanics and Engineering*, vol. 34, no. 3, pp. 511–519, 2015.
- [14] S. J. Miao, Z. J. Yang, C. Long, and F. H. Ren, "Micro-mechanical characteristics and cracks revolution laws of migmatitic granite under different loading conditions," *Journal of Jiangsu University (Natural Science Edition)*, vol. 33, no. 4, pp. 469–473, 2012.
- [15] Y. C. Yin, T. B. Zhao, Y. L. Tan, and F. H. Yu, "Reconstruction and numerical test of the mesoscopic model of rock based on Otsu digital image processing," *Rock and Soil Mechanics*, vol. 36, no. 9, pp. 2532–2540, 2015.
- [16] H. C. Heard, "Thermal expansion and inferred permeability of climax quartz monzonite to 300°C and 27.6 MPa," *International Journal of Rock Mechanics and Mining Science & Geomechanics Abstracts*, vol. 17, no. 5, pp. 289–296, 1980.
- [17] J. T. Fredrich, B. Evans, and T.-F. Wong, "Effect of grain size on brittle and semibrittle strength: implications for micro-mechanical modelling of failure in compression," *Journal of Geophysical Research*, vol. 95, no. B7, pp. 10907–10920, 1990.
- [18] R. H. C. Wong, K. T. Chau, and P. Wang, "Microcracking and grain size effect in Yuen Long marbles," *International Journal of Rock Mechanics and Mining Science & Geomechanics Abstracts*, vol. 33, no. 5, pp. 479–485, 1996.
- [19] Y. H. Hatzor, A. Zur, and Y. Mimran, "Microstructure effects on microcracking and brittle failure of dolomites," *Tectonophysics*, vol. 281, no. 3–4, pp. 141–161, 1997.
- [20] E. Eberhardt, B. Stimpson, and D. Stead, "Effects of grain size on the initiation and propagation thresholds of stress-induced brittle fractures," *Rock Mechanics and Rock Engineering*, vol. 32, no. 2, pp. 81–99, 1999.
- [21] H. X. Lan, C. D. Martin, and B. Hu, "Effect of heterogeneity of brittle rock on micromechanical extensile behavior during compression loading," *Journal of Geophysical Research*, vol. 115, no. B1, pp. 1–14, 2010.

## Research Article

# Stability of a Rock Tunnel Passing through Talus-Like Formations: A Case Study in Southwestern China

Shaoqiang Zhang,<sup>1</sup> Wenqiang Li,<sup>1</sup> Jiashan Tan,<sup>1</sup> Bokuan Li,<sup>1</sup> Xiaochang Li,<sup>2</sup> Shuaifeng Wang,<sup>2</sup> and Zixin Zhang<sup>2,3</sup>

<sup>1</sup>PowerChina Roadbridge Group Co., Ltd., Beijing 100048, China

<sup>2</sup>Department of Geotechnical Engineering, College of Civil Engineering, Tongji University, Shanghai 200092, China

<sup>3</sup>Key Laboratory of Geotechnical Engineering, Ministry of Education, Tongji University, Shanghai 200092, China

Correspondence should be addressed to Shuaifeng Wang; 1410264@tongji.edu.cn

Received 9 June 2021; Revised 1 July 2021; Accepted 8 July 2021; Published 24 July 2021

Academic Editor: Guowen Xu

Copyright © 2021 Shaoqiang Zhang et al. This is an open access article distributed under the Creative Commons Attribution License, which permits unrestricted use, distribution, and reproduction in any medium, provided the original work is properly cited.

Tayi tunnel is one of the component tunnels in the Jian-Ge-Yuan Highway Project located in Yunnan Province, southeast of China. It mainly passes through talus-like formations comprised of rock blocks of diverse sizes and weak interlayers with clayey soils with different fractions. Such a special composition leads to the loose and fractured structure of talus-like formations, which is highly sensitive to the excavation perturbation. Therefore, Tayi tunnel has become the controlled pot of the whole highway project as the construction speed has to be slowed down to reduce the deformation of surrounding talus-like rock mass. To better understand the tunnel-induced ground response and the interaction between the surrounding rock mass and tunnel lining, a comprehensive in situ monitoring program was set up. The in situ monitoring contents included the surrounding rock pressure on the primary lining, the primary lining deformation, and the stress of steel arches. Based on the monitoring data, the temporal and the long-term spatial characteristics of mechanical behavior of surrounding rock mass and lining structure due to the excavation process were analyzed and discussed. It is found that the excavation of lower benches released the surrounding rock pressure around upper benches, resulting in the decrease of the surrounding rock pressure on the primary lining and the stress of steel arches. In addition, the monitoring data revealed that the primary lining sustained bias pressure from the surrounding rock mass, which thereby caused unsymmetrical deformation of the primary lining, in accordance with the monitored displacement data. A dynamically adaptive support system was implemented to strengthen the bearing capacity of the lining system especially in the region of an extremely weak rock mass. After such treatment, the deformation of the primary lining has been well controlled and the construction speed has been considerably enhanced.

## 1. Introduction

Southwestern China has a complex terrain and complicated geological conditions with crisscrossed mountains and rivers, inducing complex geotechnical formations such as round gravel and mudstone mixture [1], layered phyllite strata [2], and rock-soil mixtures [3]. The talus-like rock masses, widely distributed in Yunnan Province in western China, are a special kind of geotechnical mixture, which is distinguishingly different from the common rocks, soils, or rock-soil mixture. The talus-like rock masses are mainly

distributed in the elurium, colluvium, and diluvial layers of Quaternary System. The main components of the talus-like rock masses are rock blocks with diverse sizes with interlayers filled with weak rock or clayey soils with different fractions, which can be regarded as special weak rock masses. Different from the traditional rock-soil mixture, the talus-like formations are a special kind of geotechnical mixture and have very complicated compositions with a wide range of grain diameters.

The recent studies about geotechnical mixture are mainly focused on the traditional talus development [4, 5]

and the rock-soil mixture [6–10] including in situ survey and laboratory test. Coli et al. [11] carried out an in situ shear test on shale-limestone chaotic complex bimrock and calculated its strength parameters based on a limit equilibrium analysis. Afterwards, the possible correlations between the scarce direct information from the in situ shear test data and the large indirect information from the synthetic image parameters were presented based on geostatistics [12]. Xu et al. [13] obtained the rock proportion and the granular distribution of soil-rock mixture using a combined method with large-scale direct shear test and digital image analysis, which was then implemented to investigate the mixture's shear strength characteristics and failure mechanism. Kalender et al. [14] developed a preliminary empirical strength criterion for determining the strength parameters of an unwelded rock-soil mixture by considering the mechanical behavior of the boundaries between matrix and blocks based on in situ and lab tests data. Afifpour and Moarefvand [15] conducted a series of uniaxial compression tests on artificial bimrocks models with high rock block proportions to investigate the bimrocks' mechanical behavior. In addition to the physical tests, the numerical simulation is also a mighty approach to investigate the mechanical and failure mechanisms of rock-soil mixture. Tsesarsky et al. [16] presented the influences of volumetric block proportion, block shape, and block orientation on the elastic moduli using finite element simulation. Xu et al. [17] developed a new multi-circle representation method of random polygonal blocks to generate the mesostructure model of a rock-soil mixture and implemented the model into simulating the mechanical behaviors of rock-soil mixture. Meng et al. [18] presented a numerical study on the elastic property of a rock-soil mixture using random mesostructure generation and found that the elastic modulus decreases gradually with an increase in the model size. Khorasani et al. [19] derived an equation linking the safety factor of bimslope (a slope formed by bimrocks) with volumetric block proportion using physical tests and corresponding numerical simulations, making it possible to evaluate the range of safety factors based on volumetric block proportion. Although there are series of studies on rock-soil mixtures and talus formations, there are still no guides or criteria especially for the talus-like formations, which brings uncertainty and hidden danger to the supporting structure design of tunnels and slopes excavated in such type of rock mass.

This paper investigates the stability of a tunnel passing through talus-like rock masses via site survey and field monitoring. Firstly, the paper describes the basic information about the project case. In the project, the in situ monitoring items included the pressure on the primary lining from the surrounding rock mass, the stress of steel arches, and the deformation of the primary lining. Afterwards, the influence of construction activities on the talus-like ground and the stability characteristics of the tunnel in talus-like rock masses are analyzed based on in situ monitoring. Finally, a dynamically adaptive support system is presented based on the mechanical characteristics of talus-like formations.

## 2. Project Background

**2.1. Project Overview.** The Jian-Ge-Yuan Highway Project is located in the southern Yunnan Province, linking up the Jianshui County, Gejiu City, and Yuanyang County, as shown in Figure 1. The length of the project is about 124.5 km, with 100 bridges and 29 tunnels. The length of bridges and tunnels occupies 72% of the total length of the project. Tayi tunnel, one of the component tunnels in the Jian-Ge-Yuan Highway Project, is located at the junction of Jianshui County and Yuanyang County, as shown in Figure 1(b). There are two lines in the tunnel: the left line is 2616 m long (from Z5K62 + 502 to Z5K65 + 118) and the right line is 2593 m long (from K62 + 489 to K65 + 082). The buried depth mainly ranges from 100 m to 250 m with a maximum depth of 297 m.

**2.2. Geological Conditions.** Tayi tunnel passes across Red River fault zone, resulting in developed secondary structures and complex lithology due to the rupturing movement. The tunnel mainly passes through moderately to strongly weathered slate mixed up with siltstone, limestone, mudstone, and soil. Dense fractures and minor structures in the rock mass are heavily developed with sharply steep dip angles and disordered dip directions. The development of weak bands with irregular distribution brings up fragmented and loose rock masses with poor integrity, inducing a low ability of self-stabilization of the excavated tunnel.

Up to now, 10 boreholes have been conducted to explore the geological conditions along the tunnel route, the detailed information of which is listed in Table 1. The encountered rock mass was evaluated according to the Chinese standard for engineering classification of rock masses [20] and code for design of road tunnels [21]. In general, the rock mass can be divided into different categories ranging from grade I to grade V based on the hardness degree, intactness index, and the quantitatively basic quality index BQ. The BQ value is obtained as

$$BQ = 90 - 3R_C + 250K_V, \quad (1)$$

where  $R_C$  is the uniaxial compressive strength of the rock mass and  $K_V$  is the intactness index of the rock mass. The higher the grade is, the more fragmented and weathered the rock mass will be. In Tayi tunnel, grade IV rock mass accounts for about 30%, and grade V covers about 70% of the route. The revealed rock mass in the boreholes is shown in Figure 2, where the range of tunnel section indicates the values of depth of tunnel vault and invert, respectively. It should be noted that the given range of the tunnel section is usually larger than the actual excavation height of the tunnel (Figure 2).

The surrounding rock masses exhibit an obvious characteristic of hybrid formation composited by rock and weak interlayer filled with soil or other weaker rock as shown in Figure 2. Figure 3 gives some examples revealed during the tunnel excavation showing the complex formation. At chainage Z5K62 + 936 of the left line, the rock mass is composited by slate and weak interlayer filled with



FIGURE 1: Site location (a) and layout plan (b) of the Jian-Ge-Yuan Highway Project. The site location is based on the standard map (no. GS(2019) 1684) by Ministry of Natural Resources of the People's Republic of China. The layout plan is based on the online map by National Platform for Common Geospatial Information Services of the People's Republic of China.

mudstone and has a highly loose and fragile structure with low strength (Figure 3(a)), which can be easily crushed by hand. Figures 3(b) and 3(c) show a type of fractured slate sandwiched by clay soil and a mixed rock mass formed by slate, limestone, and carbonaceous mudstone at Z5K63 + 966 and Z5K64 + 455, respectively. In the right line, twisted layers composed by slate and limestone, isolated rock blocks cut by weak mudstone interlayers, and limestone with carbonaceous mudstone interlayer were explored at K62 + 860, K64 + 530, and K64 + 570, as shown in Figures 3(d)–3(f), respectively. The abovementioned geological mixture composed by rock and soil (or weaker rock) revealed in Tayi tunnel is quite different from the traditional rock-soil mixture (often called talus formation) as explored by previous studies [17, 22–24], which can be regarded as rock-in-soil talus. Thus, we tentatively call such a kind of rock masses composed by rock and soil as talus-like formations. They are sensitive to the excavation perturbation, inducing that Tayi tunnel has become the controlled pot of the whole highway project as the construction speed has to be slowed down in order to reduce the deformation of surrounding talus-like ground. The explored engineering problems in the tunnel include (1) large deformation of the primary lining (Figure 4(a)), (2) rock collapse of the excavation surface and side walls (Figures 4(b) and 4(c)), and (3) broken primary lining (Figure 4(d)).

**2.3. Construction Design and Support System.** Tayi tunnel is constructed using the bench cut method with three steps as shown in Figure 5. The heights of the three benches are 3.98 m, 3.76 m, and 2.86 m from the top-down, respectively (Figure 5(b)). Usually, the length of the upper bench is about 8 m to ensure enough space for the operation of excavation machinery. The excavated tunnel is designed to be supported by a compound primary lining composed by mortar anchors, steel meshes, I-beam steel arches (Figure 5(c)), and shotcrete. After the installation of steel arches of each bench, two-foot reinforcement bolts (42 mm radius and 3.5 m

length) are used on both sides to strengthen the bearing capacity of steel arches (Figure 5(a)). As shown in Figure 5(b), the spacing along the excavation direction of steel arches is 80 cm and thus the longitudinal spacing of mortar anchors is set as 80 cm, while the circumambient spacing is 120 cm. According to the longitudinal spacing of steel arches, the length of each excavation step of the upper bench is set as 1.6 m and the excavation length of middle and lower benches is set as 2.4 m, i.e., two and three times of the spacing, respectively. The secondary lining is in the form of cast-in situ reinforced concrete with 45 cm thickness, of which the reinforcement design is shown in Figure 5(d). The reserved deformation between the primary and second linings is 10 cm. Before excavation of the upper bench, grouting tremies with 42 mm radius, 3.5 mm thickness, and 4.5 m length are used to pre-support the surrounding rock masses. The longitudinal spacing of the tremies is 80 cm to match the installation of steel arches and the circumambient is 30 cm. The inclination angle to pipe the tremies is set as 40° to ensure the splicing length between two adjacent tremies is larger than 3.9 m. It should be noted that this system support is designed for the general grade IV~V surrounding rock masses.

### 3. Insight from the In Situ Monitoring

To investigate the mechanical characteristics of the primary lining in talus-like rock masses, in situ monitoring was established in Tayi tunnel, including the pressure on the primary lining from surrounding rock, the stress of steel arches, and the deformation of the primary lining.

**3.1. Monitoring Scheme.** The deformation of the primary lining was measured by the total station. There were 5 monitoring points in each monitoring section as shown in Figure 6(a), which were mainly located on the upper bench. The monitoring points were established after spraying the shotcrete of the primary lining. The primary

TABLE 1: Detailed information of boreholes.

Borehole no.	Chainage (left line)	Chainage (right line)	Depth of borehole (m)	Range of tunnel section (m)	[BQ]	Grade
BH-01	—	K62 + 875	80.69	72.34~80.69	265	IV ~ V
BH-02	Z5K63 + 396.4	K63 + 375.64	145.01	126.13~145.01	215	V
BH-03	Z5K63 + 620.67	K63 + 597	141.7	128.8~141.7	92.5	V
BH-04	—	K63 + 643	153.5	140~153.5	105	V
BH-05	Z5K63 + 769.3	K63 + 753	200.6	185.2~200.6	272	IV
BH-06	Z5K63 + 842.65	K63 + 817.7	209.5	195~209.5	255	IV ~ V
BH-07	Z5K63 + 954.91	K63 + 930	255.2	233.5~255.2	312	IV
BH-08	Z5K64 + 180.23	K64 + 156.45	305	278.7~300.1	275	IV
BH-09	Z5K64 + 310.46	K64 + 286	305.3	283~305.3	267	IV ~ V
BH-10	—	K64 + 700	213.67	193.08~213.67	265	IV ~ V

Note: [BQ] is the estimated BQ value according to the geological conditions of boreholes.



FIGURE 2: Pictures for the revealed rock mass by boreholes.



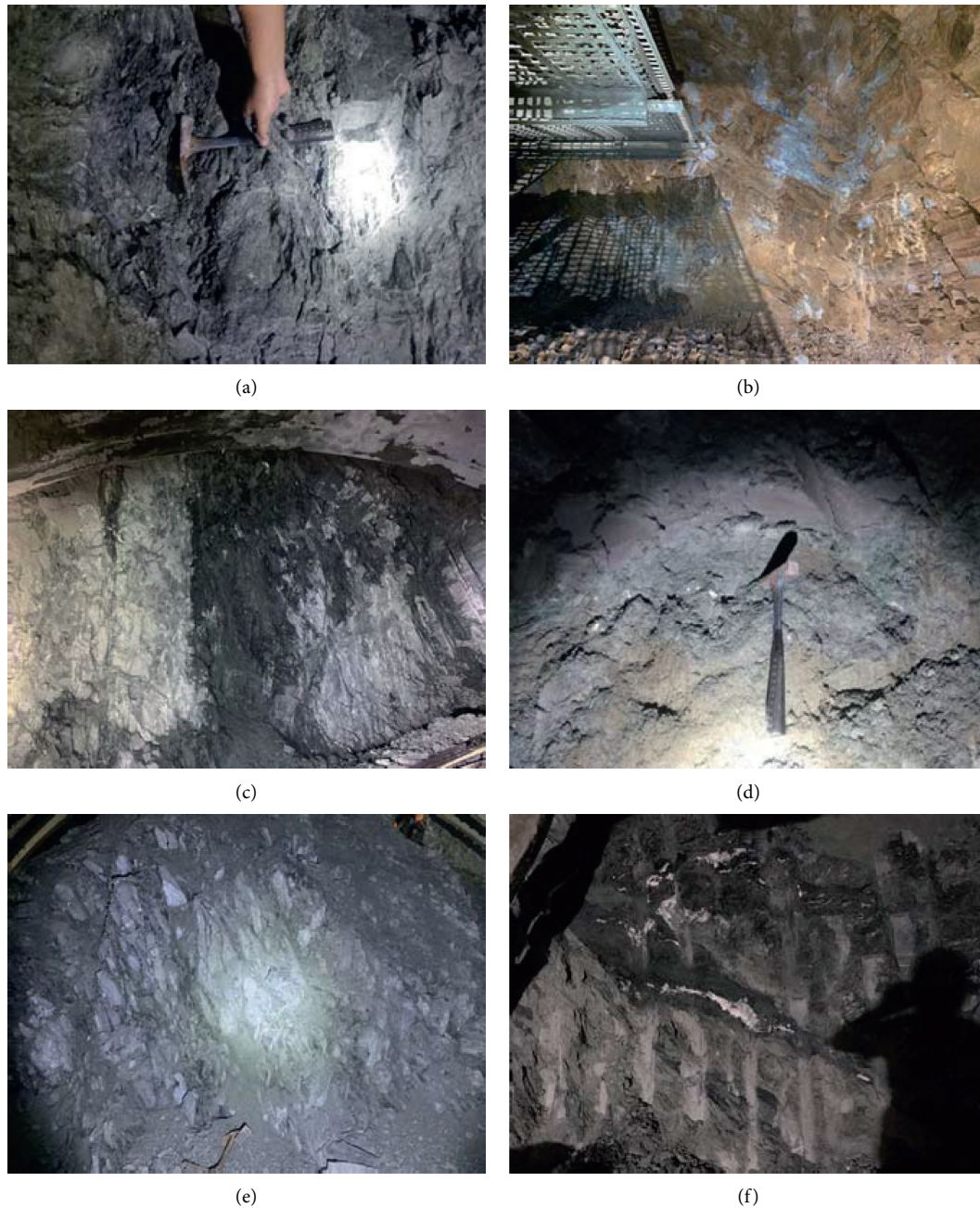


FIGURE 3: Talus-like rock mass encountered during the tunnel excavation: (a) slate and weak interlayer filled with mudstone at Z5K62 + 936; (b) slate and weak interlayer filled with weathered rock and soft soil at Z5K63 + 966; (c) mixture of slate, limestone, and carbonaceous mudstone at Z5K64 + 455; (d) twisted layers composited by slate and limestone at K62 + 860; (e) isolated rock blocks cut by interlayers filled with weak mudstone at K64 + 530; (f) limestone with carbonaceous mudstone interlayer at K64 + 570.

lining deformation was carried out every 5 m along the tunneling direction and measured twice a day. 7 monitoring points are designed to measure the pressure on the primary lining from surrounding rock and the stress of steel arches as shown in Figure 6(b). The pressure on the primary lining from surrounding rock was measured by vibrating wire pressure transducers, which were located on the outer surface of steel arches (Figures 6(b) and 7). The stress of steel arches was monitored by vibrating wire stress transducers, which were located in the junction of

the web and flanges of the steel I-beam as shown in Figures 6(b) and 7. These transducers were fixed after the location of steel arches and before spraying shotcrete. Two monitoring sections in the left line, i.e., Z5K64 + 500 and Z5K64 + 540, were chosen to obtain the surrounding rock pressure and steel arch stress, which were measured once a day. The measurement items are summarized in Table 2. It should be noted that the tunnel was excavated from a larger to a smaller value of chainage, i.e., from Z5K64 + 540 to Z5K64 + 500.

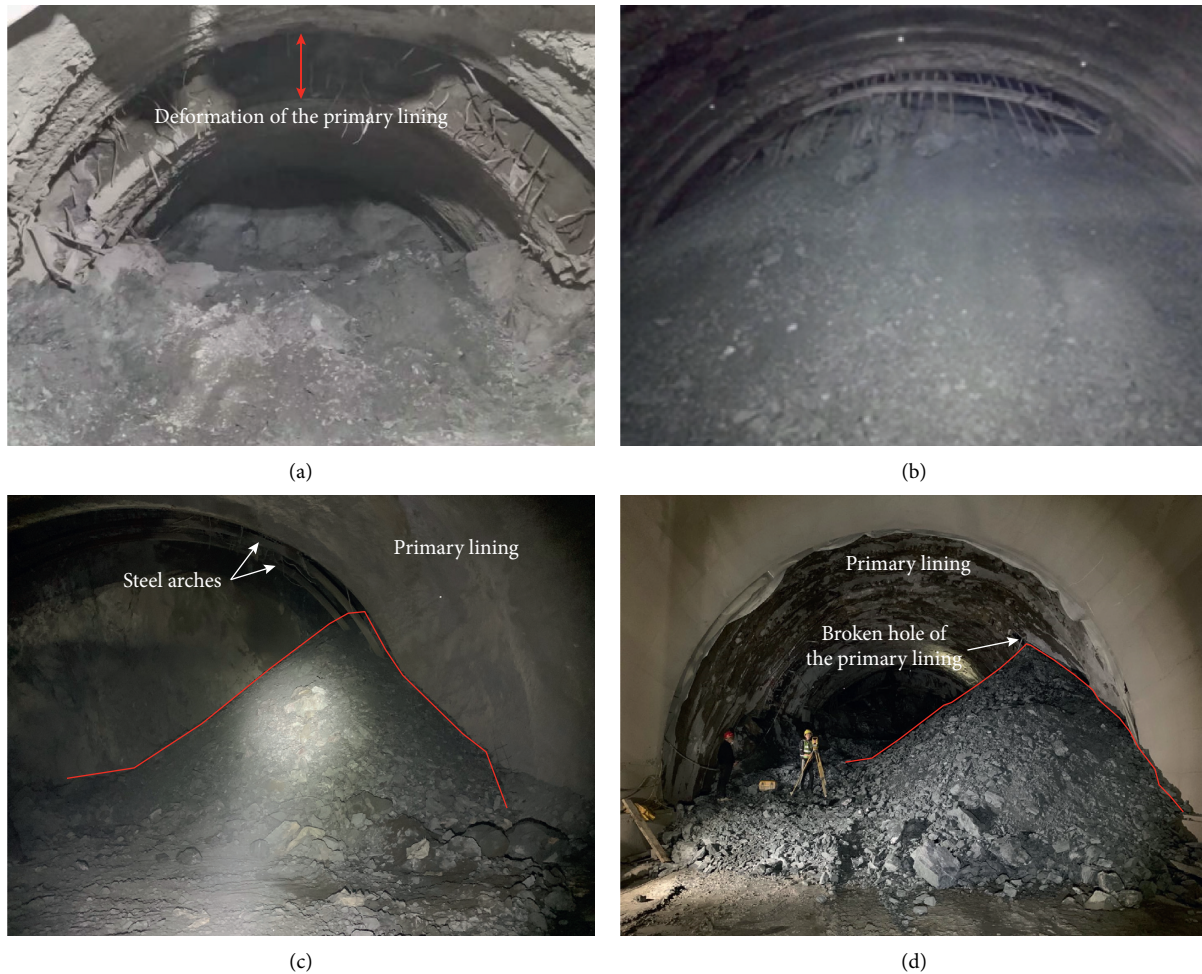


FIGURE 4: Engineering problems in Tayi tunnel: (a) large deformation of the primary lining due to soft surrounding rock mass; (b) collapse of the tunnel excavation face; (c) collapse of the tunnel side wall after installing steel arches but before spraying shotcrete of the primary lining; (d) broken primary lining after spraying shotcrete.

### 3.2. Results and Analysis

#### 3.2.1. Deformation of Primary Lining

(1) *Influence of Construction Activities on Primary Lining.* Tayi tunnel was shut down from the noon of September 19<sup>th</sup> in 2020 to the morning of September 24<sup>th</sup> in 2020 due to scheduled maintenance of large-scale mechanical equipment. Therefore, it is reasonable to regard the duration from September 20<sup>th</sup> to 23<sup>rd</sup> as downtime, when the chainage of the excavation face was Z5K64 + 576.6. The monitoring data from September 11<sup>th</sup> to 28<sup>th</sup> were selected to show the deformation of the primary lining before, during, and after the downtime. Taking Z5K64 + 600 as an example, Figure 8 illustrates the displacements of five monitoring points (as shown in Figure 6). The diurnal displacement of the primary lining during the downtime was smaller than the data before and after the downtime, especially from September 21<sup>st</sup> to 23<sup>rd</sup>. Figure 9 shows the diurnal displacement of point A at the tunnel vault in chainages from Z5K64 + 610 to Z5K64 + 580, which yields the same rule with Figure 8. It can be concluded that the deformation of primary lining caused

by the construction activities, including face excavation, boring, and drilling pipes, is larger than the deformation caused by surrounding rock creep in the talus-like ground. In addition, the construction activities have more impact on the closer sections (Z5K64 + 610 to 600) than the farside sections (Z5K64 + 595 to 580).

(2) *Spatial-Temporal Evolution of Primary Lining Deformation.* Figure 10 shows the time-history curve of deformation of primary lining at Z5K64 + 500 and Z5K64 + 540. All the monitoring points were measured on the first day when they were located, inducing that the horizontal axis indicated the number of monitoring days and begun from 1. The time-history curves of different monitoring points yield a similar evolution rule: the diurnal displacement increased rapidly soon after the excavation of the upper bench, then dropped down, and finally tended to be a stable small value about 31 days after the excavation of the upper bench; i.e., the total displacement reached a steady value. In general, the excavation of middle and lower benches influenced the deformation of the primary lining in the form of increasing the diurnal displacement at Z5K64 + 500. However, such a

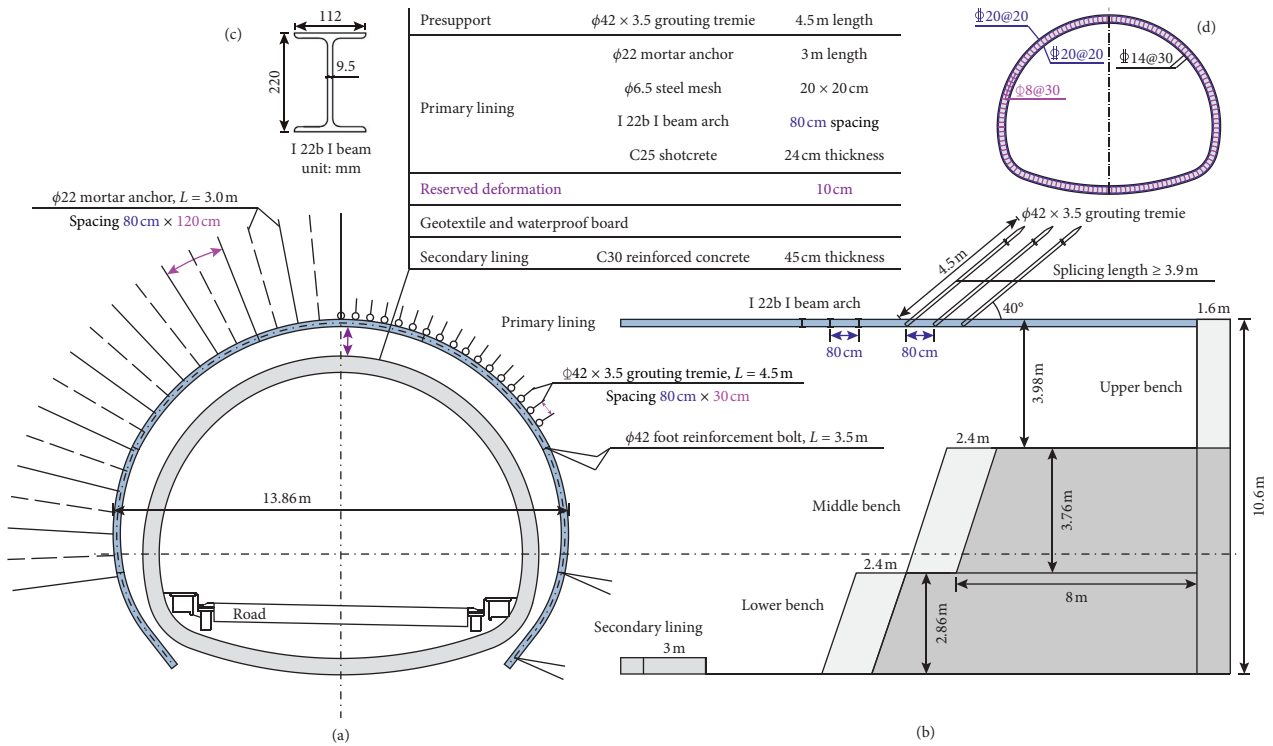


FIGURE 5: Schematic diagram of construction design for supporting system: (a) cross section; (b) longitudinal section; (c) geometrical information of I 22b I beam; (d) reinforcement design of the secondary lining.

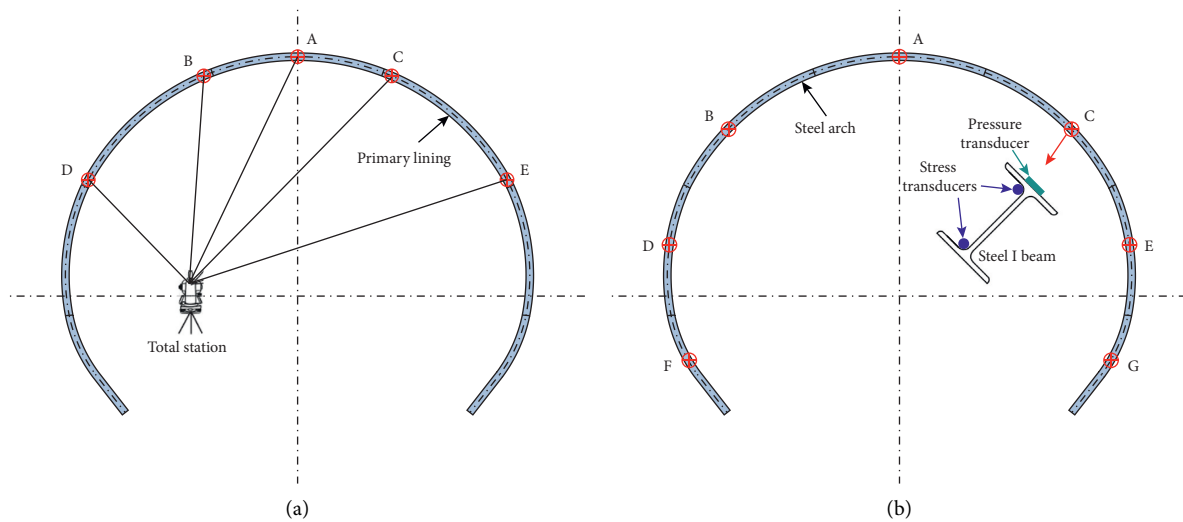


FIGURE 6: Monitoring points of (a) deformation of the primary lining and (b) surrounding rock pressure and steel arch stress.

phenomenon was not distinct at Z5K64 + 540. In terms of the spatial distribution (Figure 11), the primary lining bore an uneven and asymmetrical deformation at both sections. The maximum total displacement was located at the left or right spandrel of the primary lining while the minimum value happened to the springing.

3.2.2. Surrounding Rock Pressure on Primary Lining. In Figure 12, almost all the monitoring points had positive data; i.e., the force on the primary lining from the

surrounding rock is pressure. In consideration of the deformation shown in Figure 10, the surrounding rock shrunk after the excavation, which accords with the rational analysis. It should be noted that points D and G at Z5K64 + 500 had small negative values after the excavation. The reason might be that there was a small gap or void between the primary lining and the surrounding rock induced by the concrete shrinkage, which would cause a small magnitude of tension on the surface of the transducers.

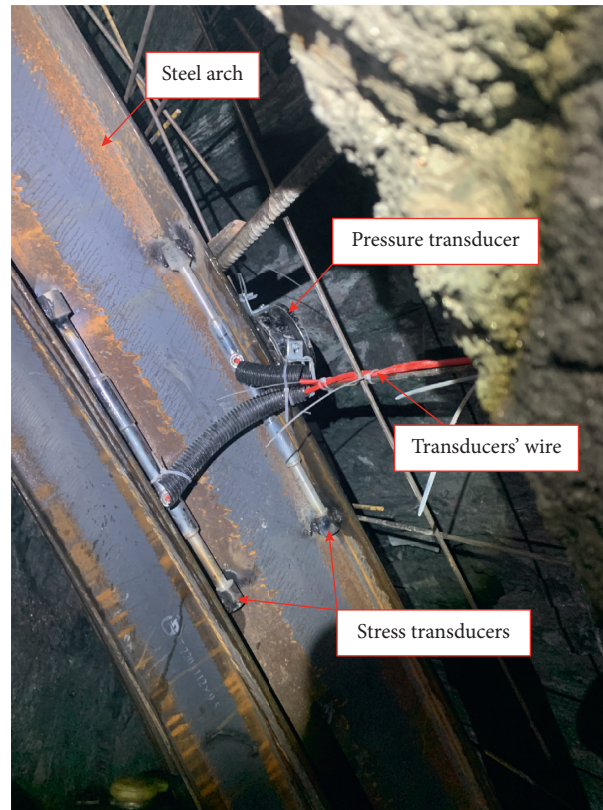


FIGURE 7: Locations of pressure and stress transducers.

(1) *Temporal Evolution of Surrounding Rock Pressure.* The surrounding rock pressure on the primary lining increased rapidly in the first 5 days after the excavation of the upper bench as shown in Figures 12(a) and 12(c). Afterwards, the surrounding rock pressure decreased in the subsequent several days. Once the middle bench was excavated, the surrounding rock pressure around the upper bench dropped. Meanwhile, the pressure on the primary lining of the middle bench increased. Similarly, the surrounding rock pressure on the primary lining of the upper and middle benches dropped slightly after the installation of the primary lining of the lower bench. The reason inducing the decrease is that the excavation of lower benches can release some amount of surrounding rock pressure around upper benches. In addition, the excavation of the lower bench had a relatively bigger impact on the surrounding rock pressure on the primary lining of the middle bench than the one of the upper bench. The peak value of the surrounding rock pressure on the primary lining of upper bench appeared 4~6 days after the excavation. As shown in Figures 10(a) and 10(c), the surrounding rock pressure tended to be stable about 35 days after the excavation of the upper bench. Moreover, the steady values decreased from top to bottom, revealing that the upper part of the primary lining bears more surrounding rock pressure than the lower part.

(2) *Spatial Evolution of Surrounding Rock Pressure.* The spatial distribution of the surrounding rock pressure in Figures 12(b) and 12(d) had an obvious characteristic of

discreteness due to coupling factors such as surrounding rock properties, excavation patterns, supporting parameters, and in situ stress level. The peak and steady values at sections Z5K64 + 500 and Z5K64 + 540 were quite different. In general, the deformation at Z5K64 + 540 was larger than the one at Z5K64 + 500 as shown in Figure 12, inducing larger peak and steady values at Z5K64 + 540. According to the site survey, the dominating formations around the two sections were both strongly weathered slate while there was a small interlayer of soft carbonaceous mudstone around Z5K64 + 540, resulting in a worse ground condition at this section. Therefore, the section of Z4K64 + 540 had a larger peak and steady values in surrounding rock pressure.

Influenced by the in situ stresses and uneven excavation of the tunnel periphery, the surrounding rock pressure showed obvious asymmetry. For the primary lining of the upper bench, the pressure on the right was larger than the left in both sections. However, the pressure on the primary lining of the middle and lower benches yielded an opposite rule. The spatial distribution of the surrounding rock pressure along the perimeter of the tunnel also had an obvious characteristic of discreteness. In general, the surrounding rock pressure around the upper part was larger than the lower part.

3.3. *Stress of Steel Arches.* At each monitoring point, two stress transducers measured the stresses of the outer and inner flanges of the steel I-beam. The actual stress of the steel arch can be calculated by averaging the two values. Figure 13

TABLE 2: Measurement items for mechanical characteristics of the primary lining.

	Measurement items		
	Surrounding rock pressure	Steel arch stress	Primary lining deformation
Monitoring section	Z5K64 + 500	✓	✓
	Z5K64 + 540	—	✓
	Every 5 m	—	✓
Instrument	Vibrating wire pressure transducer	Vibrating wire stress transducer	Total station
Monitoring frequency	1 time/day	1 time/day	2 times/day

Note: the primary lining deformation was measured twice a day at 8 am and 6 pm, whereas the surrounding rock pressure and steel arch stress were measured once a day at 6 pm. Therefore, the monitoring data in the following used the data recorded at 6 pm.

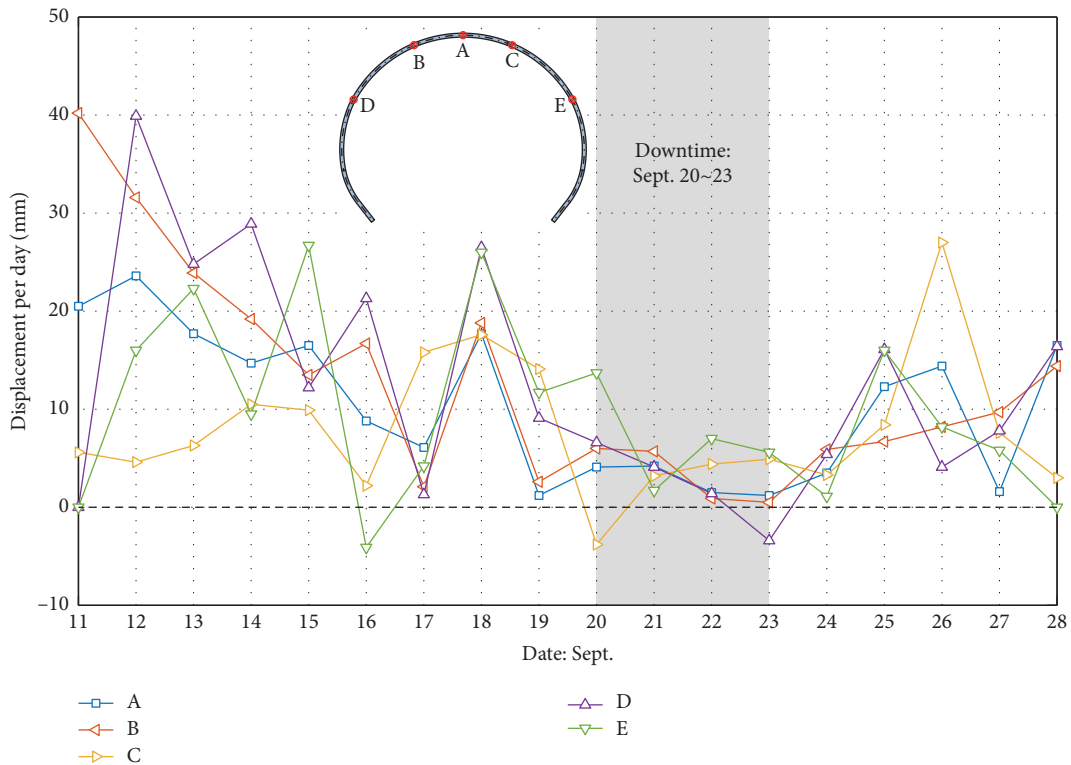


FIGURE 8: Displacement of monitoring points in chainage Z5K64 + 600 from September 11<sup>th</sup> to 28<sup>th</sup> in 2020.

illustrates the stress of steel arches at the section of Z5K64 + 500. Similar to the rules of surrounding rock pressure, the stress of steel arches in the upper bench increased rapidly soon after the excavation, then dropped, and finally tended to be stable. The stress of steel arches at middle and lower benches was less affected by the excavation than the upper bench, which first increased and then tended to be stable. There is no clear descent stage of the data curve of middle and lower benches. The excavation of lower benches released the surrounding rock pressure on the primary lining, inducing the decrease of the force undergone by the primary lining. This phenomenon appeared in the form of the stress decline of the steel arches as shown in Figure 13(a). The stress of steel arches tended to be stable about 40 days after the excavation of the upper bench. Similar to the surrounding rock pressure, the stress of steel arches unevenly distributed along the tunnel periphery (Figure 13(b)).

In the upper bench, the stress of steel arches at the tunnel vault was the largest and the right spandrel bore larger stress than the left spandrel. In the stable stage of the data curve, the steady stress decreased from upper benches to lower benches.

#### 4. Control Measures for Tunnel Support in Talus-Like Formations

4.1. Mechanical Characteristics of Talus-Like Formations. Generally, the mechanical characteristics of talus-like rock mass are similar to common weak rock masses [25–30] or layered rock masses [31–33]. However, there are still differences between the two types of rock masses. Firstly, the talus-like rock masses are more affected by the excavation activities than the common weak rock masses. With the bench cut method, the lower benches obviously release the

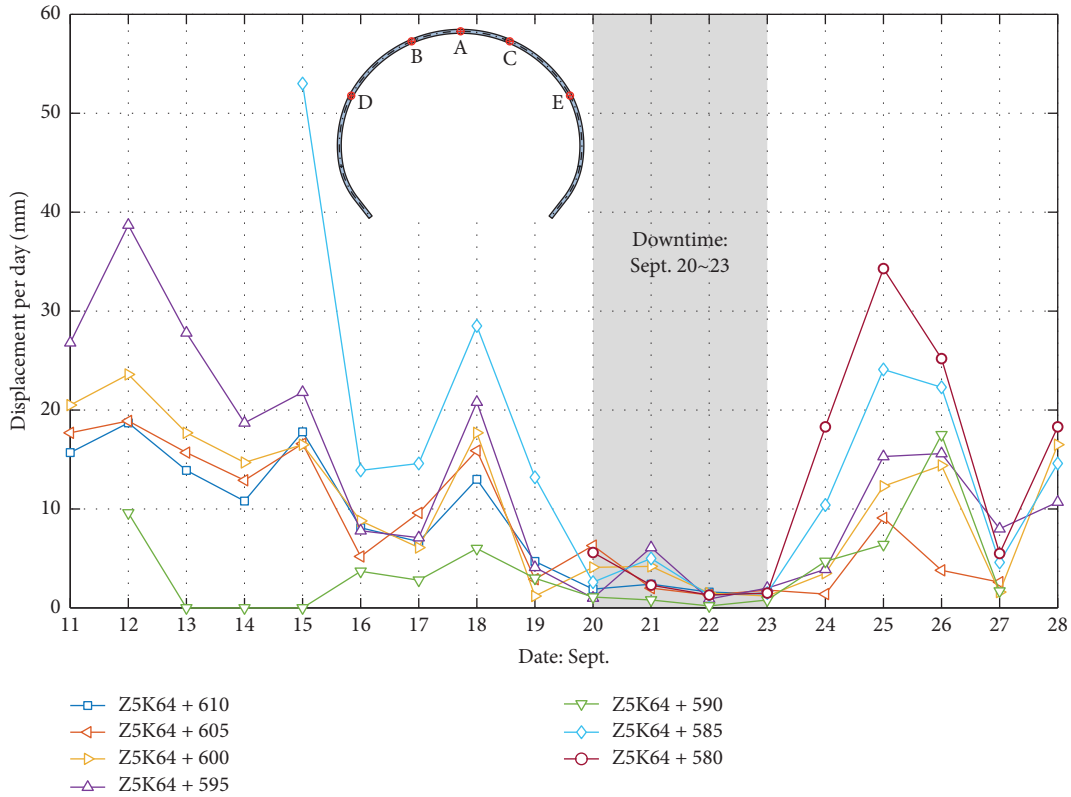


FIGURE 9: Displacement of point A (tunnel vault) at chainages from Z5K64 + 610 to Z5K64 + 580 during September 11<sup>th</sup> to 28<sup>th</sup> in 2020.

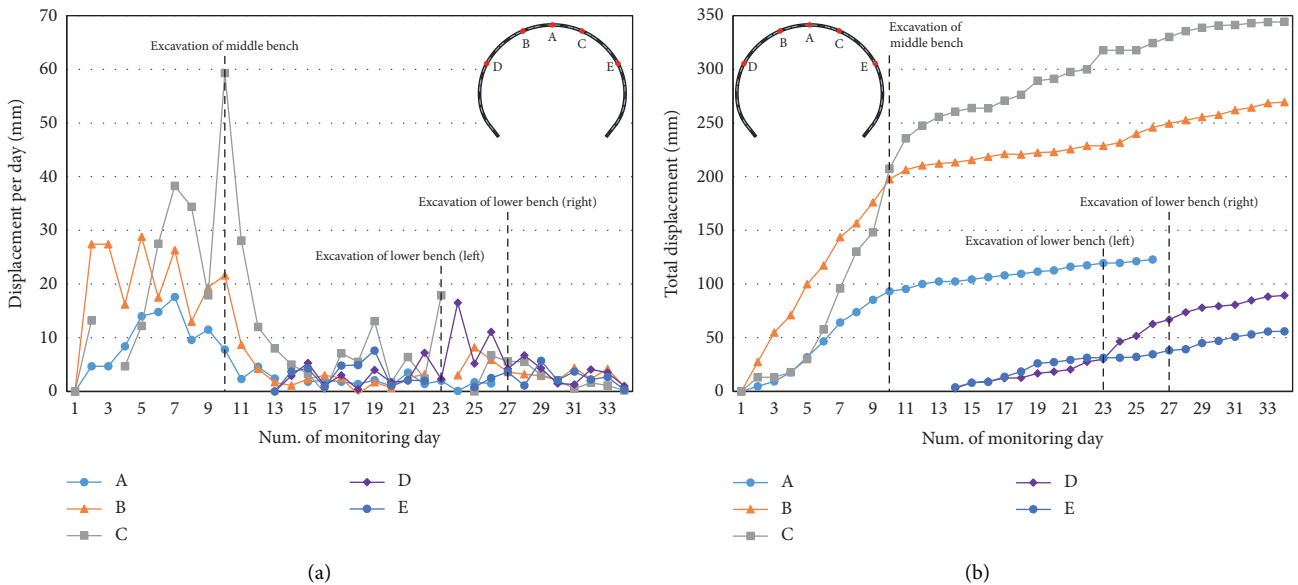


FIGURE 10: Continued.

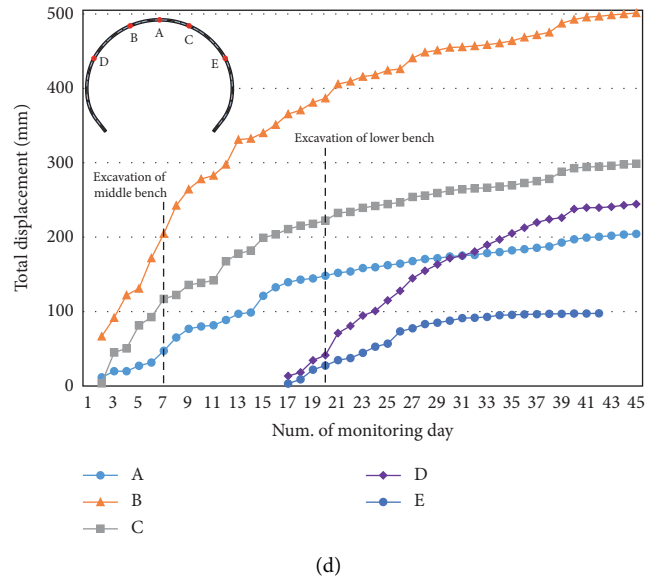
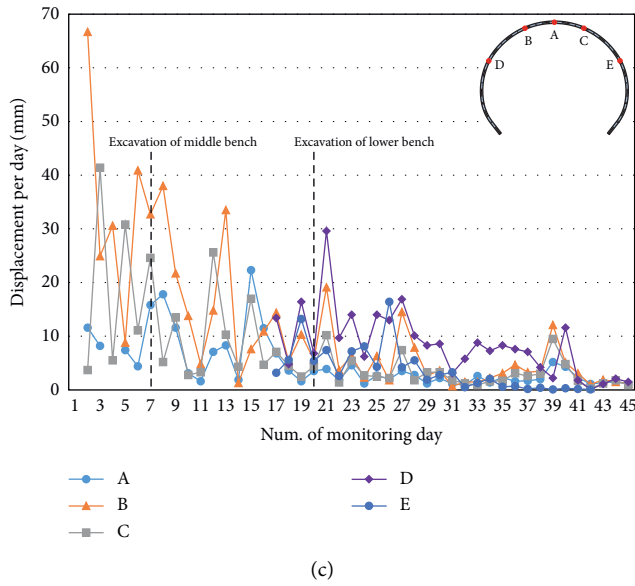


FIGURE 10: Time-history curve of the deformation of the primary lining: (a) diurnal and (b) accumulative displacement at Z5K64 + 500; (c) diurnal and (d) accumulative displacement at Z5K64 + 540.

surrounding rock pressure around the upper benches, inducing the decline of the surrounding rock pressure on the primary lining and the stress of steel arches. After the installation of the primary lining of the lower benches, the surrounding rock pressure and the stress of steel arches increase slightly and finally tend to be stable. The increasement and speed of the stress of steel arches are larger than the ones of surrounding rock pressure. Secondly, the talus-like rock masses have more complex formations of rock blocks with wide-range sizes and soils with different fractions. Therefore, it is extremely difficult to ensure the evenness of the tunnel periphery during mechanical excavation, which will induce uneven and asymmetrical contact between the surrounding rock mass and the primary lining. As a result, the surrounding rock pressure on the primary lining, the inner stress of the steel arches, and the deformation of the primary lining usually have a characteristic of discreteness and nonuniformity along the tunnel periphery. Accordingly, the evolution of the interaction between the surrounding rock and the primary lining can be concluded into three stages: (1) the deformed surrounding rock mass contacts with the primary lining and exerts sharp pressure on the primary lining, and the deformation of the surrounding rock mass is larger than the one of the primary lining; (2) the interactional pressure between the surrounding rock mass and the primary lining releases and decreases, and the deformation rate of the surrounding rock mass becomes smaller than the one of the primary lining; (3) the surrounding rock pressure tends to be stable and the deformations of the surrounding rock mass and the primary lining become coordinating.

In consideration of the complex formations and weakness of the talus-like formations, the deformation of surrounding rock masses should be emphatically disposed during the tunnel excavation. Termly advanced detection is

recommended to obtain the information of rock mass properties ahead of the excavation face, such as the fragmentation degree, the lithological components, and water content. It is also suggested that the forepoling is established in time and changes momentarily if the advanced detection explores a worse rock mass. The invert part should be excavated and installed timely to enclose the primary lining into integrity to ensure the performance of the lining. Moreover, the secondary lining should be installed as soon as possible when the deformation of the primary lining tends to be stable to diminish the exposure duration of the primary lining.

**4.2. Dynamically Adaptive Support System in Talus-Like Formations.** In consideration of the significant influence of the talus-like formations on the tunnel support system, a reasonable modification of the support system had been processed. Firstly, the talus-like formations, which had been classified into grade V rock mass, were divided into three subclasses according to the ground condition: (1) the extremely weak and fractured rock mass without water inflow as Vd-1; (2) the extremely weak and fractured rock mass with water inflow as Vd-2; (3) the extremely weak and fractured rock mass mixed with some amount of soil and water inflow as Vd-3. It should be noted that the item “Vd” came from the geological investigation report of Tayi tunnel and the letter “d” herein is just a notation showing that such a type of rock mass is weaker and more dangerous than grade V rock mass. Secondly, a dynamically adaptive support system was proposed to adapt to the varying conditions of talus-like formations as shown in Figure 14. The spacing of steel arches was changed to 60 cm and thus the excavation length of the upper bench was altered to 120 cm for grades Vd-1 and Vd-2 rock masses and 60 cm for grade Vd-3 rock

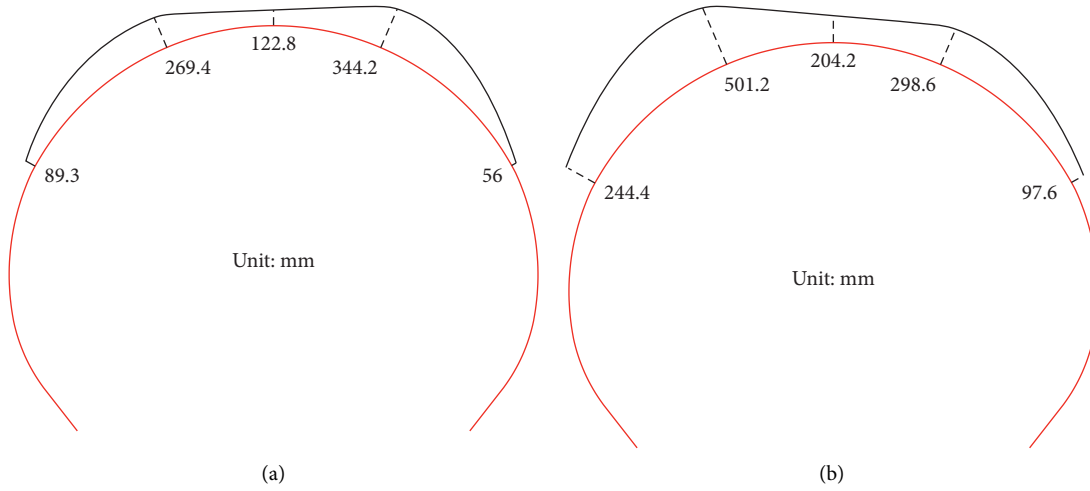


FIGURE 11: Spatial distribution of total displacement of the primary lining at (a) Z5K64 + 500 and (b) Z5K64 + 540.

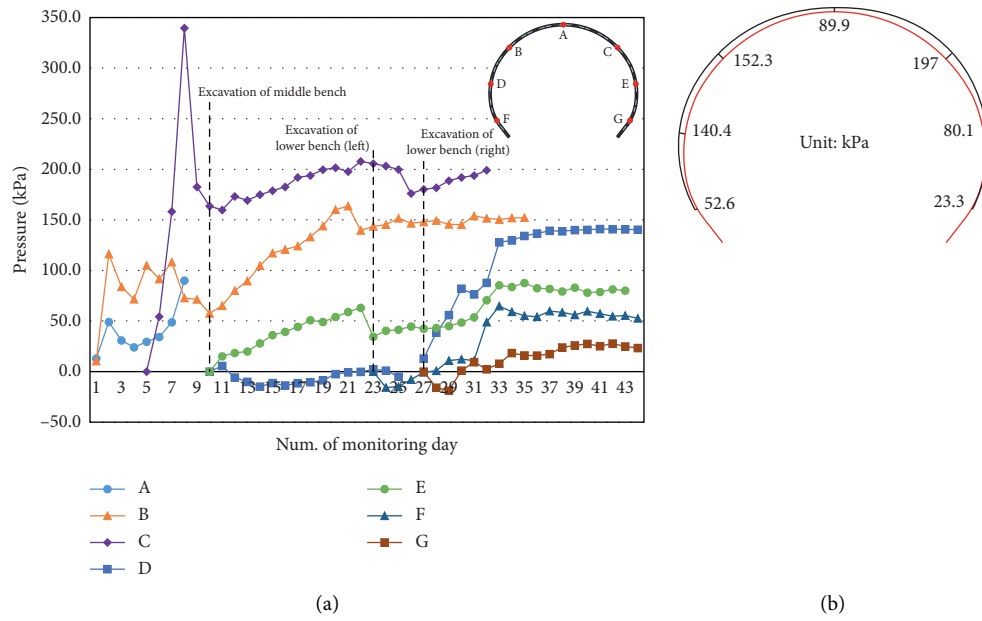


FIGURE 12: Continued.



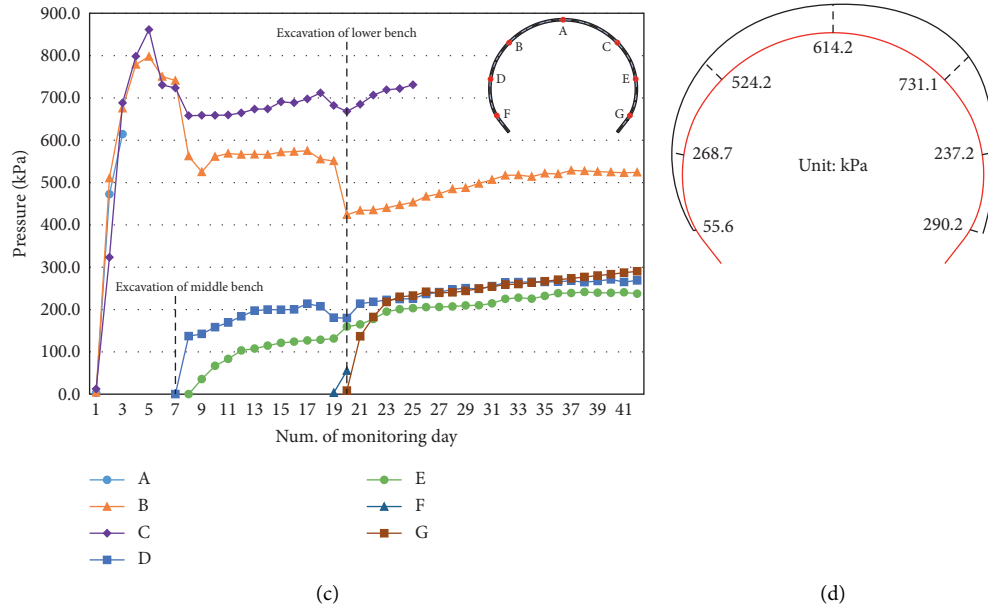


FIGURE 12: Surrounding rock pressure on the primary lining: (a) time-history curve and (b) spatial distribution at Z5K64 + 500; (c) time-history curve and (d) spatial distribution at Z5K64 + 540. The spatial distribution diagrams were based on the last data of the time-history curve.

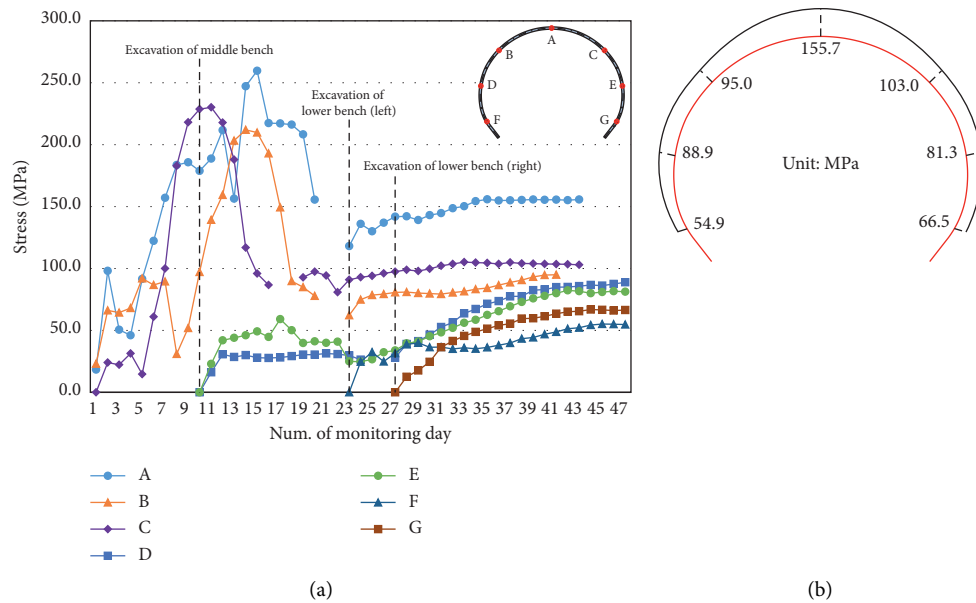


FIGURE 13: (a) Time-history curve and (b) spatial distribution of steel arch stress at Z5K64 + 500. The spatial distribution diagrams were based on the last data of the time-history curve.

mass, respectively. The excavation length of the middle and lower benches was set as 180 cm, i.e., three times of the steel arch spacing. In the dynamically adaptive support system, the pre-support scheme used pipe shed to prevent the deformation of the surrounding rock mass ahead of the excavation face. As for the primary lining, stronger structural elements were used to ensure that the deformed primary lining would not invade the design space of the secondary lining. Especially for grade Vd-3 rock mass, a double-layer

primary lining (Figure 15) was adopted to prevent large deformation of surrounding rock mass. In addition, the reversed deformation between the linings and the secondary lining parameters were also adaptable according to the ground conditions. The detailed parameters of the dynamically adaptive support system are listed in Table 3. Every 6 m (ten times the excavation step) during the excavation, a combination method with the transient electromagnetic method, ground penetrating radar, and advance

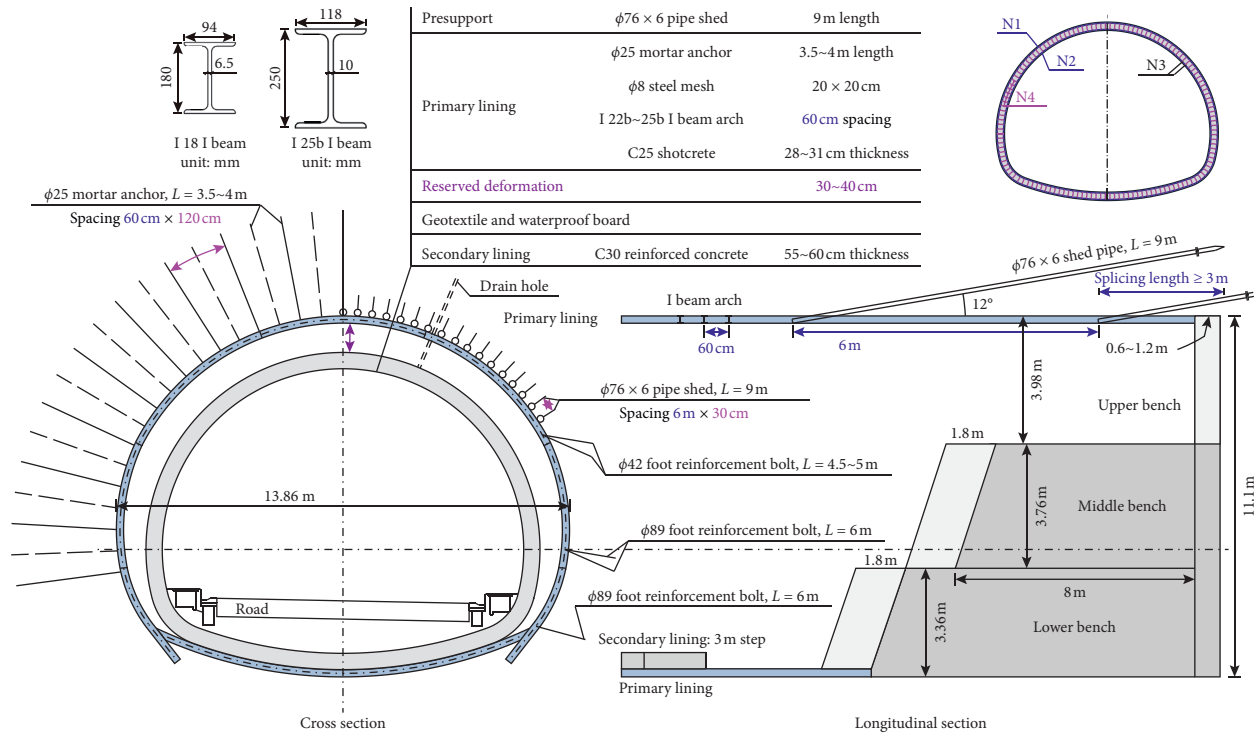


FIGURE 14: Schematic diagram of the dynamically adaptive support system in talus-like formations adopted in Tayi tunnel.

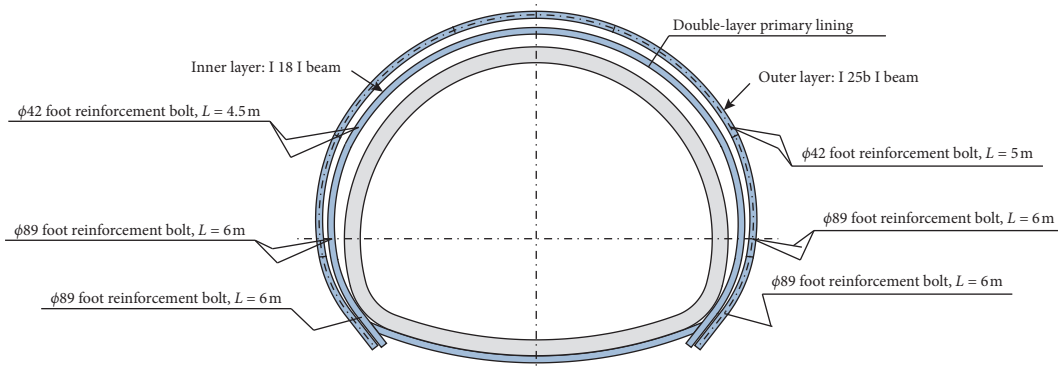


FIGURE 15: Configuration of foot reinforcement bolts in the double-layer primary lining for grade Vd-3 rock mass.

TABLE 3: Configuration of dynamically adaptive support system in talus-like formations in Tayi tunnel.

Supporting system	Vd-1	Vd-2	Vd-3
Presupport	$\phi 76 \times 6$ pipe shed, 9 m length, 6 m $\times$ 30 cm spacing, splicing length $\geq 3$ m		
Mortal anchor	3.5 m length	$\phi 25$ , 60 cm $\times$ 120 cm spacing	4 m length
Steel mesh		$\phi 8$ , 20 cm $\times$ 20 cm spacing	
Steel arch	I 22b	I 25b	Double layer
Shotcrete	28 cm	31 cm	Double layer
Foot reinforcement bolt (each side)	Upper bench: $\phi 42 \times 2$ , 4.5 m length Middle bench: $\phi 89 \times 2$ , 6 m length Lower bench: $\phi 89 \times 1$ , 6 m length	Upper bench: $\phi 42 \times 2$ , 5 m length	Matched to steel arch
Reversed deformation	30~35 cm	35~40 cm	35~40 cm

TABLE 3: Continued.

Supporting system	Vd-1	Vd-2	Vd-3
		C30	
Reinforced concrete	50 cm	60 cm	60 cm
Secondary support	N1: $\phi 22@20$	N1: $\phi 22@16.67$	N1: $\phi 22@16.67$
Reinforcement	N2: $\phi 22@20$	N2: $\phi 22@20$	N2: $\phi 22@20$
	N3: $\phi 14@30$	N3: $\phi 14@30$	N3: $\phi 14@30$
	N4: $\phi 8@30$	N4: $\phi 8@30$	N4: $\phi 8@30$

Note: the primary support for Vd-3 is in the form of double-layer as shown in Figure 15. The unit for diameter of pipes, anchors, and steel bars is mm. The steel bars in N1, N2 and N3 are HRB 400 while the ones in N4 are HPB 300.

exploratory drilling was employed to detect the geological and hydrological conditions ahead of the excavation face to determine the subclass of the surrounding rock masses and the appropriate support parameters.

As stated above, the talus-like formations are sensitive to the excavation activities and the construction speed of Tayi tunnel has to be slowed down to reduce the deformation of surrounding rock mass and prevent the rock collapse. With the original support system (Figure 5) before August of 2020, the average excavation speed was less than 20 m per month in grade IV/V rock masses. The first-edition dynamically adaptive support system began to be used after August 2020 and the construction speed had been promoted to 30~40 m per month in grade V rock mass. Afterwards, the dynamically adaptive support system was improved in January 2021 as shown in Figures 14 and 15. As a result, the construction speed had been enhanced to 70~80 m per month in grade V rock mass (including the abovementioned grade Vd rock masses) and 160~180 m per month in grade IV rock mass. The maximum deformation of the primary lining was reduced to less than ~400 mm after the adoption of the dynamically adaptive support system.

## 5. Conclusion

This paper investigates the stability of Tayi tunnel passing through talus-like rock masses via site survey and in situ monitoring. In the project, the in situ monitoring items included the surrounding rock pressure on the primary lining, the stress of steel arches, and the deformation of the primary lining. The main conclusions are as follows.

- (1) The deformation of the primary lining caused by the construction activities is larger than the deformation caused by surrounding rock creep in the talus-like ground. The construction activities have more impact on the closer sections than the farside sections.
- (2) With the bench cut method, the surrounding rock pressure and the stress of steel arches increase rapidly soon after the excavation of the upper bench, then slightly drop down, and finally tend to be stable. The lower benches obviously release the surrounding rock pressure around the upper benches, inducing the decline of the surrounding rock pressure on the primary lining and the stress of steel arches.
- (3) In terms of spatial distribution, the monitoring data usually has a characteristic of discreteness and

nonuniformity along the tunnel periphery due to the uneven and asymmetrical contact between the surrounding rock mass and the primary lining which is inherently dominated by the uneven excavation space caused by complex formations of talus-like rock masses.

- (4) It is suggested that the deformation of the surrounding rock masses should be emphatically disposed during the tunnel excavation in the talus-like ground. Termly advanced detection, flexible forepoling, timely closure of primary lining, and well-timed installation of secondary lining are recommended measures to reduce the deformation of the talus-like rock masses.
- (5) A dynamically adaptive support system was implemented to strengthen the bearing capacity of the lining system according to the geological conditions of talus-like formations. After such treatment, the deformation of the primary lining has been well controlled and the construction speed has been considerably enhanced.

## Data Availability

The data used to support the findings of this study are included within the article.

## Conflicts of Interest

The authors declare that they have no conflicts of interest.

## Acknowledgments

The research was supported by the National Natural Science Foundation of China (Grant no. 52008307) and POWER-CHINA Roadbridge Group Co., Ltd. (Grant no. HHZ-JGY-FW-03).

## References

- [1] Q. Wang, X. Xie, and I. Shahrou, "Deep learning model for shield tunneling advance rate prediction in mixed ground condition considering past operations," *IEEE Access*, vol. 8, pp. 215310–215326, 2020.
- [2] Z. Chen, C. He, G. Xu, G. Ma, and D. Wu, "A case study on the asymmetric deformation characteristics and mechanical behavior of deep-buried tunnel in phyllite," *Rock Mechanics and Rock Engineering*, vol. 52, no. 11, pp. 4527–4545, 2019.

- [3] J. Liu, J. Wei, H. Hu, J. Wu, S. Sun, and D. P. Kanungo, "Research on the engineering geological conditions and stability evaluation of the B2 talus slide at the jin'an bridge hydropower station, China," *Bulletin of Engineering Geology and the Environment*, vol. 77, no. 1, pp. 105–125, 2018.
- [4] H. Obanawa and Y. Matsukura, "Mathematical modeling of talus development," *Computers & Geosciences*, vol. 32, no. 9, pp. 1461–1478, 2006.
- [5] H. Xing, L. Liu, and Y. Luo, "Water-induced changes in mechanical parameters of soil-rock mixture and their effect on talus slope stability," *Geomechanics and engineering*, vol. 18, no. 4, pp. 353–362, 2019.
- [6] X. Li, Q. L. Liao, and J. M. He, "In situ tests and a stochastic structural model of rock and soil aggregate in the three gorges reservoir area, China," *International Journal of Rock Mechanics and Mining Sciences*, vol. 41, no. 3, pp. 494–499, 2004.
- [7] D. Cen, D. Huang, and F. Ren, "Shear deformation and strength of the interphase between the soil-rock mixture and the benched bedrock slope surface," *Acta Geotechnica*, vol. 12, no. 2, pp. 391–413, 2017.
- [8] X. Sun, X. Li, B. Zheng, J. He, and T. Mao, "Study on the progressive fracturing in soil and rock mixture under uniaxial compression conditions by CT scanning," *Engineering Geology*, vol. 279, no. 4, Article ID 105884, 2020.
- [9] H. Dong, B. Peng, Q.-F. Gao, Y. Hu, and X. Jiang, "Study of hidden factors affecting the mechanical behavior of soil-rock mixtures based on abstraction idea," *Acta Geotechnica*, vol. 16, no. 2, pp. 595–611, 2021.
- [10] W.-J. Xu and H.-Y. Zhang, "Research on the effect of rock content and sample size on the strength behavior of soil-rock mixture," *Bulletin of Engineering Geology and the Environment*, vol. 80, no. 3, pp. 2715–2726, 2021.
- [11] N. Coli, P. Berry, and D. Boldini, "In situ non-conventional shear tests for the mechanical characterisation of a bimrock," *International Journal of Rock Mechanics and Mining Sciences*, vol. 48, no. 1, pp. 95–102, 2011.
- [12] N. Coli, P. Berry, D. Boldini, and R. Bruno, "The contribution of geostatistics to the characterisation of some bimrock properties," *Engineering Geology*, vol. 137–138, pp. 53–63, 2012.
- [13] W. J. Xu, X. Qiang, and R. L. Hu, "Study on the shear strength of soil-rock mixture by large scale direct shear test," *International Journal of Rock Mechanics and Mining Sciences*, vol. 48, no. 8, pp. 1235–1247, 2011.
- [14] A. Kalender, H. Sonmez, E. Medley, C. Tunusluoglu, and K. E. Kasapoglu, "An approach to predicting the overall strengths of unwelded bimrocks and bimsoils," *Engineering Geology*, vol. 183, pp. 65–79, 2014.
- [15] M. Afifpour and P. Moarefvand, "Mechanical behavior of bimrocks having high rock block proportion," *International Journal of Rock Mechanics and Mining Sciences*, vol. 65, pp. 40–48, 2014.
- [16] M. Tsesarsky, M. Hazan, and E. Gal, "Estimating the elastic moduli and isotropy of block in matrix (bim) rocks by computational homogenization," *Engineering Geology*, vol. 200, pp. 58–65, 2016.
- [17] W.-J. Xu, L.-M. Hu, and W. Gao, "Random generation of the meso-structure of a soil-rock mixture and its application in the study of the mechanical behavior in a landslide dam," *International Journal of Rock Mechanics and Mining Sciences*, vol. 86, pp. 166–178, 2016.
- [18] Q. X. Meng, H. L. Wang, W. Y. Xu, and M. Cai, "A numerical homogenization study of the elastic property of a soil-rock mixture using random mesostructure generation," *Computers and Geotechnics*, vol. 98, pp. 48–57, 2018.
- [19] E. Khorasani, M. Amini, M. F. Hossaini, and E. Medley, "Statistical analysis of bimslope stability using physical and numerical models," *Engineering Geology*, vol. 254, pp. 13–24, 2019.
- [20] The National Standards Compilation Group of People's Republic of China, *GB/T 50128-2014 Standard for Engineering Classification of Rock Masses*, China Planning Press, Beijing, China, 2014.
- [21] Chongqing Communications Technology Research and Design Institute, *JTG D70-2010, Code for Design of Road Tunnel*, China Communications Press, Beijing, China, 2010.
- [22] H. Sonmez, E. Tuncay, and C. Gokceoglu, "Models to predict the uniaxial compressive strength and the modulus of elasticity for ankara agglomerate," *International Journal of Rock Mechanics and Mining Sciences*, vol. 41, no. 5, pp. 717–729, 2004.
- [23] S. Sun, P. Xu, J. Wu et al., "Strength parameter identification and application of soil-rock mixture for steep-walled talus slopes in southwestern China," *Bulletin of Engineering Geology and the Environment*, vol. 73, no. 1, pp. 123–140, 2014.
- [24] Z.-L. Zhang, W.-J. Xu, W. Xia, and H.-Y. Zhang, "Large-scale in-situ test for mechanical characterization of soil-rock mixture used in an embankment dam," *International Journal of Rock Mechanics and Mining Sciences*, vol. 86, pp. 317–322, 2016.
- [25] P. F. Li, S. M. Tian, Y. Zhao, Y. Q. Zhu, and S. D. Wang, "In-situ monitoring study of mechanical characteristics of primary lining in weak rock tunnel with high geostress," *Chinese Journal of Rock Mechanics and Engineering*, vol. 32, no. Supp. 2, pp. 3509–3519, 2013, in Chinese.
- [26] Q. Fang, W. Su, D. L. Zhang, and F. C. Yu, "Tunnel deformation characteristics based on on-site monitoring data," *Chinese Journal of Rock Mechanics and Engineering*, vol. 35, no. 9, pp. 1884–1897, 2016, in Chinese.
- [27] X. L. Wang, J. X. Lai, R. S. Garnes, and Y. B. Luo, "Support system for tunnelling in squeezing ground of qingling-daba mountainous area: a case study from soft rock tunnels," *Advances in Civil Engineering*, vol. 2019, Article ID 8682535, 2019.
- [28] J. X. Chen, Z. L. Xu, Y. B. Luo, J. K. Song, W. W. Liu, and F. F. Dong, "Application of the upper-bench CD method in super large-span and shallow tunnel: a case study of letuan tunnel," *Advances in Civil Engineering*, vol. 2020, Article ID 8826232, 2020.
- [29] Q. G. Liang, J. Fang, and P. He, "Analysis on tunnel surrounding rock pressure characteristics based on field measured statistics," *Chinese Journal of Underground Space and Engineering*, vol. 16, no. 2, pp. 555–566, 2020, in Chinese.
- [30] Q. Hong, H. Lai, Y. Liu, X. Ma, and J. Xie, "Deformation control method of a large cross-section tunnel overlaid by a soft-plastic loess layer: a case study," *Bulletin of Engineering Geology and the Environment*, vol. 80, no. 6, pp. 4717–4730, 2021.
- [31] Z. Chen, C. He, G. Xu, G. Ma, and W. Yang, "Supporting mechanism and mechanical behavior of a double primary support method for tunnels in broken phyllite under high geo-stress: a case study," *Bulletin of Engineering Geology and the Environment*, vol. 78, no. 7, pp. 5253–5267, 2019.

- [32] G. Xu, C. He, J. Wang, and Z. Chen, "Study on the mechanical behavior of a secondary tunnel lining with a yielding layer in transversely isotropic rock stratum," *Rock Mechanics and Rock Engineering*, vol. 53, no. 7, pp. 2957–2979, 2020.
- [33] X. Sun, C. Zhao, Z. Tao, H. Kang, and M. He, "Failure mechanism and control technology of large deformation for muzhailing tunnel in stratified rock masses," *Bulletin of Engineering Geology and the Environment*, vol. 80, no. 6, pp. 4731–4750, 2021.

## Research Article

# Investigation on Physicomechanical Properties and Constitutive Model of Tuff in Mila Mountain Tunnel under Dry and Saturated Conditions

Zhihao He,<sup>1,2</sup> Xiangjun Pei ,<sup>1,2</sup> Shenghua Cui ,<sup>1,2</sup> Wentai Sun,<sup>3</sup> Luguang Luo,<sup>1,2</sup> and Chengruiwei He<sup>4</sup>

<sup>1</sup>State Key Laboratory of Geohazard Prevention and Geoenvironment Protection, Chengdu University of Technology, Chengdu, Sichuan 610059, China

<sup>2</sup>College of Environmental and Civil Engineering, Chengdu University of Technology, Chengdu, Sichuan 610059, China

<sup>3</sup>CCCC Second Highway Consultants Co., Ltd., Wuhan, Hubei 430070, China

<sup>4</sup>College of Civil Engineering, Hefei University of Technology, Hefei, Anhui 230009, China

Correspondence should be addressed to Xiangjun Pei; [peixj0119@tom.com](mailto:peixj0119@tom.com)

Received 18 April 2021; Accepted 12 June 2021; Published 15 July 2021

Academic Editor: Guowen Xu

Copyright © 2021 Zhihao He et al. This is an open access article distributed under the Creative Commons Attribution License, which permits unrestricted use, distribution, and reproduction in any medium, provided the original work is properly cited.

Many tunnel engineering accidents are generally caused by water softening tuff of high porosity. Experimental and theoretical analytical methods, including rock ultrasonic testing, X-ray diffraction (XRD), microscopic observation, uniaxial compression test, and scanning electron microscope (SEM), are employed to analyze the physicomechanical properties of tuff in Mila Mountain tunnel under dry and saturated conditions. Then, the mechanism of tuff softening in water is explained. Finally, the statistical damage constitutive model of tuff is established. It was revealed that the tuff compositions were dominated by quartz and clay minerals accounting for more than 90%, and clay minerals, anhydrite, and pyrite were mainly soluble minerals. After being saturated with water, the soluble minerals in the tuff are dissolved, and the porosity and wave velocity are increased; however, the elastic modulus and peak strength are decreased, indicating that water softening was distinct. Water softening after saturation was due to the mineral compositions and microstructure characteristics of tuff in Mila Mountain tunnel; specifically, as the tuff characterized by high porosity was conducive to water absorption, the soluble minerals in the tuff were corroded and swelled by water, dissolving, loosening, and softening the tuff structure; then, its mechanical behavior was degraded. It was demonstrated by the experimental results consistent with theoretical results that the model can be employed to express the constitutive behavior of tuff in Mila Mountain tunnel under dry and saturation conditions. The findings provide insights into macroscale deterioration of tuffs and theoretical knowledge for the tunnel excavation and support of Mila Mountain tunnel.

## 1. Introduction

Tuff, a special kind of rock and widely distributed in earth crust, is formed after sedimentation and high temperature and characterized by lower density, high porosity, and easiness to deform after water softening [1–5]. The issue of tuff strata cannot be avoidable on many engineering constructions, for instance, deep-buried long tunnels [6] and deep underground geological disposal site [7]. Thus, in order to take effective measurements in tuff engineering applications, it is necessary to explain the mechanical characteristics and establish

constitutive model of tuff. Recently, there are many studies on tuff in engineering applications [8–10]. For example, owing to good processability, tuffs have been used as building stones all around the world since ancient times [2, 11]. As natural materials, tuffs possess variable chemical, mineralogical, and reactive attributes. Hence, tuffs in building sector are its additional application in cement production [12, 13]. These research results are conducive to reveal the tuffs characteristics in engineering applications [14].

Meanwhile, there are studies in which physicomechanical features and failure mechanism of the tuffs from several regions

were determined [15]. It was concluded from these studies that tuffs are a volcanic rock with high porosity and low strength, and the pink tuffs in Midas Monument have higher strength than those of white tuffs [16]. By field investigations and numerical modelling, Salve et al. investigated the flow-field evolution, drainage of fracture flow paths, and seepage characteristics in unsaturated fractured welded stuffs [17, 18]. In the field of rock mechanics, uniaxial compressive strength (UCS) is one of the most widely used parameters used to evaluate mechanical property of various rock types [19]. Previous studies have suggested that UCS is controlled by total porosity, water saturation, and the type of rock-forming minerals [19]. For example, Martin et al. investigated the mechanical properties and microstructure of tuff under shock condition and pointed out that strength and moduli of tuff significantly degraded at shock condition, which is associated with microstructural damage in the form of microcracks and crushed pores [20]. Li et al. argued that different pore properties lead to different mechanical deterioration and tuff failure mode for tuff [21]. An investigation into the effect of water saturation on deterioration of tuff showed when the initial degree of saturation of tuff exceeded 70%, one freeze-thaw cycle causes a decrease in the uniaxial compressive strength, a decrease in the  $P$ -wave velocity, and an increase in the porosity of the rock. While when the initial degree of saturation is lower than 70%, one freeze-thaw cycle has minimal effect on the same properties [22]. Togashi et al. found that the maximum and minimum principal strain orientations are rotated by approximately  $90^\circ$  from the wet state to dry state [23]. These studies on the mechanical characteristics and fracture mechanism of tuffs with different moistures and porosities are conducive to thorough comprehension on the characteristics of high porosity and water softening of tuff. However, considering that the issue of water softening tuffs with high porosity is not avoidable in tunnel engineering, researches are few on the mechanical characteristics and fracture mechanism of tuffs under dry and saturated conditions in the tunnel engineering applications in alpine and high-altitude areas.

In this paper, porosity characteristics, mineral compositions, and microstructural characteristics of tuffs were investigated to figure out the basis of water softening tuffs under dry and saturated conditions through ultrasonic testing on rock mass, XRD, and microscopic observation. In addition, through uniaxial compression and SEM experiments, the mechanical and failure characteristics of tuffs in the tunnel of Mila Mountain were studied to reveal the characteristics of water softening tuffs. According to the above experiments and results, it was concluded that the main reason for water softening tuffs was due to high porosity which was conducive to water absorption, and then, soluble mineral compositions of tuffs were corroded and swelled by water. Furthermore, a constitutive model was established under dry and saturated conditions based on a series of mechanics tests to calculate microfractures in volcanic tuff, which facilitated the numerical analysis of tunnel excavation and support design. The findings provided insights into macroscale deterioration of tuffs and theoretical basis for the tunnel excavation and support of Mila Mountain.

## 2. Test Introduction

**2.1. Engineering Background.** Mila Mountain tunnel, one of the key highway renovation projects in the section of Nyingchi to Lhasa belonging to the national highway numbered as 318 route in Tibet located at the junction of Gongbo'gyamda County and Maizhokunggar County where the average elevation is 4763.5 m, and the maximum reaches 5020 m, characterized by thin air, low pressure, poor nature, and geological conditions, is an extra-long highway tunnel at the highest elevation in the world designed with double holes in separation for 30 ~ 39 m in distance, 5727 m in length for the left hole, and 5720 m for the right, about 375 m at the maximum depth, 5.0 m for the height, and 10.25 m for the width. The surrounding rocks of the tunnel are dominated by IV and V grade tuffs, accounting for 85%. As shown in Figure 1, tunnel collapse, gushing, mud bursting, and deformation after initial support have occurred frequently in tunnel construction because of tuffs characteristics, for instance, microfractures development, collapse, water softening and decomposition, and dramatic degradation of tuffs mechanical property, etc. According to as-built records, the daily water yield increased from 8000 m<sup>3</sup>/d at the beginning to 12000 m<sup>3</sup>/d at the fault zone, and the maximum water inflow reached 38600 m<sup>3</sup>/d. The key to resolving the above problems such as deformation, gushing, and collapse is to reveal the mechanical characteristics of tuffs under dry and saturated conditions; therefore, the tuff at the bursting site in the tunnel of Mila Mountain was selected as the object for experiments. The tuff used in this research was collected from buried depth of 316 m of Mila Mountain tunnel at Pile no. ZK4477 + 371 in Lhasa, Tibet Autonomous Region, China. Testing specimens have uniform texture, and the mean density is 2.53 g/cm<sup>3</sup>.

**2.2. Sample Preparation and Test Procedure.** The physico-mechanical characteristics of tuff are the basis for further analysis of its water deterioration effect, fracture mechanism, and establishment of constitutive model. Therefore, in order to obtain the basic physico-mechanical characteristics of tuff in the tunnel of Mila Mountain, rock ultrasonic testing, X-ray diffraction (XRD), microscopic observation, uniaxial compression test, and scanning electron microscope tests were carried out. The specific testing flow is depicted in Figure 2.

Firstly, vacuum saturation test was done on the sample numbered as SAT1~SAT5 by Rock Vacuum Saturation Meter DP-SJA at Rock Mechanics Laboratory of Chengdu University of Technology (CDUT), lasting for 72 h in order to make sure that the sample was in full saturation.

Secondly, the samples numbered as DRY1~DRY5, SAT1~SAT5 were tested by Automatic Acquisition Acoustic Detector FDP204-SW at the laboratory.

Thirdly, Diffractometer DMAX-3C and Jiangnan XP-213 Transmission Polarized Light Microscope from the test center of CDUT were used to observe the samples' compositions and microstructures under dry and saturated conditions. In X-ray diffraction test, small quantities of

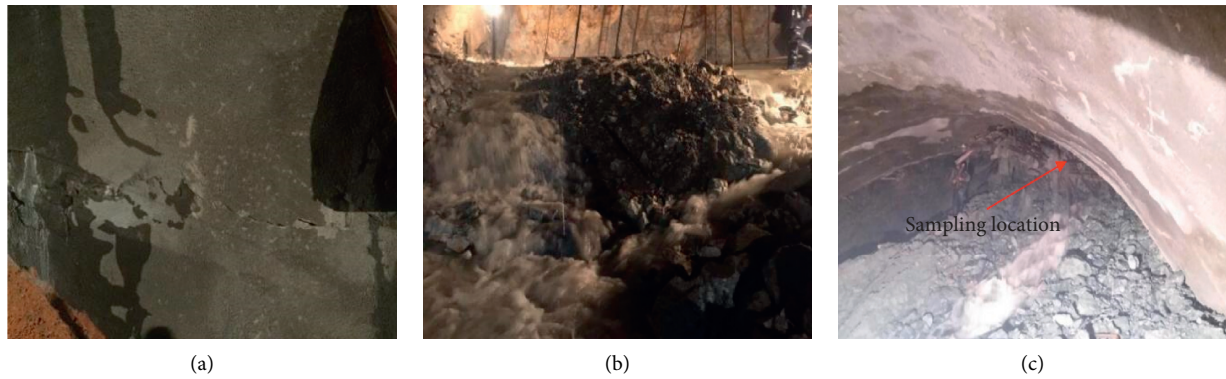


FIGURE 1: Images of initial supports cracking (a), water inrush phenomenon (b), and sampling points (c) of the Mila Mountain tunnel.

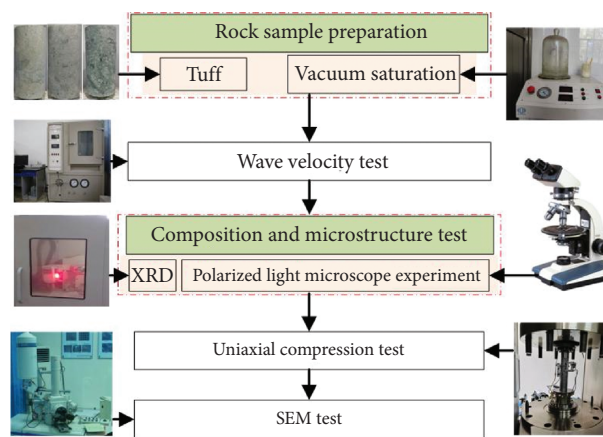


FIGURE 2: Experimental flowchart.

samples in each sample were ground into powders with the grain size within 5 mm; then, the fresh and unweathered powders were screened for cutting, grinding, gluing, slicing, and grinding to achieve the standard thickness, 30  $\mu\text{m}$ ; then, they were observed by microscope on the polarized light microscope experiment.

Fourth, uniaxial compression test was done by MTS815Teststar from the laboratory of CDUT. Grinding machine and abrasive paper were applied to grind both ends of the cylindrical samples whose height is 100 mm. Loading rate was controlled by displacement as recommended by International Society for Rock Mechanics (ISRM) in this test. Specifically, 1 kN force was preloaded to make the rock sample fixed; then, axial loading was carried out at the loading rate of 0.1 mm/min until the specimen was failure.

Finally, SEM was used to observe the typical blocks of tuff samples after the above tests using Electron Microscope (Hitachi S-3000N) from CDUT and further to reveal the microfractures characteristics.

### 3. Test Results and Analysis

**3.1. Analysis on Structure Characteristics.** Mineral compositions analysis, optical microscopic observation, and wave velocity testing were made on tuffs under dry and saturated conditions, in order to explain the effect of water on the

microstructure of tuffs in the tunnel of Mila Mountain. The results are shown in Table 1 and Figures 3 and 4.

As shown in Table 1, the compositions of tuffs in the tunnel of Mila Mountain contained quartz, clay minerals, plagioclase, anhydrite, pyrite, siderite, gypsum, K-feldspar, etc., of which quartz and clay minerals were in proportion of more than 90%. The mineral compositions of the tuffs were unchanged under dry and saturated conditions, while the proportions changed under two different conditions, which was due to water dissolution and corrosion; that is, the clay mineral content in the tuffs under saturated condition was lower 2% than that under dry condition, and quartz content increased by 3% in that case.

It can be seen from the rock slice on microscope in Figure 3 that the primary compositions of tuffs in the tunnel of Mila Mountain are volcanic glass (55%) and matrix (45%), of which matrix is mainly composed by microlite with grain diameter 10–20  $\mu\text{m}$  and little opaque mineral distributed in stellate with grain diameter 50–150  $\mu\text{m}$ , and volcanic glass is in the shape of nearly round or oval particles with grain diameter 100–250  $\mu\text{m}$ , or even 300–800  $\mu\text{m}$  for less, and the majority of volcanic glass experienced argillization; little is corroded and evolves into dissolved pore. Porosity of sheet is poor, and mainly composed of intragranular pores. Most of the pores are isolated and distributed sporadically, with the grain diameter 50–250  $\mu\text{m}$ , few can reach 300–400  $\mu\text{m}$  which



TABLE 1: Mineralogical composition of the tested tuff samples (weight %).

Sample no.	Quartz	Clay minerals	Plagioclase	Anhydrite	Pyrite	Siderite	Gypsum	K-feldspar
D-1	60	30	3	2	2	1	1	1
S-1	65	28	2	1	1	1	1	1

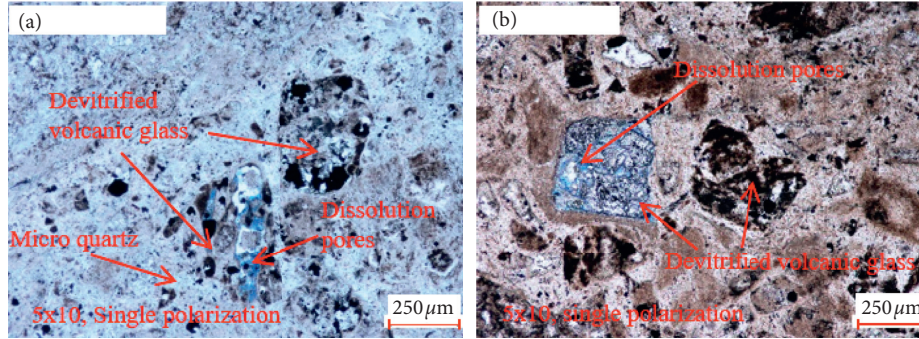


FIGURE 3: Polarized light microscopy image on the tunnel tuffs of Mila Mountain under dry and saturated conditions. (a) MLS-DRY. (b) MLS-SAT.

is formed after corrosion in the volcanic glass particles. By contrastive analysis, it can be found that corrosion happened interiorly in more volcanic glass after saturation, sheet porosity changed obviously, and surface porosity was increased from 1 to 2% under dry condition to 3–5% under saturated condition, confirming that tuffs porosity of tunnel in Mila Mountain increased after saturation and corrosion.

In Figure 4, the mean  $P$ -wave velocity of the tuffs under saturated condition in the range of 4600–4900 m/s is 4761 m/s, faster than 4681 m/s, that under dry condition in the range of 4500–4900 m/s, is increasing by 1.71%, which results from the fact that the solid-gas two-phase is changed into solid-liquid two-phase for the sample, while the propagation velocity of  $P$ -wave in water is faster than that in air; thus, the velocity increases.

**3.2. Analysis on Deformation and Fracture Characteristics.** As shown in Figures 5 and 6 in which stress-strain curves under uniaxial compression test on tuffs were depicted, the deformation curve can be divided into 4 phases, compaction, linear elasticity, peak, and postpeak. Due to porous tuffs, the first phase of compaction is generally evident; however, the compaction is not obvious in Figure 7; the stress-strain curve of sandstone, because sandstone is a typical kind of hard rock in sedimentary rocks, is featured with compact structure and primary pore inside the rock which are not developed [23]. In the experiment, the tuff porosity increased due to water corrosion and made the proportion increase at compaction phase under saturation condition. To further analyze the effect of microfracture on deformation at compaction phase, the ratio of the stress/strain value at compaction and peak phase was taken as the parameter for quantitative evaluation to calculate the proportion of compaction phase in the whole deformation process. Compared with Gao et al. [24], the stress/strain value is 0.000513 at the end phase of compaction for sandstone in

Figure 7, 0.011957 at peak phase, and the ratio is 4.3%; The value is 0.001 under dry condition at the end phase of compaction, the mean is 0.002387 at peak phase, and the ratio is 38.5%, while under saturated condition, it is 0.0012 at the end phase of compaction, the mean is 0.002387 at peak phase, and the ratio is 50.3%, respectively. The above results verified that tuff in the tunnel of Mila Mountain possessed high porosity, and water corrosion had positive relation with porosity, which was consistent with the observation result by polarized light microscopy.

Meanwhile, under dry and saturated conditions, the stress/strain for most of the tuff samples dropped vertically after experiencing peak stress, and the residual phases were indistinct. According to Wawersik analysis by uniaxial compression test in which stress-strain curve of rock can be classified into type I and II (Figure 8), type II was the unstable microfracture [25]; that is, the samples possessed strain storage capacity and released suddenly; without the aid of external force, fracture occurred and expanded within the samples, which was called as brittle fracture. In this experiment, tuff samples were brittle fracture under both conditions.

The macrofracture characteristics of tuff in the tunnel of Mila Mountain under dry and saturated conditions are shown in Figure 9. Overall, after uniaxial compression test, the 3 samples presented nearly vertical and thorough macrotensile fracture under dry condition, and DRY 3 developed several tensile fracture planes. Further analysis on DRY 3 was made, and the results are shown in Figure 9(c), in which the sample was fractured immediately into block masses and many tiny rocks after the rubber band was loosened, and lots of failure cracks spread within the main block, proving that the fracture was complete. Furthermore, fracture surface was smooth without powder, indicating that block slippage and friction did not occur after peak stress, in consistency with the conclusion that residual stress was indistinct. And the three samples presented similar features under saturated condition, but some secondary shear fracture planes developed.

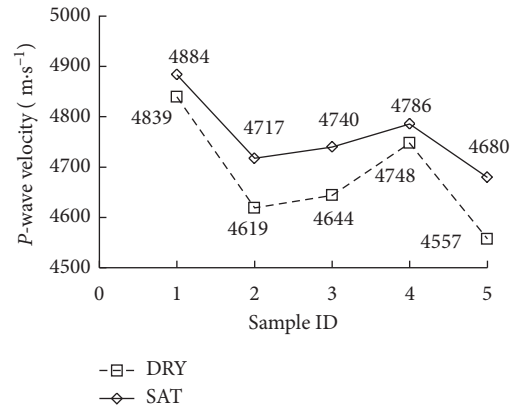


FIGURE 4: P-wave velocity test results of tuff in Mila Mountain tunnel under dry and saturated conditions.

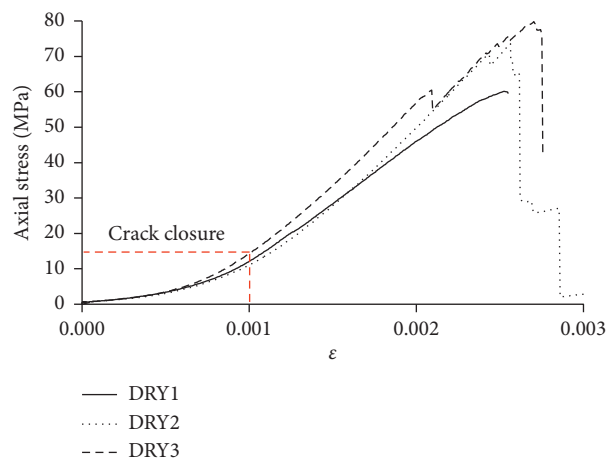


FIGURE 5: Tuff stress-strain curves under dry condition obtained from uniaxial compression test.

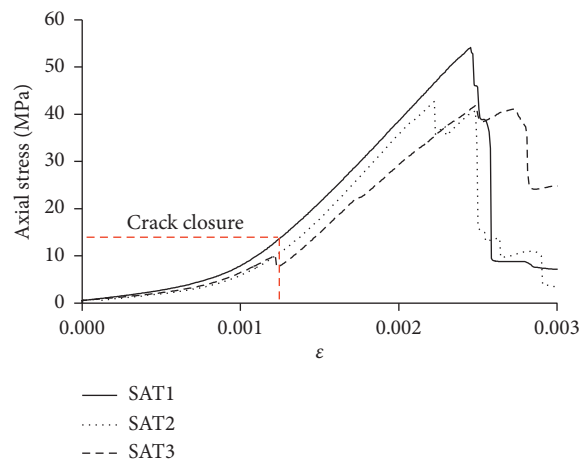


FIGURE 6: Tuff stress-strain curves under saturated condition obtained from uniaxial compression test.

It can be seen from the experiments of optical microscopic observation and wave velocity testing that the pore development of tuffs in the tunnel of Mila Mountain was the typical inhomogeneous media, and the fracture process was microcrack formation, development, and convergence with the occurrence, evolution of different types of cracks

including transcrystalline crack, intergranular crack, and the coupling. In Figure 10, typical samples of DRY 3 and SAT 1 after fracture were the objects for SEM to analyze the microstructure, fracture distribution characteristics of fracture surface, in which under dry condition, the tuff surface was coated with clay and the structure was compact, though the

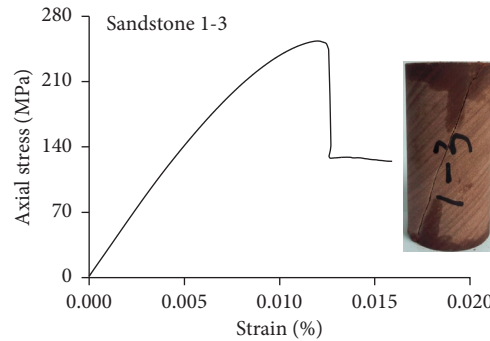


FIGURE 7: The stress-strain curve of a sandstone [24].

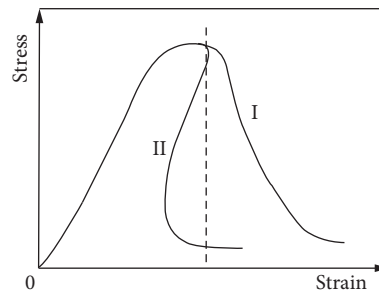


FIGURE 8: Rock failure types after uniaxial compression [25].

cracks with diameter  $300\ \mu\text{m}$  were observable on the surface, and clear cracks inside the tuff and transcrystalline crack, as well as few grains with diameter  $50\ \mu\text{m}$  on the surface when amplified, indicating that the mechanical behavior of the samples performed well to some extent. While under saturated condition, although the tuff surface was coated with clay as well, the structure was incompact, on which there were more pores and a mass of micro mineral grains with diameter  $300\ \mu\text{m}$ ; in addition, no observable cracks but distinct mineral grains with diameter  $50\ \mu\text{m}$  indenting can be found on the surface when amplified, indicating the poor mechanical behavior of the sample. Through comparison, the reason for the degraded mechanical behavior of tuff under saturated condition was that due to water corrosion, tuff porosity increased, then the structure became incompact, strength was lowered, and mechanical property was weakened, though no observable cracks were developed on the surface.

**3.3. Mechanical Parameter Analysis.** Figures 11 and 12 depicted the details of tuff in the tunnel of Mila Mountain under dry and saturated conditions at peak phase, in which the relationship between peak stress and strain at peak stress was positive in general, excluding SAT-3. Respectively, the mean peak stress was  $71.2\ \text{MPa}$  and  $46.2\ \text{MPa}$ , and the mean strain at peak stress was  $0.002595$  and  $0.002387$  under dry and saturated condition, revealing that the tuff mechanical behavior was degraded after saturation as the stress decreased by  $35\%$ , and the strain at peak stress decreased by  $8\%$ , compared with that under dry condition.

Figure 13 is the elastic modulus of tuff in the tunnel of Mila Mountain under dry and saturated conditions in which the mean elastic modulus was  $34.2\ \text{GPa}$  and  $19.8\ \text{GPa}$ , respectively, reduced by  $42\%$ , revealing that effect of water softening on the mechanical behavior of tuff was significant.

**3.4. Mechanism.** Mineral compositions and structural features were studied in this section to explain the mechanism that tuff was characterized by increased porosity, wave velocity, and lowered strength after saturation, which were concluded from the above experiments.

It can be learnt from Table 1 that clay minerals, accounting for larger proportion,  $30\%$ , in the tuff compositions, included several kinds of hydrophilic expansive minerals, such as montmorillonite, illite, and kaolinite. During saturation, illite can be transformed into clay mineral having high expansibility, for example, montmorillonite or kaolinite; on the other hand, due to the fact that for montmorillonite minerals, its lattice activity had a close relationship with the internal surface which can adsorb larger number of water molecules,  $c$ -axis interplanar crystal spacing can be fully expanded to  $600\ \text{\AA}$ , and the spacing was only  $9.6\ \text{\AA}$  under dry condition; montmorillonite minerals can be dispersed into single space unit in the extreme. Transformation and decomposition properties of hydrophilic expansive minerals of clay minerals in tuff led to the change of mineral structure and gradually grains aggregation (Figure 10(b)). With saturation time passing, grains swelled after fully submerged by water, and repulsive force was stronger than adsorption force between grains which had

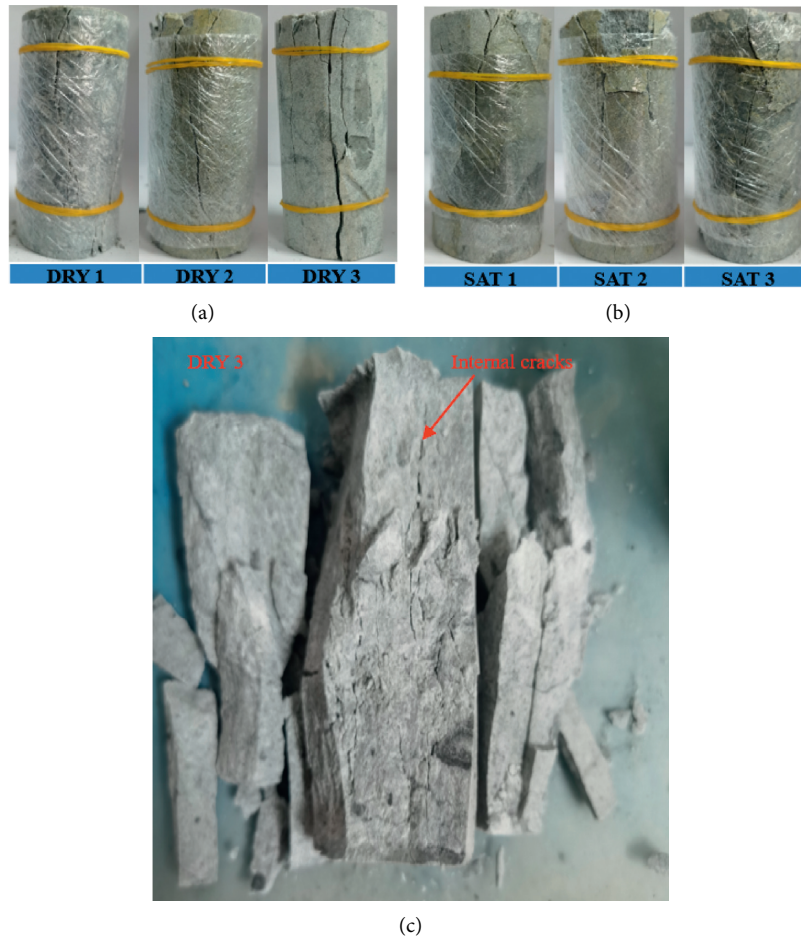


FIGURE 9: Macrofracture characteristic pattern of the tuffs in the tunnel of Mila Mountain after uniaxial compression.

thick hydration shells, leading to the structure failure and lower stress. In terms of rock structure, initial fissure, porosity developed well in the tuff sample, during saturation, water flowed into the sample along cracks and pores, then swelling, softening occurred; meanwhile, hydration shells absorbed on fine grains which were generated from water corrosion accelerated the volume swelling. The anisotropic swelling force made the anisotropic stress in the sample, triggering the change of pore structure and then grains movement, further swelling, softening, and disaggregation. In addition, cements in the sample contained  $K^+$ ,  $Na^+$ ,  $Ca^{2+}$ ,  $Mg^{2+}$ ,  $S^{2-}$ , and  $Cl^-$  ions, of which the soluble cements were dissolved or diluted after water and interaction; then, grains were disconnected and disaggregation occurred. After absorbing water, the phase state of the ions existing in pore solution changed and the ions were crystallized, leading to the sample volume swelling; for example, the chemical formula for anhydrite volume swelling was shown as  $CaSO_4 + 2H_2O \rightarrow CaSO_4 \cdot 2H_2O$ .

Finally, tuff in the tunnel of Mila Mountain contained a proportion of pyrite, a kind of mineral which was unstable, easy to weathering, and possessed strong reducibility. Fe and S in pyrite were reductive chemical elements of lower valence extremely easy to oxidation. Sulfuric acid generated from the oxidization of lower valence sulfur corroded the

tuff due to its acidity; further, it made combination reaction with other minerals; then, sulfate was produced. Sulfuric acid and sulfate were dissolved and washed away in water, accelerating tuff development and loosening the structure, which further provided passage for water into tuff.

According to the above analysis, the reason for the content reductions of clay minerals, anhydrite and pyrite, in the tuffs in the tunnel of Mila Mountain was water corrosion after saturation. The mechanism of water softening tuff was that soluble minerals in tuff were corroded and swelled after water; then new grains were generated and moved with the ions in pores, dissolving, loosening and softening the tuff structure; finally, its mechanical behavior was degraded.

#### 4. Constitutive Model on Tuff in the Tunnel of Mila Mountain

**4.1. Model Selection.** A reasonable constitutive model considering water softening effect is the key to accurate prediction and judgment of the reliability and stability of rock engineering, such as tunnel surrounding rock stability and water inrush numerical calculation. Therefore, the author would like to establish the constitutive model of tuff under dry and saturated conditions. Based on the experimental results of polarized light microscope experiment, tuff in the

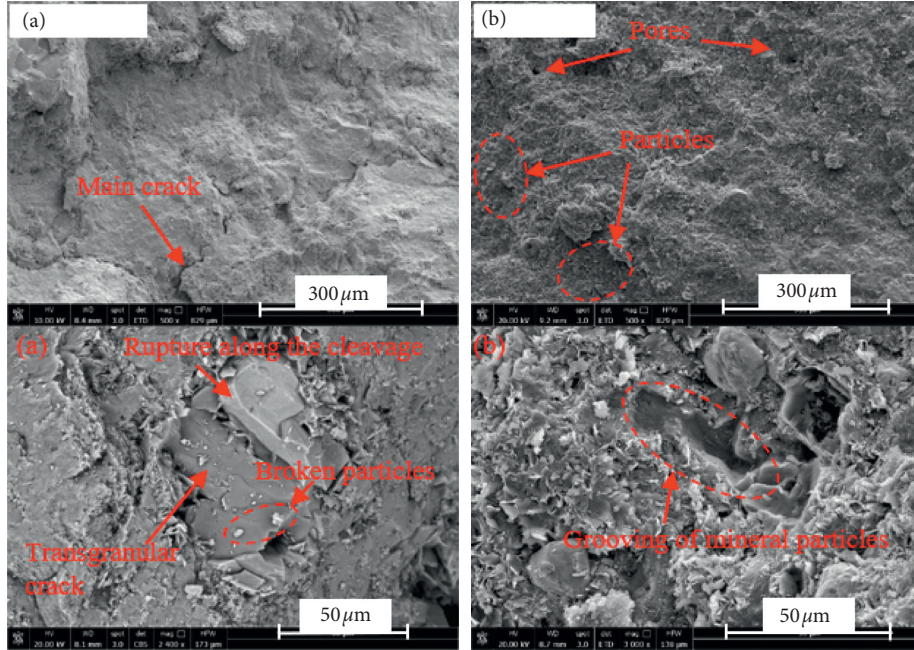


FIGURE 10: Microfracture characteristic pattern of the tuffs in the tunnel of Mila Mountain after uniaxial compression. (a) DRY 3. (b) SAT 1.

tunnel of Mila Mountain was the compacted combination of volcanoclastic material with diameter less than 3 mm, hydrolyzed materials by tephra or cemented clay materials, characterized by high porosity, fine granularity, and grains of large specific surface area. The conventional elasticity or elastic-plastic model failed to explain the deformation mechanism; nonlinearity and drop at postpeak on the stress-strain curve were distinct. Assumed that the microstructure of the rock presented masses of cracks and randomly distributed pores, damage statistical constitutive model could be applied to explain the nonlinear characteristic on the basis of interior defects in rock. Thus, considering the characteristics of high porosity and nonlinear stress-strain curves of the tuff in the Milashan tunnel, a damage statistical constitutive model was selected to describe the constitutive behavior of the tuff under dry and saturated water conditions.

**4.2. Model Building.** Researches on damage statistical constitutive model on rock have made great improvement, thanks to the introduction of damage statistical theory. According to the random distribution of defects in rock materials and Weibull distribution of microelement strength of rock, many scholars have established the corresponding statistical damage constitutive model of rock based on the results of rock compression tests [26–29]. The applicability of damage statistical constitutive model to tuff before and after saturation was explored, based on the previous studies. Affected by interior defects existing in rock such as random distributed pores, cracks, joints, etc., rock strength was undetermined and randomly changed. The strength of microelements was not exactly the same, and according to damage mechanism, the process was continuous from the

beginning of damage to failure. Therefore, there are assumptions as follows [30, 31]:

- (1) Rock is isotropy macroscopically.
- (2) Microelement has two states: failure and nonfailure.
- (3) Microelement before failure complies with Hooke's law.
- (4) Though strengths of microelements are not the same, but comply with Weibull distribution law, and its probability density function is

$$P(F) = \frac{m}{F_0} \left(\frac{F}{F_0}\right)^{m-1} \exp\left[-\left(\frac{F}{F_0}\right)^m\right], \quad (1)$$

where  $F$  is microelement strength and  $m$  and  $F_0$  are the parameters of Weibull distribution law, indicating the mechanical property of rock.

Continuous failures of microelements could degrade rock properties and induce fracture.  $N_f$  is the amount of damaged microelements on some stress condition, the ratio of the total amount of failures to the sum of microelements ( $N$ ) is called a statistical damage variable, and the equation is

$$D = \frac{N_f}{N}. \quad (2)$$

When the stress is set to be  $F$ , then the amount of the damaged microelements  $N_f$  is

$$N_f = \int_0^F N f(\sigma) d\sigma = N \int_0^F f(\sigma) d\sigma = N \left\{ 1 - \exp\left[-\left(\frac{F}{F_0}\right)^m\right] \right\}. \quad (3)$$

Damage variable  $D$  is calculated by substituting equation (3) into (2):

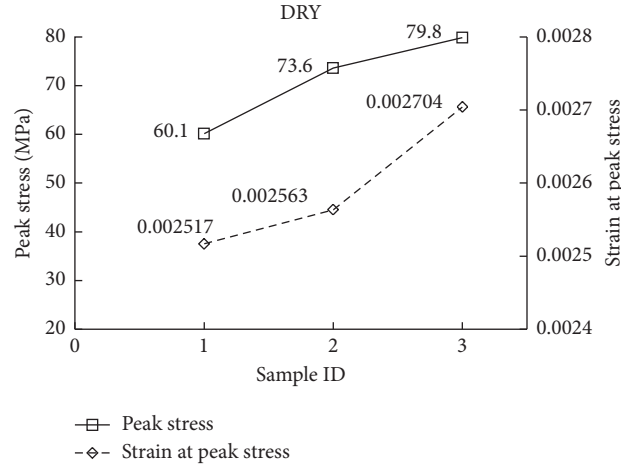


FIGURE 11: Pattern of the tuffs in the tunnel of Mila Mountain at peak phase under dry condition.

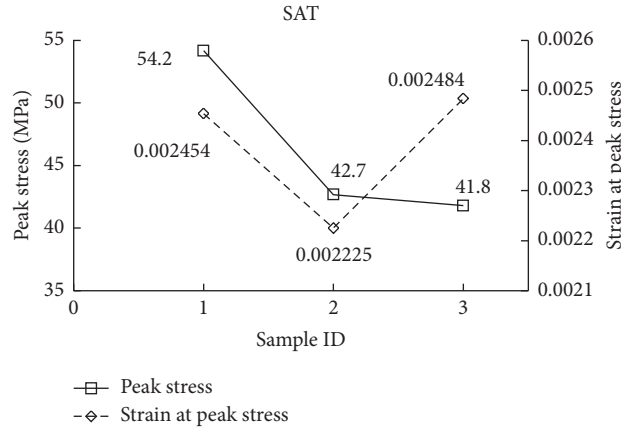


FIGURE 12: Pattern of the tuffs in the tunnel of Mila Mountain at peak phase under saturated condition.

$$D = 1 - \exp \left[ - \left( \frac{F}{F_0} \right)^m \right]. \quad (4)$$

$$\sigma_i = E \varepsilon_i \exp \left[ - \left( \frac{F}{F_0} \right)^m \right] + \mu (\sigma_j + \sigma_k). \quad (7)$$

Drucker-Prager law is taken to judge the microelement damage in rock; that is,

$$F = f(\sigma) = \alpha_0 I_1 + \sqrt{J_2}. \quad (5)$$

$\alpha_0 = \sin \varphi / \sqrt{9 + 3 \sin^2 \varphi}$ , of which  $I_1$  is the first invariant of stress tensor,  $J_2$  is the second invariant of stress tensor, and their calculations are shown as follows:

$$I_1 = \sigma_x^* + \sigma_y^* + \sigma_z^* = \sigma_1^* + \sigma_2^* + \sigma_3^*, \quad (6)$$

$$J_2 = \frac{1}{6} [(\sigma_1^* - \sigma_2^*)^2 + (\sigma_2^* - \sigma_3^*)^2 + (\sigma_3^* - \sigma_1^*)^2].$$

$F$ , the random variable, is selected to get damage statistical constitutive model, according to the Drucker-Prager law and strain equivalence theory of Lemaitre [30, 31], as follows:

According to the research results of Cao and Li [30, 31], constitutive parameters,  $m$  and  $F_0$ , are calculated below under uniaxial condition:

$$m = \frac{1}{\ln(E \varepsilon_c / \sigma_c)}. \quad (8)$$

$$\left( \frac{F_c}{F_0} \right)^m = \frac{1}{m}, \quad (9)$$

where  $E$  is elasticity modulus,  $\sigma_c$  is peak strength,  $\varepsilon_c$  is the strain at peak strength, and  $F_c$  corresponds to  $F$  at peak strength.

4.3. Model Verification. Through comparison between theory result and uniaxial test result on tuff samples from the tunnel of Mila Mountain under dry and saturated conditions, the constitutive model was verified as shown in Figure 14 in which

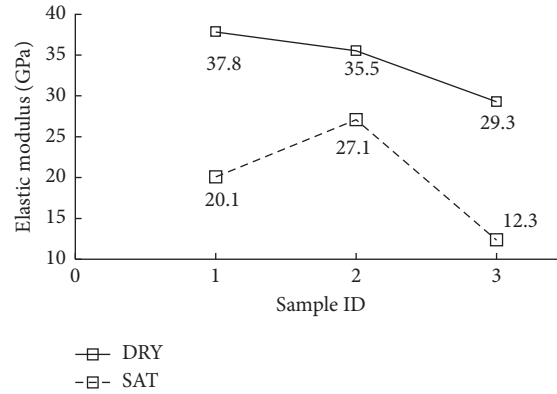


FIGURE 13: Elastic modulus of tuff in the tunnel of Mila Mountain under dry and saturated conditions.

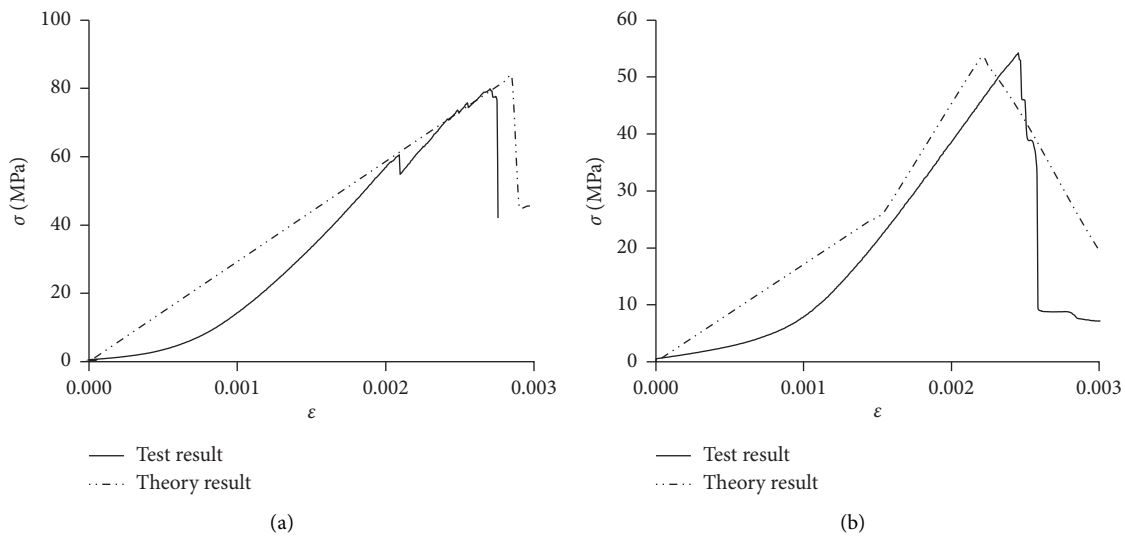


FIGURE 14: Experimental and theoretical stress-strain curves under dry and saturated conditions. (a) DRY 3. (b) SAT 1.

the two curves, test result and theory result, matched well in general, indicating that damage statistical constitutive model was applicable to express tuff constitutive behaviors.

## 5. Conclusion

This paper, in order to provide some theoretical and data support for the construction of tuff tunnel, the physico-mechanical parameters, failure mechanism, and constitutive model of tuff in Mila Mountain tunnel under dry and saturated conditions were studied by experimental and theoretical analytical methods. According to the experimental results, water softening mechanism and mechanical characteristics have been analysed under dry and saturated conditions; then, the stress-strain curves from tests were simulated by a damage statistical constitutive model; finally, the conclusion can be made as follows.

(1) Quartz and clay minerals were dominated in tuff compositions in the tunnel of Mila Mountain, accounting for more than 90%, and quartz content

increased after saturation, while clay minerals content was reduced.

- (2) Soluble minerals were corroded in the tuff after saturation, and porosity and wave velocity increased; however, elasticity modulus and peak strength were lowered severely, reaching 42% and 35%, respectively.
- (3) The mechanical characteristics of tuff after saturation were determined by the mineral compositions and structure characteristics of tuff in the tunnel of Mila Mountain; specifically, as the tuff characterized by high porosity convenient for water infiltration, the soluble minerals in the tuff were corroded and swelled by water; then, new grains were generated and moved with the ions in pores, dissolving, loosening, and softening the tuff structure; then, its mechanical properties were degraded.
- (4) Theory result and test result matched well under dry and saturated conditions, revealing that damage statistical constitutive model was applicable to

express the constitutive behavior of tuff in the tunnel of Mila Mountain.

## Data Availability

The datasets used and analysed during this study are included within the manuscript.

## Conflicts of Interest

None of the authors have any conflicts of interest regarding the publication of this study.

## References

- [1] E. Emir, A. Konuk, and G. Daloğlu, "Strength enhancement of Eskisehir tuff ashlar in Turkey," *Construction and Building Materials*, vol. 25, no. 7, pp. 3014–3019, 2011.
- [2] C. Di Benedetto, P. Cappelletti, M. Favaro et al., "Porosity as key factor in the durability of two historical building stones: neapolitan yellow tuff and Vicenza stone," *Engineering Geology*, vol. 193, pp. 310–319, 2015.
- [3] S. Peng, X. Li, Z. Wu, J. Chen, and X. Lu, "Study of the key technologies of application of tuff powder concrete at the Daigo hydropower station in Tibet," *Construction and Building Materials*, vol. 156, pp. 1–8, 2017.
- [4] A. Ababneh and F. Matakah, "Potential use of Jordanian volcanic tuffs as supplementary cementitious materials," *Case Studies in Construction Materials*, vol. 8, pp. 193–202, 2018.
- [5] B. Balegh, H. Sellaf, and A. Hadjmostefa, "Effect of ceramic waste on mechanical and geotechnical properties of tuff treated by cement," *Case Studies in Construction Materials*, vol. 13, Article ID e00368, 2020.
- [6] A. Yassaghi, H. Salari-Rad, and H. Kanani-Moghadam, "Geomechanical evaluations of Karaj tuffs for rock tunneling in Tehran-Shomal Freeway, Iran," *Engineering Geology*, vol. 77, no. 1-2, pp. 83–98, 2005.
- [7] M. B. Gray, J. A. Stamatakos, D. A. Ferrill, and M. A. Evans, "Fault-zone deformation in welded tuffs at Yucca Mountain, Nevada, USA," *Journal of Structural Geology*, vol. 27, no. 10, pp. 1873–1891, 2005.
- [8] T. Topal and V. Doyuran, "Engineering geological properties and durability assessment of the Cappadocian tuff," *Engineering Geology*, vol. 47, no. 1-2, pp. 175–187, 1997.
- [9] T. Esaki and K. Jiang, "Comprehensive study of the weathered condition of welded tuff from a historic stone bridge in Kagoshima, Japan," *Engineering Geology*, vol. 55, pp. 121–130, 1999.
- [10] A. Çavdar and Ş. Yetgin, "Availability of tuffs from northeast of Turkey as natural pozzolan on cement, some chemical and mechanical relationships," *Construction and Building Materials*, vol. 21, no. 12, pp. 2066–2071, 2007.
- [11] M. U. Toprak and M. A. Arslanbaba, "Possibility of using Kütahya volcanic tuff as building stone: microstructural evaluation and strength enhancement through heat treatment," *Construction and Building Materials*, vol. 110, pp. 128–134, 2016.
- [12] E. Ekinci, I. Türkmen, F. Kantarci, and M. B. Karakoç, "The improvement of mechanical, physical and durability characteristics of volcanic tuff based geopolymers by using nano silica, micro silica and styrene-butadiene latex additives at different ratios," *Construction and Building Materials*, vol. 201, pp. 257–267, 2019.
- [13] Y. Hadj aissa, I. Goual, and B. Benabed, "Mix-design and properties of self-compacting concrete made with calcareous tuff," *Journal of Building Engineering*, vol. 27, Article ID 100997, 2020.
- [14] M. Korkanç and B. Solak, "Estimation of engineering properties of selected tuffs by using grain/matrix ratio," *Journal of African Earth Sciences*, vol. 120, pp. 160–172, 2016.
- [15] Y. G. Xiao, C. H. Li, J. Cao, Y. Wang, Z. Q. Hou, and N. Hu, "Investigation of the effects of freeze-thaw cycles on geomechanical and acoustic characteristics of tuff specimens under different stress paths," *Advances in Civil Engineering*, vol. 2020, Article ID 6689181, 20 pages, 2020.
- [16] T. Topal and B. Sözmen, "Deterioration mechanisms of tuffs in Midas monument," *Engineering Geology*, vol. 68, no. 3-4, pp. 201–223, 2003.
- [17] R. Salve, J. S. Y. Wang, and C. Doughty, "Liquid-release tests in unsaturated fractured welded tuffs: I. Field investigations," *Journal of Hydrology*, vol. 256, no. 1-2, pp. 60–79, 2002.
- [18] C. Doughty, R. Salve, and J. S. Y. Wang, "Liquid-release tests in unsaturated fractured welded tuffs: II. Numerical modeling," *Journal of Hydrology*, vol. 256, no. 1-2, pp. 80–105, 2002.
- [19] M. Beiki, A. Majidi, and A. D. Givshad, "Application of genetic programming to predict the uniaxial compressive strength and elastic modulus of carbonate rocks," *International Journal of Rock Mechanics and Mining Sciences*, vol. 63, pp. 159–169, 2013.
- [20] J. W. Martin, J. T. Fredrich, C. W. Felice, and S. J. Green, "Mechanical properties and microstructure of shock-conditioned tuff," *International Journal of Rock Mechanics and Mining Science & Geomechanics Abstracts*, vol. 30, no. 7, pp. 669–675, 1993.
- [21] L. Li, Y. Tan, B. Huang, and X. Deng, "Pore property as an indicator of macro-deterioration in slightly weathered tuffs," *Engineering Geology*, vol. 267, Article ID 105492, 2020.
- [22] T. C. Chen, M. R. Yeung, and N. Mori, "Effect of water saturation on deterioration of welded tuff due to freeze-thaw action," *Cold Regions Science and Technology*, vol. 38, no. 2-3, pp. 127–136, 2004.
- [23] Y. Togashi, T. Imano, M. Osada, K. Hosoda, and K. Ogawa, "Principal strain rotation of anisotropic tuff due to continuous water-content variation," *International Journal of Rock Mechanics and Mining Sciences*, vol. 138, Article ID 104646, 2021.
- [24] M. B. Gao, T. B. Li, L. B. Meng, C. C. Ma, and H. L. Xing, "Identifying crack initiation stress threshold in brittle rocks using axial strain stiffness characteristics," *Journal of Mountain Science*, vol. 15, no. 6, pp. 1371–1382, 2018.
- [25] W. R. Wawersik and C. Fairhurst, "A study of brittle rock fracture in laboratory compression experiments," *International Journal of Rock Mechanics and Mining Science and Geomechanics Abstracts*, vol. 7, no. 5, pp. 561–575, 1970.
- [26] D. Krajcinovic and M. A. G. Silva, "Statistical aspects of the continuous damage theory," *International Journal of Solids and Structures*, vol. 18, no. 7, pp. 551–562, 1982.
- [27] J. Lemaitre, "A continuous damage mechanics model for ductile fracture," *Journal of Engineering Materials and Technology*, vol. 107, no. 1, pp. 83–89, 1985.
- [28] X. Li, W. G. Cao, and Y. H. Su, "A statistical damage constitutive model for softening behavior of rocks," *Engineering Geology*, vol. 143–144, pp. 1–17, 2012.
- [29] M. Gao, T. Li, T. Wei, and L. Meng, "A statistical constitutive model considering deterioration for brittle rocks under a coupled thermal-mechanical condition," *Geofluids*, vol. 2018, Article ID 3269423, 10 pages, 2018.



- [30] W. G. Cao and X. Li, "A new discussion on damage softening statistical constitutive model for rocks and method for determining its parameters," *Rock and Soil Mechanics*, vol. 29, no. 11, pp. 2952–2956, 2008.
- [31] M. H. Yang, M. H. Zhao, and W. G. Cao, "Method for determining the parameters of statistical damage softening constitutive model for rock," *Journal of Hydraulic Engineering*, vol. 36, no. 3, 2005.